# Quasi-Static Impact of Foldcore Sandwich Panels


**Joseph M. Gattas**

Magdalen College

A thesis submitted for the degree of Doctor of Philosophy in the Department of Engineering Science, University of Oxford.

Trinity Term, 2013

# Abstract

## Quasi-Static Impact of Foldcore Sandwich Panels

Joseph M. Gattas

Magdalen College

A thesis submitted for the degree of Doctor of Philosophy in the Department of Engineering Science, University of Oxford. Trinity Term, 2013.

This thesis considered the design of new and improved foldcore sandwich panels suitable for high-performance energy absorption applications. This was achieved by utilising origami geometry design techniques to alter foldcore structures such that they possessed different mechanical behaviours and failure modes. The major findings of this thesis were in three areas as follows.

First, a modified planar foldcore geometry was developed by introducing sub-folds into a standard foldcore pattern. The new geometry, deemed the *indented foldcore*, successfully triggered a high-order failure mode known as a travelling hinge line failure mode. This was found to have a much higher energy absorption than the plate buckling failure mode seen in an unmodified foldcore structure. A comprehensive numerical, theoretical, and experimental analysis was conducted on the indented core, which included the development of a new foldcore prototyping method that utilised 3D printed moulds. It was shown that compared to available commercial honeycomb cores, the indented foldcore had an improved uniformity of energy absorption, but weaker overall peak and crushing stresses.

Second, rigid origami design principles were used to develop extended foldcore geometries. New parametrisations were presented for three patterns, to complete a set of Miura-derivative geometries termed *first-level derivatives*. The first-level derivative parametrisations were then combined to create complex, *piecewise geometries*, with compatible faceted sandwich face geometry also developed. Finally, a method to generate rigid-foldable, *curved-crease geometry* from Miura-derivative straight-crease geometry was presented. All geometry was validated with physical prototypes and was compiled into a MATLAB Toolbox.

Third, the performance of these extended foldcore geometries under impact loadings was investigated. An investigation of *curved-crease foldcores* showed that they were stronger than straight-crease foldcores, and at certain configurations can potentially match the strength, energy-absorption under quasi-static impact loads, and out-of-plane stiffness of a honeycomb core. A brief investigation of foldcores under low-velocity impact loadings showed that curved-crease foldcores, unlike straight-crease foldcores, strengthened under dynamic loadings, however not to the same extent as honeycomb. Finally, an investigation of single-curved *foldcore sandwich shells* was conducted. It was seen that foldcore shells could not match the energy-absorption capability of an over-expanded honeycomb shell, but certain core types did exhibit other attributes that might be exploitable with future research, including superior initial strength and superior uniformity of response.

**Keywords:** quasi-static impact, foldcore, folded shell structures, curved-crease, origami, single-curved sandwich shell.

# Acknowledgements

This thesis would not have been possible without the ongoing personal, professional, and financial support provided to me by friends, family, and colleagues.

Within the Department of Engineering Science, I would like to thank my supervisor Dr. Zhong You and post-doctoral student Jiayao Ma, whose guidance and advice has led my work into unexpected and exciting areas. For their advice in constructing and testing prototypes, I would also like to thank Igor Dyson, Bob Scott, Maurice Keeble-Smith, Cleveland Williams, Clive Baker, and technicians in the Workshop and Stores. I would also like to thank my fellow graduates, both in Engineering Science and at Magdalen College, for their social and academic interest and support.

I am also extremely grateful for the financial support provided by the Sir General John Monash Award, without which this thesis would not have been possible. My thanks also to DSTL for project grant CDE28201, which enabled construction of the prototypes tested in the thesis.

Finally, I would like to thank my exceedingly patient girlfriend Lizzie Cowley and my parents Michael and Therese, brothers Nicholas and Benedict, and sister Susannah, who have all provided phenomenal encouragement from afar.

# Contents

# Figures

# Tables

# Nomenclature

| | |
|---|---|
| $a$ | Pattern constant: straight side length |
| $a_s, a_i$ | Standard and indented side lengths. |
| $b$ | Pattern constant: zigzig side length. |
| $b^*$ | Dimensionless aspect ratio. |
| $c_1$,$c_2$ | Unit vectors aligned to pattern folded directions. |
| $c, d$ | Elliptical curve scale parameters. |
| $d_w$ | Foldcore shell width. |
| $g, h$ | Elliptical curve shift parameters. |
| $h_d$ | Crush depth. |
| $h^*$ | Dimensionless crush strain. |
| $i, i'$ | Straight crease line counters. |
| $j$ | Zigzag crease line counter. |
| $k, k'$ | Subdivided curved-crease line counters. |
| $l$ | Faceted face length. |
| $l_a, l_b, l_t$ | Unit length, width and height. |
| $m, n$ | Pattern constants: number of straight and zigzag crease lines. |
| $p^*$ | Dimensionless indented ratio. |
| $q$ | Toroidal radius. |
| $r, \theta$ | Cylindrical coordinate system. |
| $r$ | Travelling hinge radius. |
| $s$ | Honeycomb cell size or total curved-crease split line count. |
| $t_p$ | Plate thickness. |
| $t_f$ | Face thickness. |

$u, v, w$ 3D Cartesian coordinate system of elliptical curve vertices.

$v$ Material Poisson's ratio.

$w$ Pattern constant: unfolded plate width.

$\bar{w}$ Pattern variable: folded width.

$x, y, z$ 3D Cartesian coordinate system for pattern vertices.

$A_p$ Plate area.

$E$ Young's Modulus.

$E_o$ Out of plane stiffness.

$E_1, E_2, E_3$ Energy absorption contributors.

$\dot{E}$ Rate of energy absorption.

$E^*$ Dimensionless energy absorption parameter.

$K, J$ Curved-crease rigid panel row and column count.

$L, W, H$ Global length, width and height.

$M_o$ Material plastic bending moment per unit length.

$N_o$ Material compressive strength per unit length.

$P$ Crush force.

$P^*$ Normalised crush force.

$R$ Pattern variable: folded radius.

$U^*$ Dimensionless uniformity ratio.

$V_t$ Tangential plate velocity.

$V$ Unit volume.

$V_p$ Core plate volume.

$V^{i,j}$ Pattern vertex at the intersection of the $i^{th}$ and $j^{th}$ crease lines.

$W^{p,j}$ Pattern vertex at the intersection of the $p^{th}$ and $j^{th}$ crease lines.

$\alpha$ Pattern variable: local panel rotation angle.

$\gamma$ Pattern variable: lateral panel rotation angle.

$\delta$ Crush plate displacement.

$\dot{\delta}$ Crush plate velocity.

$\varepsilon_o$ Out of plane strain.

| | |
|---|---|
| $\phi$,$\phi_w$ | Pattern constants: sector angles. |
| $\eta_A$ | Pattern variable: longitudinal edge angle. |
| $\eta_Z$ | Pattern variable: lateral edge angle. |
| $\theta_A$ | Pattern variable: longitudinal dihedral angle. |
| $\theta_Z$ | Pattern variable: lateral dihedral angle. |
| $\kappa$ | Toroidal longitudinal rotation angle. |
| $\varphi$ | Pattern constant: curved-crease gradient. |
| $\rho$ | Pattern constant: polar rotation angle. |
| $\bar{\rho}$ | Pattern variable: folded polar rotation angle. |
| $\sigma, \sigma^*$ | Crush stress or dimensionless crush stress. |
| $\sigma_U$ | Material ultimate stress. |
| $\sigma_Y$ | Material yield stress. |
| $\sigma_o$ | Material flow stress. |
| $\tau$ | Toroidal lateral rotation angle. |
| $\xi, \xi_{a2}, \xi_{b1}$ | Pattern variables: longitudinal panel rotation angles. |
| $\zeta, \zeta_k$ | Pattern variables: lateral panel rotation angles. |
| $^{m}$,$^{s}$ | Superscripts denoting master and slave pattern parameters. |
| $^{A}$ | Superscript denoting Arc pattern parameter. |
| $^{AM}$ | Superscript denoting Arc-Miura pattern parameter. |
| $^{ND}$ | Superscript denoting Non-Developable Miura pattern parameter. |
| $^{NF}$ | Superscript denoting Non-Flat Foldable Miura pattern parameter. |
| $_{1,2}$ | Subscripts denoting alternate pattern edge parameters. |
| $_{avg}$ | Subscript denoting average parameter value. |
| $_{c,f}$ | Subscripts denoting close or far pattern edge parameters. |
| $_{d}$ | Subscript denoting parameter value at densification strain. |
| $_{i,o}$ | Subscripts denoting inner or outer pattern edge parameters. |
| $_{j}$ | Subscript denoting parameter at $j^{th}$ zigzag crease. |
| $_{min}$, $_{max}$ | Subscript denoting minimum and maximum parameter value. |
| $_{s,l}$ | Subscripts denoting short or long pattern edge parameters. |
| $_{M,V}$ | Subscripts denoting mountain or valley crease parameters. |

# Chapter 1

# Introduction

## 1.1 Rigid Origami Geometry and Foldcores

Rigid origami are a set of origami patterns that permit continuous motion between folded states without the need for twisting or stretching of the facets between the creases (Tachi, 2009). As such, they can be readily manufactured from rigid engineering sheet materials such as timber (Weinand, 2009), metal (Schenk *et al.*, 2011), or composites (Heimbs *et al.*, 2010). Among many rigid origami patterns, the Miura pattern is one of the most commonly used in engineering, architectural, and design applications, as it possesses additional useful characteristics including developability, flat-foldability, and a planar single degree-of-freedom kinematic mechanism.

Alterations to Miura pattern attributes allows for the creation of derivative rigid-foldable patterns with a larger range of surface geometries, including non-zero single and double curvature (Khaliulin, 2005). Miura and Miura-derivative patterns have been used for many recent applications, including deployable folded plate shelters (De Temmerman *et al.*, 2007; Künstler and Trautz, 2011; Gioia *et al.*, 2012), sub-sea pipelines (Albermani *et al.*, 2011), and vehicle crash boxes (Ma and You, 2011). However their most prevalent engineering use is seen in foldcore

sandwich panels (Miura, 1972).

Foldcore sandwich panels consist of a partially folded core based on the Miura pattern, which is then sandwiched between two stiff facings, Figure 1.1. They have recently been investigated in the aerospace and composite engineering industries as a potential substitute to honeycomb panels, as they possess a number of favourable properties that are not possible with other types of high-performance sandwich panel, including ready adaptation for curved profiles, continuous internal channels that prevent moisture build-up (Heimbs, 2013), isotropic strength coefficients (Miura, 1972), and the ability to continuously manufacture foldcores from an unfolded sheet (Kling, 2006).

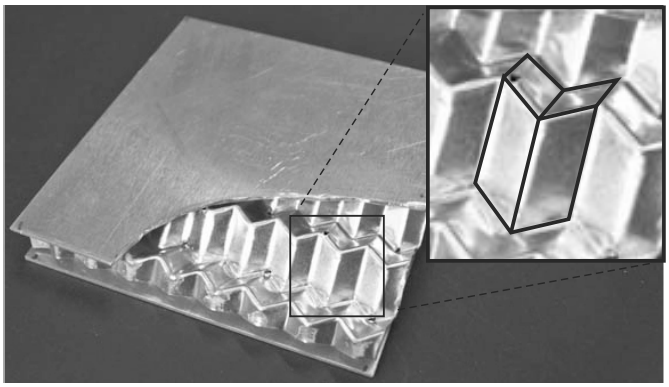

Figure 1.1: Foldcore sandwich panel with Miura core pattern.

## 1.2 Energy-Absorbing Sandwich Panels

Energy-absorbing devices are employed in a wide range of everyday situations to reduce the risk of injury and damage to impacting objects, be they pedestrians, cyclists, vehicles, or structures. Many of these devices are required to absorb a maximum of energy with a minimum weight, and in these cases energy-absorbing sandwich panels can be utilised.

Applications of such panels can be found in aerospace structures, where impact-resistant components include the nosecone, wing leading edge, engine nacelle, vertical and horizontal stabiliser leading edges, fuselage, and front and rear bulkheads

of an aeroplane, Figure 1.2. These components must resist bird-strike, explosion, or crash loads, and in many cases are required to further withstand high static loads. There are also many potential applications in vehicle safety systems, where thin panel components that are required to absorb energy include the car bonnet, to protect pedestrians, cyclists, and motorists during front-on collisions; and door panels to protect the vehicle occupants during side-on collisions.

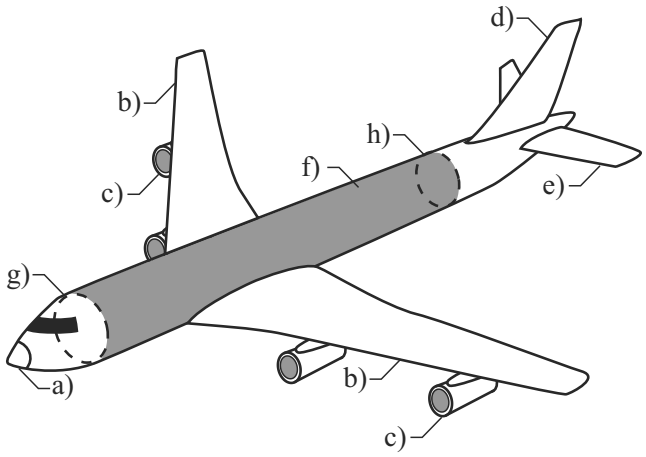


Figure 1.2: Impact resistant aircraft components a) nosecone, b) wing leading edge, c) engine nacelle, d) and e) vertical and horizontal stabiliser leading edges f) fuselage structure, g) and h) front and rear pressure bulkheads.

Hexagonal honeycomb core sandwich panels are often used for these high-performance applications, as they possess very efficient static properties and a high energy-absorbing failure mode. These have been successfully tested as energy-absorbing components of aircraft (Meng *et al.*, 2009) and vehicles (Asadi *et al.*, 2007), but suffer several drawbacks, including a non-uniform failure mode and anticlastic curvature when bent. This last attribute is particularly problematic, as many of the above mentioned components require single or double-curvature. Several honeycomb variants have been designed to overcome this anticlastic behaviour (Hexcel Corporation, 1999), however the available core geometries and shell curvatures are limited. Moreover, the honeycomb shapes have to be severely distorted to form curved surfaces.

Numerous studies have suggested the possibility of developing curved foldcore panel geometry using origami design techniques (Miura, 1972; Nojima and Saito,

2006; Fischer *et al.*, 2009; Talakov, 2010; Alekseev, 2011; Künstler and Trautz, 2011), however the mechanical performance of such structures remains an unexplored area.

## 1.3 Aim, Scope, and Layout

The aim of this dissertation is to design new and improved foldcore sandwich panels suitable for high-performance energy-absorption applications. It is achieved by utilising origami geometry design techniques to alter core structures in order to achieve different mechanical behaviours and failure modes. The focus of the thesis is on aluminium foldcores, which possess ductile failure modes. This thesis is also limited to the consideration of Miura-derivative rigid origami geometry, as the majority of existing foldcores possess a basic Miura core geometry.

The thesis structure consists of four chapters as follows. Chapter 2 is a literature review encompassing research in the two areas of energy-absorbing sandwich panels and origami geometry. In the first area, particular focus is given to sandwich panels used in energy-absorbing applications. In the second area, particular focus is given to rigid origami geometry and Miura-derivative origami patterns.

Chapter 3 shall use origami design techniques to develop a modified foldcore geometry that has much-improved energy absorption attributes. The new geometry, deemed the indented foldcore, is first analysed with an extensive numerical and theoretical investigation. Two experimental studies are then conducted on the new geometry, with the second study developing a new manufacturing method that utilises 3D printed moulds. Comparisons are made with both existing foldcores and commercially available aluminium honeycomb cores.

Chapter 4 covers three topics related to the development of extended foldcore geometry. New parametrisations for three rigid plate geometries are presented. These complete a set of Miura-derivative geometries termed first-level derivatives,

generated by altering a single characteristic of a base Miura pattern. It will then be shown how these can be combined with compatible core and face geometry to form complex sandwich panel assemblies with a minimum parametrisation. Finally, a method to generate rigid-foldable curved-crease geometry from Miura-derivative geometry is presented. All geometry presented in the chapter is validated with physical prototypes and is compiled into a MATLAB Toolbox.

Chapter 5 examines the application and performance of extended foldcore geometry by applying the manufacturing and numerical analysis methods developed in Chapter 3 to the extended geometries developed in Chapter 4. Four studies are conducted: the quasi-static impact resistance of planar curved-crease foldcores, the out-of-plane stiffness and dynamic impact loading of planar foldcores, the performance of selected planar foldcores in complete sandwich panel assemblies, and the performance of single-curved foldcore sandwich shells. Where possible, comparisons between new foldcore designs and existing honeycomb panels are made.

Conclusions and discussion on future work are given in Chapter 6, which concludes the dissertation.

# Chapter 2

# Literature Review

## 2.1 Energy-Absorbing Sandwich Structures

### 2.1.1 General Principles

A large range of protective structures and devices are employed in every day situations to reduce the risk of injury and damage to people, property, and the environment. Typically this damage arises from a low or high-speed impact between different objects, be they pedestrians, cyclists, vehicles, or structures. All energy absorption devices are designed to convert the kinetic energy from these impacts into a different, less damaging forms of energy during contact. Regardless of application or form, a good energy absorption device should have the following properties (Lu and Yu, 2003):

- *Irreversible energy conversion:* Energy absorbers should convert kinetic energy to inelastic energy to avoid elastic snapback.
- *Restricted and constant reactive force:* A low peak force, $P_{max}$ limits peak acceleration and a constant reactive force, $P_{avg}$ avoids high rates of deceleration.

- *Long stoke:* An increase in crush displacement $h_d$ equals an increase work done by the energy absorber.
- *Lightweight with high Specific Energy Absorption capacity (SEA):* SEA is defined as the energy absorbed per unit mass.
- *Stable and repeatable deformation mode:* Generally impacts have uncertain working loads, so energy absorbers must work reliably across range of loading conditions.
- *Low cost and ease of installation:* Typically energy absorbers are single-use devices, and need to be replaced after every accident.

The performance of a device in the first four metrics can be assessed using its force-displacement response, measured as the reacting force on an object when impacting the energy-absorbing device. Two results on this plot are of key interest: the maximum crush force $P_{max}$, and average crush force $P_{avg}$. Good energy-absorbing devices should have a low maximum force $P_{max}$ to limit damaging peak accelerations, and a high, constant average force $P_{avg}$, paired with a long stroke prior to reaching the densification region $h_d$, in order to absorb maximum impact energy, defined as $E = P_{avg}h_d$. The ratio of maximum to average crush force is defined as the uniformity ratio $U$, with ideal energy-absorbing devices possessing a ratio approaching unity, corresponding to a rectangular profile on a force-displacement plot. These values are highlighted on the force-displacement plot generated from the crush of a honeycomb cell under out-of-plane impact, Figure 2.1.

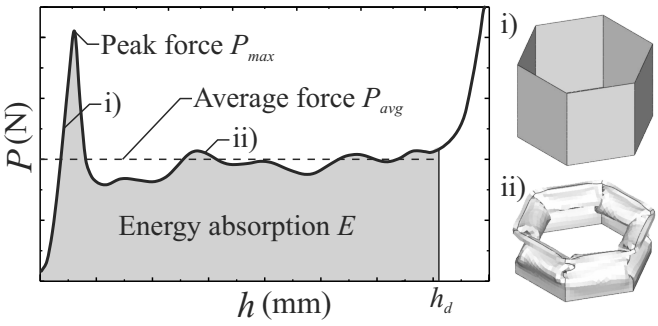


Figure 2.1: Force-displacement response and failure mode of a honeycomb cell.

### 2.1.2 Energy Absorbing Sandwich Panels

The structural sandwich panel was one of the first lightweight and high-performance structural elements developed by engineers (Gay and Hoa, 2007). Consisting of two thin facings bonded to a lighter core, sandwich panels were initially used because they possess a very high weight-specific bending stiffness. However, sandwich panels have subsequently been found to be capable of possessing high weight-specific energy absorption properties, and have therefore been employed in related applications. For example, multi-layered corrugated fibreboard sandwich panels can be used in packaging applications, due to their low cost and their near-uniform force-displacement response under impact loadings (Rouillard and Sek, 2007; Wang *et al.*, 2011). Selected sandwich cores with notable energy-absorbing attributes are briefly discussed below.

#### Eggbox Core

Eggbox cores are a type of core structure that can be designed to have a very efficient energy-absorbing failure mode. At certain configurations, the eggbox core possesses a *travelling hinge line* failure mode, in which shell inversion occurs at the narrow end of the conical eggbox unit and propagates through the core along a circular travelling hinge line (Deshpande and Fleck, 2003). This plasticizes a large area of core material twice, once as it rolled into the travelling hinge line and again when it unrolled out of the travelling hinge line, and as such absorbs large amounts of energy. The core exhibits a low reaction force at the initial inversion, and then the reaction force gradually increases as the travelling hinge line expands across a larger cross-section of the conical unit, Figure 2.2. The failure mode is very sensitive to imperfections, which causes the core to revert to a non-symmetric failure mode. This sensitivity is a problematic attribute for an energy absorbing device and so the eggbox core is rarely employed.

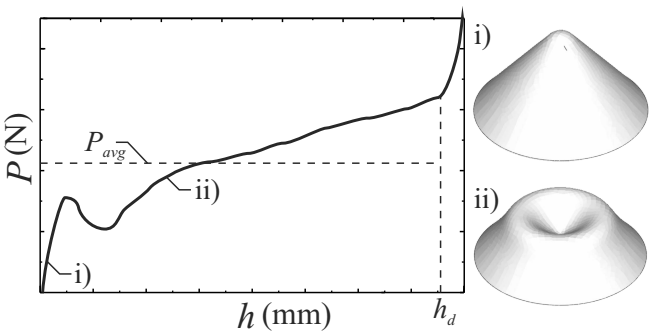


Figure 2.2: Force-displacement response and failure mode of an eggbox core.

**Honeycomb Core**

In aeronautical applications, lightweight components are needed that are able to resist high static loads and/or high impact loads. For example, with reference to Figure 1.2, structural components include fuselage structure and front and rear pressure bulkheads. Impact-resistant components include the nosecone, wing leading edge, engine nacelle, and vertical and horizontal stabiliser leading edges. These latter components must resist bird-strike, explosion, or crash loads, and therefore energy-absorption design criteria must be considered in design, often in addition to severe static load cases.

Hexagonal honeycomb cores are commonly used for such high-performance applications, as they possess both a very high stiffness-to-weight ratio and a high energy-absorbing failure mode. The force-displacement plot generated from the crushing a honeycomb core is as shown in Figure 2.1. It can be seen that there is an extremely high initial peak force arising from the hexagonal geometry, giving the core a high stiffness-to-weight ratio. This peak is followed by a steep post-buckling reduction in force and subsequent oscillations in the reaction force. These oscillations occur as sequential folding elements form in the core cell walls, which is a typical honeycomb core failure mode (Wierzbicki, 1983; Wierzbicki and Abramowicz, 1984). This method of failure forms a large number of static hinge lines across the honeycomb core, resulting in a high average reactive force and a large amount of energy absorption (Zarei Mahmoudabadi and Sadighi, 2011; Giglio

*et al.*, 2012; Kee Paik *et al.*, 1999). Despite this high average force, the failure mode is non-uniform, in that there is there is a large difference between peak and average reaction forces. Various methods to improve the honeycomb uniformity have been suggested, including pre-crushing the honeycomb core (Hexcel Corporation, 2006b), or arranging multilayer honeycomb configurations (Yang and Qiao, 2008) Although not directly related to honeycomb cores, a previous study by Ma and You (2011) has used rigid-origami design principles to alter the failure mode of a thin-walled tube from a progressive folding element mode similar to that seen in a honeycomb core, to an improved travelling hinge line failure mode similar to that seen in an eggbox core. Meng *et al.* (2009) investigated a honeycomb energy absorption device attached to the floor of an aircraft fuselage, to mitigate crash impact loads. Asadi *et al.* (2007) investigated an aluminium honeycomb bonnet which was shown to be capable of producing a controlled deceleration of a pedestrian head impact.

### Foam and Lattice Cores

Foam cores can also be used to give sandwich panels with good weight-specific strength and energy absorption capabilities (Ashby, 2000), and with the additional useful property of exhibiting an ideal, uniform force-displacement response during failure (Crupi and Montanini, 2007). This uniform failure mode arises from the continuous failure at the micro-scale of individual foam ligaments. Foam cores also possess additional useful properties, including the ability to incorporate integral face skins during manufacture (Crupi *et al.*, 2013), the ability to control core performance at both the microscale and macroscale through alterations to the foam structure and foam density respectively (Di Landro *et al.*, 2002), and the ability to form complex geometric profiles, to be discussed separately in the next section. Zheng *et al.* (2011) investigated foam panels as energy absorption devices attached to the floor of an aircraft fuselage, similar to the honeycomb

panel investigation discussed above. Ryan *et al.* (2010) investigated aluminium foam core orbital debris shields. The study demonstrated that foam cores could have superior energy-absorption to existing honeycomb core debris shields, as secondary impacts on individual foam ligaments could assist with impactor break-up and thus energy-absorption.

Various methods to improve the energy-absorption capability of foam cores through the direct alteration of foam cell geometry have also been proposed. Zhou *et al.* (2012) demonstrated that a graded foam core, that is a foam core with variable density through the panel thickness, can have superior impact resistance to a typical constant-density core. Studies have also investigated methods to manufacture foams directly at a micro-scale using selective laser melting. This manufacturing technique allowed for the creation of lattice cores, which are foam cores with regular, bespoke, foam cell geometry (McKown *et al.*, 2008; Smith *et al.*, 2011). The lattice core cells could be directly altered to improve energy-absorption, for example by reinforcing a tetrahedral-like foam cell with vertical column ligaments.

### 2.1.3 Sandwich Shells

For many applications, sandwich shells with single or double-curvature are required. When typical honeycomb cores are bent, orthogonal axes of the core bend about reversed radii of curvature, forming an anticlastic surface that is not suitable for single-curved sandwich shells. There are several honeycomb variants designed to overcome this anticlastic behaviour, including Ox-core, Flex-Core, and Double-Flex, however their capabilities are restricted for several reasons. Ox-core is obtained when a standard honeycomb is over-expanded such that the hexagonal core cells are stretched towards a rectangular configuration (Hexcel Corporation, 1999), Figure 2.3(b). This decreases the lateral shear strength and increases the longitudinal shear strength, thus increasing and decreasing their radii of curva-

tures respectively and enabling a single-curved core to be formed. Flex-Core and Double-Flex are altered cell configurations that are similarly designed to reduce anticlastic behaviours, but are further capable of high weight-specific compressive properties that can exceed that of comparable planar honeycombs (Hexcel Corporation, 2006a), Figure 2.3(c). While capable of fitting tighter curvatures than Ox-Core, Flex-Core and Double-Flex are still limited by a maximum bend radius, beyond which cell geometry is warped and mechanical properties are reduced. Guida *et al.* (2008) investigated birdstrike on a tailplane leading edge constructed from a Flex-Core sandwich panel.

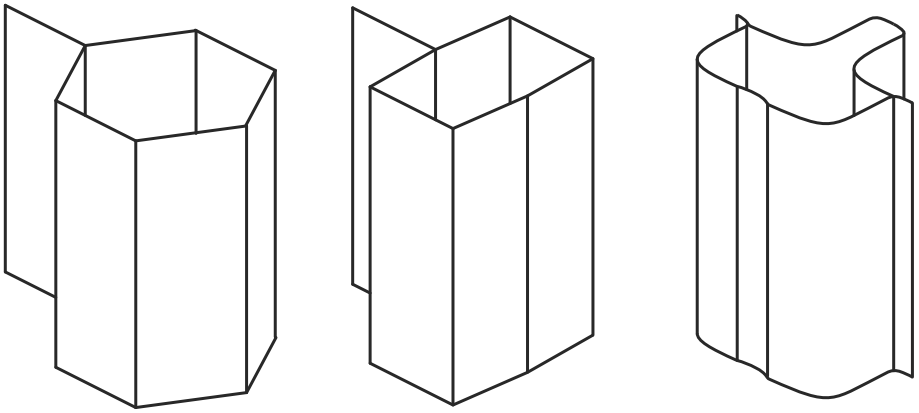

Figure 2.3: Honeycomb, Ox-Core, and Flex-Core unit cell geometries.

Foam cores can be more easily employed for sandwich shell applications, due to the homogeneous nature of the foam material. They can be manufactured either by trimming a block of foam to a desired shape and bonding suitable faces, or by directly casting the foam within a mould. A common and much-studied example of such a shell is protective helmets, which consist of expanded polystyrene foam core with polycarbonate face sheets (Di Landro *et al.*, 2002). High-performance aluminium foam shells were investigated by Shen *et al.* (2010), and were seen to potentially have superior blast resistance to flat plates, due to an improved collapse mode and the panel curvature favourably reflecting the blast wave.

## 2.2 Origami Geometry

### 2.2.1 Miura and Miura-Derivative Origami Patterns

The Miura pattern, Figure 2.4, is a fundamental origami pattern that is commonly used for engineering and architectural applications. Miura and Miura-derivative geometry will be extensively used in this thesis and so existing geometric conventions are discussed here.

The Miura pattern unfolds with a single degree-of-freedom kinematic mechanism along a planar surface. It is constructed from a symmetric, degree-4 vertex, which is to say that it consists of four intersecting crease lines which are symmetric about a horizontal centreline, Figure 2.5(a). The kinematics of such a vertex is a special case of a general 4-degree vertex described in Huffman (1976), and is shown in existing literature (Tachi, 2010) to possess several useful characteristics, including: *developability*, it can be folded from a continuous flat sheet; *flat-foldability*, all panels are co-planar when the pattern is fully folded (Hull, 2006); *rigid-foldability*, the pattern folds without twisting or stretching of the facets between the creases; and *tessellation*, it utilises a repetitive unit cell geometry constructed from a single repeating plate size (Klett and Drechsler, 2011). Pioneering applications of the Miura pattern include foldable subway maps and packaged solar panels for space deployment (Miura, 2009). Recent application has been seen in the aerospace industry with foldcore sandwich panels, consisting of a partially folded Miura pattern sandwiched between two stiff facings, to be discussed separately in Section 2.3.

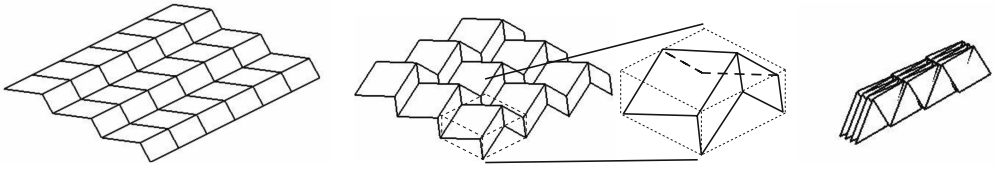

(a) Unfolded or developed (b) Partially-folded with repeated unit (c) Flat-folded

Figure 2.4: Folded states of a Miura pattern.

Alterations to various Miura pattern attributes allows for the creation of derivative rigid-foldable patterns with a larger range of surface geometries, including non-zero single and double curvature. Khaliulin (2005) explored techniques for generating derivative patterns from a base Miura geometry and listed many of derivative geometries. Derivative patterns have been used for many recent applications, including: curved foldcores (Nojima and Saito, 2006; Fischer *et al.*, 2009; Talakov, 2010; Alekseev, 2011; Zakirov and Alexeev, 2006), folded plate shelters (De Temmerman *et al.*, 2007; Weinand, 2009; Künstler and Trautz, 2011; Gioia *et al.*, 2012), sub-sea pipelines (Albermani *et al.*, 2011), and vehicle crash boxes (Ma and You, 2011).

Geometric modelling approaches used in studies vary widely, as particular geometric parameters are typically only derived as needed. This thesis adopts the consistent parametrisation developed in Wu (2010) for the base Miura pattern and two single-curved derivative geometries: the Arc and Arc-Miura patterns. These three parametrisations are briefly outlined here as they will be extensively used in later chapters.

### Miura Pattern

An unfolded unit of the Miura pattern, constructed from four identical parallelogram plates, is shown in Figure 2.5(a). It can be seen that the unfolded configuration can be completely determined by three parameters: side lengths $a$ and $b$, and sector angle $\phi$.

Four parameters are useful in defining a particular folded configuration: dihedral angles $\theta_A$ or $\theta_Z$, and edge angles $\eta_A$ or $\eta_Z$, Figure 2.5(b). Unit vectors $c_1$ and $c_2$ are defined as aligned along crease $a$ and $b$ folded directions respectively, Figure 2.5(b). The dot product of these two vectors gives the following relationship:

$$(1 + \cos\eta_Z)(1 - \cos\eta_A) = 4\cos^2\phi \tag{2.1}$$

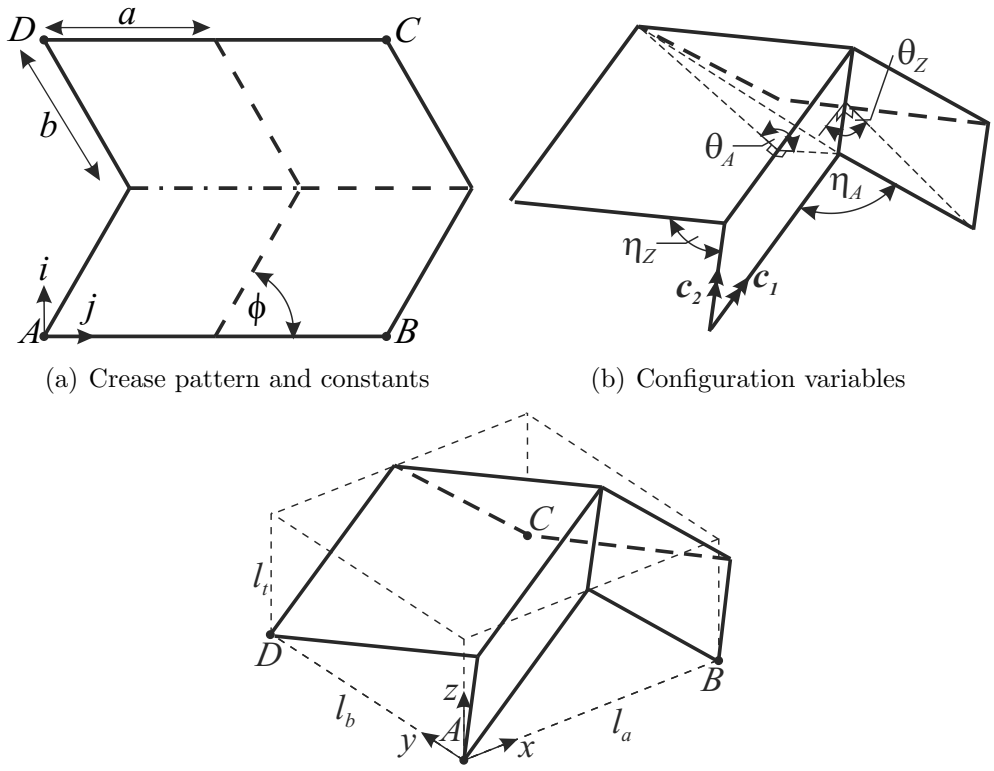


(a) Crease pattern and constants

(b) Configuration variables

(c) Unit cell geometry

Figure 2.5: Parameters of the Miura pattern.

Applying the cosine law to triangles formed by auxiliary lines perpendicular to straight and zigzag creases allows the following two relationships to be established between dihedral and edge angles:

$$\cos\eta_A = \sin^2\phi\cos\theta_Z - \cos^2\phi \tag{2.2}$$

$$\cos\eta_Z = \sin^2\phi\cos\theta_A + \cos^2\phi \tag{2.3}$$

Equations (2.1–3) can be combined to form the following explicit relationship between the two dihedral angles:

$$\cos\theta_A = 1 + \frac{4(\cos\theta_Z - 1)}{(\cos\theta_Z + 1)(\cos 2\phi - 1) + 4} \tag{2.4}$$

The edge angles can be related to unit cell variables length $l_a$, width $l_b$, and height $l_t$, Figure 2.5(c), with:

$$l_a = 2a\sin(\eta_A/2) \tag{2.5}$$

$$l_b = 2b\sin(\eta_Z/2) \tag{2.6}$$

$$l_t = a\cos(\eta_A/2) \tag{2.7}$$

Using the above parameters, we can express the locations of all vertices in any folded configuration. For the pattern shown in Figure 2.5(a), number all its $m$ straight pattern lines from the bottom and $n$ zigzag lines from the left. The vertex at the intersection of the $i^{th}$ straight crease line and the $j^{th}$ zigzag crease line is denoted by $V^{i,j}$, where $i = 1, 2, ...m$, and $j = 1, 2, ...n$. In a 3D Cartesian coordinate system with origin and orientation shown in Figure 2.5(c), the coordinate vector $(x, y, z)$ of $V^{i,j}$ can be given as:

$$x = \begin{cases} (j-1)a\sin(\eta_A/2) & \text{for odd } i \\ (j-1)a\sin(\eta_A/2) + b\cos(\eta_Z/2) & \text{for even } i \end{cases} \tag{2.8}$$

$$y = (i-1)b\sin(\eta_Z/2) \tag{2.9}$$

$$z = \begin{cases} 0 & \text{for odd } j \\ a\cos(\eta_A/2) & \text{for even } j \end{cases} \tag{2.10}$$

To summarise, twelve parameters have been defined in the Miura pattern: $a, b, \phi$,$m$, $n, \theta_A, \theta_Z, \eta_A, \eta_Z, l_a, l_b$, and $l_t$. The first five parameters are collectively called the *pattern constants*, as they remain constant regardless of the pattern folded state. The remaining seven parameters are collectively called the *pattern variables*, as they vary for different folded configurations of the same pattern. Amongst these, six independent geometric relations have been established, Equations (2.1–3) and (2.5–7), thus six independent parameters are required to find all remaining parameters and a unique Miura pattern configuration. Typically, when a pattern is given, the five constants are known, so any of its potential folded shapes can be plotted by specifying a single additional variable parameter. The folded process depicted in Figure 2.4 was generated from a pattern with constants $a = b = 30$mm, $\phi = \pi/3$, $m = n = 7$, and by varying parameter $\theta_A$ from $\pi$ to 0.

### Arc Pattern

Flipping the crease orientation for alternative zig-zag lines in a Miura pattern generates an Arc pattern. To retain foldability, the flipped crease must have a flipped polarity, which causes all pattern vertices to lie along a longitudinally-curved arc profile, hence the pattern name.

An unfolded repeating unit of the Arc pattern, constructed from four identical trapezoidal plates, is shown in Figure 2.6(a). Three pattern constants are defined as before: side lengths $a_1$ and $b$, and sector angle $\phi$. Two more dependent constants are useful to derive: side length $a_2 = 2b\cos\phi + a_1$, where $a_1 < a_2$, and panel width $w = b\sin\phi$.

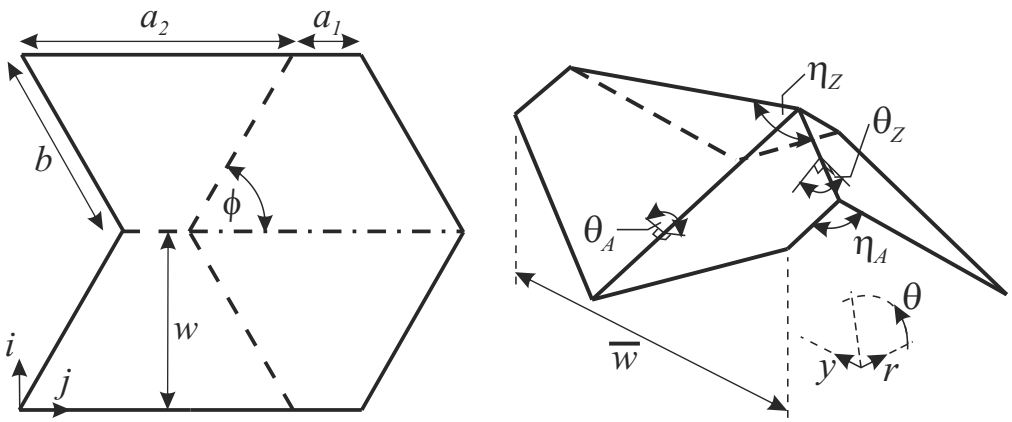


(a) Crease pattern and constants

(b) Configuration variables

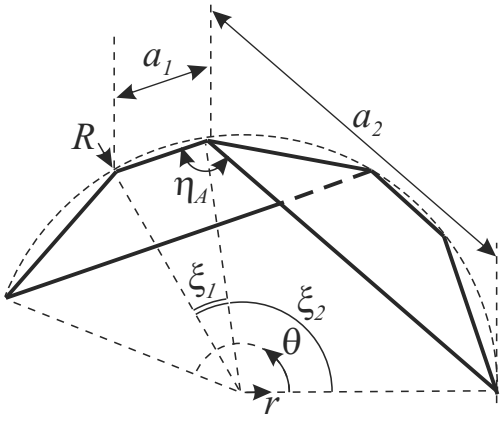


(c) Front ($r$-$\theta$) projection

Figure 2.6: Arc pattern geometry.

The configuration parameters $\theta_A, \theta_Z, \eta_A, \eta_Z$, are as defined for the Miura pattern,

and so Equations (2.1–3) remain valid, Figure 2.6(b). An additional folded width parameter $\bar{w}$ is convenient to define:

$$\bar{w} = b\sin(\eta_Z/2) = w\sin(\eta_Z/2)/\sin\phi \tag{2.11}$$

The front projection of a partially folded unit is shown in Figure 2.6(c), where it can be seen that vertices lie along an arc of radius $R$. The central angles subtended by creases $a_1$ and $a_2$ can be denoted by angles $\xi_1$ and $\xi_2$ respectively. The following relations can be found using triangle geometry:

$$\xi_1 + \xi_2 = 2(\pi - \eta_A) \tag{2.12}$$

$$R = a_1/(2\sin(\xi_1/2)) \tag{2.13}$$

$$R = a_2/(2\sin(\xi_2/2)) \tag{2.14}$$

Given an Arc pattern with $m$ straight and $n$ zigzag pattern lines, the location of any vertex $V^{i,j}$ $(i = 1, 2, ..., m,\ j = 1, 2, ..., n)$ in a folded configuration can be derived in a 3D cylindrical coordinate system with orientation and origin shown in Figure 2.6, where $(x, y, z)$=$(r\cos\theta, y, r\sin\theta)$. The three components ($r$,$\theta$,$y$) of $V^{i,j}$ can be given as:

$$r = R \tag{2.15}$$

$$\theta = \begin{cases} (j-1)(\xi_1+\xi_2)/2 & \text{for odd } i \text{ and odd } j \\ (j-1)(\xi_1+\xi_2)/2 + (\xi_2-\xi_1)/2 & \text{for odd } i \text{ and even } j \\ (j-2)(\xi_1+\xi_2)/2 + \xi_2 & \text{for even } i \text{ and odd } j \\ (j-1)(\xi_1+\xi_2)/2 + \xi_1 + (\xi_2-\xi_1)/2 & \text{for even } i \text{ and even } j \end{cases} \tag{2.16}$$

$$y = (i-1)b\sin(\eta_Z/2) \tag{2.17}$$

In total, seven relations, Equations (2.1–3) and (2.11–14), are found amongst eight variable parameters $\eta_Z$, $\eta_A$, $\theta_Z$, $\theta_A$, $\bar{w}$, $R$, $\xi_1$, and $\xi_2$. Thus, six independent parameters are sufficient to uniquely determine a pattern: five pattern constants plus one variable. The sequence shown in Figure 2.7 is created with $a_1 = 40$mm, $b = 20$mm, $\phi = \pi/4$, $m = 7$, $n = 5$, and specifying $\theta_A$ between $\pi$ and $\pi/4$.

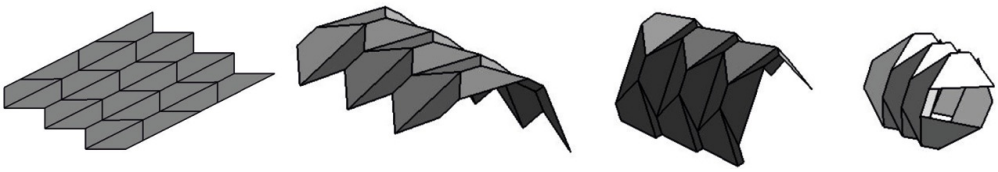

(a) Folding sequence simulated in MATLAB

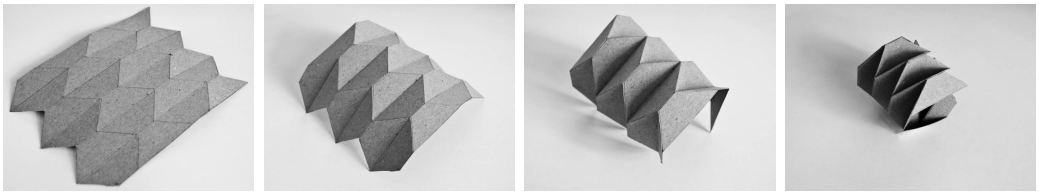

(b) Folding sequence of a paper card prototype

Figure 2.7: Arc pattern folding motion.

### Arc-Miura Pattern

Altering the alignment of alternate zig-zag creases on a Miura base pattern creates an Arc-Miura pattern. It is named after the fact that its layout bears a similarity with that of the Miura pattern, except that M- and V-vertices lie along concentric curved arc profiles. Here, M-vertices are defined as vertices found at the intersection of three mountain creases and one valley crease, and V-vertices as vertices found at the intersection of three valley creases and one mountain crease.

An unfolded unit of the Arc-Miura pattern, constructed from four identical trapezoidal plates, is shown in Figure 2.8(a). It can be seen that M-vertices and V-vertices have different sector angles $\phi_1$ and $\phi_2$ respectively. This gives the pattern four distinct side lengths, $a_1, a_2, b_1$, and $b_2$, with the stipulation that $\phi_1 > \phi_2$, $a_1 < a_2$, and $b_1 < b_2$. Among these six parameters, only four are independent, as $b_1 \sin\phi_1 = b_2 \sin\phi_2$, and $a_2 + b_1 \cos\phi_1 = a_1 + b_2 \cos\phi_2$.

A partially folded Arc-Miura unit is shown in Figure 2.8(b). It can be thought of as the combination of two overlapping Miura units, one M-vertex with sector angle $\phi_1$, and one V-vertex with sector angle $\phi_2$. A common lateral dihedral angle $\theta_A$ exists between the two, however the remaining configuration parameters are different. If subscript M or V denotes an M- or V-vertex configuration variable,

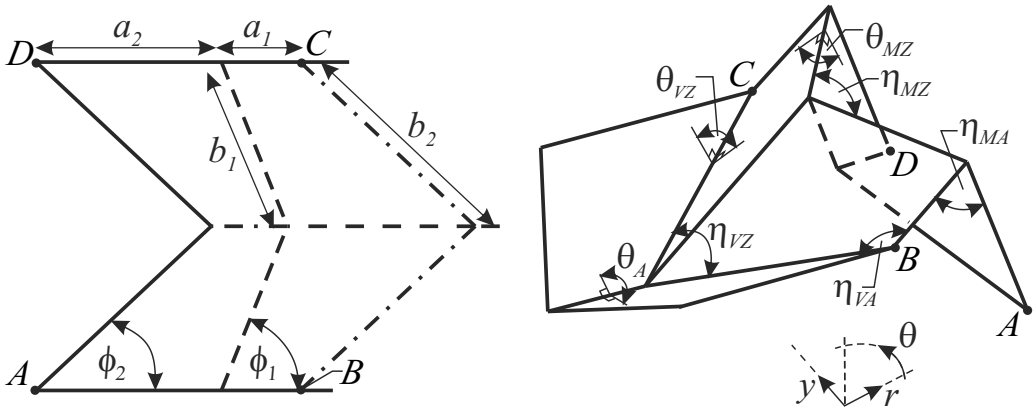


(a) Crease pattern and constants

(b) Configuration variables

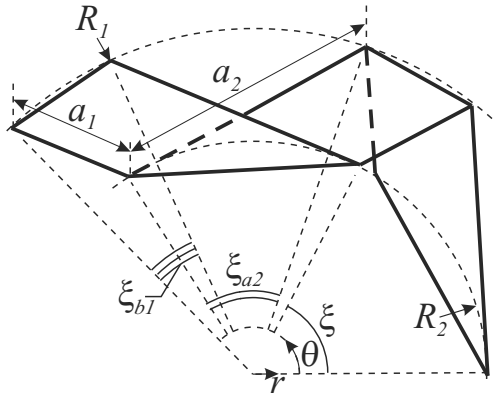


(c) Front ($r$-$\theta$) projection

Figure 2.8: Arc-Miura pattern geometry.

two longitudinal dihedral angles, $\theta_{MZ}$, and $\theta_{VZ}$, and four edge angles, $\eta_{MZ}$, $\eta_{VZ}$, $\eta_{MA}$, and $\eta_{VA}$, can be defined. Equations (2.1–3) can be reformulated at both M- and V-vertices to give the following six equations:

$$(1 + \cos\eta_{MZ})(1 - \cos\eta_{MA}) = 4\cos^2\phi_1 \tag{2.18}$$

$$\cos\eta_{MA} = \sin^2\phi_1\cos\theta_{MZ} - \cos^2\phi_1 \tag{2.19}$$

$$\cos\eta_{MZ} = \sin^2\phi_1\cos\theta_A + \cos^2\phi_1 \tag{2.20}$$

$$(1 + \cos\eta_{VZ})(1 - \cos\eta_{VA}) = 4\cos^2\phi_2 \tag{2.21}$$

$$\cos\eta_{VA} = \sin^2\phi_2\cos\theta_{VZ} - \cos^2\phi_2 \tag{2.22}$$

$$\cos\eta_{VZ} = \sin^2\phi_2\cos\theta_A + \cos^2\phi_2 \tag{2.23}$$

A sectional view of the curved Arc-Miura profile is shown in Figure 2.8(c). It can

be seen that all M-vertices and all V-vertices lie along concentric radii $R_1$ and $R_2$ respectively, and each unit is subtended by fold angle $\xi$. From triangle geometry, the following equations can be established:

$$\xi = \eta_{VA} - \eta_{MA} \tag{2.24}$$

$$R_1 = \sqrt{(a_1^2 + a_2^2 - 2a_1a_2\cos\eta_{VA})/(2(1-\cos\xi))} \tag{2.25}$$

$$R_2 = \sqrt{(a_1^2 + a_2^2 - 2a_1a_2\cos\eta_{MA})/(2(1-\cos\xi))} \tag{2.26}$$

Given an Arc-Miura pattern with $m$ straight and $n$ zigzag lines, the location of any vertex $V^{i,j}$ $(i = 1, 2, ..., m,\ j = 1, 2, ..., n)$ in a folded configuration can be derived in a 3D cylindrical coordinate system where $(x, y, z)$=$(r\cos\theta, y, r\sin\theta)$, with origin and orientation shown in Figure 2.8. The three components ($r$,$\theta$,$y$) of $V^{i,j}$ can be given as:

$$r = \begin{cases} R_1 & \text{for odd } j \\ R_2 & \text{for even } j \end{cases} \tag{2.27}$$

$$\theta = \begin{cases} (j-1)\xi/2 & \text{for odd } i \text{ and odd } j \\ (j-1)\xi/2 + \xi_{b1} & \text{for even } i \text{ and odd } j \\ (j-2)\xi/2 + \xi - \xi_{a2} & \text{for odd } i \text{ and even } j \\ (j-2)\xi/2 + \xi_{b1} + \xi_{a2} & \text{for even } i \text{ and even } j \end{cases} \tag{2.28}$$

$$y = (i-1)b_1\sin(\eta_{MZ}/2) \tag{2.29}$$

where $\xi_{a2}$ and $\xi_{b1}$ are the central angles subtended by creases $a_2$ and $b_1$ respectively. They can be derived from the law of cosines as below:

$$\xi_{a2} = \arccos((R_1^2 + R_2^2 - a_2^2)/(2R_1R_2)) \tag{2.30}$$

$$\xi_{b1} = \arccos((2R_1^2 - b_1^2\cos^2(\eta_{MZ}/2))/(2R_1^2)) \tag{2.31}$$

To summarise, for an Arc-Miura pattern we have associated twelve variables, $\theta_{MZ}$, $\theta_{VZ}$, $\theta_A$, $\eta_{MZ}$, $\eta_{VZ}$, $\eta_{MA}$, $\eta_{VA}$, $\xi$, $\xi_{a2}$, $\xi_{b1}$, $R_1$ and $R_2$, with eleven Equations (2.18–26), (2.30–31). Thus seven independent parameters, six constants and one variable,

are required to uniquely determine a pattern. For example, the sequence shown in Figure 2.9 is generated with $a_1 = 40\text{mm}$, $b_1 = 40\text{mm}$, $\phi_1 = 4\pi/9$, $\phi_2 = 7\pi/9$, $m = n = 7$, and by specifying $\theta_A$ continuously changing from $\pi$ to 0.

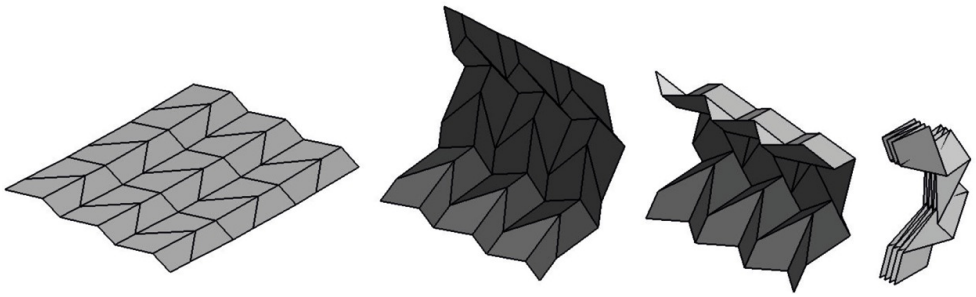

(a) Folding sequence simulated in MATLAB

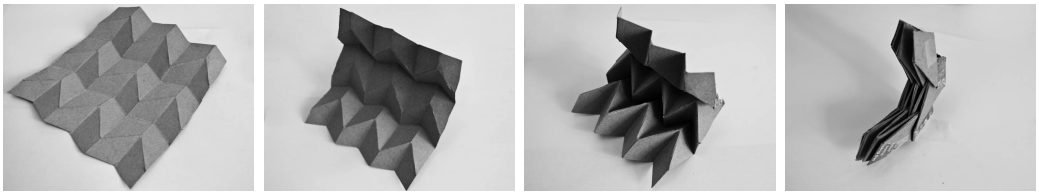

(b) Folding sequence of card prototype

Figure 2.9: Arc-Miura folding motion.

### 2.2.2 Curved-Crease Origami Patterns

Curved crease origami differs from prismatic, or straight crease origami, in that the folded surface of the pattern is bent during the folding process. Curved-crease arrangements are widely studied in mathematics, where differential geometric analysis is used to investigate folded shapes (Demaine *et al.*, 2011a,b; Huffman, 1976). The potential for adapting such geometries for use in engineering application has long been known (Miura, 1972), however limited studies in this area have been conducted. This is in part because of the difficulty in parametrising curved-crease geometries, but more so because of the difficulty in manufacturing curved surfaces from rigid sheet materials. For instance, Buri *et al.* (2011) constructed beams from curved timber sheets fitting curved-crease origami geometry, but sheet curvature was seen to cause warping in the assembled structure.

To overcome these limitations, recent studies have suggested the possibility of de-

veloping rigid-foldable approximations of curved-crease geometries. This is done by fitting rigid planar quadrilateral plates, or a PQ mesh, to a curved surface. The PQ mesh can be generated with manual rulings on a physical prototype (Tachi, 2011), or solved using intensive computer processes (Kilian *et al.*, 2008). Rigid-foldable curved-crease origami patterns have two advantages over bent-surface curved-crease origami patterns: it is simpler to simulate folding motion as they can be designed to a possess single degree-of-freedom kinematic mechanism, and they are simpler to construct from rigid engineering sheet materials as the pattern panels maintain zero-local curvature. PQ mesh fitting has successfully been used in industrial applications of curved-crease geometry. For example, Epps and Verma (2013) used the technique to manufacture and fold curved-crease architectural facades.

## 2.3 Foldcore Sandwich Structures

### 2.3.1 Foldcore Panels

Foldcore sandwich panels, Figure 1.1, have been created as a potential substitute for honeycomb panels, as they possess a number of favourable properties that are not possible with other types of high-performance sandwich panel (Heimbs, 2013). For example, a foldcore can be designed to have isotropic strength coefficients (Miura, 1972), can be insensitive to manufacturing defects (Heimbs *et al.*, 2007), and can be continuously manufactured by folding a flat sheet (Zakirov and Alekseev, 2007; Basily and Elsayed, 2004; Kling, 2006).

Foldcores also have reasonably high weight-specific properties, particularly out-of-plane impact resistance, due to the formation of an efficient plate buckling failure mode (Heimbs, 2013; Nguyen *et al.*, 2005). A force-displacement response generated from this plate-buckling mode is shown in Figure 2.10. The high initial force occurs because of the high buckling resistance of the core plates, which are continuously supported on four sides from the core architecture. Post-buckling, the foldcore undergoes a significant reduction in reaction force as it collapses about stationary hinge lines formed across buckled core regions. Although efficient in terms of energy absorption capability, the foldcore still possesses the same drawback as the honeycomb core, namely a steep reduction in post-buckling reaction force causing a non-uniform force-displacement response.

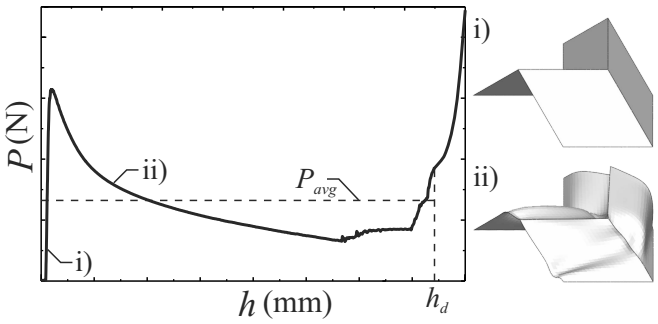


Figure 2.10: Force-displacement response and failure mode of a foldcore.

### 2.3.2 Foldcore Shells

Numerous studies have suggested the possibility of developing curved foldcore panel geometry using origami design techniques (Miura, 1972; Nojima and Saito, 2006; Fischer *et al.*, 2009; Talakov, 2010; Alekseev, 2011; Künstler and Trautz, 2011). Such structures are hypothesised to be capable of a much wider range of curvatures than honeycomb variants, with the further benefit of a unit geometry that can be optimised for particular mechanical behaviours. The mechanical performance of such structures remains an unexplored area.

# Chapter 3

# Indented Foldcores

The foldcore has been found to fail with a plate buckling failure mode when subjected to out-of-plane impact loads. Despite good energy absorption capability, the plate buckling mode possesses a very non-uniform stress-displacement response. In the past, various methods have been exploited to alter the design of energy absorption devices to increase their energy absorption capability. For instance, indentations have been used in thin-walled crash boxes to achieve more uniform failure responses (Ma and You, 2011). This chapter explores the possibility of introducing an indentation to a foldcore to trigger a failure mode with substantially improved energy absorption capabilities.

## 3.1 Preliminary Study

### 3.1.1 Geometry

The indented foldcore geometry is simply created by introducing a small indent along top ridge of standard foldcore pattern. The unfolded and folded configurations of both core types are shown in Figure 3.1.

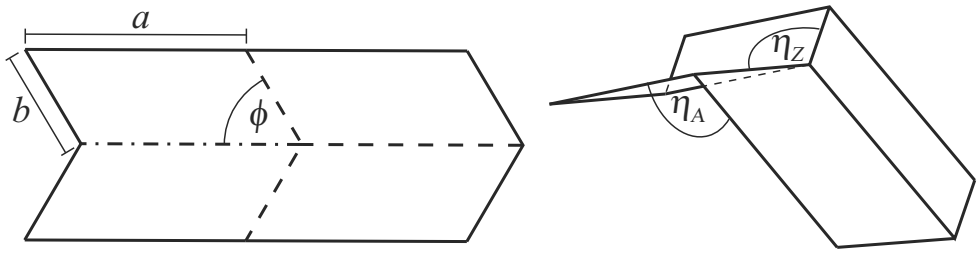


(a) Standard foldcore

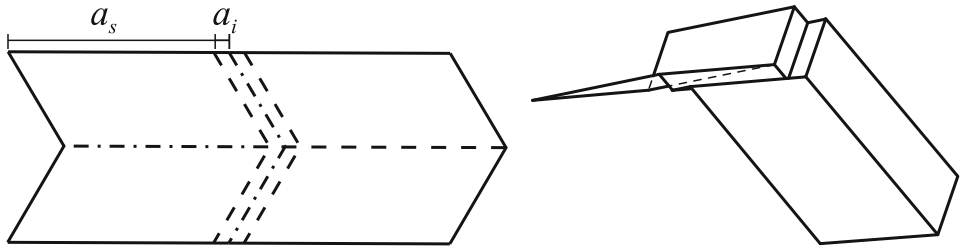


(b) Indented foldcore

Figure 3.1: Unfolded crease pattern, on left; folded configuration, on right.

As discussed in Section 2.2, the standard foldcore unit geometry is a Miura pattern that can be uniquely identified with four parameters: side lengths $a$ and $b$, pattern angle $\phi$, and a single pattern variable to define the folded configuration, for example edge angle $\eta_A$. An additional plate thickness parameter $t_p$ is also introduced as the foldcore has non-zero thickness. This is used to calculate core density $\alpha$, which is the volume of core plates $V_p$ contained in a unit volume $V$:

$$\alpha = \frac{V_p}{V} = \frac{4abt_p \sin\phi}{l_a l_b l_t} = \frac{t_p}{a} \frac{2\sin\phi}{\sin(\eta_A)\sin(\eta_Z/2)} \tag{3.1}$$

It can be seen from the indented foldcore crease pattern that the indent can be thought of as a short, inverted Miura pattern with side length $a_i$, where the sub-

script $i$ denotes indent. For geometric compatibility, the inverted Miura segment must have the same $b$ and $\phi$ as the original Miura segment, and to preserve rigid foldability it must have the same, although inverted, folded configuration. Therefore a single extra dimensional constant, $a_i$, is needed to uniquely define the indented pattern. It is also convenient to define the standard side length $a_s = a - a_i$ and the dimensionless *indented ratio* $p^* = a_i/a$. Henceforth the superscript $^*$ shall be used to denote dimensionless parameters. Note that from Equations (2.5–7) it can be seen that an indented foldcore will have identical length $l_a$ and width $l_b$ width to a standard foldcore with identical $a$, $b$, $\phi$, and $\eta_A$ parameters, but will have a smaller height, equal to:

$$l_t = a_s \cos(\eta_A/2) \tag{3.2}$$

### 3.1.2 Hypothetical Collapse Mechanism

The inverted ridge on the indented foldcore geometry is hypothesised to act as a line imperfection that could an trigger an initial plate failure at the core ridge, which would then develop into a top-down travelling hinge line. This failure would be similar to the efficient failure mode of the eggbox core discussed in Section 2.1.2. However, it differs from the eggbox core in that the travelling hinge line would maintain a constant length throughout the duration of the crush, Figure 3.2, creating a near-uniform force-displacement response.

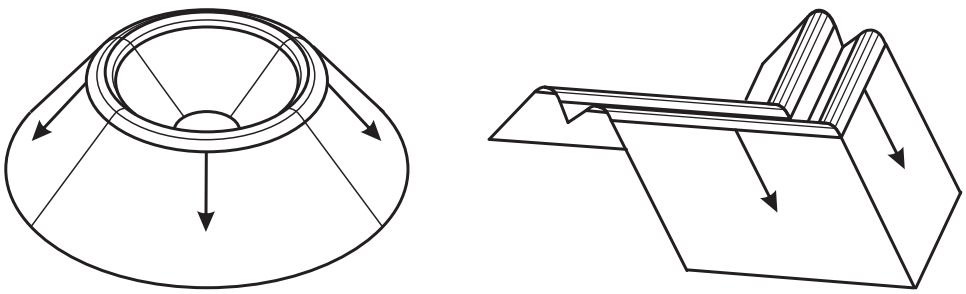

(a) Eggbox failure (b) Indented foldcore hypothetical failure

Figure 3.2: Travelling hinge line failure modes.

### 3.1.3 Numerical Study

To assess whether the indented foldcore exhibits the hypothesised failure mode, a numerical study was conducted on an indented and standard foldcore with a set of arbitrarily chosen initial geometric parameters. A standard model, A1$^s$, had geometric parameters $a = 30.8$mm, $b = 15.4$mm, $\phi = \pi/3$, $\eta_A = 2\pi/3$, and $t_p = 0.49$mm. This gave a core with $l_t = 15$mm and $\alpha = 4\%$, which is similar to commonly available honeycomb cores. Henceforth the superscript $s$ shall be used to denote a standard model. The indented model A1 was given identical geometry, except with the indented parameter set to $p^* = 1/15$. To define identical geometry, it is convenient to replace the parameters $b$ and $t_p$ with dimensionless aspect ratios $b^* = b/a$ and density $\alpha$, which from Equation (3.1) is seen to be proportional to $t_p/a$. Models A1$^s$ and A1 are depicted in Figure 3.1(a) and (b), respectively, and their relevant geometric parameters are listed in Table 3.1.

Table 3.1: Initial foldcore parameters.

| *Model* | $a_s$ (mm) | $b^*$ | $p^*$ | $\alpha$ | $\phi$ (°) | $\eta_Z$ (°) | $\eta_A$ (°) |
|---|---|---|---|---|---|---|---|
| A1$^s$ | 30.8 | 0.5 | 0 | 0.04 | 60.0 | 120.0 | 109.5 |
| A1 | 30.8 | 0.5 | 0.067 | 0.04 | 60.0 | 120.0 | 109.5 |

A numerical simulation of both cores being crushed between two rigid bodies was conducted using a quasi-static, large-displacement analysis in finite element software ABAQUS/Explicit. The core mesh was constructed with S4R shell elements with mesh size approximately equal to $a/80$. A small bend radius was used in place of the sharp ridge crease lines seen in the idealised origami geometry, as this is a more realistic approximation of the shape of a formed metallic foldcore, Figure 3.3. A ductile, annealed, pure aluminium material was selected for the analysis, with isotropic elastic-plastic material properties of $E = 69$GPa, $v = 0.33$, $\sigma_Y = 28$MPa, $\sigma_U = 83$MPa, $\rho = 2710$kg/m$^3$, and strain hardening data obtained from material sample tests are shown in Table 3.2.

Table 3.2: True plastic stress-strain data for aluminium material.

| Strain | 0.0 | 0.004 | 0.021 | 0.054 | 0.095 | 0.132 |
|---|---|---|---|---|---|---|
| Stress (MPa) | 28 | 43.8 | 60.0 | 71.5 | 78.6 | 83.3 |

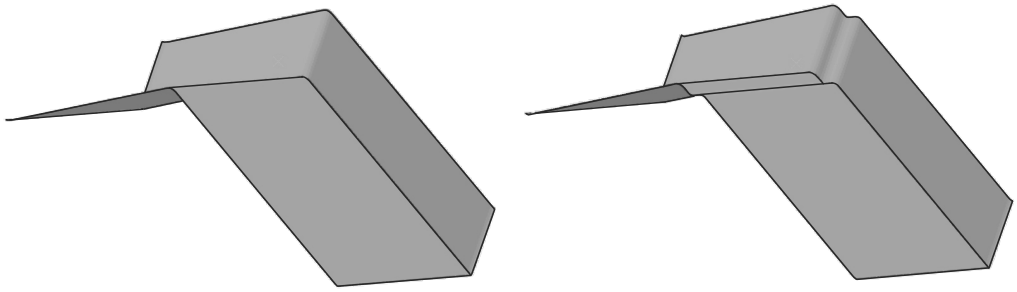

(a) Standard foldcore (b) Indented foldcore

Figure 3.3: Meshed unit geometries with ridge bend radius.

Fixed boundary conditions were applied along the four base edges, and periodic boundary constraints applied along side edges. Loading was applied by crushing the structure between two rigid panels, with the top plate given smooth-step crush displacement of up to approximately $65\% l_t$. To ensure a quasi-static analysis, the loading velocity was set at 2m/s, which limited the kinetic energy to internal energy ratio to be less than 5%, as recommended in the Abaqus User Manual (Simulia, 2009). Top panel contact, bottom panel contact, and self-self contact were all modelled with surface-surface tangential friction conditions, with a friction coefficient of 0.25.

### 3.1.4 Simulation Results and Discussion

From the numerical analysis, the force-displacement responses of the indented and standard models were obtained. To facilitate comparison between the models, crush force $P$ and crush displacement $h$ are normalised to dimensionless stress and strain parameters $\sigma^* = \sigma/\sigma_Y = P/(l_a l_b \sigma_Y)$ and $h^* = h/l_t$ respectively. The energy absorption $E^*$ is the integral of dimensionless stress-strain curve, and the total energy absorbed, $E_d^*$, is attained at the densification strain, $h^* = h_d^*$. The densification strain $h_d^*$ varies slightly between cores but is typically seen to be between 0.55 and 0.65. From these values, the average dimensionless stress is

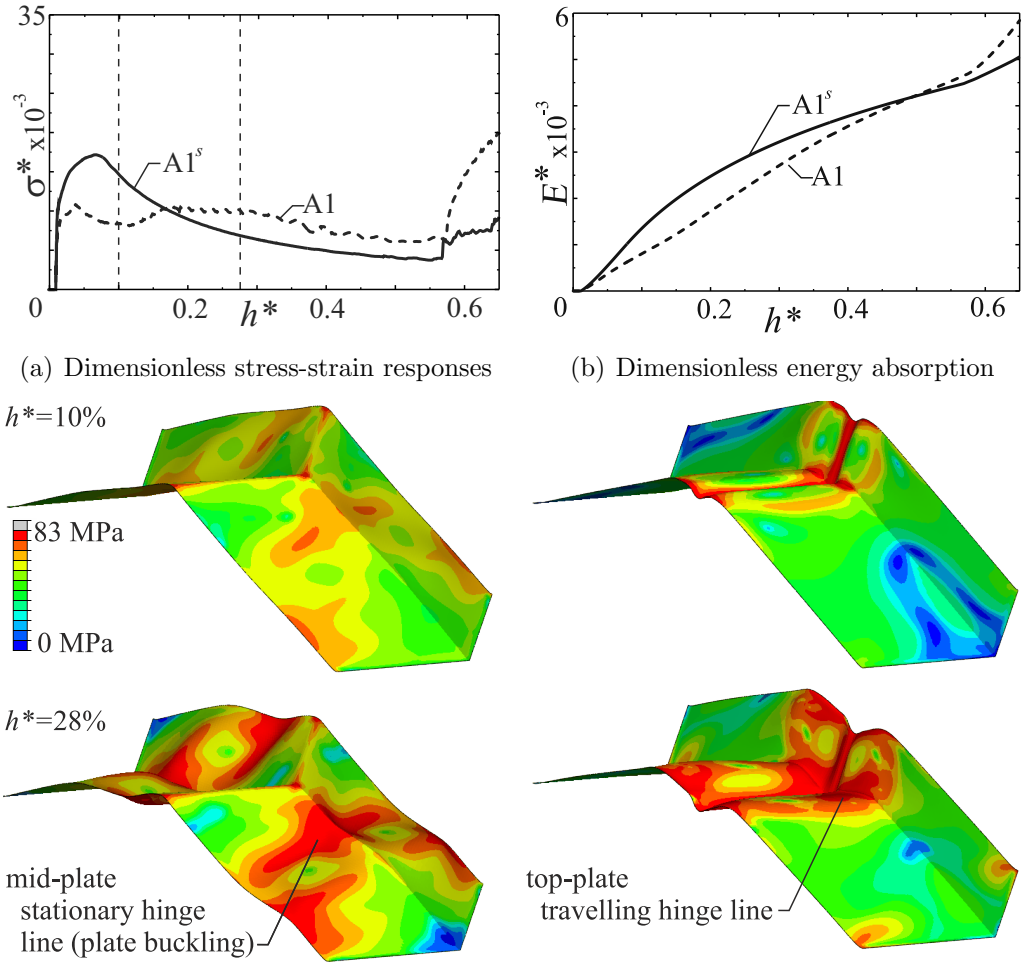


(a) Dimensionless stress-strain responses

(b) Dimensionless energy absorption

(c) Von-Mises stress in model A1$^s$

(d) Von-Mises stress in model A1

Figure 3.4: Results of initial numerical models.

calculated as, $\sigma^*_{avg} = E^*_d/h^*_d$, and the uniformity ratio $U^*$ is defined as $U^* = \sigma^*_{max}/\sigma^*_{avg}$=$P_{max}/P_{avg}$.

Dimensionless responses for the initial numerical models are shown in Figure 3.4(a)-(b), and relevant values summarised in Table 3.3. It can be seen that the indented core has a significantly different failure response to the standard core, indicating that the indent was successful in altering the failure mode of the foldcore. It can be seen that compared with the standard core, the indented core has a reduction in $\sigma^*_{max}$ of 37.2% and an increase in $\sigma^*_{avg}$ of 5.1%.

Inspection of the core failure modes, Figure 3.4(c)-(d), shows that the indented core initially has plasticity along the top ridge near the indent, in contrast to mid-plate in the standard core. The standard core continues to weaken after this

Table 3.3: Results of initial study models.

| *Model* | $h_d^*$ | $E_d^*$ $\times 10^{-3}$ | $\sigma_{max}^*$ $\times 10^{-3}$ | $\sigma_{avg}^*$ $\times 10^{-3}$ | $U^*$ |
|---|---|---|---|---|---|
| A1$^s$ | 0.6 | 4.7 | 16.9 | 7.8 | 2.2 |
| A1 | 0.57 | 4.7 | 10.6 | 8.2 | 1.3 |

initial buckling, whereas the indented buckling line propagates until approximately $h^* = 23\%$ to create a slight travelling hinge line, after which secondary plate buckling occurs towards the base supports. This confirms that an indent is capable of forming a more suitable energy-absorbing failure mode with travelling hinge lines, however the optimum geometry to maximise energy-absorption has yet to be explored.

## 3.2 Parametric Study

### 3.2.1 Geometry

The next stage in the investigation of the indented foldcore is to assess the effect of each geometric parameter on the formation of a particular failure mode. There are six foldcore parameters of interest, which can be placed into two categories: parameters $\phi$, $\eta_A$, and $\eta_Z$, which control the configuration of the core plates, and parameters $b^* = b/a$, $p^*$, and $\alpha$, which control the core plate aspect ratios.

#### Pattern Configurations

Plate angle $\phi$, longitudinal edge angle $\eta_A$, and lateral edge angle $\eta_Z$, are related by Equation (2.1). Keeping one parameter constant while varying the other two allows an investigation into the effect of each parameter on the failure mode of an indented core. Four models were generated for each of the three parameters, with geometry for the twelve models chosen to create good distribution across the configuration space of Equation (2.1), see Figure 3.5.

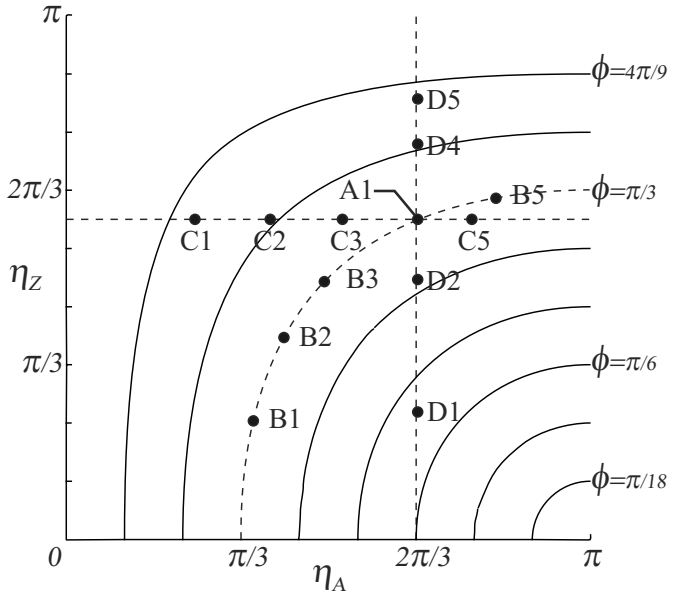


Figure 3.5: Distribution of pattern configuration models.

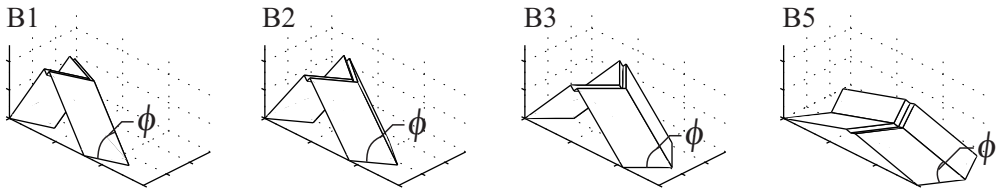


(a) Constant $\phi$ models

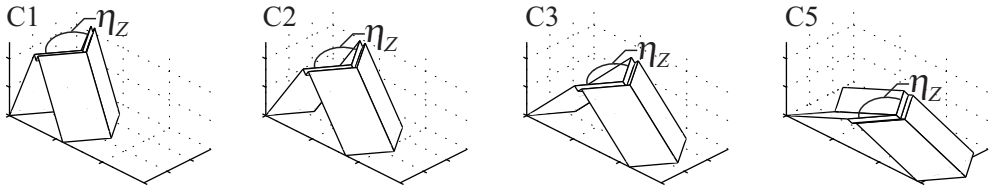


(b) Constant $\eta_Z$ models

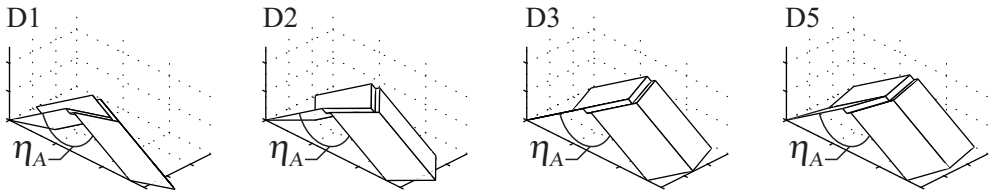


(c) Constant $\eta_A$ models

Figure 3.6: Pattern configuration model geometry.

Models B1, B2, B3, and B5 possess a constant $\phi$ parameter and so represent different folded configurations of the same base pattern. Models C1, C2, C3, and C5 possess a constant $\eta_A$ and represent different longitudinal steepness configurations. Similarly, the constant $\eta_Z$ models D1, D2, D4, and D5 correspond to different lateral steepness configurations. The skipped model number in each set, that is B4, C4, and D3, are those that correspond to the base geometry A1. The twelve unit geometries are shown in Figure 3.6 and the altered parameters are shown in Table 3.4(a). Note the aspect ratio parameters are not listed as they are the same as those for model A1 given in Table 3.1.

### Aspect Ratios

As before, a range of models were generated for each of the three aspect ratio parameters, $b^*$, $p^*$, and $\alpha$, by altering the geometry of the base model A1. Models E1, E2, E4, and E5 range from a wide to a narrow foldcore unit geometry, with side length aspects of $b^* = 2, 1, 0.25$, and $0.125$ respectively. Models F1, F2, F3, and F5

Table 3.4: Parametric study model parameters.

(a) Pattern configuration models

| *Model* | $\phi$ (°) | $\eta_Z$ (°) | $\eta_A$ (°) |
|---|---|---|---|
| A1 | 60.0 | 109.5 | 120.0 |
| B1 | 60.0 | 42.9 | 65.0 |
| B2 | 60.0 | 69.6 | 75.0 |
| B3 | 60.0 | 90.0 | 90.0 |
| B5 | 60.0 | 117.7 | 150 |
| C1 | 77.2 | 109.2 | 45.0 |
| C2 | 70.7 | 109.6 | 70.0 |
| C3 | 64.8 | 109.4 | 95.0 |
| C5 | 56.6 | 108.3 | 140 |
| D1 | 36.9 | 45.1 | 120.0 |
| D2 | 52.5 | 90.7 | 120.0 |
| D4 | 70.6 | 134.9 | 120.0 |
| D5 | 77.1 | 150.1 | 120.0 |

(b) Aspect ratio models

| *Model* | $b^*$ | $p^*$ | $\alpha$ |
|---|---|---|---|
| A1 | 0.5 | 0.067 | 0.04 |
| E1 | 2.0 | 0.067 | 0.04 |
| E2 | 1.0 | 0.067 | 0.04 |
| E4 | 0.25 | 0.067 | 0.04 |
| E5 | 0.125 | 0.067 | 0.04 |
| F1 | 0.5 | 0.0 | 0.04 |
| F2 | 0.5 | 0.017 | 0.04 |
| F4 | 0.5 | 0.05 | 0.04 |
| F5 | 0.5 | 0.25 | 0.04 |
| G1 | 0.5 | 0.067 | 0.02 |
| G3 | 0.5 | 0.067 | 0.06 |
| G4 | 0.5 | 0.067 | 0.08 |

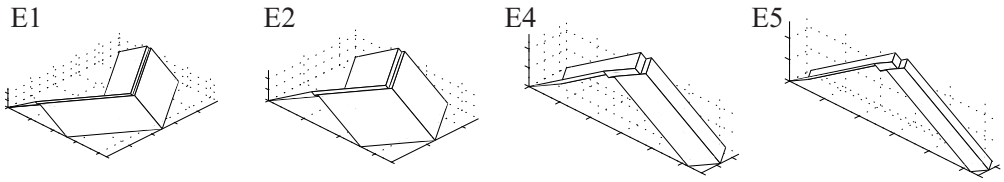


(a) Side length aspect ratio $b^*$ models

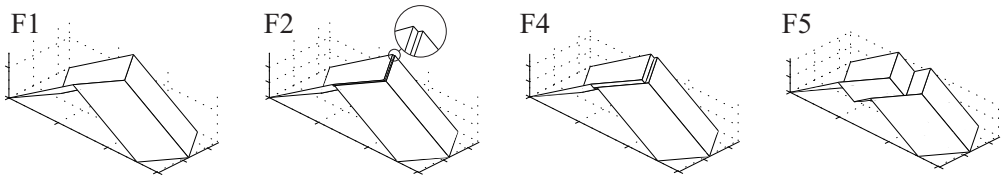


(b) Indent aspect ratio $p^*$ models

Figure 3.7: Aspect ratio model geometry.

range from a small to large indent depth, with indent aspects of $p^* = 0, 0.017, 0.05$, and 0.25 respectively. Finally, models G1, G3, and G4 range from low to high densities of $\alpha = 2\%, 6\%$, and 8%, respectively. The skipped model number in each set, that is E3, F3, and G2, are those that correspond to the base geometry A1. The eight unit geometries of the E and F models are shown in Figure 3.7 and the altered parameters for all eleven models are shown in Table 3.4(b). Note the configuration parameters are not listed as they are the same as model A1.

### 3.2.2 Simulation Results and Discussion

The twenty-four pattern configuration and aspect ratio models were numerically analysed under quasi-static loading in the manner previously described. Dimensionless results and representative failure modes are shown and discussed below.

#### Pattern Configuration Results

A range of failure modes is seen in the constant $\phi$ models B1-B5. Model B1 exhibits a plate buckling behaviour, typified by a sharp initial peak force followed by a steep drop in reaction force, Figure 3.8(a). Inspection of the stress plot, Figure 3.9(a), shows the hinge lines formed during the initial buckle remain stationary for the crush duration. Models B2 and B3 show the start of a travelling hinge line failure mode, typified by a double-peak in the force-displacement plot. From the stress plot, Figure 3.9(b), it can be seen that this double-peak corresponds to an initial inversion about the indent, a slight dip in strength as this buckle propagates, and then a second peak prior to the onset of plate buckling at approximately $h^* = 20\%$. The second peak is very brief as the hinge line does not propagate for long, and so the models are still considered to be dominated by plate buckling behaviours. Models B4 and B5 exhibit the same failure previously discussed for model A1, that is initial buckling and subsequent propagation around the top indent, followed by buckling and rotation about the base supports.

Relevant values from the stress-displacement plots are listed in Table 3.5. By plotting the uniformity ratio against the average stress for each model we are able to establish an optimum model for energy-absorption, that is the model with a low $U^*$ with a high $\sigma^*_{avg}$, Figure 3.8(b). Model B3 is seen to be the optimum model of B1-B5, showing that a short-duration travelling hinge line failure mode is better suited for energy-absorption applications than a plate buckling mode.

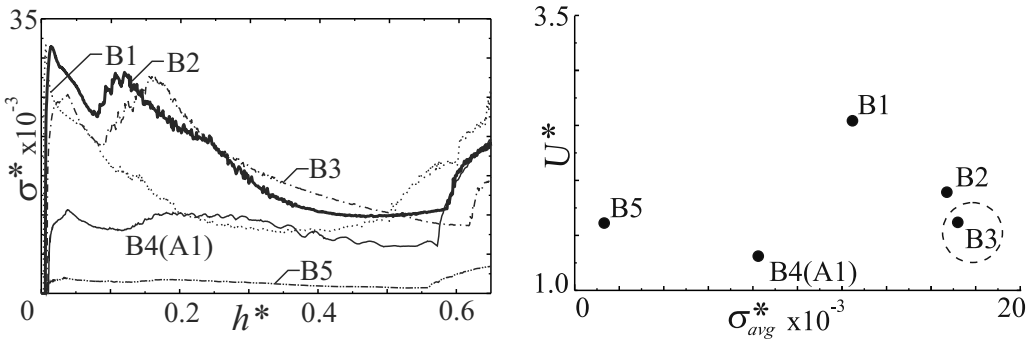


(a) Dimensionless stress-strain responses (b) Energy absorption suitability

Figure 3.8: Dimensionless results of constant $\phi$ models B1-B5.

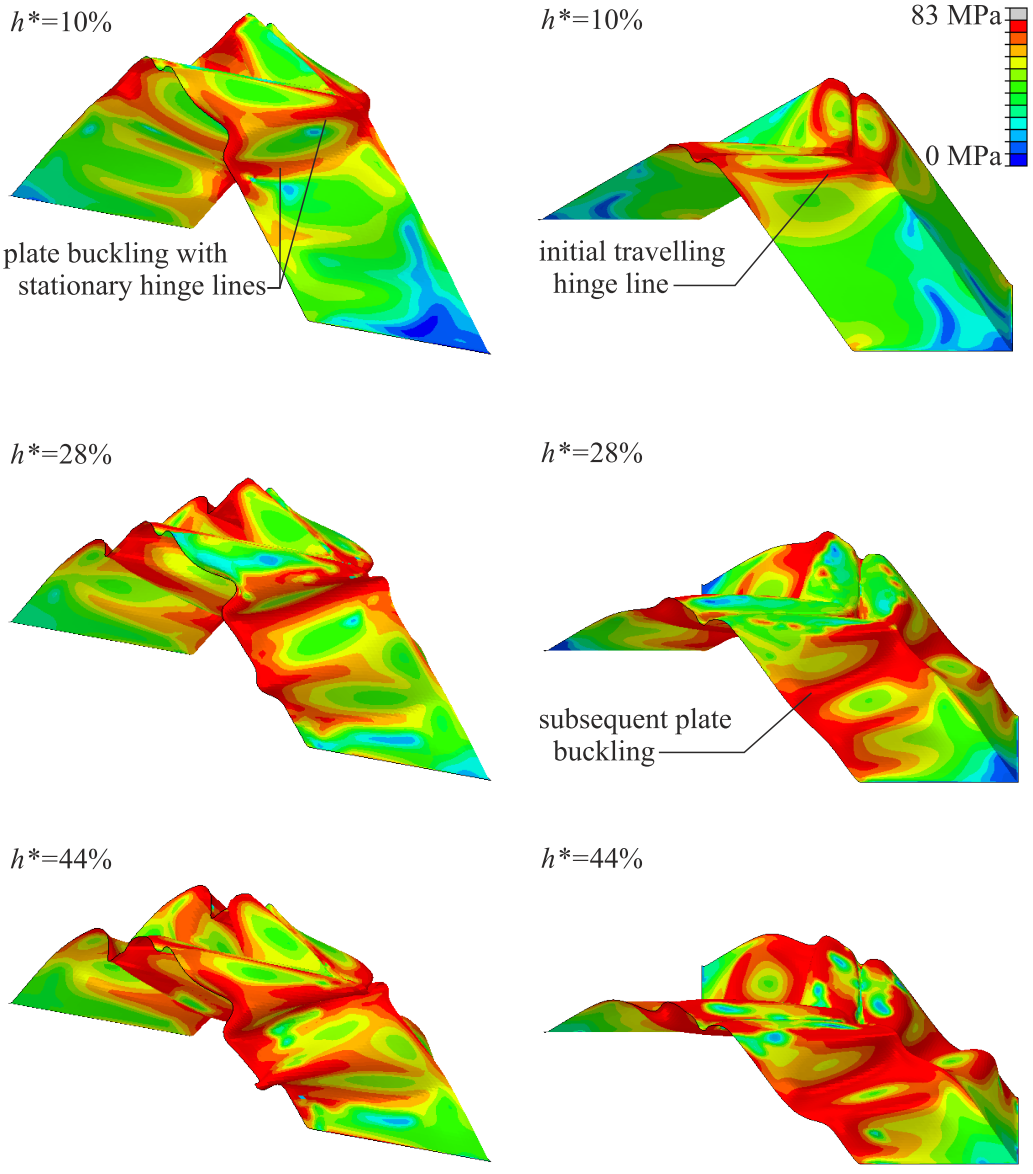


(a) Model B1 (b) Model B3

Figure 3.9: Hinge formation and Von-Mises stress in constant $\phi$ models

Table 3.5: Results of configuration parameter numerical models.

| *Model* | $h_d^*$ | $E_d^*$ $\times 10^{-3}$ | $\sigma_{max}^*$ $\times 10^{-3}$ | $\sigma_{avg}^*$ $\times 10^{-3}$ | $U^*$ |
|---|---|---|---|---|---|
| A1 | 0.57 | 4.7 | 10.6 | 8.2 | 1.3 |
| B1 | 0.60 | 7.5 | 31.7 | 12.5 | 2.5 |
| B2 | 0.60 | 10 | 31.5 | 16.7 | 1.9 |
| B3 | 0.58 | 9.9 | 27.6 | 17.2 | 1.6 |
| B5 | 0.56 | 0.7 | 2.0 | 1.3 | 1.6 |
| C1 | 0.60 | 9.5 | 34.5 | 15.8 | 2.2 |
| C2 | 0.60 | 10.5 | 32.9 | 17.4 | 1.9 |
| C3 | 0.57 | 10.4 | 22.0 | 18.3 | 1.2 |
| C5 | 0.56 | 1.8 | 4.4 | 3.2 | 1.4 |
| D1 | 0.51 | 6.0 | 16.8 | 11.8 | 1.4 |
| D2 | 0.60 | 6.5 | 14.1 | 10.8 | 1.3 |
| D4 | 0.57 | 2.8 | 8.2 | 4.9 | 1.7 |
| D5 | 0.58 | 2.0 | 7.2 | 3.4 | 2.1 |

The stress-displacement plots of the constant $\eta_Z$ models C1-C5 are shown in Figure 3.10(a). Models C1, C2, and C3 each show the double-peak which signifies an initial inversion and travelling hinge formation. However the duration of the second peak, which represents the time before the travelling hinge is lost to plate buckling behaviours, varies considerably for each model. From Figure 3.11(a), it can be seen that in model C1 this secondary buckling occurs almost immediately after initial inversion at $h^* = 10\%$. However in model C3, Figure 3.11(b), plate buckling does not occur until approximately $h^* = 35\%$, and so the travelling hinge line was maintained over a much longer period.

Relevant energy-absorption values from Table 3.5 are plotted in Figure 3.10(b). Model C3 has exceptional energy-absorption properties, with the highest $\sigma_{avg}^*$ and the lowest $U^*$. This shows that a greater duration for which the travelling hinge line is present corresponds to a smaller disparity between the peak and average stress, and therefore a much better energy-absorption capability. It also causes a near-ideal uniformity, with model C3 possessing a uniformity of 1.2 that is close to the ideal value of unity.

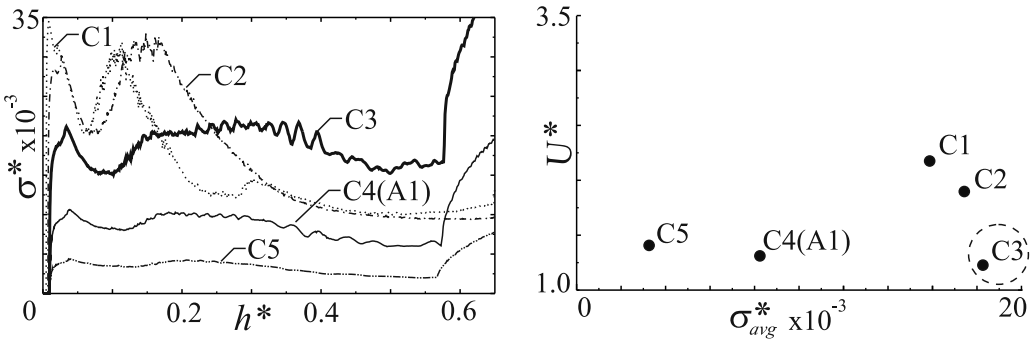


(a) Dimensionless stress-strain responses (b) Energy absorption suitability

Figure 3.10: Dimensionless results of constant $\eta_Z$ models.

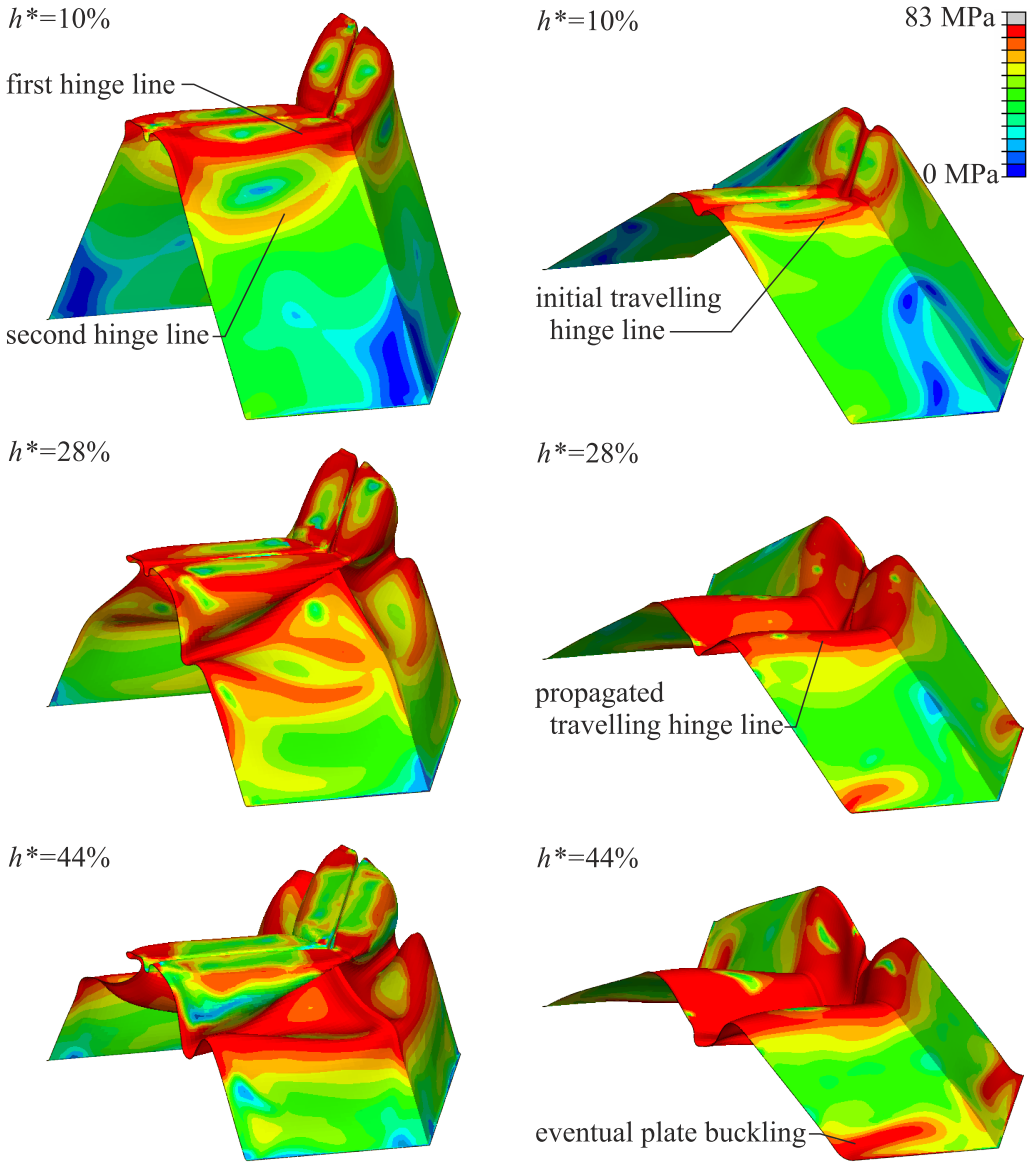


(a) Model C1 (b) Model C3

Figure 3.11: Hinge formation and Von-Mises stress in constant $\eta_Z$ models

A slightly different pattern is seen in the constant $\eta_A$ models D1-D5, with the steepest configuration D1 having a plate buckling mode with the highest specific energy absorption, Figure 3.12(a). Inspection of the plate stresses shows that this plate buckling occurs about the long diagonal of the core plates, as opposed to the middle or top of the core plates as seen above. Although this model has a higher $\sigma^*_{avg}$ than the travelling hinge line failure seen in the remaining models, the failure mode seen in model D2 is still judged to be the optimum arrangement as it has a better uniformity ratio, Figure 3.12(b).

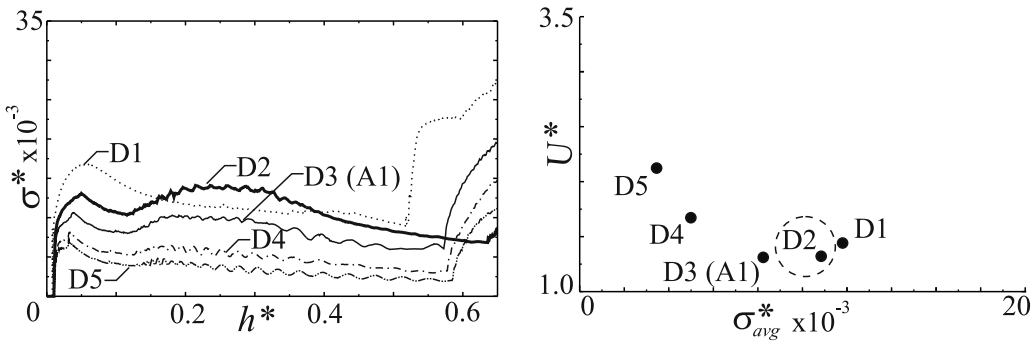


(a) Dimensionless stress-strain responses (b) Energy absorption suitability

Figure 3.12: Dimensionless results of constant $\eta_A$ models.

To summarise, pattern configuration parameters strongly affect the location of the initial plate buckling and subsequent formation and duration of travelling hinge line failure modes. Steep patterns can cause either plate buckling, or initial hinge inversion followed immediately by plate buckling, that is to say no hinge line propagation, shown in Figure 3.9(a) and Figure 3.11(a). These modes have reasonably high values of $\sigma^*_{avg}$ but generally poor $U^*$, due to the sharp reduction in reaction stress following the initial buckle. Shallower patterns typically cause top-plate buckling, followed by buckling and rotation about the base supports, shown in Figure 3.4(d). These give failure modes with a poor $\sigma^*_{avg}$ but generally good $U^*$. Between these two extremes exist core configurations that allow travelling hinge formation and propagation at high stress levels, creating cores with both a uniform stiffness response and a high specific energy absorption, shown in Figure 3.11(b).

### Aspect Ratio Results

The dimensionless stress-strain results of the five side length aspect ratio models E1-E5 are shown in Figure 3.13(a) and Table 3.6. Three distinct failure modes are seen. The narrowest model E5, with $b^* = 0.125$, shows a beam buckling failure mode, typified by an initial peak stress followed by an immediate post-buckling stress reduction, Figure 3.14(a). The widest model E1, with $b^* = 2$, has a plate buckling mode that is similar to the beam buckling mode, but with a less severe post-buckling stress reduction, Figure 3.14(b). Inspection of the plate stresses shows that the plate aspect of model E5 is too narrow to cause plate buckling and the plate aspect of model E1 is too wide to allow a travelling hinge line to form.

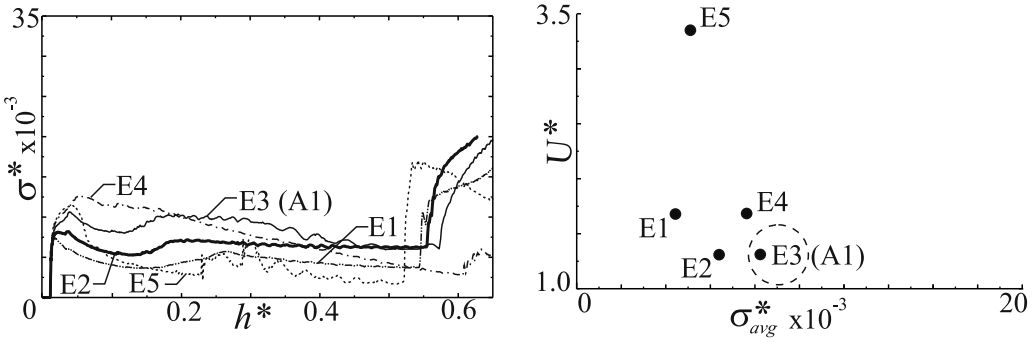


(a) Dimensionless stress-strain responses (b) Energy absorption suitability

Figure 3.13: Dimensionless results of side length aspect $b^*$ models.

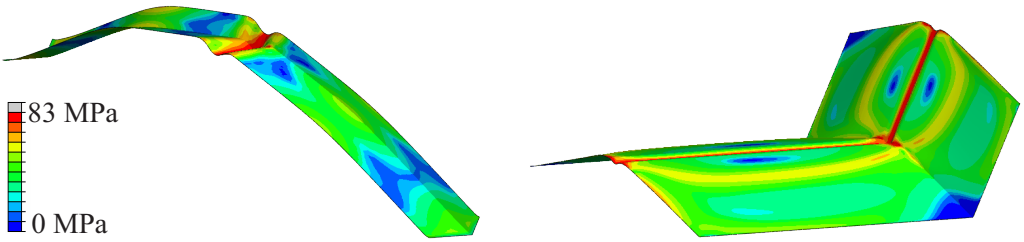


(a) Narrow model E5 (b) Wide model E1

Figure 3.14: Von-Mises stress of side length aspect models at $h^*$=10%.

The middle aspect ratio, model E3 with $b^* = 0.5$, exhibits the previously seen travelling hinge failure mode. The two final models, E2 and E4, show failure modes that are combinations of the three discussed above. From Figure 3.13(b) we can see that in terms of energy absorption suitability, the beam buckling mode is least suited, with a very high $U^*$, and that the travelling hinge line mode is

Table 3.6: Results of aspect ratio numerical models.

| *Model* | $h_d^*$ | $E_d^*$ $\times 10^{-3}$ | $\sigma_{max}^*$ $\times 10^{-3}$ | $\sigma_{avg}^*$ $\times 10^{-3}$ | $U^*$ |
|---|---|---|---|---|---|
| A1 | 0.57 | 4.7 | 10.6 | 8.2 | 1.3 |
| E1 | 0.54 | 2.4 | 7.4 | 4.4 | 1.7 |
| E2 | 0.55 | 3.5 | 8.2 | 6.3 | 1.3 |
| E4 | 0.60 | 4.5 | 12.6 | 7.6 | 1.7 |
| E5 | 0.52 | 2.6 | 17.1 | 5.1 | 3.4 |
| F1 | 0.60 | 4.7 | 16.9 | 7.8 | 2.2 |
| F2 | 0.60 | 4.6 | 17.1 | 7.6 | 2.2 |
| F3 | 0.60 | 5.5 | 12.8 | 9.1 | 1.4 |
| F5 | 0.41 | 1.2 | 3.6 | 3.0 | 1.2 |
| G1 | 0.55 | 1.4 | 3.0 | 2.5 | 1.2 |
| G3 | 0.60 | 9.8 | 20.7 | 16.3 | 1.3 |
| G4 | 0.60 | 16.7 | 33.0 | 27.8 | 1.2 |

again better suited than the plate buckling mode.

The dimensionless stress-strain plots of the indent aspect models F1-F5 are shown in Figure 3.15(a) and relevant values are summarised in Table 3.6. It can be seen that there is no change in the failure mode from F1 to F2, indicating that a minimum threshold indent depth must be reached before the indent is effective at changing the core failure mode. In this case the minimum threshold is reached in model F3 with $p^* = 0.05$. Increasing the indent depth significantly beyond this minimum threshold does not provide any further advantage, with models F4 and F5 both having poorer performance in terms of energy-absorption capabilities, Figure 3.15(b). Model F3 is therefore judged to possess the best indent aspect ratio.

Finally, results of the four density study models G1-G4 are shown in Figure 3.16(a). It can be seen that denser models have a stronger response and that the failure mode remains essentially unchanged up to model G4, with a density of $\alpha = 8\%$. Inspection of the stress distribution of model G4, Figure 3.16(b) confirms that it fails in a similar manner to model A1, Figure 3.6(c), with the main difference being a larger area of stress distribution across the thicker core plates.

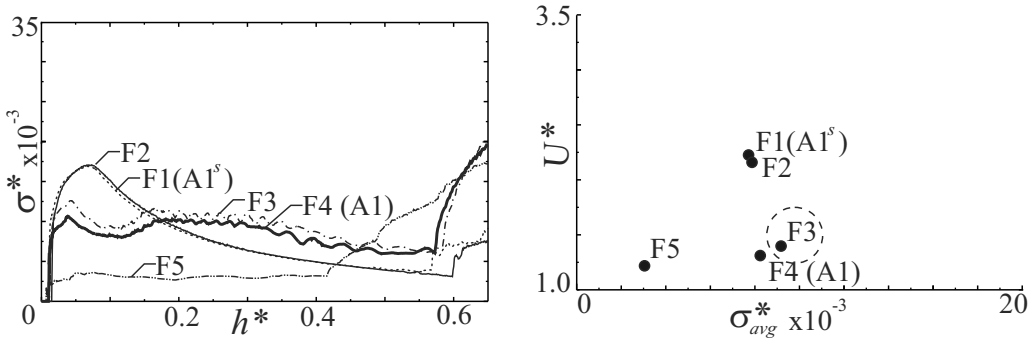


(a) Dimensionless stress-strain responses (b) Energy absorption suitability

Figure 3.15: Dimensionless results of indent aspect $a_i^*$ models.

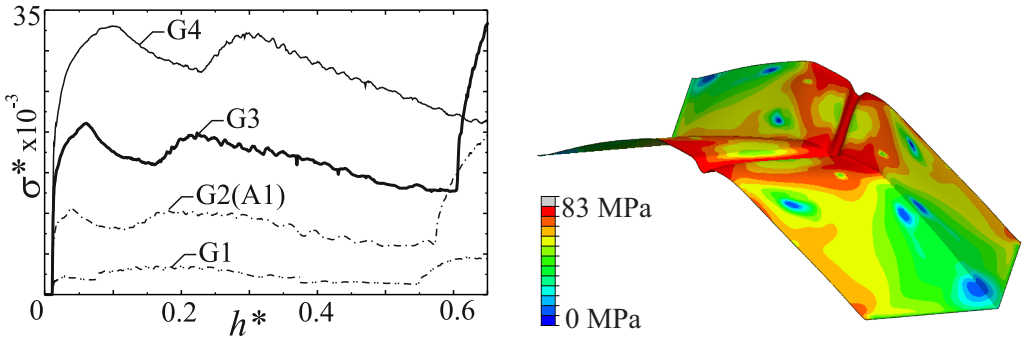


(a) Dimensionless stress-strain responses (b) Von-Mises stress of G4 at $h^* = 28\%$

Figure 3.16: Dimensionless results of density $\alpha$ models.

The results of the twenty-one models A1-F5 have been collated and plotted in Figure 3.17(a). Note that the density study models G1-G4 are excluded, as models of different densities are not directly comparable on a $\sigma^*_{avg}$-$U^*$ plot. It can be seen that model C3 is the optimum indented model, with a 123.1% improvement in $\sigma^*_{avg}$ and a 7.7 % reduction in $U^*$, compared to the initial geometry A1.

### 3.2.3 Standard Foldcore Optimisation and Comparison

In order to fairly compare the improved indented geometry with a standard foldcore, an improved standard foldcore geometry need also be established. Therefore seventeen equivalent standard models, A1$^s$-E5$^s$, were constructed from indented model geometric parameters, with the four indent aspect models excluded. Note that the superscript $s$ is used here to indicate a standard, unindented foldcore. Results from the standard foldcore numerical simulations are listed in Table 3.7

Table 3.7: Results of equivalent standard models.

| *Model* | $h_d^*$ | $E_d^*$ $\times 10^{-3}$ | $\sigma_{max}^*$ $\times 10^{-3}$ | $\sigma_{avg}^*$ $\times 10^{-3}$ | $U^*$ |
|---|---|---|---|---|---|
| A1$^s$ | 0.60 | 4.7 | 16.9 | 7.8 | 2.2 |
| B1$^s$ | 0.60 | 8.4 | 37.6 | 14 | 2.7 |
| B2$^s$ | 0.60 | 11.3 | 42.0 | 18.8 | 2.3 |
| B3$^s$ | 0.60 | 10.8 | 36.5 | 17.9 | 2.1 |
| B5$^s$ | 0.60 | 1.2 | 3.3 | 1.9 | 1.8 |
| C1$^s$ | 0.60 | 11.1 | 51.4 | 18.5 | 2.8 |
| C2$^s$ | 0.60 | 11.8 | 46.2 | 19.7 | 2.4 |
| C3$^s$ | 0.60 | 9.2 | 32.8 | 15.3 | 2.2 |
| C5$^s$ | 0.60 | 2.3 | 6.8 | 3.9 | 1.8 |
| D1$^s$ | 0.53 | 6.8 | 19.1 | 12.9 | 1.5 |
| D2$^s$ | 0.60 | 5.6 | 17.8 | 9.3 | 2.0 |
| D4$^s$ | 0.60 | 4.7 | 15.5 | 7.9 | 2.0 |
| D5$^s$ | 0.60 | 3.7 | 14.5 | 6.2 | 2.4 |
| E1$^s$ | 0.60 | 4.5 | 13.5 | 7.4 | 1.9 |
| E2$^s$ | 0.55 | 5.5 | 14.8 | 10.0 | 1.5 |
| E4$^s$ | 0.60 | 6.0 | 17.3 | 10.0 | 1.8 |
| E5$^s$ | 0.53 | 2.8 | 14.1 | 5.3 | 2.7 |

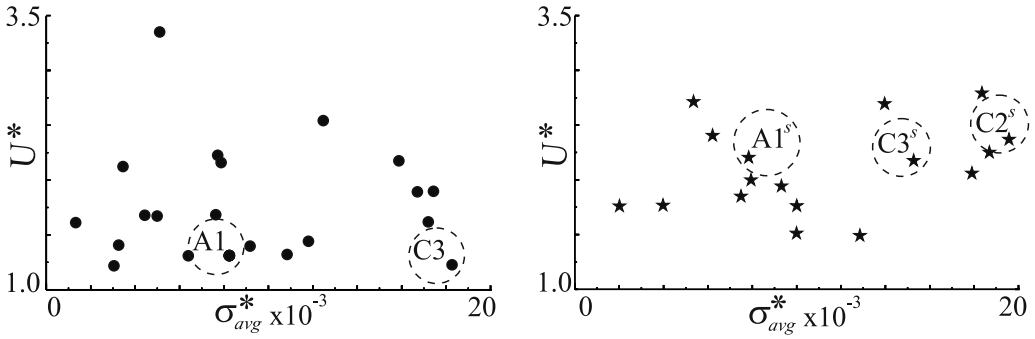


(a) Indented models (b) Standard models

Figure 3.17: Distribution of indented and standard model results.

and plotted in Figure 3.17(b). It can be seen that the standard configuration with the highest $\sigma_{avg}^*$ is C2$^s$, with a 152.3% improvement in $\sigma_{avg}^*$ and a 7.4% increase in $U^*$, compared to the initial model A1$^s$. Also highlighted in Figure 3.17(b) is model C3$^s$, which is seen to have a 22.3% lower $\sigma_{avg}^*$ compared to model C2$^s$. Indented and standard foldcores are therefore seen to have different optimum configurations, with C3 optimum for the former and C2$^s$ optimum for the latter. This is unsurprising since they involve different failure modes, as will be seen below.

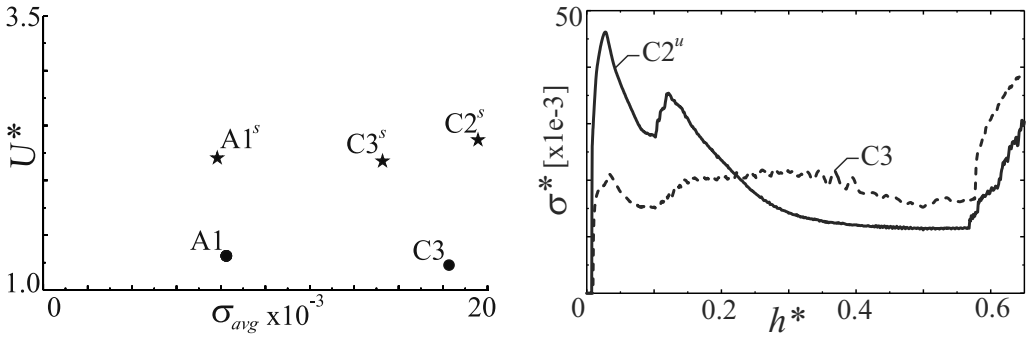


(a) Energy absorption suitability (b) Dimensionless stress-strain responses

Figure 3.18: Comparison of optimum indented and standard models.

Figure 3.18(a) shows a direct comparison between the optimised indented geometry C3, the equivalent standard geometry C3$^s$, and the optimised standard C2$^s$. Comparing C3 and C3$^s$, it can be seen that the indented model offers a significant improvement, with a large increase of 19.6% in $\sigma^*_{avg}$ and a large reduction of 45.4% in $U^*$. Comparing C3 and C2$^s$ the indented model is again seen to be an improvement, with a slight reduction of 7.2% in $\sigma^*_{avg}$ but a large reduction of 50.7% in $U^*$. By either comparison, it can be seen that the indented core is much better suited for energy-absorption applications requiring a uniform stress response.

Figure 3.19 shows the hinge formation and stress propagation for the C3 and C2$^s$ models. It can clearly be seen that the uniform indented response is due to a very stable travelling hinge line progression. The initial hinge formation at the top ridge of the pattern keeps the remaining plate area relatively undistorted, allowing the inversion to propagate and the resisting stress to remain high. By comparison, the standard core has a higher initial stress because the initial plate buckle plasticises a larger area, however this distorts the rest of the core plates, causing them to subsequently collapse at a reduced stress level. If model C3 is taken as an optimum travelling hinge line failure mode, and model C2$^s$ is taken as an optimum plate buckling failure mode, it can be concluded that the travelling hinge line is better suited for energy-absorption purposes.

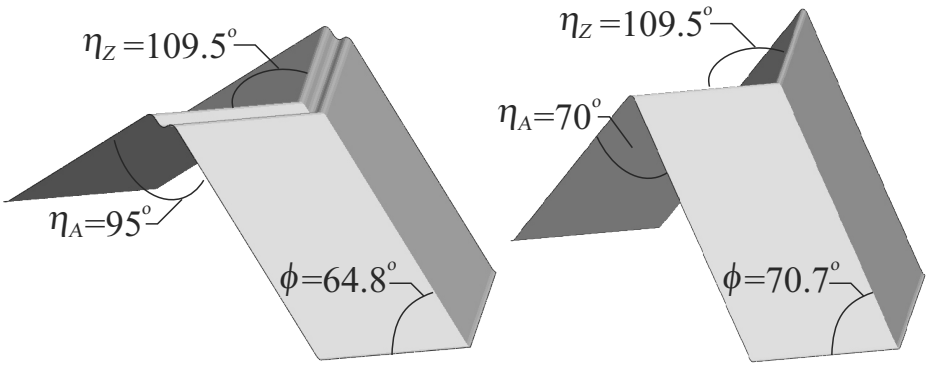


(a) Optimum indented model C3 and standard model C2$^s$

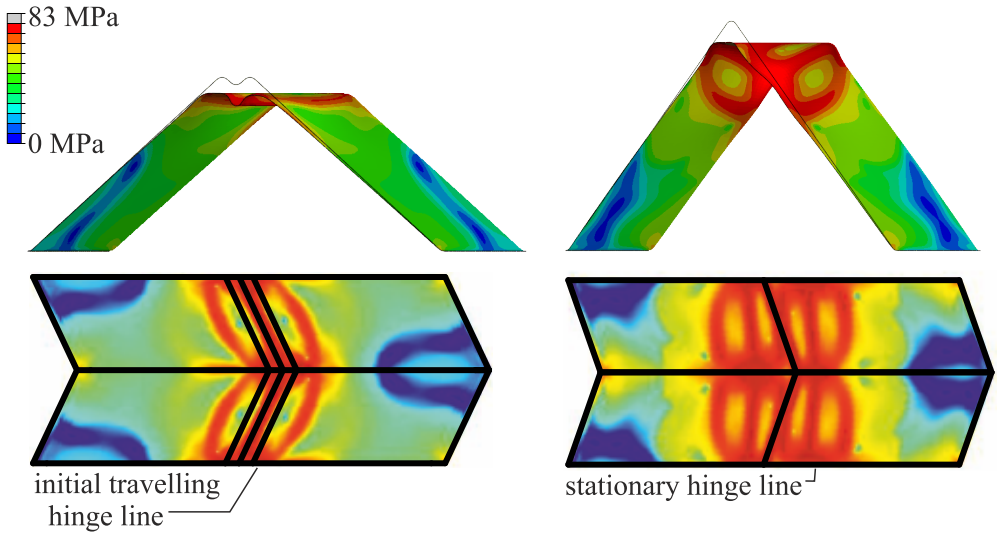


(b) Model C3 and C2$^s$ at $h^* = 10\%$

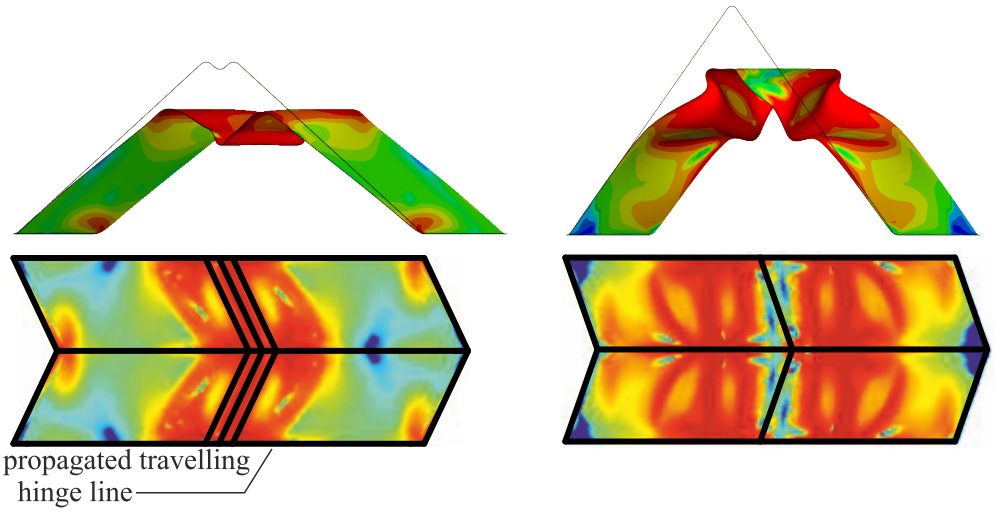


(c) Model C3 and C2$^s$ at $h^* = 28\%$

Figure 3.19: Side view and projected view showing Von-Mises stress and hinge propagation on optimal indented (left) and standard (right) foldcores.

As a final comparison, models C3 and C2$^s$ were rerun with different densities of $\alpha = 2\%, 6\%$, and 8%. These results, along with the original $\alpha = 4\%$ models, are listed in Table 3.8 and plotted in Figure 3.20. It can be seen that the usefulness of indent fades at higher densities, that is to say that in comparison to standard models at the same density, the indented models have an increasingly lower $\sigma^*_{avg}$ and decreasingly lower $U^*$, as the density increases. Inspection of two stress-displacement curves at a higher density, Figure 3.20(b), shows that the travelling hinge line failure mode is still present, however it does not appear to strengthen at the rate that the plate buckling mode does. A possible explanation for this is suggested in the following section. In terms of uniformity, the indented response is approximately constant whereas the standard core improves as the density increases. These two differences combine to erode the benefits of employing an indented foldcore as the density increases.

Table 3.8: Optimal foldcore geometries at alternative densities.

| | C3 | | | C2$^s$ | | |
|---|---|---|---|---|---|---|
| $\alpha$ | $\sigma^*_{max}$ | $\sigma^*_{avg}$ $\times 10^{-3}$ | $U^*$ $\times 10^{-3}$ | $\sigma^*_{max}$ | $\sigma^*_{avg}$ $\times 10^{-3}$ | $U^*$ $\times 10^{-3}$ |
| 0.02 | 7.4 | 5.1 | 1.4 | 14.7 | 5.0 | 2.9 |
| 0.04 | 22.0 | 18.3 | 1.2 | 46.2 | 19.7 | 2.4 |
| 0.06 | 41.8 | 35.0 | 1.2 | 84.5 | 38.0 | 2.2 |
| 0.08 | 69.7 | 56.4 | 1.2 | 124.0 | 66.0 | 1.9 |

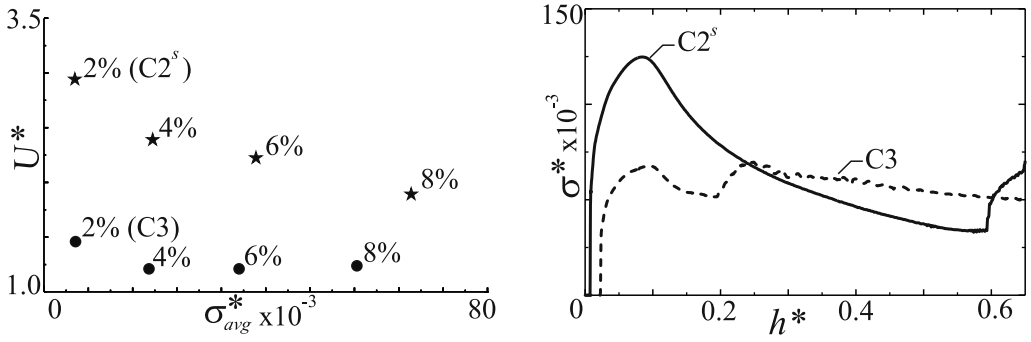


(a) Energy absorption suitability (b) Models C2$^s$ and C3 at $\alpha = 8\%$

Figure 3.20: Comparison of optimum foldcore geometries at different densities.

## 3.3 Analytical Prediction of Ideal Failure Mode

Using the energy method, it is possible to develop a theoretical prediction of the energy absorbed by an idealised travelling hinge line failure mode. Based on the method used in Wierzbicki and Abramowicz (1984), the model states that the energy absorbed in the crushing of a thin-walled element is the sum of energy absorbed by:

- $E_1$: Travelling plastic hinge lines.
- $E_2$: Intersection points between two travelling hinge lines.
- $E_3$: Stationary (static) hinge lines.

The material is assumed to be rigid-perfectly plastic with a constant value of flow stress $\sigma_o$ to account for strain-hardening. The plastic flow stress can be calculated by (Santosa, 2000):

$$\sigma_o = \sqrt{\frac{\sigma_Y \sigma_U}{1+n}} \tag{3.3}$$

Given plate thickness $t_p$, the material compressive strength $N_o$ and plastic bending moment $M_o$ per unit length are then:

$$N_o = \sigma_o t_p \tag{3.4}$$

$$M_o = \frac{\sigma_o t_p^2}{4} = \frac{N_o t_p}{4} \tag{3.5}$$

### 3.3.1 $E_1$: Travelling Hinge Lines

A kinematically admissible collapse mechanism is assumed for a single core element based on the travelling hinge line failure mode observed in the numerical models, specifically model C3, Figure 3.21(a). This mechanism forms four cylindrical trav-

elling hinge surfaces, $C_1, C_2, C_3$, and $C_4$. As each travelling hinge sweeps through an area of material, energy is dissipated through the bending and unbending of the plate material to radius $r$. The energy dissipated by this travelling hinge line is equal to:

$$E = 2A_p \frac{M_o}{r} \tag{3.6}$$

where $A_p$ is the area of material plasticised by the travelling hinge. From the assumed kinematic mechanism, Figure 3.21(b), it can be see that the final crush height $\delta_{max}$ is equal to half of the total core height:

$$\delta_{max} = l_t/2 = a_s \cos(\eta_A/2)/2 \tag{3.7}$$

Projecting this deformation onto the unfolded core plates, it can be seen that the total area of plasticised plate is equal to half of the area of the inclined plates, Figure 3.21(c). The energy absorbed by the four travelling hinge lines is therefore given by:

$$E_1 = 4\frac{M_o}{r} a_s b \sin\phi \tag{3.8}$$

### 3.3.2 $E_2$: Intersection of Travelling Hinge Lines

At the intersection of two discontinuous travelling hinge lines, a localised toroidal zone of stress from material discontinuity arises. In the assumed collapse mechanism, core symmetry constraints cause four of these intersection zones to form, $T_1, T_2, T_3$, and $T_4$, Figure 3.21(a). From Wierzbicki and Abramowicz (1984), the following simplified formula is given for the rate of energy dissipation $\dot{\mathrm{E}}$ over the deformed surface, assuming the contribution to energy dissipated from circumferential extension is large relative to that from continuous bending:

$$\dot{E} = \int_A N_o \frac{V_t \sin\kappa}{q} \mathrm{d}A \tag{3.9}$$

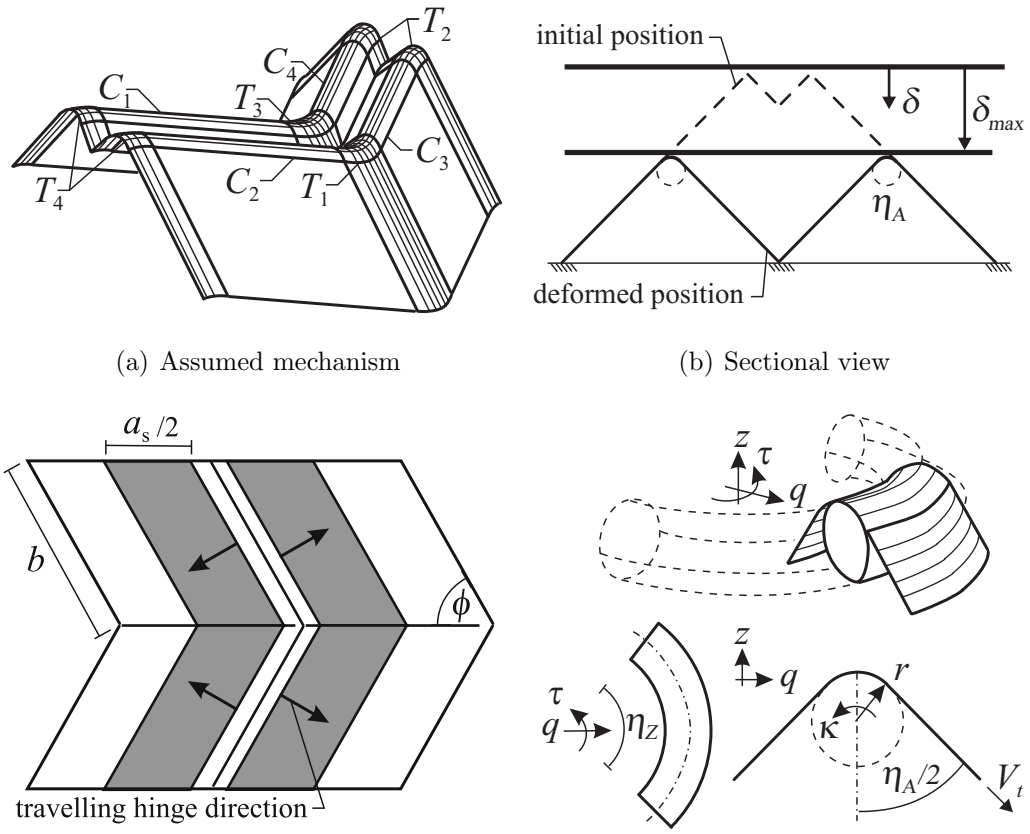


(a) Assumed mechanism (b) Sectional view

(c) Area plasticised by travelling hinge lines (d) Toroidal surface at intersection points

Figure 3.21: Idealised collapse mechanism for indented foldcore.

where $V_t$ is the tangential velocity of the plate over the deformation surface, and $q$, $\kappa$, and $A$ are the radius, rotation angle and area of the deformed plate over the toroidal surface respectively, shown in Figure 3.21(d). The surface element $\mathrm{d}A$ can be reformulated as:

$$\mathrm{d}A = q\mathrm{d}\tau r\mathrm{d}\kappa \tag{3.10}$$

$$\text{where } -\eta_Z/2 < \tau < \eta_Z/2 \text{ and } \eta_A/2 < \kappa < \pi - \eta_A/2$$

This allows Equation (3.9) to be reformulated as:

$$\begin{aligned}\dot{E} &= N_o V_t r \int_{-\eta_Z/2}^{\eta_Z/2}\int_{\eta_A/2}^{\pi-\eta_A/2} \sin\kappa \mathrm{d}\kappa\mathrm{d}\tau \\ &= 2N_o V_t r\cos(\eta_A/2)\int_{-\eta_Z/2}^{\eta_Z/2}\mathrm{d}\tau \\ &= 2N_o V_t r\cos(\eta_A/2)\eta_Z \end{aligned} \tag{3.11}$$

The vertical velocity of the top plate $V$ can be defined relative to the vertical

displacement of the top crushing plate $\delta$ as $V = \dot{\delta}$. From geometry, this can be related to tangential velocity $V_t$ by:

$$V_t = V/\cos(\eta_A/2) = \dot{\delta}/\cos(\eta_A/2) \tag{3.12}$$

Substituting Equations (3.12) and (3.5) into Equation (3.11) gives the following:

$$\dot{E} = 8M_o\eta_Z\frac{r}{t_p}\dot{\delta} \tag{3.13}$$

The total energy per travelling hinge intersection can then be found by integrating this equation over the total crush height given in Equation (3.7).

$$\begin{aligned}\int \dot{E} &= 8M_o\eta_Z\frac{r}{t_p}\int_0^{\delta_{max}} \mathrm{d}\delta \\ E &= 4a_sM_o\frac{r}{t_p}\eta_Z\cos(\eta_A/2)\end{aligned} \tag{3.14}$$

The total energy absorbed by the four travelling hinge intersection points is therefore given by:

$$E_2 = 16a_sM_o\frac{r}{t_p}\eta_Z\cos(\eta_A/2) \tag{3.15}$$

### 3.3.3 Total Energy

No static hinge lines are formed in the assumed collapse mechanism, so the total energy absorbed is equal to the sum of energy from the cylindrical travelling hinge lines and their toroidal intersections:

$$\begin{aligned}E &= E_1 + E_2 \\ &= 4a_sM_o\left(\frac{b\sin\phi}{r} + 4\frac{r}{t_p}\eta_Z\cos(\eta_A/2)\right) \\ &= 4a_sM_o\left(\frac{k_1}{r} + k_2r\right)\end{aligned} \tag{3.16}$$

$$\text{where } k_1 = b\sin\phi \text{ and } k_2 = 4\eta_Z\cos(\eta_A/2)/t_p$$

The hinge radius $r$ is chosen to give a minimum energy solution. This is found

when the derivative of Equation (3.16) with respect to $r$ is equal to zero:

$$\frac{\mathrm{d}E}{\mathrm{d}r} = 0 = 4a_s M_o \left(-\frac{k_1}{r^2} + k_2\right)$$
$$r = \sqrt{k_1/k_2} \tag{3.17}$$

Substituting Equations (3.17) and (3.5) into Equation (3.16) gives expressions for total energy $E$, and the average reaction force needed to generate this energy absorption $P$:

$$\begin{aligned} E &= 8a_s M_o \sqrt{k_1 k_2} \\ &= 4a_s \sigma_o t_p \sqrt{b t_p \sin\phi \eta_Z \cos(\eta_A/2)} \end{aligned} \tag{3.18}$$

$$\begin{aligned} P = \frac{E}{\delta_{max}} &= \frac{E}{a_s/2\cos(\eta_A/2)} \\ &= 8\sigma_o t_p \sqrt{t_p b \sin\phi \eta_Z/\cos(\eta_A/2)} \end{aligned} \tag{3.19}$$

Note that these equations have been formulated to show total energy absorbed up to the maximum crush displacement $\delta_{max}$. However Equations (3.8) and (3.15) can be reformulated as a function of $\delta$ to show that $E$ varies linearly with crush displacement, and $P$ is a constant value independent of crush depth. As the reaction force is constant, $P = P_{avg} = P_{max}$, and $U = 1$.

Finally the previous equation can be reduced to a dimensionless value as follows:

$$\begin{aligned} \sigma^* = \frac{P}{l_a l_b \sigma_Y} &= \frac{P}{4\sigma_Y ab \sin(\eta_Z/2)\sin(\eta_A/2)} \\ &= 2\frac{\sigma_o}{\sigma_Y}\frac{t_p}{a}\sqrt{\frac{t_p}{b}\frac{\eta_Z \sin\phi}{\cos(\eta_A/2)}}\frac{1}{\sin(\eta_Z/2)\sin(\eta_A/2)} \end{aligned} \tag{3.20}$$

### 3.3.4 Theoretical and Numerical Comparison

Theoretical values for $\sigma^*$ for the four alternate density C3 models are listed in Table 3.9. Theoretical values were calculated with $a = 16.4$mm, $b = 8.2$mm, $t_p$ as

shown in Table 3.9, and configuration parameters as shown in Figure 3.19(a). $\sigma_o$ was obtained with Equation 3.3 using the aforementioned values of $\sigma_U$ and $\sigma_Y$ and a typical aluminium strain hardening exponent of $n = 0.22$. Figure 3.22 shows the theoretical stress plotted against $\sigma^*_{max}$ and $\sigma^*_{avg}$ from Table 3.8.

Table 3.9: Theoretical crush stress for model C3 at alternative densities.

| $\alpha$ | $t_p$ (mm) | $\sigma^*$ $\times 10^{-3}$ |
|---|---|---|
| 0.02 | 0.13 | 8.4 |
| 0.04 | 0.27 | 23.9 |
| 0.06 | 0.40 | 43.8 |
| 0.08 | 0.53 | 67.5 |

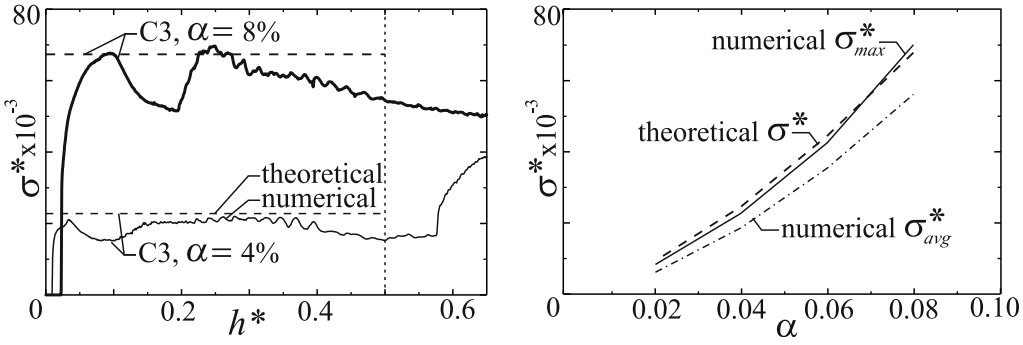


(a) Responses of $\alpha = 4\%$ and $\alpha = 8\%$ models (b) Comparison at different densities

Figure 3.22: Comparison of numerical and theoretical stresses for model C3.

It is apparent that the theory can accurately predict the maximum stress achieved in the C3 models, with a maximum overestimation of 14.1% at $\alpha = 2\%$ and underestimation of 3.1% at $\alpha = 8\%$. However is also apparent that there are two flaws in the theoretical model. First, there is a dip in stiffness that occurs during the initial plate inversion that is not accounted for in the current theory. Second, the theoretical collapse mechanism predicts that the travelling hinge should exist until $h^* = 50\%$, whereas numerical models show plate buckling behaviours dominate past approximately $h^* = 35\%$. A comparison of the theoretical and numerical displacement of model C3 at $\alpha = 4\%$, Figure 3.23(a) confirms that the assumed theoretical collapse mechanism is valid over the region that the travelling hinge line exists, and that once plate buckling behaviours occur beyond this point the assumed mechanism is no longer valid. The two flaws mean that the theoretical model is unable to accurately predict the average crush force.

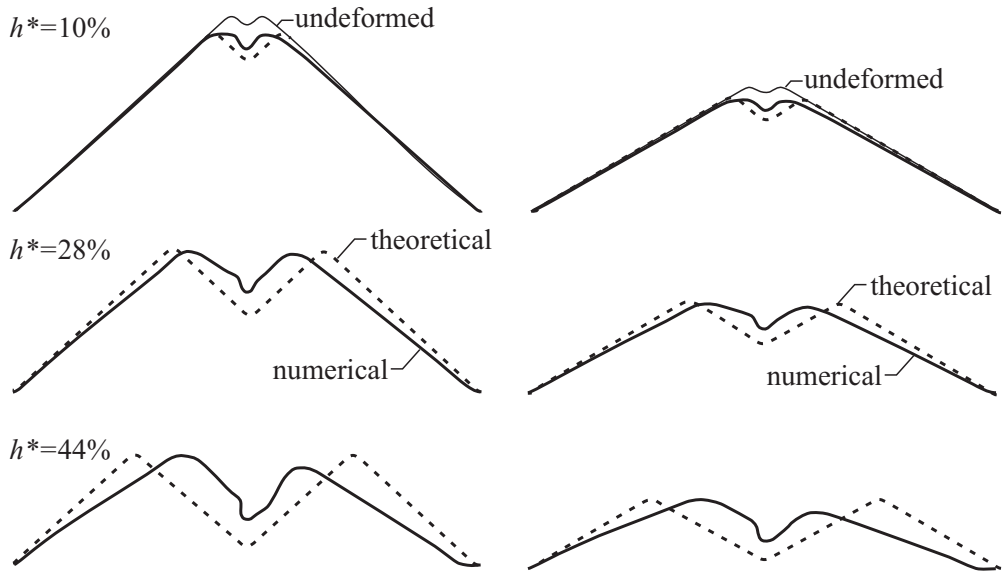


(a) Model C3 (b) Model A1

Figure 3.23: Comparison of numerical and theoretical displacements.

Although good correlation is seen for model C3, the theory poorly predicts the maximum force of other indented models. For example, model A1 had $\sigma^*_{max} = 10.6 \times 10^{-3}$ but is predicted by theory to have $\sigma^* = 20.1 \times 10^{-3}$. Inspection of the numerical and theoretical displacements, Figure 3.23(b), shows that the assumed mechanism still appears to be reasonably valid over the travelling hinge region, and so this discrepancy may be indicative of more serious errors in the theoretical derivation.

To summarise, the current theory is a simplified model that appears to provide a good approximation of maximum crushing stress of the optimum indented geometry, but not for other models that exhibit travelling hinge modes. Also, as theoretical predictions for foldcore plate buckling behaviour do not yet exist, the current theory cannot predict when a particular failure mode, be that plate buckling or travelling hinge line, might occur. As a final note, it was seen that the travelling hinge stress, Equation (3.20), was proportional to $t^{1.5}$, whereas typical plate buckling loads are proportional to $t^2$. This may explain why, in Section 3.2.3, the plate buckling mode was seen to strengthen at a faster rate at increasing densities, compared to the travelling hinge line mode.

## 3.4 Experiments on Large-Scale Models

An experimental investigation was conducted on indented and standard foldcores constructed with a relatively large core height of approximately 40mm. It is uncommon to use sandwich panels at this thickness, however these large initial models enable close observation of foldcore failure modes.

### 3.4.1 Geometry and Material

The indented core was designed using the ideal indented foldcore geometry presented in Section 3.2. Unit dimensions were chosen as $a = 60$mm, $b = 30$mm, $\phi = 64.8°$, $\eta_A = 95°$, and $p^* = 0.067$. To facilitate material draw during manufacture, 2mm fillets were also included at the foldcore ridge locations, giving a final unit height of $l_t = 36$mm, Figure 3.24. The total core was constructed using four units, two each in the longitudinal and lateral directions, for a global length $L$ and global width $W$ as shown in Table 3.10. Note the nomenclature for height $l_t$ is replaced with the equivalent global height $H$ for consistency.

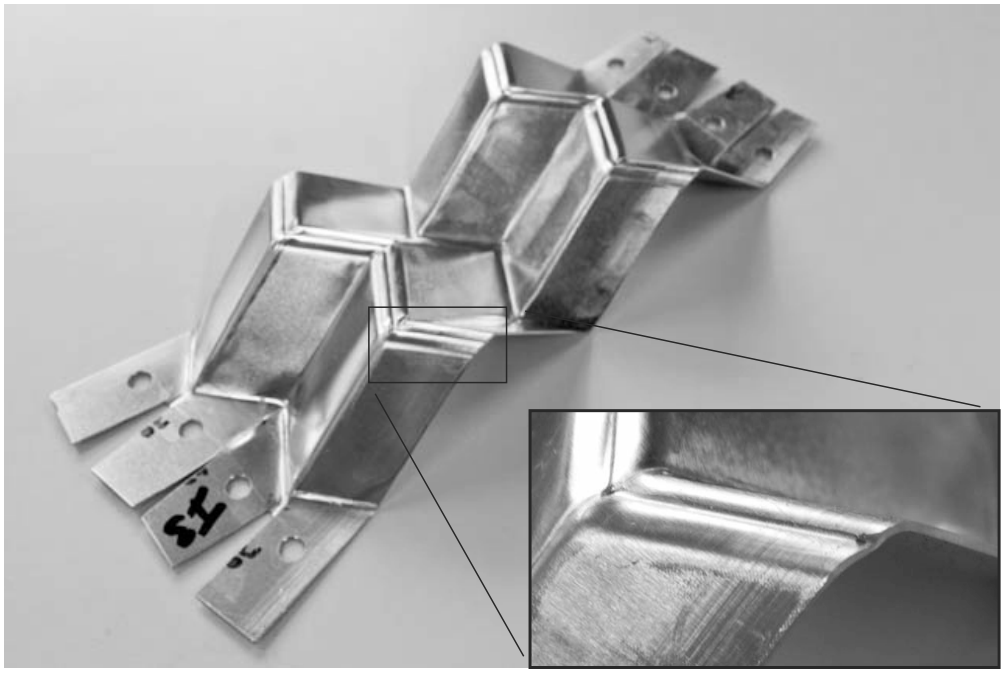

Figure 3.24: Indented foldcore constructed with $t_p = 1$mm aluminium sheet.

The standard core was designed with equivalent geometry to the indented model, with identical values for $a$, $b$, $\phi$, and $\eta_A$, and with $p^* = 0$, Figure 3.25. 2mm fillets were again added at foldcore ridge locations to give global dimensions as shown in Table 3.10. Both indented and standard cores were constructed from a pure aluminium sheet material at two sheet thicknesses, $t_p = 0.5$mm and 1.0mm, with resulting densities listed in Table 3.10.

Figure 3.25: Standard foldcore constructed with $t_p = 1$mm aluminium sheet.

### 3.4.2 Manufacturing Method

To form the standard foldcore, an aluminium sheet was first trimmed to approximately match the ideal crease pattern of the core geometry, although it was necessary to introduce two slight alterations. First, front and back tabs were added to the trimmed sheet to allow the eventual clamping of the foldcore during testing. Second, the width of the trimmed sheet was slightly truncated to prevent the material from catching on the mould edge during forming, Figure 3.26.

Male and female steel dies were used to form the foldcore in a single punch process, Figure 3.27(a). These dies were mounted on a mechanical punch press and aligned

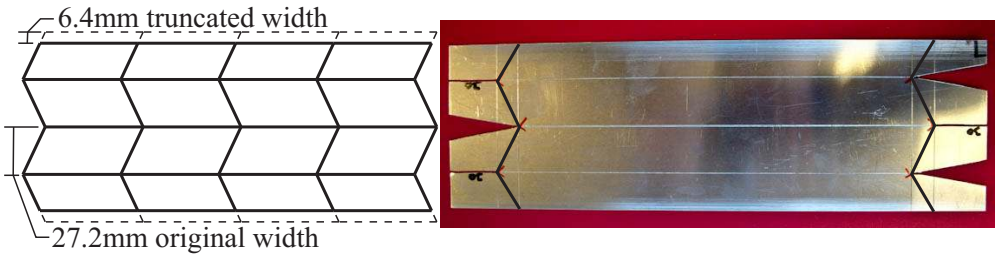


Figure 3.26: Ideal crease pattern and trimmed aluminium sheet.

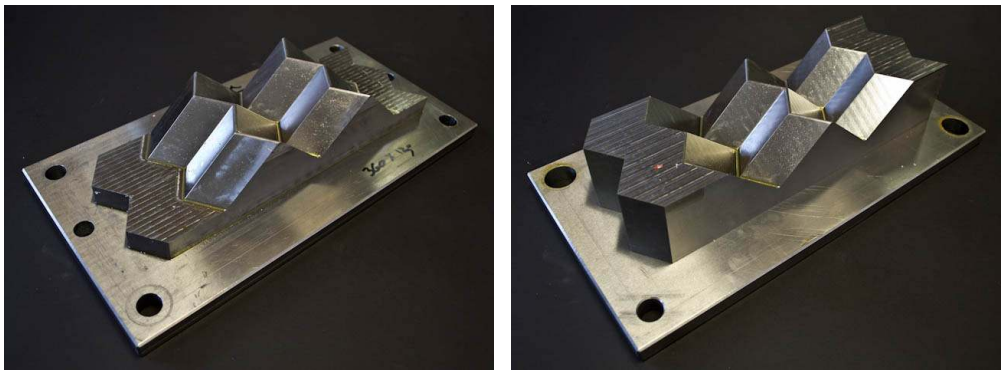

(a) Male and female standard dies

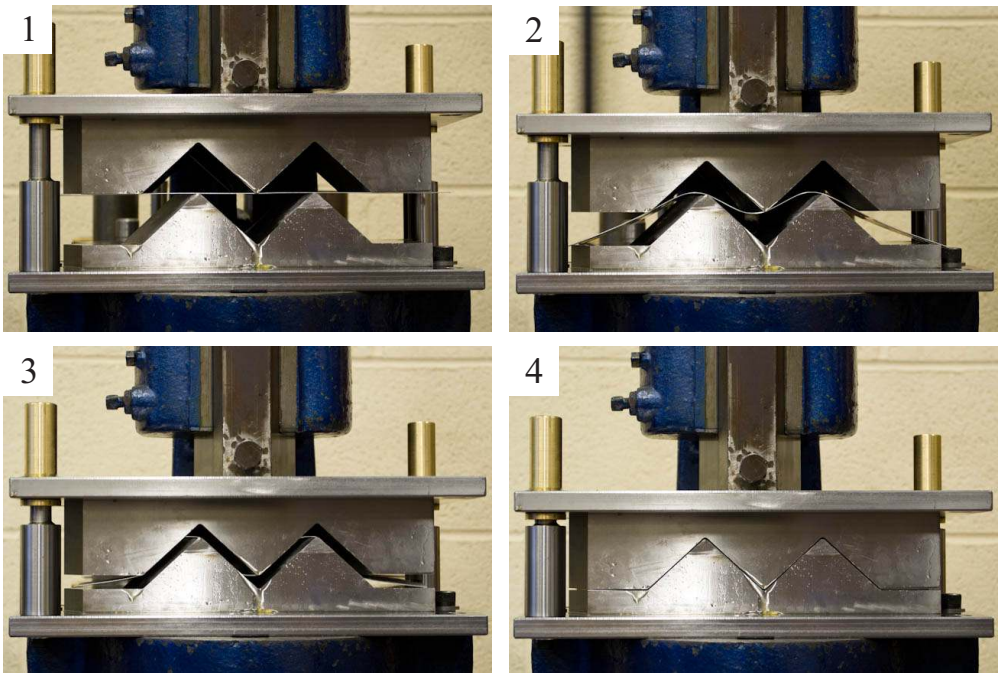


(b) Single-punch forming sequence

Figure 3.27: Manufacturing process for standard foldcore.

with corner guide pins. The trimmed sheet was placed between the dies and stamped into the final folded configuration, Figure 3.27(b).

The indented core was formed in a two-stage process. First, a standard core was formed as just described and placed in a set of indented forming dies, Figure

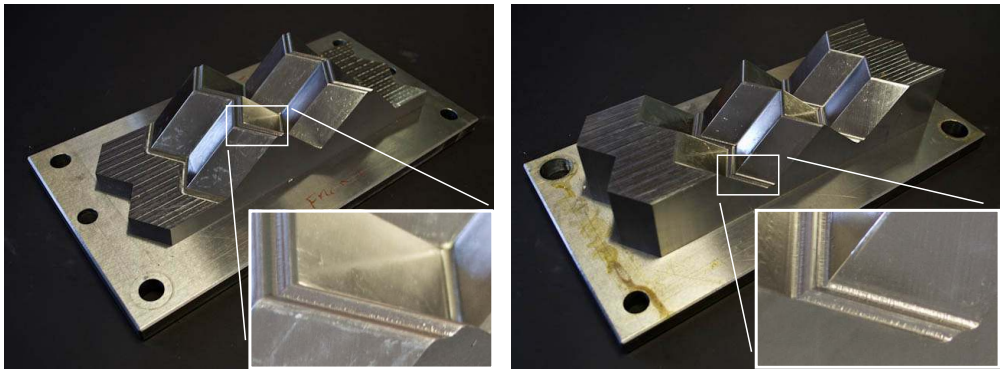

(a) Male and female indented dies

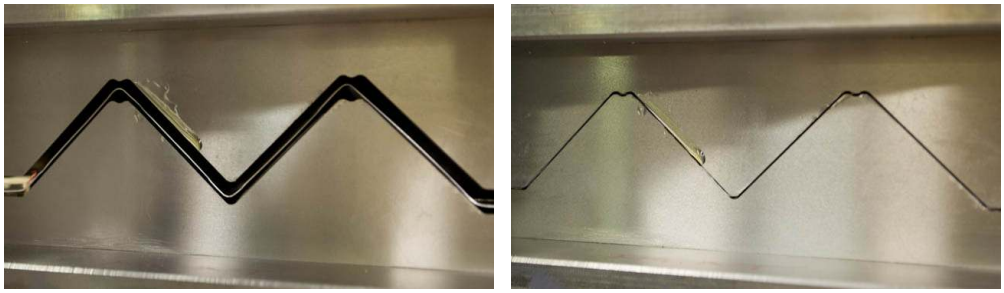

(b) Second punch to form indent

Figure 3.28: Manufacturing process for indented foldcore.

3.28(a). Second, as the standard and indented geometries were designed to be equivalent apart from the indent, the indented dies simply punched the indent into the core without altering the remaining core plates, Figure 3.28(b).

Table 3.10 shows the final formed dimensions of all foldcores to the nearest half millimeter. The two standard models with $t_p = 0.5$mm and 1.0mm are given the models names Mi05 and Mi10 respectively. Similarly the indented models are named Ind05 and Ind10. It can be seen that the formed dimensions are close to the designed dimensions. The maximum formed error is seen in the 1mm models, which are approximately 5% wider than designed. These may indicate that some spring back has taken place and/or that the material was not fully drawn during stamping. Inspection of the plates shows that the Mi10 and Ind10 models formed without significant visual imperfections, Figures 3.24 and 3.25, however the Mi05 and Ind05 models have some visible buckling ripples, Figure 3.29. Note that the density value shown in Table 3.10 is calculated from design dimensions.

Table 3.10: Global dimensions of large-scale experimental prototypes.

| *Model* | $t_p$ (mm) | $\alpha$ | Formed $L$ (mm) | Formed $W$ (mm) | Formed $H$ (mm) | Designed $L$ (mm) | Designed $W$ (mm) | Designed $H$ (mm) |
|---|---|---|---|---|---|---|---|---|
| Mi10 | 1.0 | 0.038 | 182.0 | 90.0 | 38.0 | 177.0 | 87.0 | 39.0 |
| Mi05 | 0.5 | 0.019 | 184.0 | 88.5 | 37.0 | | as above | |
| Ind10 | 1.0 | 0.040 | 181.0 | 90.0 | 35.0 | 177.0 | 87.0 | 36.5 |
| Ind05 | 0.5 | 0.020 | 180.0 | 88.5 | 35.5 | | as above | |

(a) Standard foldcore

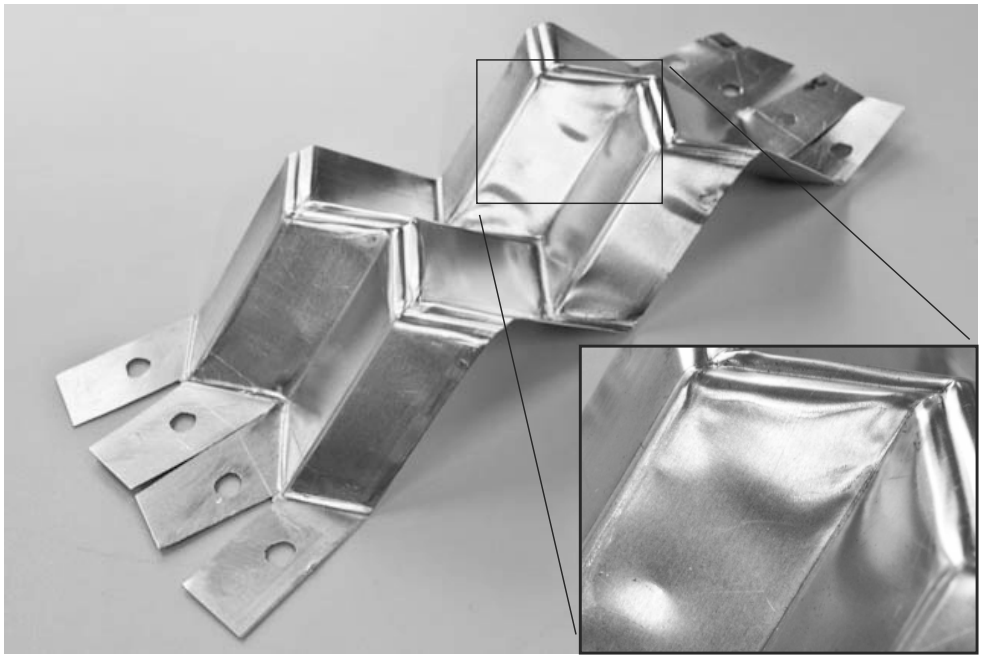

(b) Indented foldcore

Figure 3.29: Foldcores constructed with $t_p = 0.5$mm aluminium sheet.

### 3.4.3 Experimental Method and Results

Three samples of each foldcore type were constructed for testing. These were then annealed at 345°C to remove residual manufacturing stresses. Tensile tests were conducted on annealed material samples for both sheet thicknesses. The material properties given in Table 3.2 were the annealed material properties of the 0.5mm aluminium sheet. Although ostensibly the same aluminium alloy, the 1mm aluminium sheet was found to be a slightly stronger and less ductile material than the 0.5mm sheet, with $\sigma_Y = 37$MPa, $\sigma_U = 106$MPa, and strain hardening data as shown in Table 3.11.

Table 3.11: True plastic stress-strain data for 1mm thick aluminium sheet.

| Strain | 0 | 0.005 | 0.014 | 0.044 | 0.052 |
|---|---|---|---|---|---|
| Stress (MPa) | 36.8 | 89.2 | 98.2 | 105.5 | 106.4 |

For testing, the prototypes were restrained by clamping the front and back edge tabs to a rigid baseplate, Figure 3.30. These were placed into an INSTRON Universal Testing machine and crushed under quasi-static loads. Loading was applied by a rigid top plate descending at a rate of 2mm/min to a total crush depth of approximately 65% of the model height $H$, which was 24mm for the indented models and 26mm for the standard models.

The force-displacement response of the crushing plate was obtained for each test. As before, force $P$ and displacement $h$ values are normalised to dimensionless stress $\sigma^* = P/(LW\sigma_Y)$ and strain $h^* = h/H$, shown in Figure 3.31(a)-(d). Each graph shows the response of the three tested prototypes, referred to with model subscripts 1-3. These responses are averaged to obtain a typical response, referred to without a subscript. Relevant prototype results are summarised in Table 3.12. It can be seen that there is good repeatability for each geometry, with a maximum variation from average of 9%, seen in prototype $\text{Ind}10_3$.

Table 3.12: Large-scale prototype results.

| *Model* | $\sigma^*_{max}$ $\times 10^{-3}$ | $\sigma^*_{avg}$ $\times 10^{-3}$ | $U^*$ | *Model* | $\sigma^*_{max}$ $\times 10^{-3}$ | $\sigma^*_{avg}$ $\times 10^{-3}$ | $U^*$ |
|---|---|---|---|---|---|---|---|
| $Mi10_1$ | 29.4 | 11.5 | 2.56 | $Ind10_1$ | 26.9 | 16.2 | 1.66 |
| $Mi10_2$ | 27.9 | 11.2 | 2.50 | $Ind10_2$ | 25.8 | 15.8 | 1.64 |
| $Mi10_3$ | 26.7 | 10.5 | 2.54 | $Ind10_3$ | 23.1 | 13.9 | 1.66 |
| Mi10 | 27.9 | 11.1 | 2.53 | Ind10 | 25.2 | 15.3 | 1.65 |
| $Mi05_1$ | 3.7 | 2.1 | 1.78 | $Ind05_1$ | 3.7 | 2.2 | 1.70 |
| $Mi05_2$ | 3.7 | 2.2 | 1.70 | $Ind05_2$ | 3.7 | 2.2 | 1.67 |
| $Mi05_3$ | 3.7 | 2.0 | 1.87 | $Ind05_3$ | 3.7 | 2.3 | 1.62 |
| Mi05 | 3.7 | 2.1 | 1.78 | Ind05 | 3.7 | 2.2 | 1.66 |

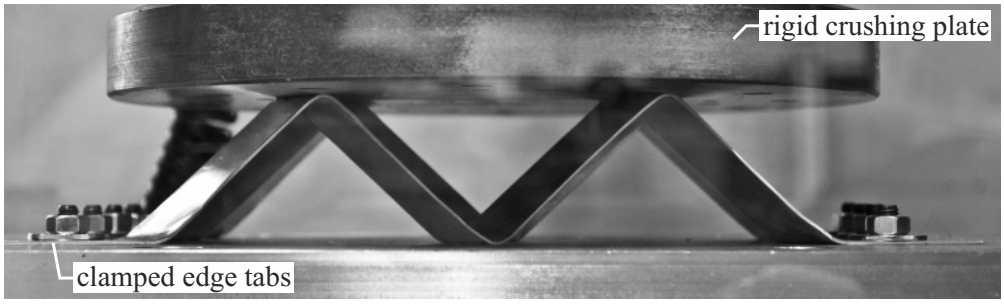


Figure 3.30: Prototype restraint and loading.

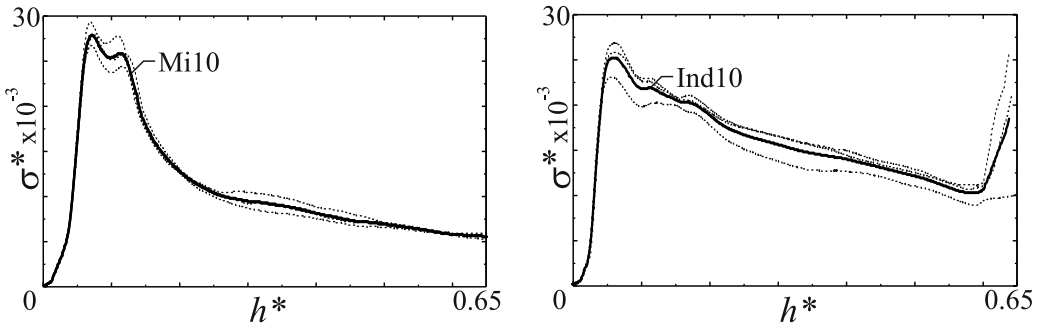


(a) Mi10 prototypes




(b) Ind10 prototypes

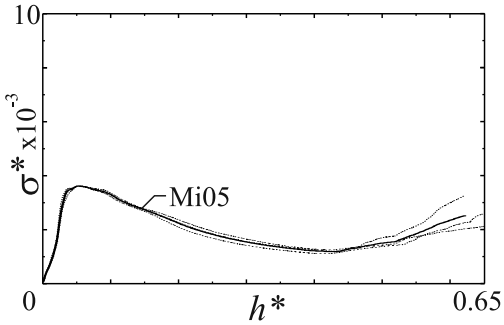


(c) Mi05 prototypes

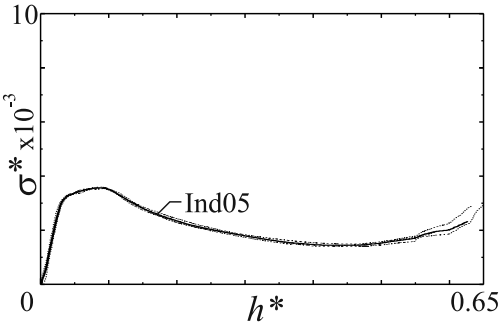


(d) Ind05 prototypes

Figure 3.31: Dimensionless stress-strain responses of large-scale prototypes.

### 3.4.4 Numerical and Theoretical Comparison

#### 1mm Prototypes

A comparison of experimental results for Mi10 and Ind10 is shown in Figure 3.32(a). It can be seen that the indent is successful in triggering an improved energy-absorbing response, with a reduction in $\sigma^*_{max}$ of 9.6% and an increase in $\sigma^*_{avg}$ of 38.6%, compared with the standard model. Inspection of the final failure modes of these cores, Figure 3.32(b)-(c), shows that their final failure modes are significantly different, with mid-plate buckling in the standard core and ridge buckling indicative of a travelling hinge line in the indented core.

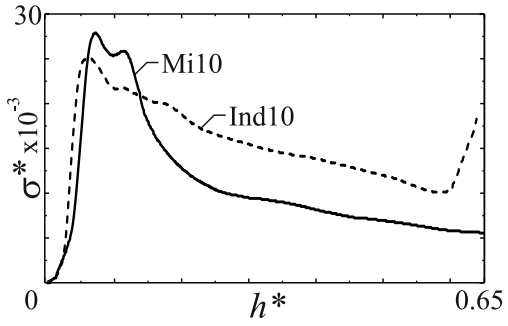


(a) Dimensionless stress-strain comparison

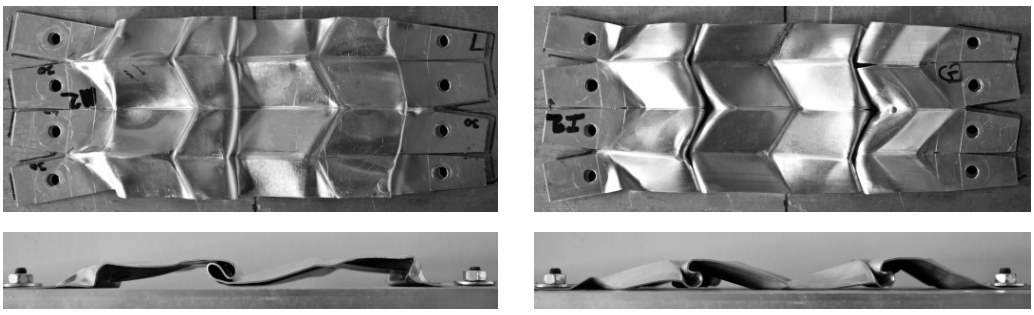

(b) Crushed Mi10 with mid-plate failure

(c) Crushed Ind10 with top-plate failure

Figure 3.32: Comparison of $t_p$ = 1mm prototype responses.

A comparison of numerical and experimental results is shown in Figure 3.33 and Table 3.13. The theoretical prediction is also included for the indented foldcore, calculated as $\sigma^* = 24.8 \times 10^{-3}$. The numerical results are obtained from models analysed in the same manner as described in the previous chapter, with two differences: 1mm sheet material properties replace the previously used material

Table 3.13: Results of $t_p = 1$mm models.

| *Result* | Mi10 | | | Ind10 | | |
|---|---|---|---|---|---|---|
| | $\sigma^*_{max}$ $\times 10^{-3}$ | $\sigma^*_{avg}$ $\times 10^{-3}$ | $U^*$ | $\sigma^*_{max}$ $\times 10^{-3}$ | $\sigma^*_{avg}$ $\times 10^{-3}$ | $U^*$ |
| Experimental | 27.9 | 11.1 | 2.53 | 25.2 | 15.3 | 1.65 |
| Numerical | 30.2 | 13.2 | 2.29 | 23.3 | 15.0 | 1.55 |

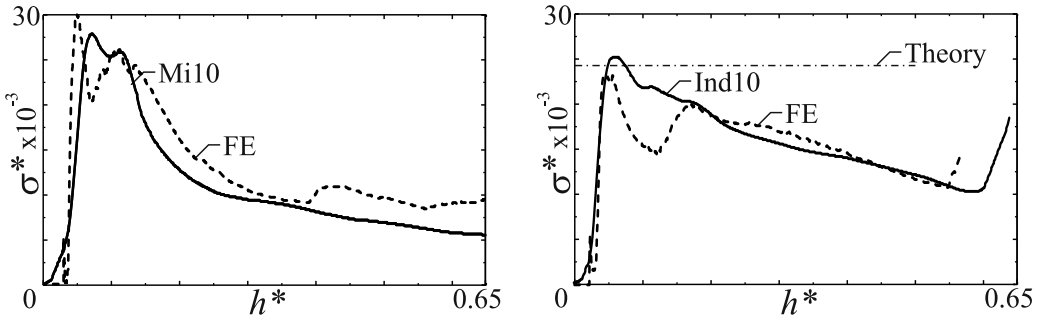


(a) Standard (b) Indented

Figure 3.33: Experimental, numerical, and theoretical results of $t_p = 1$mm models.

properties, and the entire core geometry is constructed, rather than a single periodic unit geometry. This is because there are very few foldcore units used in large-scale models, and so it is likely that free edge effects will be significant.

It can be seen that there is good correlation between numerical and experimental predictions for the standard foldcore, with a maximum difference of 18.9% in $\sigma^*_{avg}$ of Mi10. There is also good correlation between the numerical, theoretical, and experimental predictions for the indented foldcore. It can also be seen that there are slight discrepancies in the indented numerical and experimental curves, specifically the double-hump shown in the numerical but not the experimental curve. This might be attributable to plate tearing behaviour, which is observed in experimental models but not accounted for in the numerical material definition. It might also be due to imperfect formation of the indent.

The theoretical prediction is seen to still be able to provide a good estimate of $\sigma^*_{max}$ but is too simple to capture other behaviours seen in the stress-displacement response. Several of these shortcomings were discussed previously, and of particular note in this case is the decreasing, rather than uniform, stress-displacement

response. This is believed to be primarily attributable to free-edge effects arising with the removal of periodic boundary constraints. Unfortunately the manufacturing method used here cannot be used for larger core tessellations and thus used to establish the validity of the periodic unit geometry analysis method, however this will be considered in depth in the following section. Finally, a direct comparison of failure modes, Figure 3.34, shows that numerical models accurately predict the experimental failures.

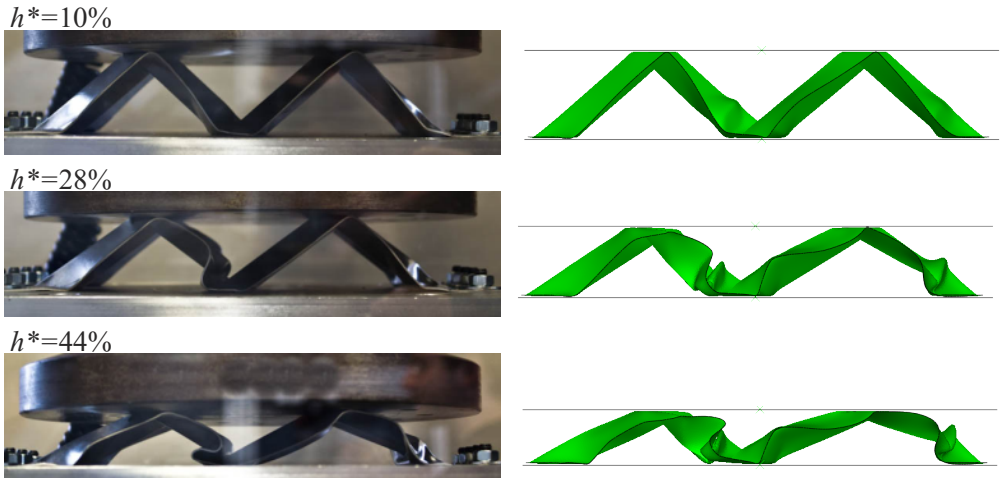


(a) Standard

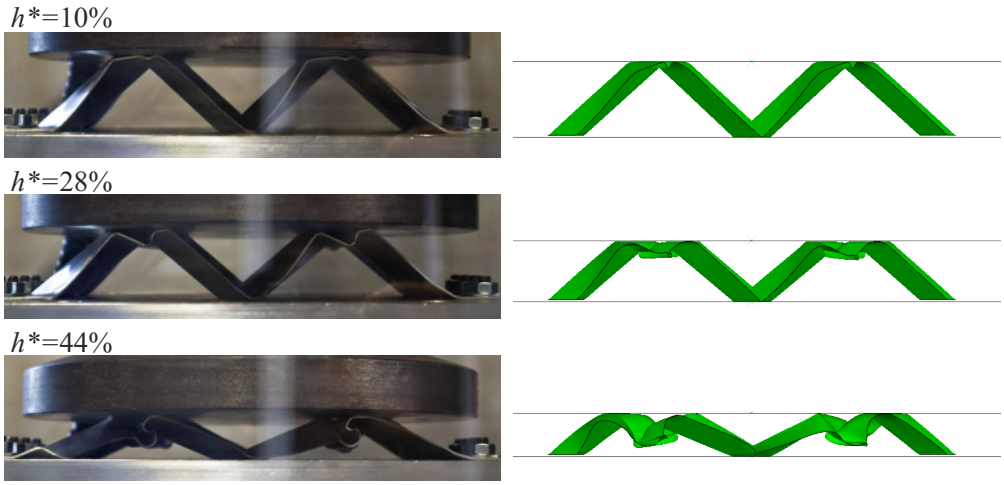


(b) Indented

Figure 3.34: Failure modes of $t_p = 1$mm models.

### 0.5mm Prototypes

A comparison of Mi05 and Ind05 experimental responses is shown in Figure 3.35(a). It can be seen that the indent does not significantly alter the failure mode of

the foldcore. There is a slight increase in $\sigma^*_{avg}$ of 7.8% however this is likely to be attributable to the increased density of the indented foldcore, rather than a change in failure mode. Inspection of the final failure modes of these cores, Figure 3.35(b)-(c), confirms that there is no significant change in the final crushed shape, with mid-plate buckling occurring in both.

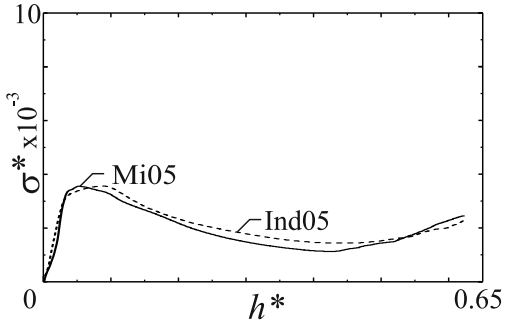


(a) Dimensionless stress-strain comparison

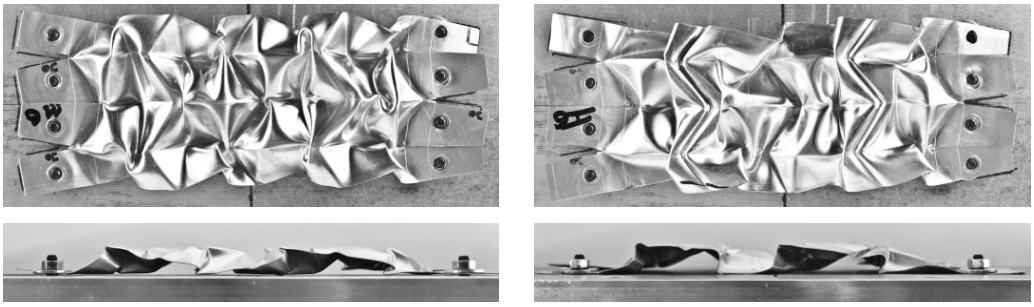

(b) Crushed Mi05 prototype

(c) Crushed Ind05 prototype

Figure 3.35: Comparison of $t_p = 0.5$mm prototype results.

A comparison of numerical and experimental results is shown in Figure 3.36 and Table 3.14. The theoretical prediction for the indented core is also in Figure 3.36(b), calculated as $\sigma^* = 6.9 \times 10^{-3}$. It can be seen that there is poor correspondence between numerical and experimental predictions for both foldcore types, which is significantly different to the results seen for the $t_p = 1$mm model results.

Table 3.14: Results of $t_p = 0.5$mm models.

| *Result* | Mi05 $\sigma^*_{max}$ $\times 10^{-3}$ | Mi05 $\sigma^*_{avg}$ $\times 10^{-3}$ | Mi05 $U^*$ | Ind05 $\sigma^*_{max}$ $\times 10^{-3}$ | Ind05 $\sigma^*_{avg}$ $\times 10^{-3}$ | Ind05 $U^*$ |
|---|---|---|---|---|---|---|
| Experimental | 3.7 | 2.1 | 1.78 | 3.7 | 2.2 | 1.66 |
| FE | 8.2 | 3.1 | 2.70 | 6.0 | 3.8 | 1.56 |

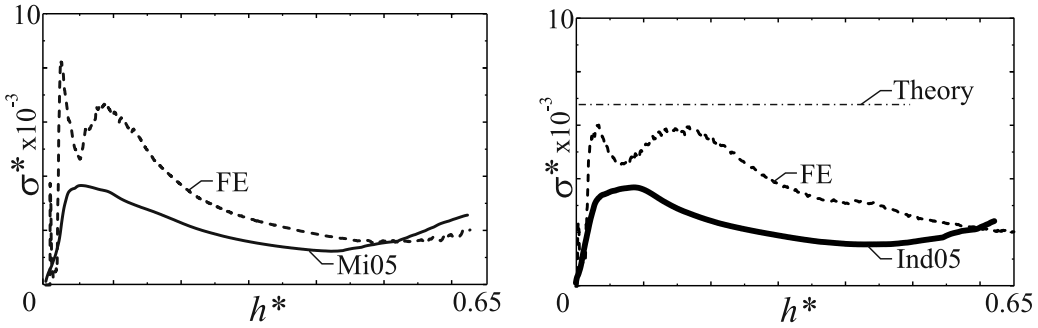


(a) Standard (b) Indented

Figure 3.36: Comparison of results of $t_p = 0.5$mm models.

This discrepancy might be attributable to visible plate buckling observed in the $t_p = 0.5$mm models, Figure 3.29, that was not observed in the $t_p = 1$mm models. For reasons that will be discussed in Section 3.5.4, the effect of these imperfections in the large-scale numerical models cannot easily be studied at this stage. However, the following section shall develop a method to introduce geometric imperfections into small-scale numerical models, thus allowing an investigation into the effect of geometric imperfections on foldcore failure modes.

## 3.5 Experiments on Small-Scale Models

A second, small-scale experimental investigation was conducted into standard and indented foldcores constructed with a height of approximately 10mm. Whereas the previous large-scale models enabled close observation of core failure modes, the small-scale models are designed to be directly comparable to commercially-available aluminium honeycomb cores. For reasons that will be discussed below, the small-scale cores also allow an investigation into the effect of geometric imperfections on observed core failure modes.

### 3.5.1 Geometry

Foldcores were designed to be comparable with the Corex 1/4" 3000 Alloy Series honeycomb (Corex Honeycomb, 2013), which has previously been analysed with attached sandwich faces under out-of-plane quasi-static impact loads in Kee Paik *et al.* (1999). The selected honeycomb core had cell size $s = 6.4$mm (1/4"), cell wall thickness $t_p = 0.0625$mm, density $\alpha = 3.0\%$, height $H = 10$mm, and was constructed from aluminium alloy 3003-H19, Figure 3.37(a). To match this honeycomb, small-scale aluminium foldcores were constructed with approximately the same height and density, which gave an optimum indented foldcore with $a = 15$mm, $b = 7.5$mm, $\phi = 64.8°$, $\eta_A = 95°$, $p^* = 0.067$, and $t_p = 0.2$mm. This gave a global height $H = 9.5$mm and density $\alpha = 3.2\%$, Figure 3.37(b). A standard foldcore was designed with equivalent geometry except with $p^* = 0$, for $H = 10.1$mm and $\alpha = 3.0\%$, Figure 3.37(c). The standard foldcore was designed with an equivalent geometry, rather than an optimum standard geometry, as it considerably reduces the number of moulds required for manufacturing, discussed further below. Both foldcores were constructed from a ductile, pure aluminium to ensure formability of the indent.

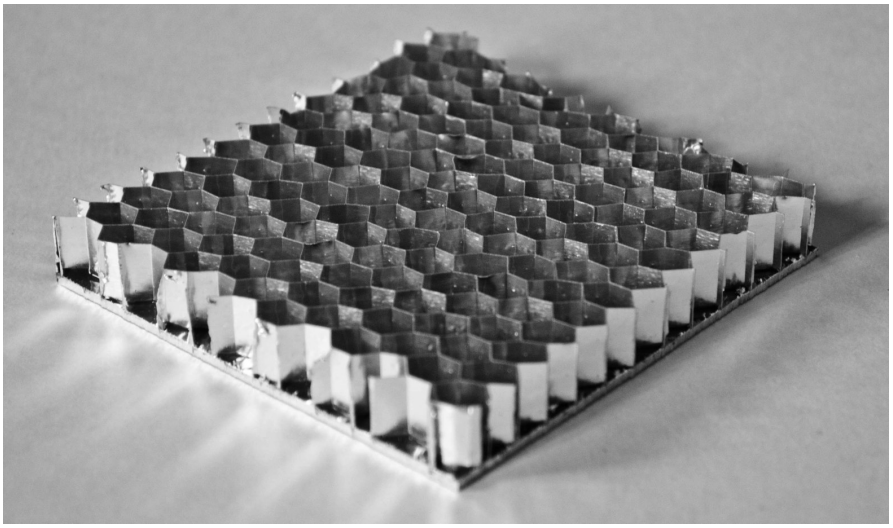

(a) Honeycomb core

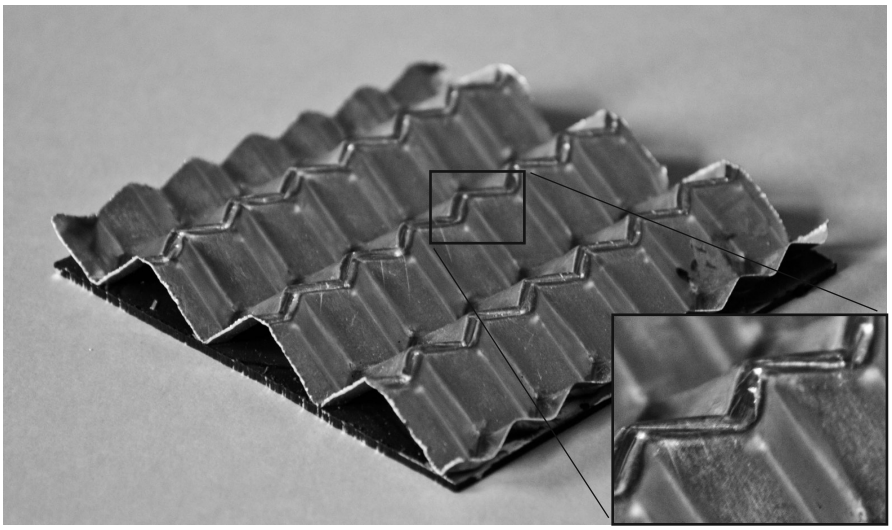

(b) Indented foldcore

(c) Standard foldcore

Figure 3.37: Small-scale aluminium prototypes.

### 3.5.2 Manufacturing Method

The small-scale aluminium foldcores were created with a new sequential stamping method that utilises 3D printed male and female moulds. To form the standard foldcore, three mould pairs were printed corresponding to gradually steepening folded pattern configurations. These folded configurations were chosen such that the width contraction of the unit geometry between each stage would be small and reasonably constant, which gave configurations set at $\eta_A = 150°$, $\eta_A = 120°$, and $\eta_A = 95°$, Figure 3.38(a).

Male and female dies were designed at each configuration such that an aluminium sheet could be stamped with a two-by-nine unit assembly. Each die was manufactured with solid ABS plastic on a Stratasys Dimension SST 3D printer, and consisted of the core geometry centred on a base plate with alignment holes placed at each corner, Figure 3.38(b)-(d). The 3D printer had a minimum bead size of 0.25mm which caused notable surface texturing on the printed moulds but otherwise matched the designed mould geometry very closely, Figure 3.38(e).

To form the standard foldcore, an aluminium sheet was first trimmed to a suitable width and placed between the initial male and female mould pair. In this instance, a suitable width was deemed to be eight units of the unfolded pattern geometry, which ensured that when the sheet was placed between a pair of moulds, Figure 3.39(a), there was no sheet material overhanging the mould edges. Once placed between the moulds, the moulds were hammered together to stamp a single formed row into the sheet. Guide pins were placed through corners of the mould pairs to ensure proper mould alignment during hammering. This was repeated continuously, using the previously stamped row to align the next row to be stamped. Once a sheet was fully stamped with the initial mould configuration, the entire process was then repeated with the next two mould configurations to create the final standard foldcore, Figure 3.39(b).

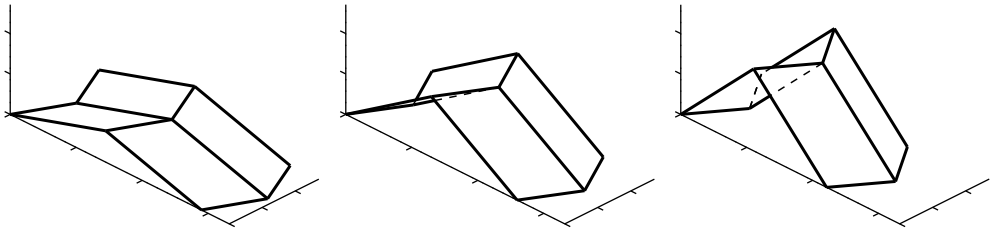

(a) Unit geometry set at $\eta_A = 150°$, 120°, and 95°.

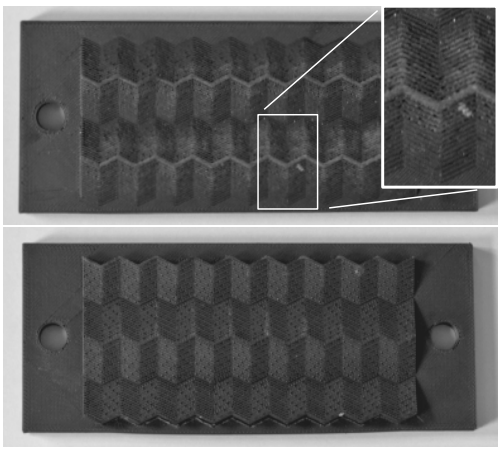

(b) Initial mould at $\eta_A = 150°$

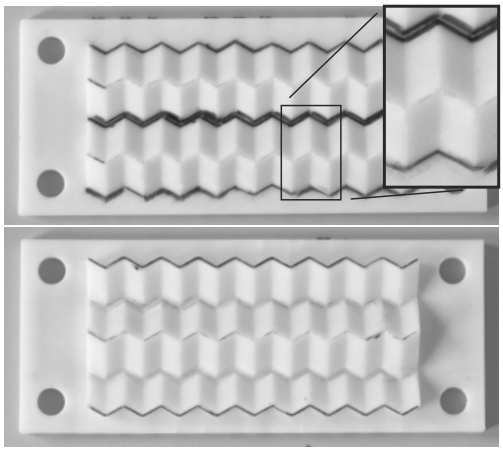

(c) Mould at $\eta_A = 120°$

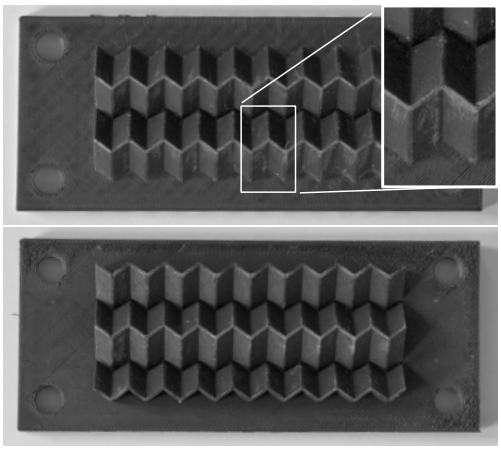

(d) Mould at $\eta_A = 95°$

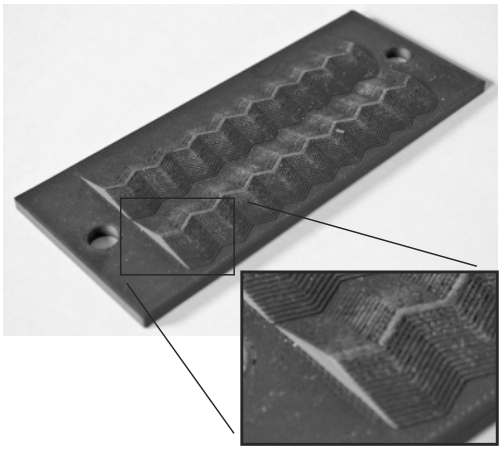

(e) 0.25mm print resolution

Figure 3.38: 3D printed male and female standard foldcore dies.

The indented foldcores were created by stamping a formed standard sheet in an additional set of indented moulds, similar to the method used to manufacture the large-scale indented models. The fourth set of moulds were designed to match the optimal indented geometry, however the small size of indent, $a_i = 1$mm, approached the resolution limit of the 3D printer and therefore was not able to properly invert the top ridge. Instead, complete inversion was achieved by manually pressing the ridge into place with the side of an awl, Figure 3.40.

Table 3.15: Global dimensions of small-scale prototypes.

| *Model* | $\eta_A$ (°) | Formed $L$ (mm) | Formed $W$ (mm) | Formed $H$ (mm) | Designed $L$ (mm) | Designed $W$ (mm) | Designed $H$ (mm) |
|---|---|---|---|---|---|---|---|
| Standard | 150 | 116.9 | 106.4 | 3.4 | 115.9 | 107.7 | 3.9 |
| Standard | 120 | 105.0 | 105.0 | 7.3 | 103.9 | 104.5 | 7.5 |
| Standard | 95 | 89.7 | 100.3 | 10.0 | 88.5 | 98.0 | 10.1 |
| Indented | 95 | as above | | 9.2 | as above | | 9.4 |

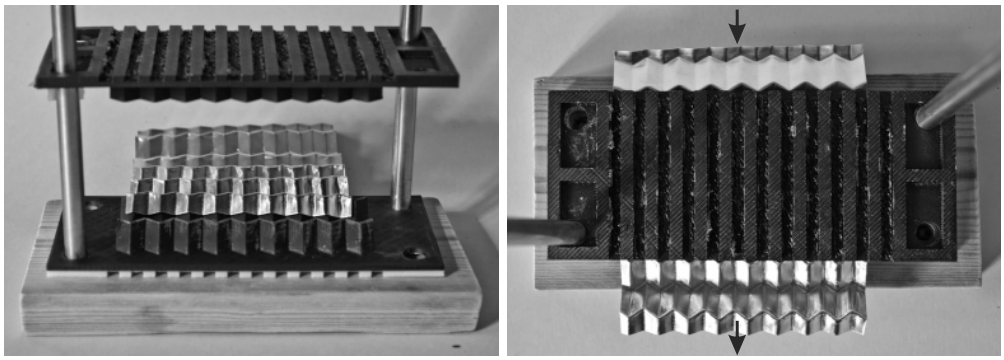

(a) Row-by-row stamping of aluminium sheet

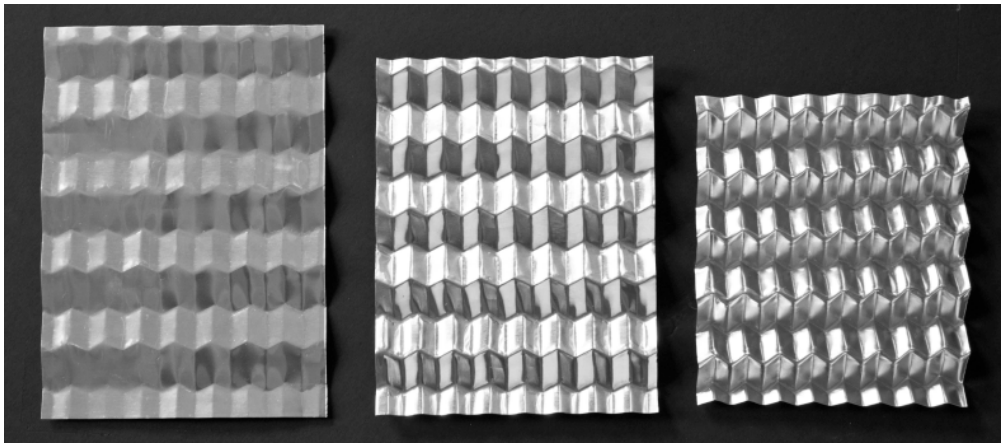

(b) Sheets formed by moulds 1, 2, and 3

Figure 3.39: Sequential stamping of standard foldcore.

Table 3.15 shows the formed and designed dimensions of the foldcores at each stage of manufacture. It can be seen that the final formed dimensions are all within 3% of the designed dimensions, indicating that the 3D printed sequential stamping method is an effective way to prototype small-scale foldcores. Visual inspection of the standard foldcores also showed few visible imperfections in the core plates, however inspection of the indented foldcores showed moderate imperfections around the manually-formed inverted ridge, Figure 3.40.

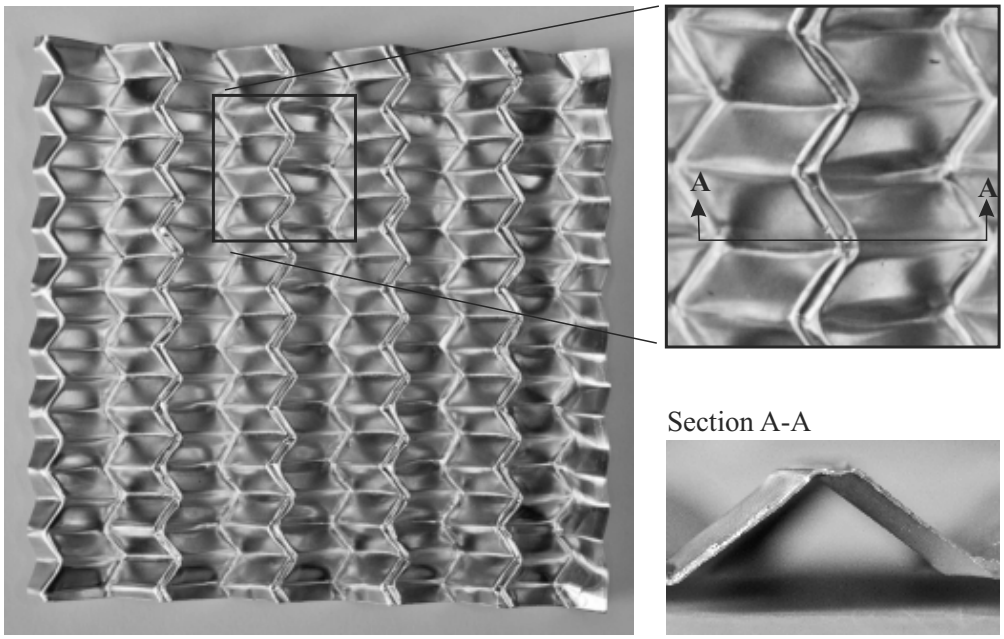


Figure 3.40: Manually formed indented foldcore.

### 3.5.3 Experimental Method and Results

Prior to testing, all foldcores were annealled at 345°C to remove residual manufacturing stresses. Tensile tests were conducted on annealed material samples. The 0.2mm thick aluminium foil was found to have similar properties to the previously used 0.5mm thick sheet, with $\sigma_Y = 24$MPa, $\sigma_U = 106$MPa, and plastic stress-strain data given in Table 3.16(a).

Table 3.16: True plastic stress-strain data for small-scale prototypes.

(a) Foldcore aluminium foil

| Strain | 0 | 0.007 | 0.019 | 0.048 | 0.106 | 0.183 | 0.260 |
|---|---|---|---|---|---|---|---|
| Stress (MPa) | 23.9 | 38.4 | 51.9 | 67.8 | 83.6 | 96.1 | 105.8 |

(b) Honeycomb 3003-H19 alloy

| Strain | 0 | 0.006 | 0.011 | 0.018 |
|---|---|---|---|---|
| Stress (MPa) | 195.0 | 209.8 | 215.4 | 216.0 |

It was not possible to obtain a material sample for the 3003-H19 alloy used in the honeycomb core prototype, however approximate material properties were obtained from literature (Kee Paik *et al.*, 1999; Boyer, 2002) as $\sigma_Y = 195$MPa, $\sigma_U = 211$MPa, and plastic stress-strain data given in Table 3.16(b).

For testing, the cores were bonded to a single aluminium face sheet, with thickness $t_f = 1.5$mm, using ET538 Permabond epoxy slow-cured at room temperature for 24 hours. These were then trimmed to a 70mm by 70mm area to create the final testing samples, shown in Figure 3.37.

Three samples of each core type were crushed between two rigid plates in an INSTRON Universal Testing machine at a quasi-static loading rate of 1mm/min. They were crushed to approximately 65% of the core height, and the force-displacement response was obtained and converted to dimensionless values. Relevant values are listed in Table 3.17 and responses for each core are shown in Figure 3.41. The model designations Mi02, Ind02, and HC are used denote the average response of the standard, indented, and honeycomb cores respectively. As before, the subscripts 1-3 are appended to the model designations to denote each prototype sample response. It can be seen that there is good repeatability for the Mi02 and HC models and reasonable repeatability for the Ind02 models.

### 3.5.4 Numerical Analysis with Geometric Imperfections

The experimental prototypes were constructed with a new manufacturing method, and so it was thought likely that they contained significant manufacturing defects. To assess the potential effect of these defects, numerical models for Mi02, Ind02, and HC were constructed with included geometric imperfections. To generate geometric imperfections, linear combinations of the first ten buckling modes of each core type were superimposed on the original, unbuckled core geometry. Unbuckled Mi02 and Ind02 numerical models were constructed in an identical manner to that described in Section 3.1. The unbuckled HC model was similar, but with additional periodic boundary constraints applied to the unit cell as shown in Figure 3.42.

The first ten buckling modes of each core type were generated with a static buckling analysis on the core geometry under out-of-plane loading, applied as a unit line

Table 3.17: Small-scale prototype results.

| *Model* | $\sigma^*_{max}$ $\times 10^{-3}$ | $\sigma^*_{avg}$ $\times 10^{-3}$ | $U^*$ |
|---|---|---|---|
| $Mi02_1$ | 11.7 | 7.5 | 1.55 |
| $Mi02_2$ | 12.2 | 7.4 | 1.64 |
| $Mi02_3$ | 12.9 | 7.8 | 1.65 |
| Mi02 | 12.2 | 7.7 | 1.58 |
| $Ind02_1$ | 11.1 | 8.4 | 1.33 |
| $Ind02_2$ | 13.2 | 8.5 | 1.56 |
| $Ind02_3$ | 12.1 | 8.4 | 1.44 |
| Ind02 | 11.8 | 8.4 | 1.41 |

| *Model* | $\sigma^*_{max}$ $\times 10^{-3}$ | $\sigma^*_{avg}$ $\times 10^{-3}$ | $U^*$ |
|---|---|---|---|
| $HC_1$ | 15.5 | 7.8 | 1.99 |
| $HC_2$ | 16.3 | 7.5 | 2.18 |
| $HC_3$ | 17.4 | 7.6 | 2.29 |
| HC | 16.4 | 7.6 | 2.15 |

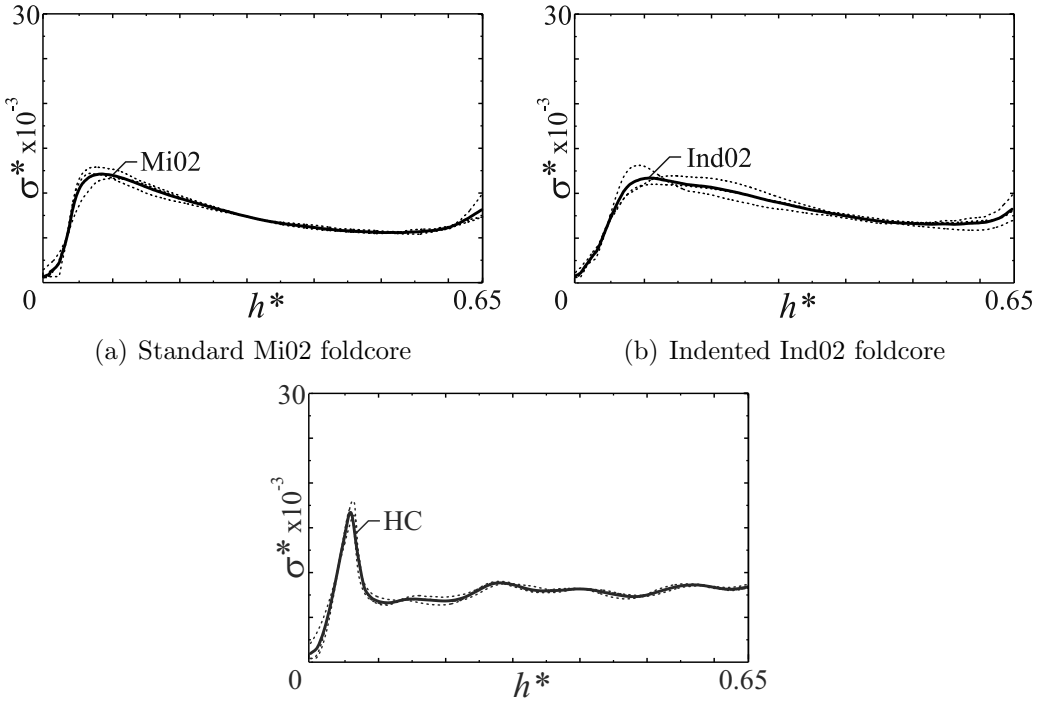


(a) Standard Mi02 foldcore

(b) Indented Ind02 foldcore

(c) HC honeycomb core

Figure 3.41: Dimensionless stress-strain response responses of scall-scale $t_p$ = 0.2mm prototypes.

load along the top edges of the unit geometry. Linear combinations of these modes were superimposed on unbuckled geometry such that the maximum displacement in each case was equivalent to 125% $t_p$, equal to the minimum 3D printer bead size of 0.25mm. For example, an imperfect geometry generated from the first buckling mode, with a maximum buckled displacement of $x$ mm, is generated with coefficients $\delta_0 + (1.25t_p/x)\delta_1 + 0\delta_2 + ... + 0\delta_{10}$, where $\delta_0$ is the initial nodal coordinates, $\delta_1$ to $\delta_{10}$ are the nodal displacements for each buckled mode, and the $(1.25t_p/x)$ coefficient is applied to give an imperfect geometry with a final

maximum displacement of 0.25mm.

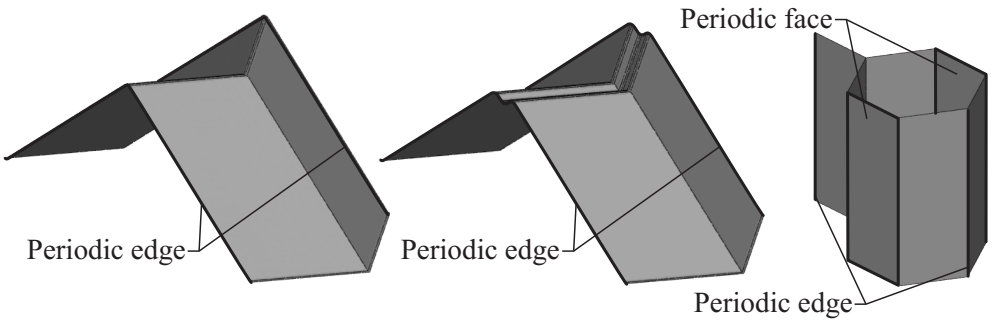


Figure 3.42: Periodic boundary conditions on standard, indented, and honeycomb unit geometries.

Note that while this assumption of a 125% $t_p$ maximum displacement is reasonable for the foldcores formed using the 3D printed moulds, it is questionably applicable for the honeycomb cores. However, as the honeycomb cores were manually expanded and bonded, it was thought that there would still be geometric imperfections, and so the 125% $t_p$ maximum displacement was retained for consistency.

Selected force-displacement results for various failure modes are reduced to dimensionless parameters and shown in Figure 3.43. The designation FE is used for numerical models with perfect, unbuckled geometry. The designation $\mathrm{FE}'_M$ is used to denote a model with geometric imperfections generated from mode $M$. For instance, $\mathrm{FE}'_1$ is generated from the first buckling mode and $\mathrm{FE}'_8$ is generated from the eighth buckling mode.

Note that the use of periodic boundary constraints meant that the generated buckling modes were all high-order mid-plate buckling modes. When the method was applied to the large-scale experimental geometry, which was modelled with free side boundaries instead of periodic boundary constraints, the generated buckling modes were all free-edge buckling modes. When superimposed, these modes caused very little geometric imperfection in the core plates away from the buckled free edge, and so this method could not be used to investigate the geometric imperfections of Ind05 and Mi05.

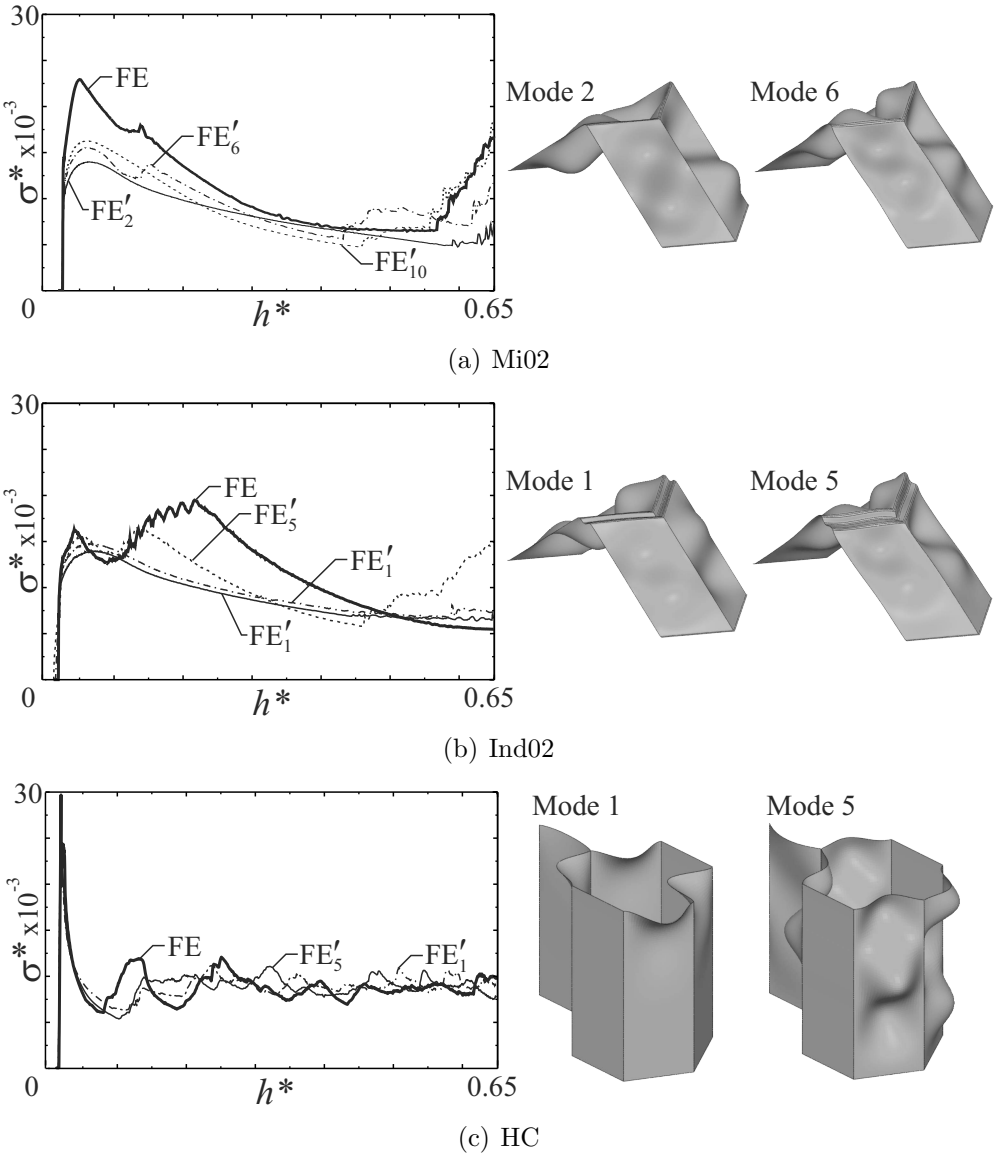


Figure 3.43: Dimensionless stress-strain responses, on left; buckled modes at exaggerated scale, on right.

### 3.5.5 Numerical Comparison

For each core type, a worst-case buckled shape is selected as a representative imperfect numerical model and given the designation FE′. The worst-case buckled shape is defined as the buckled shape that causes the lowest $\sigma^*_{avg}$, which occurs at mode 2, 1, and 5 in cores Mi02, Ind02, and HC respectively. Numerical and experimental values are listed in Table 3.18 and results are plotted in Figure 3.44.

Inspection of the foldcore results shows that the perfect FE models give a poor

Table 3.18: Results of $t_p = 0.2$mm imperfect geometry numerical models.

| *Result* | Mi02 | | | Ind02 | | | HC | | |
|---|---|---|---|---|---|---|---|---|---|
| | $\sigma^*_{max}$ $\times 10^{-3}$ | $\sigma^*_{avg}$ $\times 10^{-3}$ | $U^*$ | $\sigma^*_{max}$ $\times 10^{-3}$ | $\sigma^*_{avg}$ $\times 10^{-3}$ | $U^*$ | $\sigma^*_{max}$ $\times 10^{-3}$ | $\sigma^*_{avg}$ $\times 10^{-3}$ | $U^*$ |
| Exp | 12.2 | 7.7 | 1.58 | 11.8 | 8.4 | 1.41 | 16.4 | 7.6 | 2.15 |
| FE | 22.9 | 11.8 | 1.93 | 19.5 | 11.3 | 1.72 | 29.4 | 8.8 | 3.36 |
| FE′ | 13.9 | 8.1 | 1.71 | 14.0 | 8.9 | 1.57 | 22.5 | 8.8 | 2.57 |

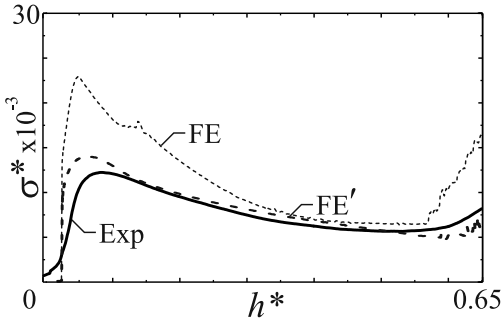


(a) Mi02

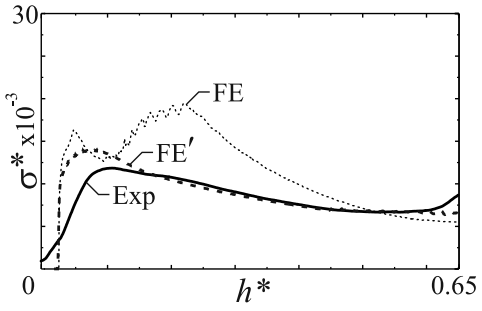


(b) Ind02

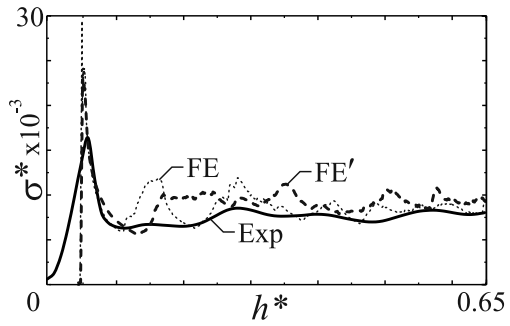


(c) HC

Figure 3.44: Comparison of $t_p = 0.2$mm numerical and experimental responses.

prediction of the observed experimental results, much like that observed for the Mi05 and Ind05 models. However, the imperfect FE′ models give a much improved numerical prediction for both foldcores. For Mi02, FE′ predictions for $\sigma^*_{max}$ and $\sigma^*_{avg}$ are within 14% and 6% of experimental results respectively. For Ind02, FE′ predictions for $\sigma^*_{max}$ and $\sigma^*_{avg}$ are within 19% and 6% of experimental results respectively.

These results show that both standard and indented foldcores can be highly sensitive to geometric imperfections. This is particularly detrimental for the indented foldcore, where imperfections cause a mid-plate buckling mode to form, rather than the originally predicted travelling hinge line failure mode. Comparisons of

the observed experimental and imperfect numerical failure modes for both the foldcores are shown in Figure 3.45(a)-(b) and it can be seen that the numerical models successfully predict a mid-plate buckling mode for both core types.

Inspection of the honeycomb results shows that FE′ predictions for $\sigma^*_{max}$ and $\sigma^*_{avg}$ are within 37% and 16% of experimental results respectively. It can also be seen that numerical and experimental models show a typical honeycomb sequential folding failure mode, Figure 3.45(c). There are two notable attributes of the honeycomb response. First, the crushing stress value for this particular core is given as 1.62MPa by the manufacturer. Dividing this value by $\sigma_Y$ gives a dimensionless value of $\sigma^*_{avg} = 8.3 \times 10^{-3}$, which is with 10% of the experimental and numerical results. Second, this value is insensitive to geometric imperfections, with both FE and FE′ possessing the same $\sigma^*_{avg}$.

The slight discrepancies for all core types are likely due to larger geometric imperfections than those accounted for in the FE′ models. This is particularly likely for the indented core with the manually formed ridge, and the honeycomb core where the effect of over or under-expansion was not considered. Free-edge effects may also be a contributing factor in the slight over-prediction of the numerical models. However, it can be seen that the discrepancies are relatively minor, and so it can be concluded that the numerical models with pre-buckled plate geometry are successfully able to predict core failure responses.

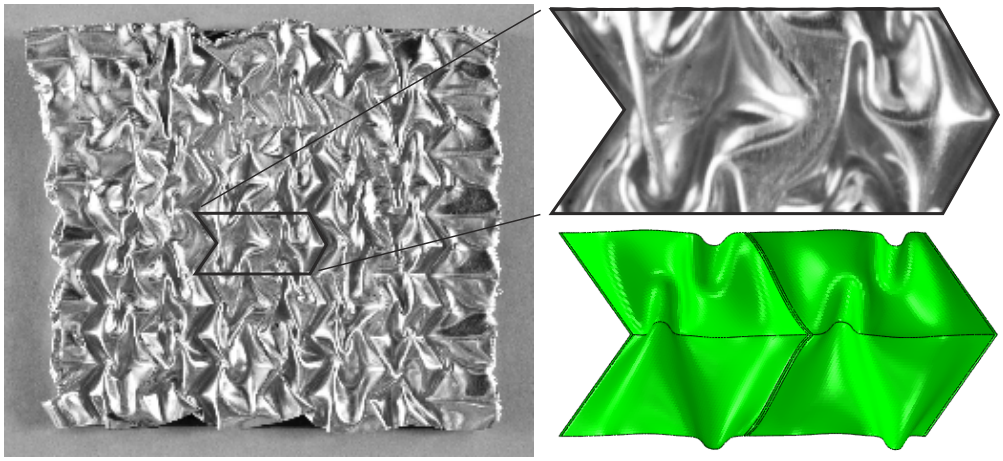

(a) Mi02

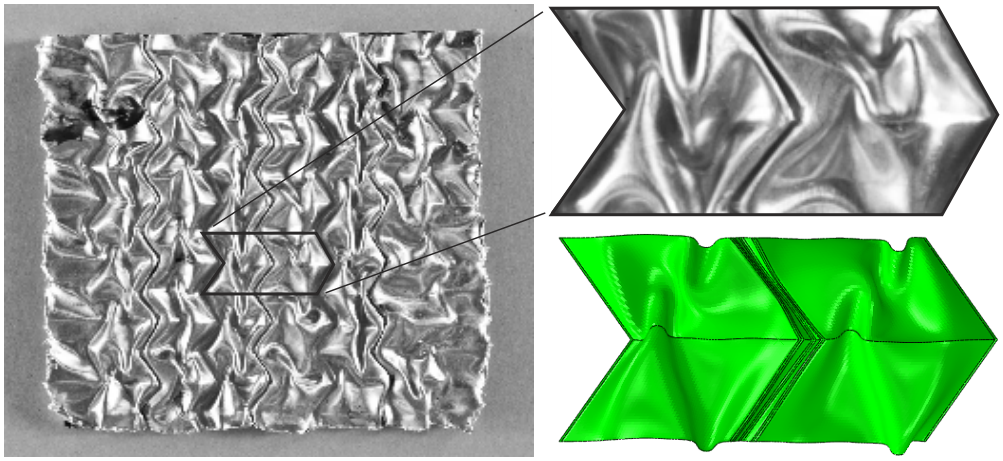

(b) Ind02

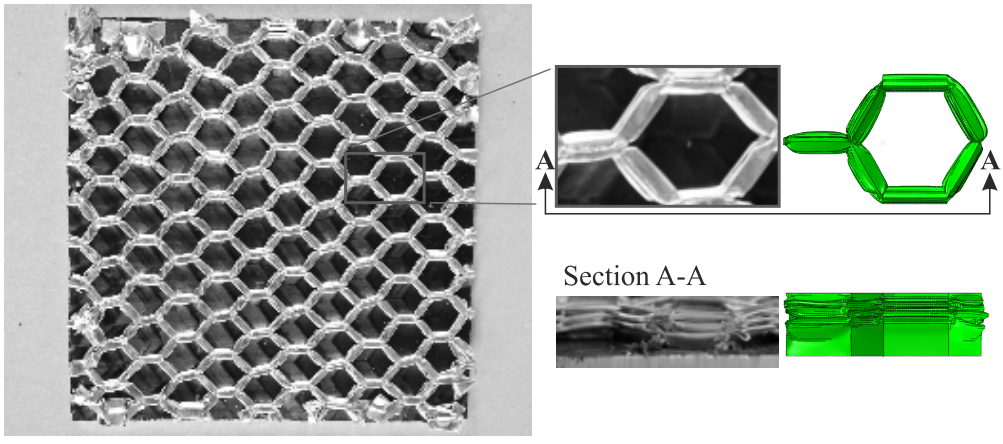


(c) HC

Figure 3.45: Final crushed core samples, on left; comparison of experimental (grey) and numerical (green) unit failure modes, on right.

### 3.5.6 Comparison of Foldcore and Honeycomb Responses

The experimental foldcore and honeycomb prototypes are constructed from significantly different aluminium alloys and so their responses are not directly comparable. However, the validated foldcore numerical models can be rerun with the honeycomb material properties, given in Table 3.16(b). As this material has a yield stress of 195MPa, the new equivalent models are given the designations Mi02-195 and Ind02-195.

Results from perfect and imperfect numerical models for both standard and indented cores are shown in Table 3.19 and Figure 3.46(a). As before, the standard Mi02-195 model is significantly affected by the introduction of geometric imperfections, with FE′ showing a 20% reduction in $\sigma^*_{avg}$ compared to FE. Interestingly, the indented results show that for this material, Ind02-195 is insensitive to geometric imperfections. The travelling hinge mode is retained in FE′, which only has a 6% reduction in $\sigma^*_{avg}$ compared to FE. Without foldcore plate buckling solutions or more extensive experimental data on foldcores constructed with different materials, it is difficult to explain why standard foldcores remain sensitive, but indented foldcores appear to become insensitive at stronger but less ductile materials. This phenomenon may be a contributing factor as to why the travelling hinge mode was only seen in the Ind10 models, which were constructed from a stronger but less ductile material than the Ind05 and Ind02 models.

A direct comparison between imperfect standard, indented, and honeycomb core types is shown in Figure 3.46(b). It can been seen that the honeycomb core has the best crushing resistance, with a $\sigma^*_{avg} = 8.8 \times 10^{-3}$. However the indented core has succeeded in its stated aim of generating a uniform failure response, with the lowest $U^* = 1.39$ at a crushing stress of $\sigma^*_{avg} = 5.3 \times 10^{-3}$. Both of these values are significant improvements on those of the standard core, which has the highest $U^* = 2.60$ and lowest $\sigma^*_{avg} = 3.2 \times 10^{-3}$.

Table 3.19: Results of foldcore models with 3003-H19 material properties.

| *Result* | Mi02-195 | | | Ind02-195 | | |
|---|---|---|---|---|---|---|
| | $\sigma^*_{max}$ $\times 10^{-3}$ | $\sigma^*_{avg}$ $\times 10^{-3}$ | $U^*$ | $\sigma^*_{max}$ $\times 10^{-3}$ | $\sigma^*_{avg}$ $\times 10^{-3}$ | $U^*$ |
| FE | 12.9 | 4.0 | 3.25 | 7.6 | 5.6 | 1.36 |
| FE′ | 8.3 | 3.2 | 2.60 | 7.3 | 5.3 | 1.39 |

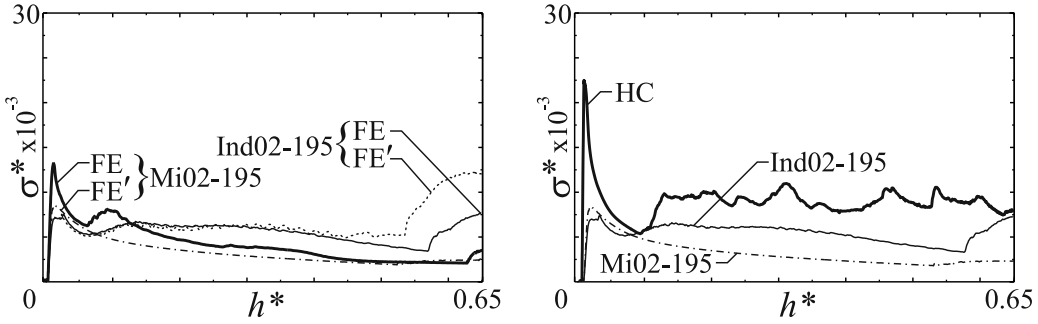


(a) Mi02-195 and Ind02-195 responses

(b) FE′ comparison

Figure 3.46: Dimensionless stress-strain responses of aluminium alloy 3003-H19 models.

To summarise, the indent significantly improves the response of a foldcore constructed from aircraft-grade aluminium alloys, in terms of suitability for energy-absorption applications. While the improvement is perhaps not enough to make it a competitive alternative to existing honeycombs, it does show that sub-folds can be designed into a foldcore to improve its performance under impact loading.

## 3.6 Conclusion

This chapter has demonstrated the energy-absorption capabilities of a new, indented foldcore geometry under out-of-plate quasi-static impact loads. A numerical parametric study established an optimum indented geometry. This was seen to possess a travelling hinge line failure mode with a high, uniform reaction stress. In contrast, an optimum standard foldcore was seen to possess a stationary hinge failure mode, which had non-uniform stress response typified by a significant weakening after initial hinge formation. Based on numerical observations, a theoretical prediction for the energy absorption of an idealised indented foldcore failure mode was developed. The theoretical model was able to provide a good approximation of the maximum crushing stress of the optimum indented geometry.

Large-scale experimental testing demonstrated that foldcores constructed with no visible geometric imperfections, that is Mi10 and Ind10, exhibited failure modes and responses as numerically and theoretically predicted. Small-scale experimental testing showed that when present, geometric imperfections suppress the travelling hinge line failure mode, and thus eliminate the advantage of indented foldcores over standard foldcores. A method for incorporating geometric imperfections into numerical models was developed to confirm these experimental observations.

Finally, foldcores were simulated with high-strength aluminium alloys, in order to be comparable to existing honeycomb cores. It was seen that with this material, the travelling hinge mode was retained even with geometric imperfections. However even with a preserved travelling hinge line failure mode, indented foldcores were seen to be substantially weaker than honeycomb cores, and so are unlikely to be a competitive alternative for high-performance energy absorption applications.

# Chapter 4

# Extended Foldcore Geometry

As discussed in Section 2.2, Wu (2010) began the process of developing and parametrising a family of rigid origami patterns developed from a Miura-base pattern, but it is incomplete. This chapter continues this process by deriving new parametrisations for three rigid plate geometries: the Non-Developable Miura pattern, the Non-Flat Foldable Miura pattern, and the Tapered Miura pattern. These parametrisations complete a group of patterns deemed the *first-level derivatives*, generated by changing a single characteristic of the Miura base pattern. This is followed with methods to combine these first-level derivatives to generate new, complex *piecewise geometries*. Subsequently, two methods to create new types of foldcores are presented: a method to attach faces to single-curved and piecewise patterns to create *folded sandwich structures*, and a method to alter Miura-derivative patterns to generate rigid-foldable *curved-crease* geometries.

## 4.1 First-Level Derivative Geometries

### 4.1.1 Non-Developable Miura Pattern

For many applications, folded plate structures can be manufactured and assembled from individually-cut plates, rather than an intact continuous sheet. As such, developability is not a necessarily a pattern requirement. Removing developability from the Miura pattern allows for the creation of a Non-Developable Miura pattern, which retains flat-foldable and rigid-foldable characteristics.

The crease pattern for a Non-Developable Miura unit is simply obtained by removing the shaded materials shown in Figure 4.1(a), where $b_i$ and $b_o$ are the inner and outer zigzag side lengths and $\Delta b = (b_o - b_i)/2$. An unfolded configuration is therefore determined by the same five parameters of the Miura pattern, $a$, $b_i$, $\phi$, $m$, and $n$, plus one additional constant $b_o$ or $\Delta b$. Four dependant constants are also useful to define: long side length $a_l^2 = a^2 + \Delta b^2 + 2a\Delta b \cos\phi$, long sector angle $\phi_l = a \sin\phi / a_l$, short side length $a_s^2 = a^2 + \Delta b^2 - 2a\Delta b \cos\phi$, and short sector angle $\phi_s = a \sin\phi / a_s$.

To parametrise the Non-Developable Miura variables, it is convenient to consider a folded half-unit of the pattern, shown in Figure 4.1(b), which is formed by taking the portion of the unfolded core plates between dot-dash centrelines of each panel row, Figure 4.1(a), and connecting common short and long edges $a_s$ and $a_l$. Points $A$, $B$, and $C$ on the boundary edge of this half-unit form a configuration equivalent to the longitudinal edge of a Miura pattern, with longitudinal edge lengths $\overline{AB} = \overline{BC} = a$, a sector angle of $\phi$ between longitudinal edges and lateral edges $\overline{AD}$ and $\overline{BE}$, and longitudinal and lateral edges lying in perpendicular planes. We can therefore define auxiliary parameters $\eta_A$ and $\eta_Z$ as used for the Miura pattern and related by Equation (2.1). These auxiliary angles can be used to find projected side lengths $\overline{PS}$, $\overline{QR}$, and $\overline{QP}$ from $\overline{AD}$, $\overline{BE}$, and $\overline{AB}$ respectively. These projected

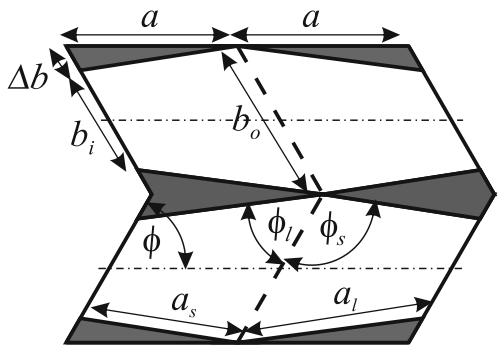


(a) Crease pattern and constants

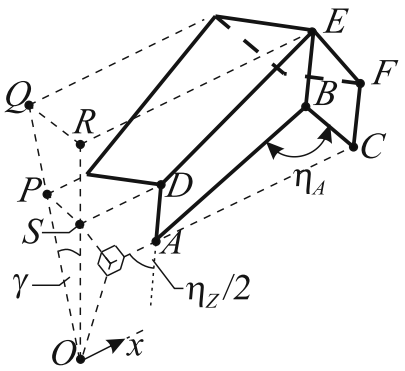


(b) Half-unit of the folded configuration

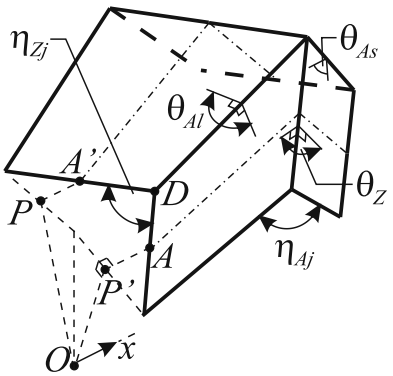


(c) Complete folded configuration

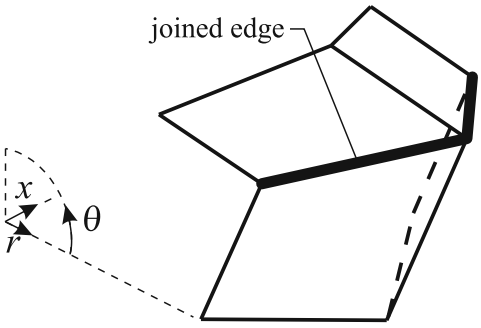


(d) Cylindrical coordinate orientation

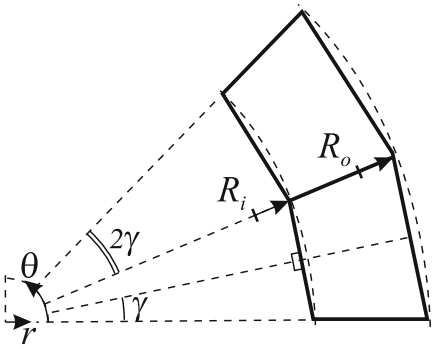


(e) Side ($r$-$\theta$) projection

Figure 4.1: Non-Developable Miura pattern geometry.

side lengths can be used to solve $\angle QOR$ in the right-angled triangles $\Delta OPS$ and $\Delta OQR$. This angle is deemed the lateral panel rotation $\gamma$, where $\tan\gamma = (\overline{QR} - \overline{PS})/\overline{QP}$. This can be expressed in terms of existing parameters as:

$$\tan\gamma = \frac{\Delta b \sin(\eta_Z/2)}{a\cos(\eta_A/2)} \tag{4.1}$$

Four additional parameters can be defined at the joined longitudinal edge: the joined edge angles $\eta_{Zj}$ and $\eta_{Aj}$, long side dihedral angle $\theta_{Al}$, and short side dihedral angle $\theta_{As}$, Figure 4.1(c). Note that dihedral angle $\theta_Z$ is equivalent to that in a

Miura pattern and so can be found with Equation (2.2). Equating lengths $\overline{AA'}$ and $\overline{PP'}$ and then considering triangles $\Delta POP'$ and $\Delta ADA'$ gives:

$$\cos\eta_{Zj} = 1 - \sin^2(\eta_Z/2)(1 + \cos 2\gamma) \tag{4.2}$$

Similarly, equating lengths $\overline{AC}$ and $\overline{DF}$ and considering triangles $\Delta ABC$ and $\Delta DEF$, gives:

$$\cos\eta_{Aj} = \frac{a_s^2 + a_l^2 - 2a^2(1 + \cos\eta_A)}{2a_s a_l} \tag{4.3}$$

Equation (2.3) can be reformulated with appropriate edge and sector angles to give the following two equations:

$$\cos\theta_{Al} = \frac{\cos\eta_{Zj} - \cos^2\phi_l}{\sin^2\phi_l} \tag{4.4}$$

$$\cos\theta_{As} = \frac{\cos\eta_{Zj} - \cos^2\phi_s}{\sin^2\phi_s} \tag{4.5}$$

It should be noted that unlike developable patterns, the long joined edge in the Non-Developable Miura pattern forms both a mountain and a valley crease polarity during deployment, which is to say that the dihedral angle $\theta_{Al}$ varies between 0 and $2\pi$. The polarity flip occurs when $\theta_{Al} = \pi$.

Finally, the assembled folded configuration of the Non-Developable Miura pattern forms a laterally curved profile with M-vertices and V-vertices lying along concentric curved profiles with radii $R_o$ and $R_i$ respectively. Different radii subscripts are used to that of the previous section as the pattern curvature is about a different axis. From Figure 4.1(b) these are found from projected side lengths $R_o = \overline{OR}$ and $R_i = \overline{OS}$:

$$R_i = \frac{b_i \sin(\eta_Z/2)}{2\sin\gamma} \tag{4.6}$$

$$R_o = \frac{b_o \sin(\eta_Z/2)}{2\sin\gamma} \tag{4.7}$$

Given a pattern with $m$ joined lines and $n$ zigzag lines and an origin and orientation as shown in Figure 4.1(d)-(e), the location of any vertex $V^{i,j}$ ($i = 1, 2, ..., m$, $j = 1, 2, ..., n$) can be plotted in cylindrical coordinates, where $(x, y, z) = (x,$

$r\cos\theta$,$r\sin\theta$). The three components ($x$,$r$,$\theta$) of $V^{i,j}$ can be given as:

$$r = \begin{cases} R_i & \text{for odd } j \\ R_o & \text{for even } j \end{cases} \tag{4.8}$$

$$\theta = 2(i-1)\gamma \tag{4.9}$$

$$x = \begin{cases} (j-1)a\sin(\eta_A/2) & \text{for odd } i \text{ and odd } j \\ (j-1)a\sin(\eta_A/2) - \Delta b\cos(\eta_Z/2) & \text{for odd } i \text{ and even } j \\ (j-1)a\sin(\eta_A/2) + b_i\cos(\eta_Z/2) & \text{for even } i \text{ and odd } j \\ (j-1)a\sin(\eta_A/2) + (b_i+\Delta b)\cos(\eta_Z/2) & \text{for even } i \text{ and even } j \end{cases} \tag{4.10}$$

To summarise, there are ten configuration variables $\eta_A$, $\eta_Z$, $\theta_Z$, $\theta_{Al}$, $\theta_{As}$, $\eta_{Aj}$, $\eta_{Zj}$, $R_i$, $R_o$, and $\gamma$, related by nine Equations (2.1), (2.3), (4.1–7). Therefore any folded configuration can be determined by specifying six dimensional constants and one configuration variable. The folding sequence in Figure 4.2 is found with $a = 40$mm, $b_o = 40$mm, $b_i = 30$mm, $\phi = \pi/3$, $m = 11$, $n = 4$, and varying $\theta_A$ from 0 to $2\pi/3$.

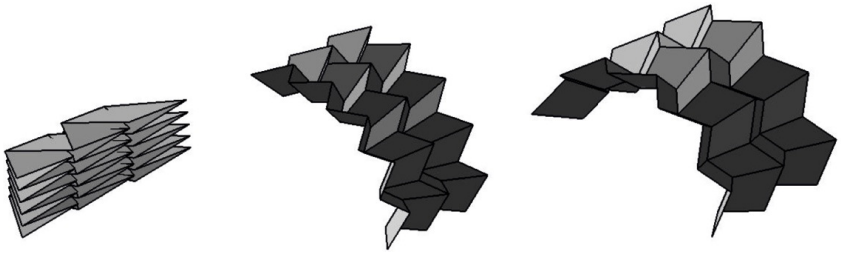

(a) Folding sequence simulated in MATLAB

(b) Folding sequence of aluminium prototype

Figure 4.2: Non-Developable Miura pattern folding motion.

### 4.1.2 Non-Flat Foldable Miura Pattern

Flat-foldability can be a useful characteristic for certain applications, for example it can allow deployable structures to be folded for storage. However it is not necessary for other applications, including foldcore construction. A planar non-flat foldable Miura variant is shown in Figure 4.3(a), and is used for packaging applications (Tessellated Group, 2013) as it forms a panel at a fully-folded configuration. This planar variant is not parametrised here, as it can be plotted with trivial modifications to the Miura parametrisation in Section 2.2. Another non-flat foldable Miura variant exists that causes the pattern to fold along a curved profile, Figure 4.3(b). It has the same axis of curvature as that of the Non-Developable Miura pattern and so may be useful as an alternative. Henceforth the term Non-Flat Foldable Miura pattern shall refer to the curved variant.

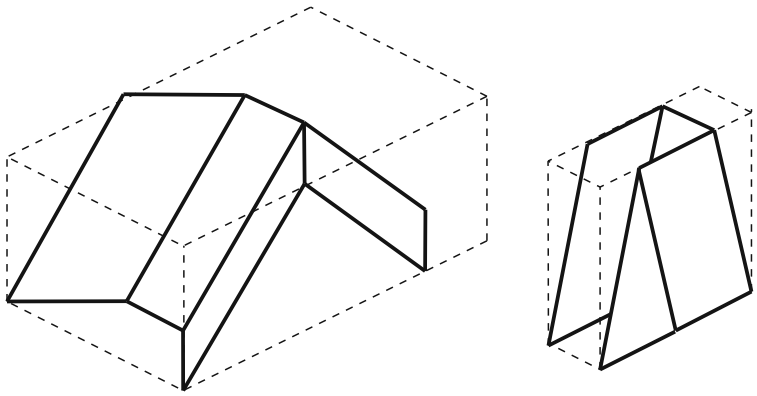

(a) Planar Non-Flat Foldable Miura variant

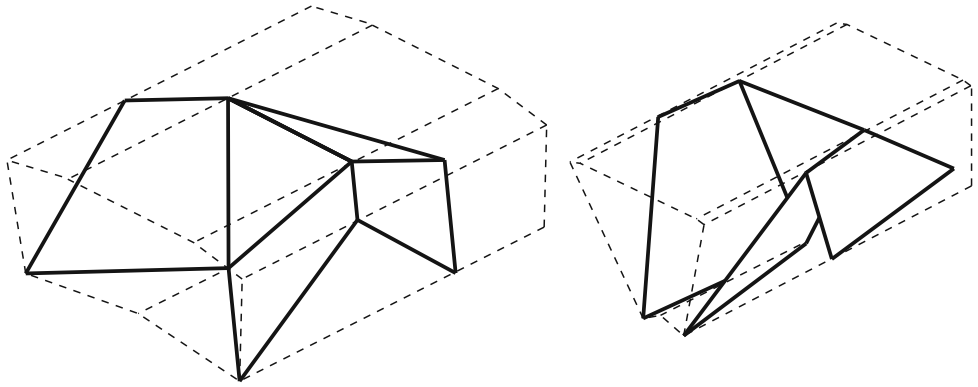

(b) Curved Non-Flat Foldable Miura variant

Figure 4.3: Partially-folded and near fully-folded half-units of Non-Flat Foldable Miura variants.

An unfolded unit of the Non-Flat Foldable Miura pattern is shown in Figure 4.4(a). It is similar to the Non-Developable Miura pattern, except that triangle plates replace the removed portions of the Non-Developable pattern. It can be completely realised from six pattern constants: $a$, $\phi$, $m$, and $n$ as used previously, plus inner and outer zigzag side lengths $b_i$ and $b_o$. Additional dependant constants $\Delta b$, $a_l$, $a_s$, $\phi_l$, and $\phi_s$ can be found in the same manner as described in the previous section, and two additional constants, triangle plate width and sector angle, are given by $w = \Delta b \sin\phi$ and $\phi_w = \pi - \phi_s - \phi_l$ respectively. The ability of a pattern to be flat-folded is determined by the Kawasaki-Justin theorem (Kawasaki, 1989), which states that flat-foldable patterns will have alternately added and subtracted sector angles summing to 0. Summing sector angles around the central vertex confirms the pattern as non-flat foldable, with $\phi_s - \phi_w + \phi_s - \phi_l + \phi_w - \phi_l = 2(\phi_s - \phi_l) \neq 0$.

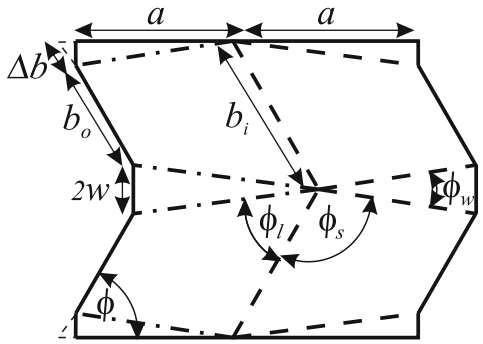


(a) Crease pattern and constants

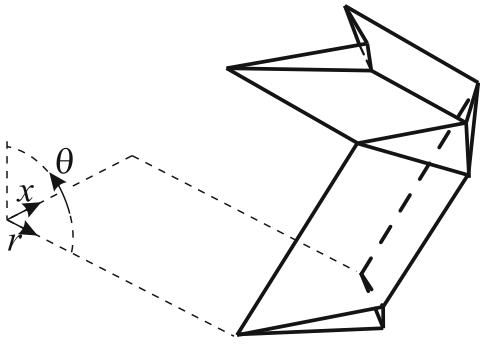


(b) Folded configuration

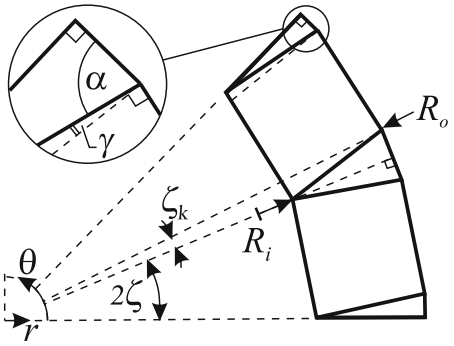


(c) Side ($r$-$\theta$) projection

Figure 4.4: Non-Flat Foldable Miura pattern geometry.

In the same manner as described in the previous section, auxiliary variables $\eta_A$ and $\eta_Z$ can be defined along perpendicular planes of the half-unit geometry, and then used to derive the required configuration variables. Four panel rotation angles can

be defined: global panel rotation angles $\zeta$ and $\zeta_k$, and local panel rotation angles $\gamma$ and $\alpha$. Equation (4.1) remains valid for $\gamma$ and the following two relations can be established using projected side lengths and triangle geometry:

$$\cos\alpha = \frac{w\cos\gamma}{a\cos(\eta_A/2)} \tag{4.11}$$

$$\zeta = \pi/2 - \gamma - \alpha \tag{4.12}$$

The folded geometry can be parametrised using cylindrical co-ordinates, Figure 4.4(b)-(c), with M-vertices and V-vertices lying along concentric circles with radii $R_o$ and $R_i$ respectively. The following three relationships between remaining variables can be established with projected side lengths:

$$R_i = \frac{b_i\sin(\eta_Z/2)}{2\sin\zeta} \tag{4.13}$$

$$R_o = \sqrt{(R_i + a\cos(\eta_A/2)\sin\alpha/\cos\gamma)^2 + w^2} \tag{4.14}$$

$$\sin\zeta_k = \frac{w}{R_o} \tag{4.15}$$

Dihedral and edge angles can derived from auxiliary variables. However this process is extensive and very similar to that described for the Non-Developable Miura pattern and so is not shown here. Given a Non-Flat Foldable Miura pattern with $m$ straight lateral lines and $n$ zigzag lines, the location of any vertex $V^{i,j}$ ($i = 1, 2, ..., m,\ j = 1, 2, ..., n$) can be plotted in cylindrical coordinates, where $(x, y, z) = (x,\ r\cos\theta, r\sin\theta)$ and origin and orientation as shown in Figure 4.4. The three components ($x$,$r$,$\theta$) of $V^{i,j}$ can be given as:

$$r = \begin{cases} R_i & \text{for odd } j \\ R_o & \text{for even } j \end{cases} \tag{4.16}$$

$$\theta = \begin{cases} 2(i'-1)\zeta & \text{for odd } j \\ 2(i'-2)/2\zeta + \zeta_k & \text{for even } j \text{ and odd } i \\ 2(i'-2)/2\zeta - \zeta_k & \text{for even } j \text{ and even } i \end{cases} \tag{4.17}$$

$$x = \begin{cases} (j-1)a\sin(\eta_A/2) & \text{for odd } j \text{ and odd } i' \\ (j-1)a\sin(\eta_A/2) + b_i\cos(\eta_Z/2) & \text{for odd } j \text{ and even } i' \\ (j-1)a\sin(\eta_A/2) + \Delta b\cos(\eta_Z/2) & \text{for even } j \text{ and odd } i' \\ (j-1)a\sin(\eta_A/2) + (b_i - \Delta b)\cos(\eta_Z/2) & \text{for even } j \text{ and even } i' \end{cases} \tag{4.18}$$

Note that the sub-designation $i' = (\mathrm{mod}(i,2)+i)/2$ is used where it gives a more concise parametrisation.

To summarise, seven Equations (2.1), (4.1), and (4.11–15) exist amongst eight pattern variables, $\eta_A$, $\eta_Z$, $R_o$, $R_i$, $\zeta$, $\zeta_k$, $\gamma$, and $\alpha$. Therefore any folded configuration can be found by specifying six dimensional constants and one configuration variable. An example folding sequence is shown in Figure 4.5 for a Non-Flat Foldable pattern with parameters $a = 15$mm, $b_o = 40$mm, $b_i = 30$mm, $\phi = \pi/3$, $m = 9$, $n = 5$, and varying $\theta_A$ continuously from $\pi/10$ to $\pi$. From the folding sequence it can be seen that the pattern is developable, but not flat-foldable.

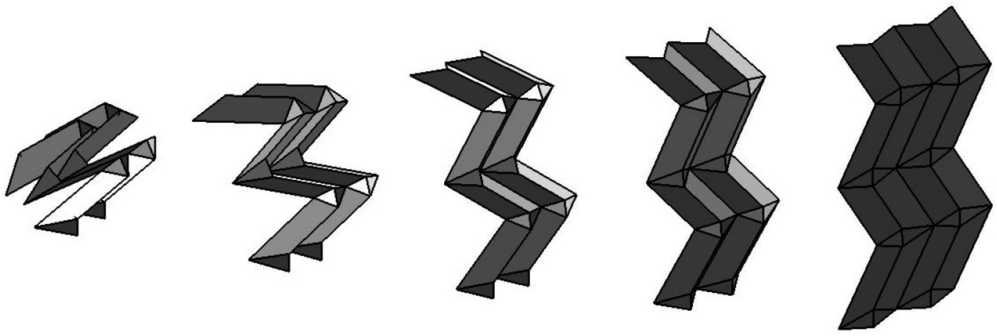

(a) Folding sequence simulated in MATLAB

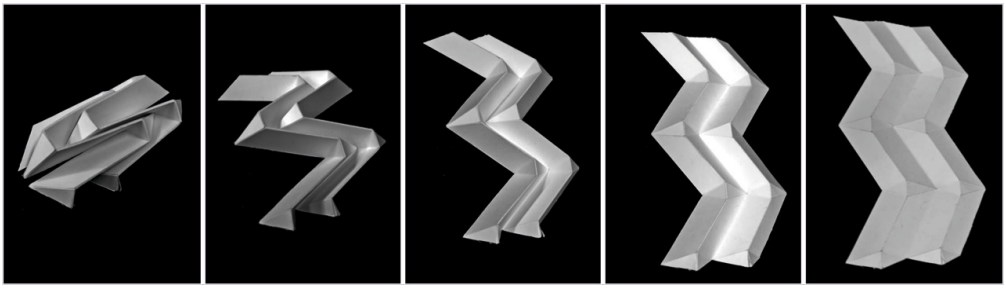

(b) Folding sequence of paper card prototype

Figure 4.5: Non-Flat Foldable Miura folding motion.

### 4.1.3 Tapered Miura Pattern

A tapered Miura pattern is obtained by inclining the straight crease lines of a Miura pattern so that they form a polar, rather than a parallel, configuration. This causes the pattern to deploy in a polar ($r$-$\theta$), rather than a rectilinear ($x$-$y$) manner, although the pattern remains globally planar.

A unit consists of four panels aligned along polar lines meeting at a centre point. The angular constant $\rho$ designates the angle between these polar lines, Figure 4.6(a). Constants $a$ and $\phi$ can be defined for both the close and far vertices, denoted by subscripts $c$ and $f$ respectively. Two of these are dependent parameters, as $\phi_f = \phi_c - \rho$, and $a_c = a_f \sin\phi_f / \sin\phi_c$. Panels on the same radial ring are identical in size, however side length $b$ increases for each added $j^{th}$ radial ring. The panel length $b$ along the $j^{th}$ zigzag crease from the origin is therefore denoted $b_j$ and found with the following equation, to give six independent, dimensional pattern constants:

$$b_j = b_1 + (j-1)a_c \sin\rho / \sin\phi_f \tag{4.19}$$

The angular relationships established between $\phi$, $\theta_A$, $\theta_Z$, $\eta_Z$ , and $\eta_A$ for the Miura pattern, Equations (2.1–3), can be reformulated for both close and far vertices, with a common $\theta_Z$ across the polar creases. This gives the following six equations between seven variables, $\theta_{cA}$, $\theta_{fA}$, $\theta_Z$, $\eta_{cZ}$, $\eta_{fZ}$, $\eta_{cA}$, $\eta_{fA}$:

$$\cos\eta_{cZ} = \sin^2\phi_c \cos\theta_{cA} + \cos^2\phi_c \tag{4.20}$$

$$\cos\eta_{cA} = \sin^2\phi_c \cos\theta_Z - \cos^2\phi_c \tag{4.21}$$

$$(1+\cos\eta_{cZ})(1-\cos\eta_{cA}) = 4\cos(\phi_c)^2 \tag{4.22}$$

$$\cos\eta_{fZ} = \sin^2\phi_f \cos\theta_{fA} + \cos^2\phi_f \tag{4.23}$$

$$\cos\eta_{fA} = \sin^2\phi_f \cos\theta_Z - \cos^2\phi_f \tag{4.24}$$

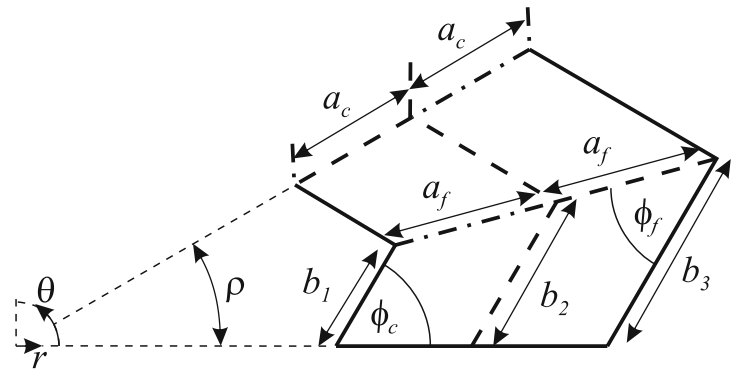


(a) Crease pattern and constants

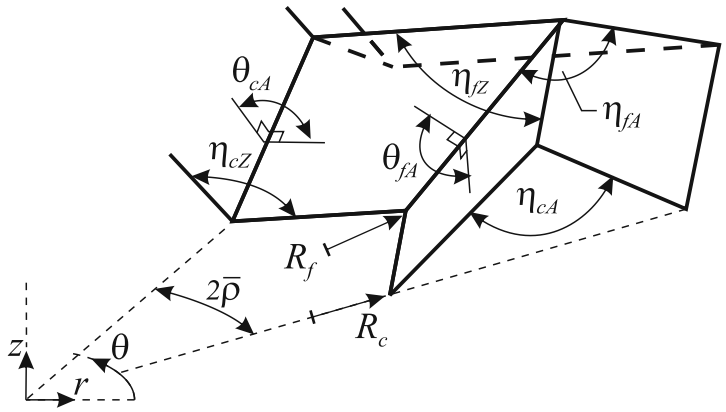


(b) Configuration variables

Figure 4.6: Tapered Miura pattern geometry.

$$(1+\cos\eta_{fZ})(1-\cos\eta_{fA}) = 4\cos(\phi_f)^2 \tag{4.25}$$

The folded geometry can be parametrised using cylindrical co-ordinates, which are found with three additional pattern variables: folded angular parameter $\bar{\rho}$, and radii $R_{c,j}$ and $R_{f,j}$, Figure 4.6(b). The following three equations can be found from geometry:

$$\bar{\rho} = (\eta_{cZ} - \eta_{fZ})/2 \tag{4.26}$$

$$R_{c,j} = b_j \sin(\eta_{fZ}/2)/\sin\bar{\rho} \tag{4.27}$$

$$R_{f,j} = b_j(\pi - \sin\eta_{cZ}/2)/\sin\bar{\rho} \tag{4.28}$$

Given a Tapered Miura pattern with $m$ polar lines and $n$ zigzag lines, the location of any vertex $V^{i,j}$ $(i = 1,2,...,m,\ j = 1,2,...,n)$ can be plotted in cylindrical coordinates, where $(x,y,z) = (r\cos\theta, r\sin\theta, z)$ and origin and orientation are as

shown in Figure 4.6. The three components ($r$,$\theta$,$z$) of $V^{i,j}$ can be given as:

$$r = \begin{cases} R_{c,j} & \text{for odd } i \\ R_{f,j} & \text{for even } i \end{cases} \tag{4.29}$$

$$\theta = (i-1)\bar{\rho} \tag{4.30}$$

$$z = \begin{cases} 0 & \text{for odd } j \\ a_c \cos(\eta_{cA}/2) & \text{for even } j \end{cases} \tag{4.31}$$

In total, nine Equations (4.20–28) are found amongst ten variables, $\theta_{cA}$, $\theta_Z$, $\eta_{cZ}$, $\eta_{cA}$, $\theta_{fA}$, $\eta_{fZ}$, $\eta_{fA}$, $\bar{\rho}$, $R_{c,j}$ and $R_{f,j}$. Therefore any folded configuration can be found by specifying six dimensional constants and one configuration variable. An example sequence is shown in Figure 4.7 for a Tapered Miura pattern with parameters $a_c = 60$mm, $b_1 = 40$mm, $\phi_c = \pi/3$, $\phi_f = 2\pi/9$, $m = n = 5$, and $\theta_{cA}$ varying continuously from 0 to $\pi$.

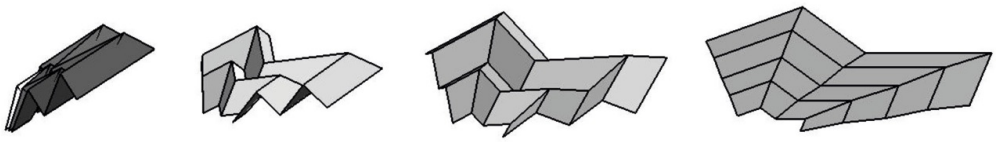

(a) Folding sequence simulated in MATLAB

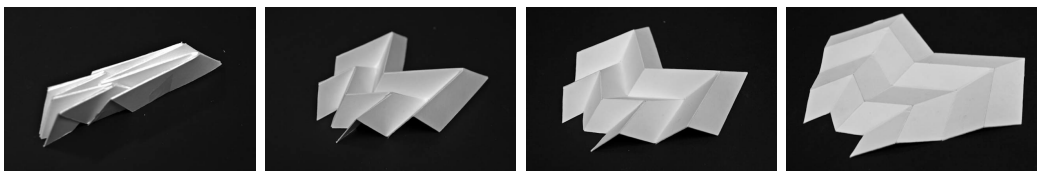

(b) Folding sequence of paper card prototype

Figure 4.7: Tapered Miura pattern folding motion.

The Tapered Miura pattern can fold to a fan-like structure, which forms a closed geometry at certain pattern configurations. Analogous closed configurations exist for other Miura-derivative patterns. While deriving these closure conditions, several patterns displayed interesting behaviour that might be useful for bi-stable structures. This particular application is outside the scope of this thesis but closure and bi-stability are briefly discussed in Appendix A.

## 4.2 Piecewise Geometries

### 4.2.1 Piecewise Geometries

By utilising the consistent parametrisation for the above set of Miura-derivative patterns, complex *piecewise geometries* can be created with preserved rigid-foldable characteristics. Piecewise geometries are created by taking an initial pattern, termed a *master* pattern, and attaching additional *slave* patterns that share common edge vertices. The common vertices can be used to remove redundant parameters in the slave patterns, thus forming complex geometry with a minimum number of required parameters. Adopting terminology from (Klett and Drechsler, 2011), such a process is a bottom-up method for generating freeform rigid-foldable geometry, as opposed to top-down methods that allow for the creation of continuously varied freeform geometries by perturbing rigid pattern vertices within allowed kinematic constraints. The process is demonstrated below by way of three examples.

To create rigid-foldable patterns with a variable longitudinal radius of curvature, piecewise geometries can be formed from combinations of Miura, Arc, and Arc-Miura patterns. For example, Figure 4.8(a) shows a master Miura pattern connected to a slave Arc-Miura pattern along a common edge. Geometric compatibility allows for the removal of four redundant slave parameters, $b_1^s = b^m$, $\phi_1^s = \phi^m$, $m^s = m^m$, and any configuration variable at that vertex, for example $\theta_{VZ}^s = \theta_Z^m$. Superscripts $m$ and $s$ are used to denote master and slave pattern parameters respectively. As there are seven parameters required to define an Arc-Miura pattern, three remaining parameters are required to completely define the piecewise assembly. These can be set to create geometric forms as required, for instance Figure 4.8(b) shows a Miura/Arc-Miura/Miura rigid-foldable arch, where $a^s$ is chosen to give a constant panel depth across straight and curved segments, and $n^s$ and $\phi_2^s$ are

chosen such that the final configuration bends around a semi-circle. Assembling freeform geometries in this manner creates folded plate structures with a minimum number of panel sizes, for example only two panel sizes are required to form the Miura/Arc-Miura/Miura arch.

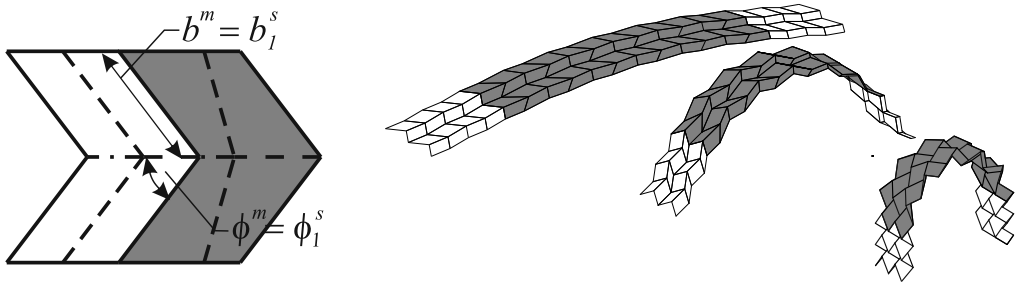


(a) Master (clear) and slave (shaded) patterns

(b) Arch shape with varying longitudinal curvature

Figure 4.8: Piecewise geometries formed from Miura/Arc-Miura assembly.

Geometries with varying lateral curvature can be created by connecting Miura, Non-Developable Miura, and Non-Flat Foldable Miura patterns. An example assembly with half-units of a master Miura pattern connected to a slave Non-Developable Miura is shown in Figure 4.9(a). The usage of a half-unit is necessary so that there is a common edge between the two patterns. Four slave parameters can be removed, $a^s = a^m$, $\phi^s = \phi^m$, $n^s = n^m$, and a configuration variable, for example $\eta_A^s = \eta_A^m$. The three remaining slave parameters $b_i^s$, $b_o^s$, and $m^s$, can be specified as desired. For example, Figure 4.9(b) shows a geometry with slave Non-Developable Miura patterns designed such that the straight Miura segments lie along perpendicular planes in the final configuration. Three panel sizes are required to create the geometry.

As a final example, piecewise geometries can be created by pairing a master pattern with self-similar slave patterns. This is equivalent to a commonly-used method for altering rigid patterns which consists of altering adjacent plate side lengths to create a varied rigid-foldable geometry. An example of this type of geometry is shown in Figure 4.10(a), in which master and slave Tapered Miura patterns are connected along a common edge. Five redundant slave parameters can be removed:

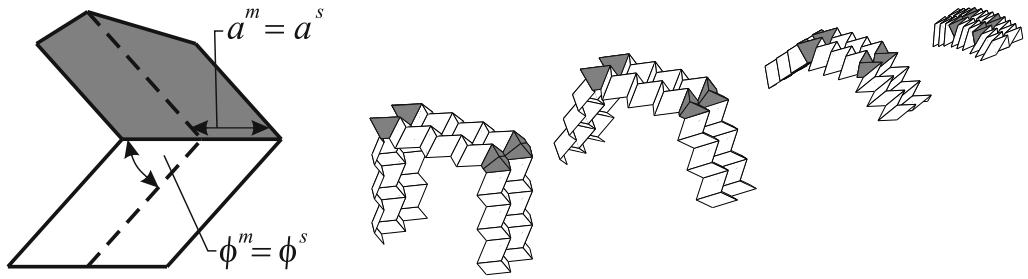


(a) Master (clear) and slave (shaded) patterns

(b) Rectangular box shape with varying lateral curvature

Figure 4.9: Piecewise geometries formed from Miura/Non-Developable Miura assembly.

$b_j^s = b_{j+1}^m$, $\phi_c^s = \phi_c^m$, $\phi_f^s = \phi_f^m$, $m^s = m^m$, and a configuration variable, for example $\theta_{cZ}^s = \theta_{cZ}^m$. This leaves two parameters free to be used as desired. The assembly shown in Figure 4.10(b) is created with Tapered Miura patterns with alternating values for $a_c$, creating a conical assembly. Sequential values for $a_c$ could instead be defined so that the folded assembly fits a shallow, doubly-curved spherical surface. When modifying the Tapered Miura pattern in this manner, the number of required panel sizes does not change between planar, conical, or spherical geometries, with a single panel size per radial ring retained for all cases.

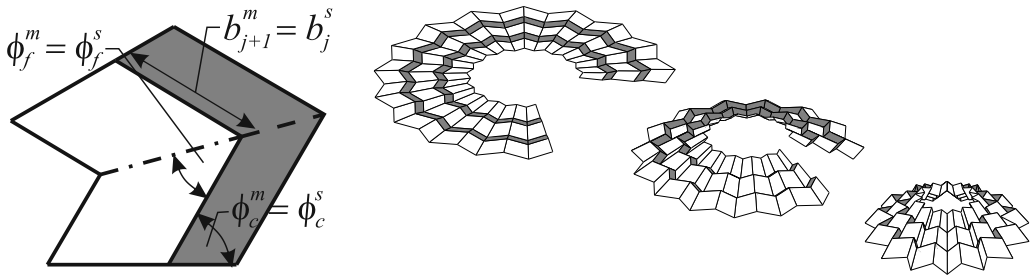


(a) Master (clear) and slave (shaded) patterns

(b) Conical shape formed with alternating Tapered Miura patterns.

Figure 4.10: Piecewise geometries formed from Tapered Miura pattern assembly.

## 4.3 Folded Sandwich Structures

When attempting to use curved first-level derivative patterns for the core of a foldcore structure, a problem is encountered. The patterns do not possess a smooth inner and outer surface, rather they have a jagged inner and outer surface that arises from only pattern vertices lying along radii of curvature. Attempting to attach continuously curved faces to these core patterns to form sandwich structures results in a sandwich panel that has weak point connections between core and face, Figure 4.11(a).

A new method is proposed to attach faceted inner and outer sandwich faces to single-curved Miura-derivative patterns. Termed *folded sandwich structures*, the new panels are able to achieve a continuous line connection between core and face sheets, Figure 4.11(b). The geometric requirements for faceted faces are presented below for four single-curved core patterns.

### 4.3.1 Non-Developable Miura Core

Faceted inner and outer sandwich faces are designed on a single core unit such that when connected, the face sheets lie along core edges, and when tessellated with the core unit, the face geometry forms a continuous inner and outer surface, Figure 4.12. This process will first be demonstrated for a Non-Developable Miura type core pattern.

The Non-Developable pattern has vertices located at inner and outer radii, so by kinking the face plate at these vertices, they will lie continuously along the inner and outer core edges. For each core unit, this creates an inner and outer face each with two facets of the same length, Figure 4.13(a)-(b). Using triangle geometry, the following expressions for inner and outer face length, deemed $l_i^{ND}$

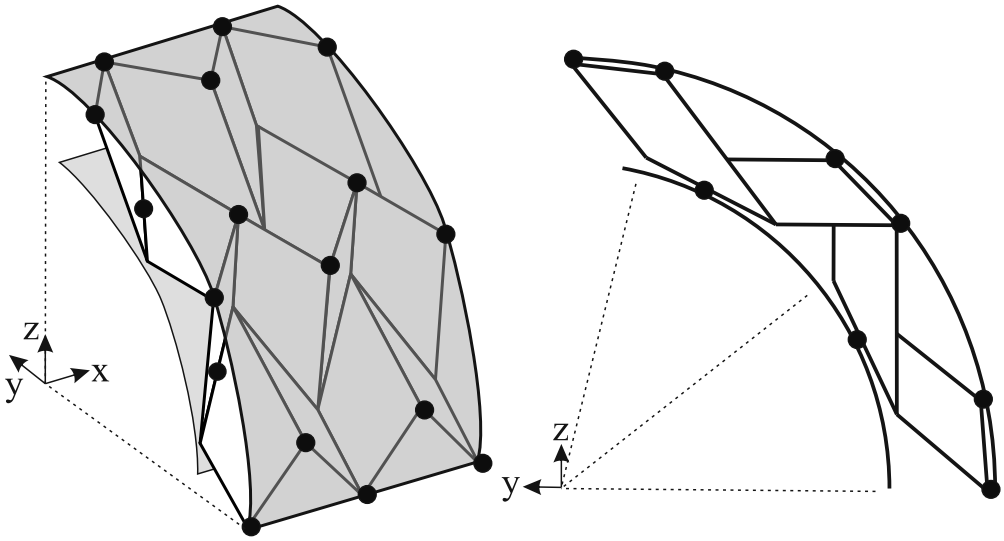


(a) Traditional sandwich panels with continuously curved face sheets and point contacts between core and faces

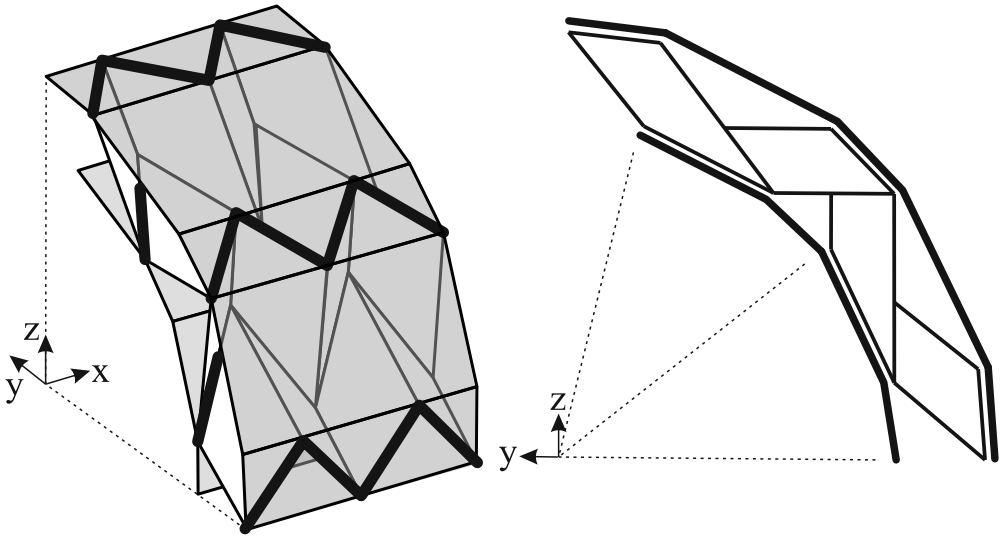


(b) Folded sandwich structure with faceted face sheets and line connections between core and faces

Figure 4.11: Comparison of traditional sandwich panel and folded sandwich structure.

and $l_o^{ND}$, respectively, can be found relative to Non-Developable core parameters established in Section 4.1:

$$l_i^{ND} = R_i\sqrt{2(1-\cos(2\gamma))} \tag{4.32}$$

$$l_o^{ND} = R_o\sqrt{2(1-\cos(2\gamma))} \tag{4.33}$$

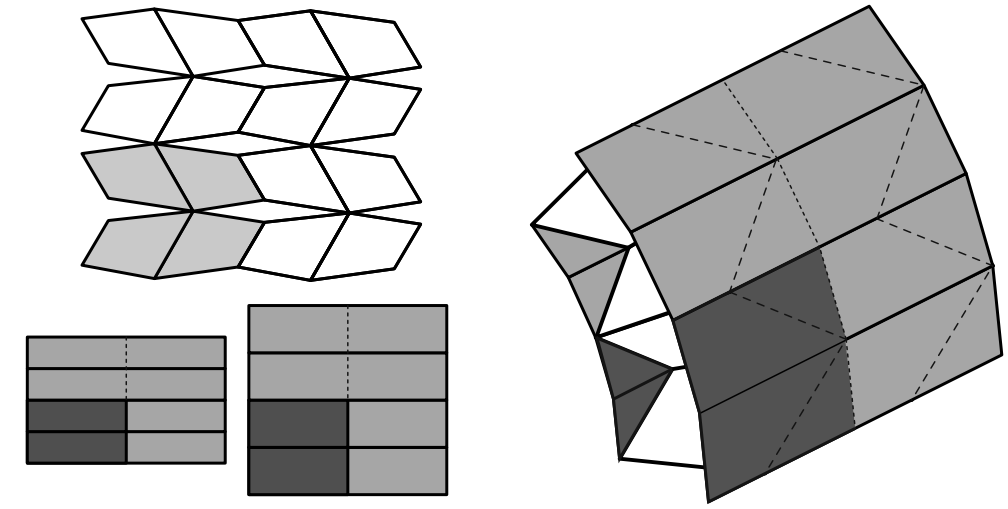

(a) Unfolded core, top; and faces, bottom (b) Perspective view of assembled panel

Figure 4.12: Tessellation of single unit of core and faceted face geometry, shown in the darker shade.

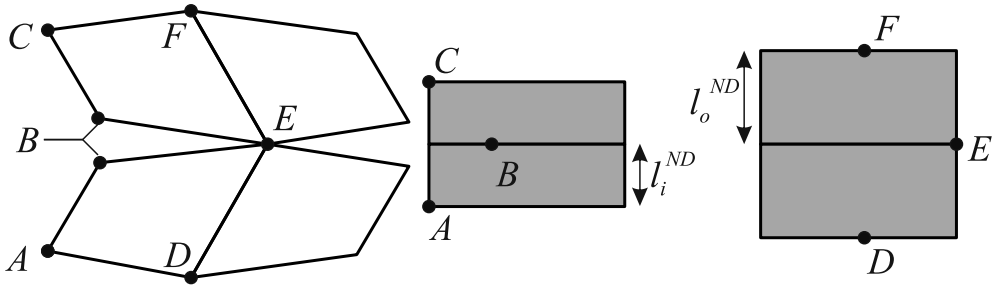


(a) Unfolded core and face patterns

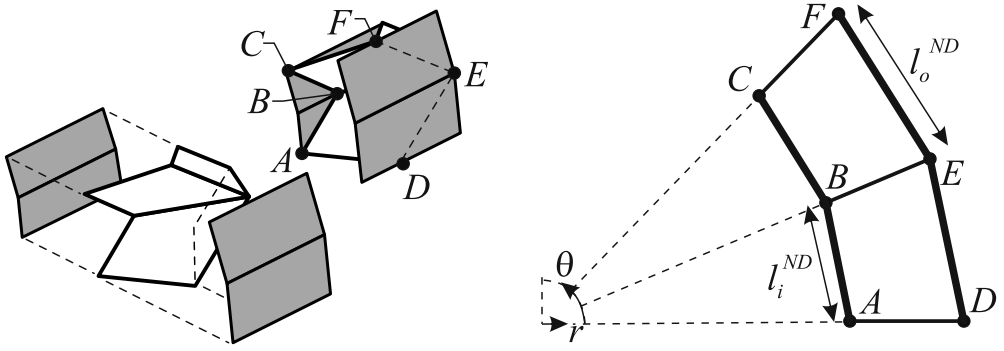


(b) Alignment and assembly (c) Face lengths

Figure 4.13: Non-Developable Miura folded sandwich structure.

### 4.3.2 Non-Flat Foldable Miura Core

Faceted sandwich faces can be designed for a Non-Flat Foldable Miura core in a similar way to that just described for the Non-Developable Miura pattern. Faces are kinked about inner and outer core vertices to create a folded sandwich that possesses two facet lengths along the outer edge, $l_{o,1}^{NF}$ and $l_{o,2}^{NF}$, and one facet length along the inner edge, $l_i^{NF}$, shown in Figure 4.14. From triangle geometry the following expressions for face lengths can be found relative to Non-Flat Foldable core parameters established in Section 4.1:

$$l_{o,1}^{NF} = R_o\sqrt{2(1-\cos(2\zeta_k))} \tag{4.34}$$

$$l_{o,2}^{NF} = R_o\sqrt{2(1-\cos(2\zeta-2\zeta_k))} \tag{4.35}$$

$$l_i^{NF} = R_i\sqrt{2(1-\cos(2\zeta))} \tag{4.36}$$

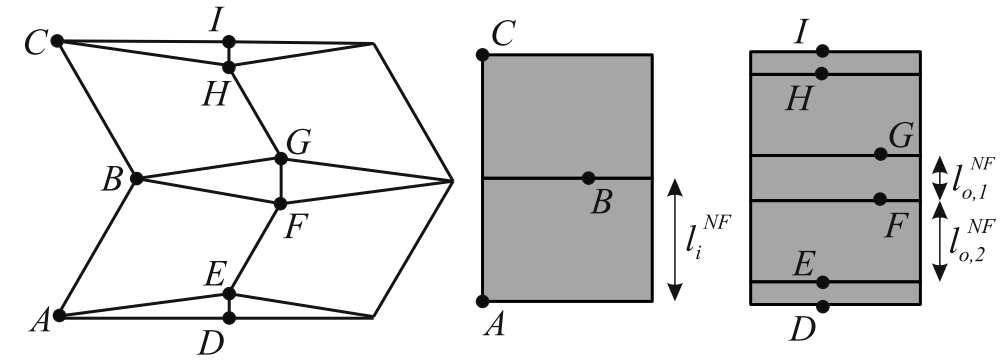


(a) Unfolded core and face patterns

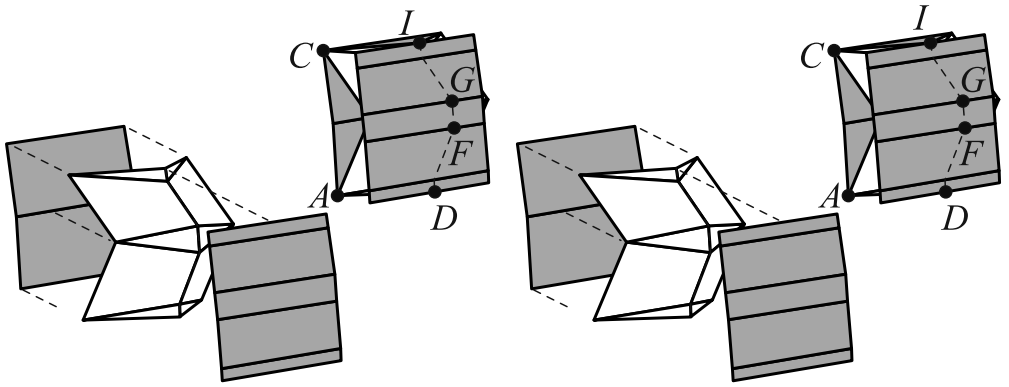


(b) Alignment and assembly (c) Face lengths

Figure 4.14: Non-Flat Foldable Miura folded sandwich structure.

Additional core parameter constraints can be introduced to design particular face lengths, for example the relation $2w = b_o \sin(\eta_Z/2)$ can be used to create a panel where $l_{o,1}^{NF} = l_{o,2}^{NF}$.

### 4.3.3 Arc-Miura Core

Unlike the previous cores, the Arc-Miura pattern does not possess a continuous outer or inner edge along the direction of curvature. It is still possible to attach faceted faces to a unit, Figure 4.15(a)-(b), however the face sheets have different core contact conditions over alternate spans. The first span is continuously bonded along the zigzag edges of the core pattern and the second span hangs unsupported between core zigzags. This means that two face lengths are required for both inner and outer faces, $l_{o,1}^{AM}$, $l_{o,2}^{AM}$, $l_{i,1}^{AM}$, and $l_{i,2}^{AM}$, Figure 4.15(c). From triangle geometry the following expressions can be found relative to the Arc-Miura core parameters shown in Section 2.2:

$$l_{of,1} = R_1\sqrt{2 - 2\cos\xi_{b1}} \tag{4.37}$$

$$l_{of,2} = R_1\sqrt{2 - 2\cos(\xi - \xi_{b1})} \tag{4.38}$$

$$l_{if,1} = R_2\sqrt{2 - 2\cos(\xi_{b1} + 2\xi_{a2} - \xi)} \tag{4.39}$$

$$l_{if,2} = R_2\sqrt{2 - 2\cos(2\xi - \xi_{b1} - 2\xi_{a2})} \tag{4.40}$$

In a similar manner to that discussed for the previous core, it is possible to design Arc-Miura core geometry for particular face length requirements, for example to reduce or remove the length of the unsupported face sections.

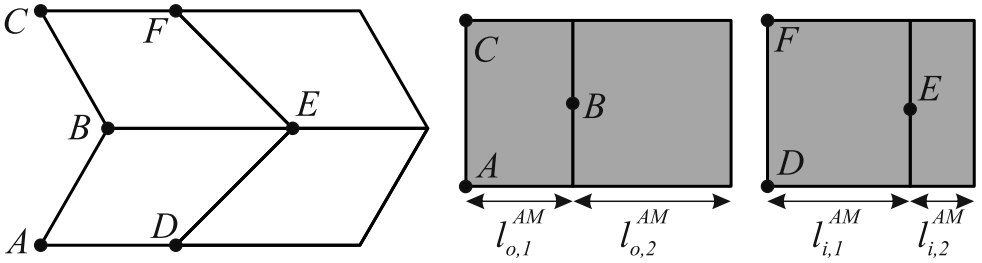


(a) Unfolded core and face patterns

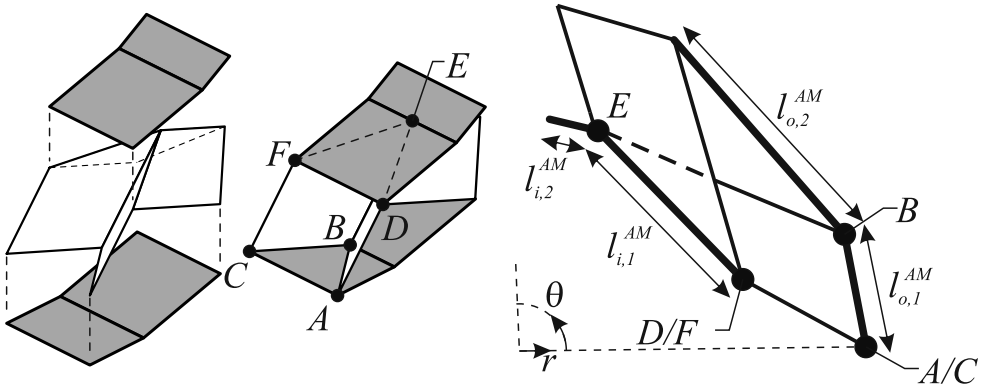


(b) Alignment and assembly (c) Face lengths

Figure 4.15: Arc-Miura folded sandwich structure.

### 4.3.4 Arc Core

Using the Arc pattern as a core structure again creates a panel with different face bonding conditions. For an Arc core, every zigzag crease lies along the same outer radius. The outer face can therefore be continuously connected along both the core zigzag and straight patterns mountain-crease lines. As there are no core vertices along the inside radius, the inner face is attached only along portions of straight valley-crease pattern lines, Figure 4.16(a)-(b).

This creates two facet lengths for the outer face, $l_{o,1}^{A}$, $l_{o,2}^{A}$, and one facet length for the inner face length $l_{i}^{A}$, Figure 4.16(c). These can be related to Arc parameters shown in Section 2.2 with the following equations:

$$l_{o,1}^{A} = R\sqrt{2 - 2\cos(\xi_2 - \xi_1)/2} \tag{4.41}$$

$$l_{o,2}^{A} = R\sqrt{2 - 2\cos\xi_1} \tag{4.42}$$

$$R_i = \frac{R\cos(\xi_1/2) - w\cos(\theta_A/2)}{\cos((\xi_1+\xi_2)/4)} \tag{4.43}$$

$$l_i^A = R_i\sqrt{2-2\cos((\xi_1+\xi_2)/2)} \tag{4.44}$$

where $R_i$ is an auxilliary inner radius parameter.

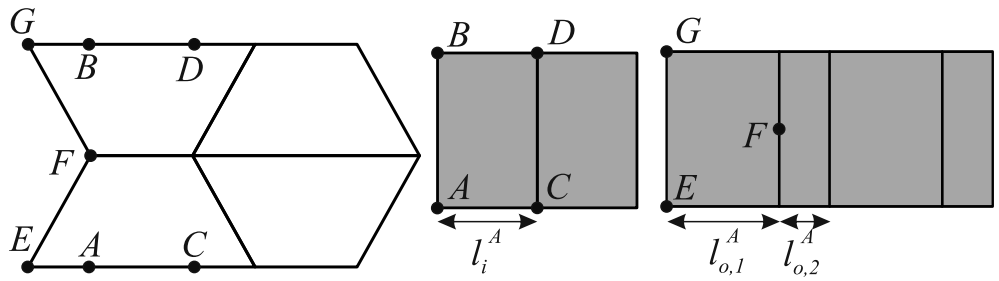


(a) Unfolded core and face patterns

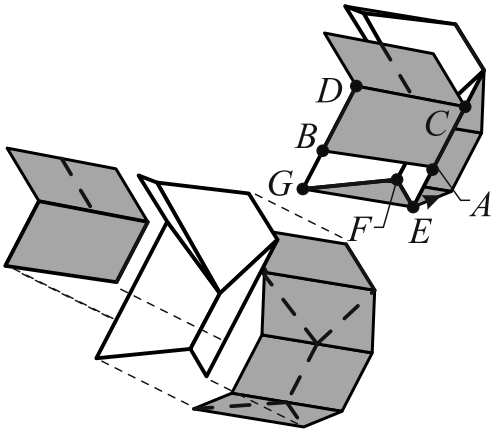


(b) Alignment and assembly

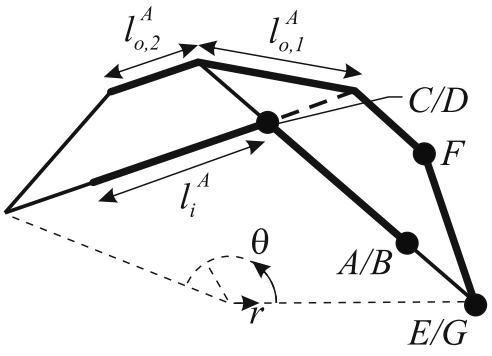


(c) Face lengths

Figure 4.16: Arc folded sandwich structure.

### 4.3.5 Piecewise Core

Piecewise folded sandwich structures can be created for the piecewise core patterns developed in Section 4.2. There are two methods with which compatible, continuous sandwich faces can be attached to piecewise core structures. The first method entails using the slave piecewise pattern parameters to design a panel with constant depth across all joined core segments. This allows the sandwich faces to be attached as designed above without the need for alterations. For example the Miura/Arc-Miura/Miura sandwich assembly shown in Figure 4.17 was designed such that the inner and outer radii of the Arc-Miura geometry met tangentially

with the top and bottom surfaces of the Miura geometry.

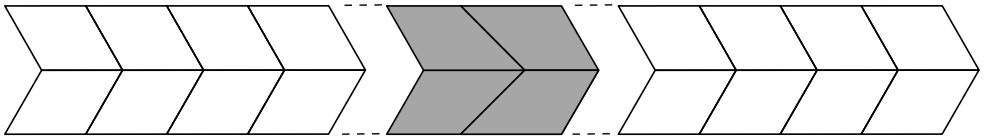

(a) Unfolded core patterns

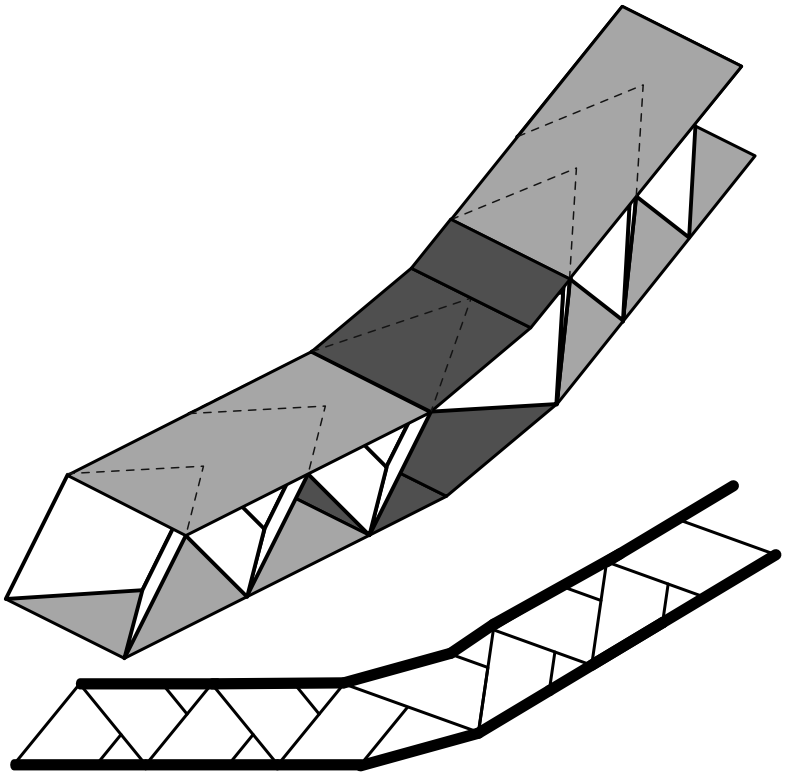

(b) Perspective and side view

Figure 4.17: Piecewise folded sandwich structure designed with constant panel depth across connected segments.

In certain instances it is impossible to design piecewise core geometry that possesses a constant panel depth. In these instances, faceted sandwich panel faces can be extended or trimmed as needed to form a continuous surface. For example, Figure 4.18 shows an Arc-Miura/Arc/Arc-Miura piecewise core geometry which has a varying panel depth. To form a continuous inner surface, small face plates are extended from the Arc-Miura geometry to meet with trimmed face plates on the Arc geometry.

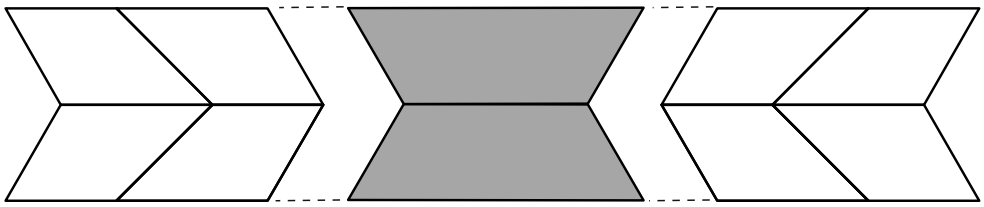

(a) Unfolded core patterns

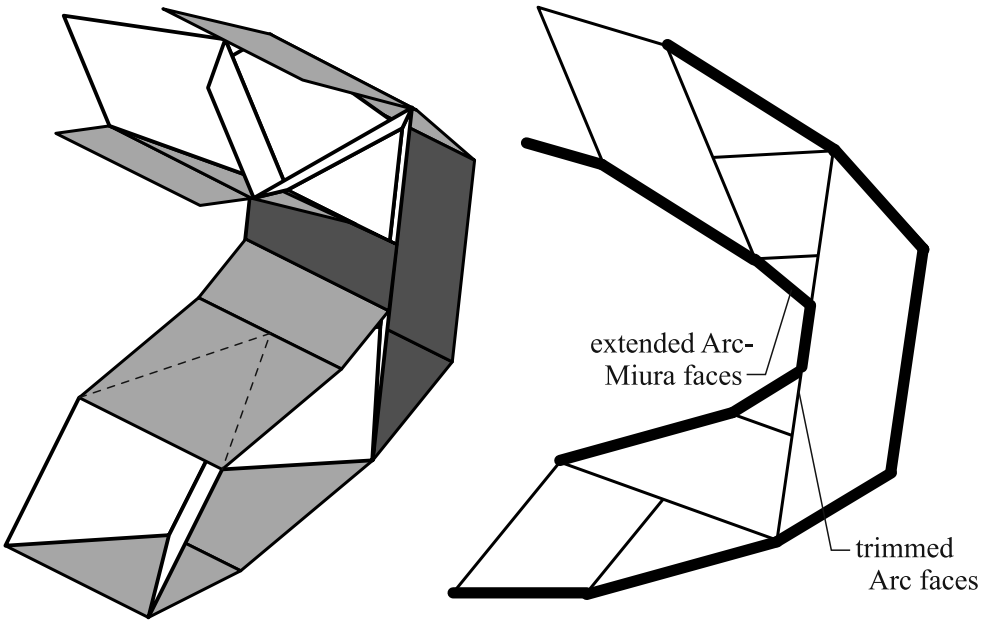


(b) Perspective and side view

Figure 4.18: Piecewise folded sandwich structure designed with varying panel depth across connected segments.

## 4.4 Curved-Crease Miura Pattern

A common method for creating curved-crease origami geometry is to invert sections of known developable surface, such as a cylinder or cone (Demaine *et al.*, 2011b). This is a relatively inefficient way to generate curved-crease geometry, as it requires defining a developable surface and an intersecting cutting plane, and then calculating the elliptical curve that occurs at the intersection of the two.

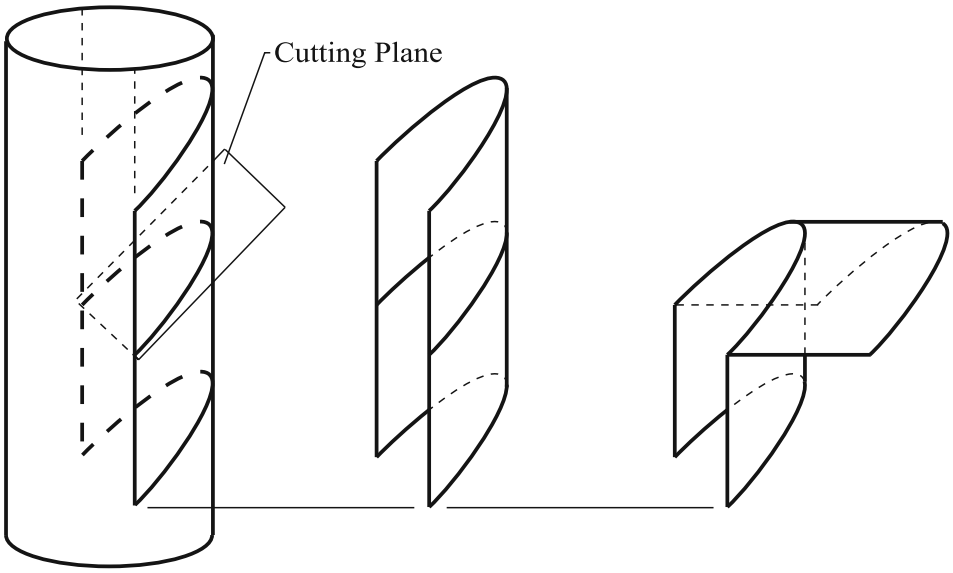


Figure 4.19: Curved-crease surface created from the inversion of a developable cylindrical surface.

By reversing this process, that is to say by first defining an elliptical surface and then projecting this ellipse along reflected axes, a much simpler method to generate curved-crease geometry is obtained. Furthermore, by fitting this ellipse through a known rigid origami pattern, specifically a Miura-derivative pattern, geometric solutions for projected axes direction, unit volume, pattern closure, and folded sandwich faces can be reused. Once this elliptical surface is obtained it can be sub-divided into prismatic rigid origami slices by enforcing a common edge angle at slice interfaces. This forms a PQ mesh, as discussed Section 2.2, and is also an embodiment of the piecewise geometries discussed in Section 4.2. It therefore allows simple simulation of pattern folded motion. Reducing the curved-crease

geometry to an assembly of planar rigid origami plates also removes the need to consider local curvature of the projected elliptical surface. These two stages, deemed the *ellipse creation* and *rigid subdivision* stages respectively, can be used together to create parametrisations for rigid-foldable curved-crease geometry.

### 4.4.1 Ellipse Creation

An elliptical curve is defined through three sequential zigzag points in a prismatic Miura base pattern, Figure 4.20(a). Equivalent ellipses can be defined through zigzag creases to either side of the initial ellipse, and a curved surface projected between them. This projection is along the longitudinal folded axes of the base pattern, Figure 4.20(b). This process successfully creates a developable, curved-crease surface for two reasons: any specified elliptical curve will form the intersection of some cutting plane and a developable surface, and the folded axes of a prismatic origami pattern form a reflection in the plane in which the zigzag nodes lie. The surface developed in this way is deemed a Curved-Crease Miura pattern. Henceforth the designation Curved-Crease will be shortened to CC.

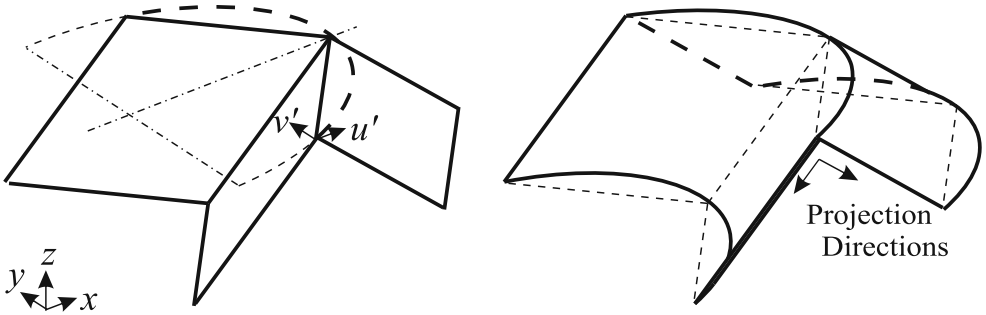


(a) Elliptical curve through three points (b) Projection along longitudinal axes

Figure 4.20: Curved crease geometry creation on a rigid prismatic base pattern.

The process for determining the ellipse in a CC-Miura pattern is as follows. The $u^j - v^j$ plane is defined as coplanar with three $j^{th}$ zigzag nodes. The $j^{th}$ ellipse

$(u^j, v^j)$ can be generally defined in this plane as:

$$\frac{(u^j - g)^2}{c^2} + \frac{(v^j - h)^2}{d^2} = 1 \tag{4.45}$$

where $c, d, g$, and $h$ are ellipse coefficients. As all $j^{th}$ zigzags on a prismatic Miura pattern are identical, the ellipse through a singular zigzag need only be solved, and the so the superscript $j$ is replaced with $'$.

The three known zigzag points do not provide enough information to find the four ellipse coefficients and a unique ellipse, rather they specify a family of possible elliptical curves. One additional parameter must be specified to determine a unique ellipse. This is defined as the gradient parameter $\varphi$, which is the the initial gradient of the elliptical curve in the $u' - v'$ plane, Figure 4.21(a). By defining $\varphi$ in addition to the base pattern geometry, a unique ellipse can be found from the following equations:

$$h = B/2 \tag{4.46}$$

$$g = \frac{2C^2}{[4C - B\tan\varphi]} \tag{4.47}$$

$$c = C - g \tag{4.48}$$

$$d = B/2\sqrt{1/(1 - \frac{g^2}{c^2})} \tag{4.49}$$

where $$B = 2b\sin(\eta_Z/2) \text{ and } C = b\cos(\eta_Z/2) \tag{4.50}$$

Gradient parameter $\varphi$ is limited to minimum and maximum bounds, $\varphi_{min}$ and $\varphi_{max}$. The lower and upper limits of $\varphi$ correspond to minimum and maximum values of coefficient $g$, at $g = -\infty$ and $g = 0$ respectively, Figure 4.21(b). Substituting these values of $g$ into Equation (4.47) allows the bounds to be determined as a function of the prismatic base pattern geometry as follows:

$$\varphi_{min} = 4C/B, \text{ when } g \to -\infty \text{ and} \tag{4.51}$$

$$\varphi_{max} = \pi/2, \text{ when } g = 0 \tag{4.52}$$

Note that an ellipse with gradient $\varphi = \varphi_{min}$ at $g \to -\infty$ is equivalent to a

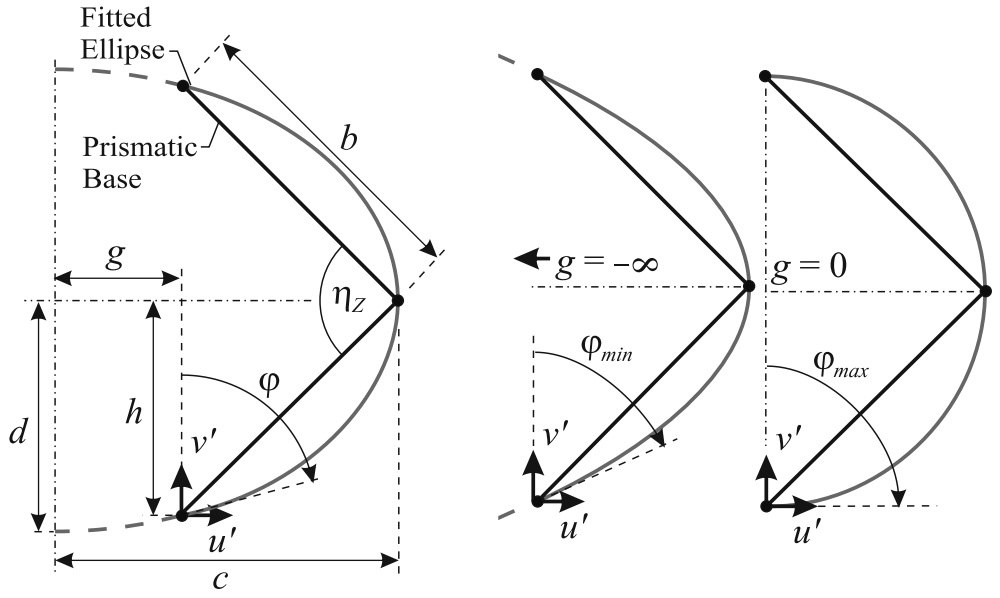


(a) Base and ellipse geometric parameters (b) Lower and upper bounds of $\varphi$

Figure 4.21: Ellipse fitted through three zigzag points.

parabola through the three original zigzag points. For geometry creation purposes it is often more convenient to express Equation (4.45) as a parametric function of $t$, where $(-t_{lim} \leqslant t \leqslant t_{lim})$:

$$u' = g + c\cos t \tag{4.53}$$

$$v' = h + d\sin t \tag{4.54}$$

$$t_{lim} = \arctan\frac{cB}{2dg} \tag{4.55}$$

It is possible to unroll the elliptical curve of the initial projected curved surface in order to obtain a crease pattern. This is achieved in two steps. First, the original ellipse is projected along the axes of each fold direction, Figure 4.22(a), to obtain a new ellipse in the $u'_2 - v'_2$ plane that represents the perpendicular section of the developable surface:

$$u'_2 = u'\frac{\cos(\eta_A/2)}{\sin(\eta_A)} \tag{4.56}$$

$$v'_2 = v' \tag{4.57}$$

Second, the projected ellipse is unrolled onto the $u'_3 - v'_3$ plane to obtain the final crease pattern, Figure 4.22(b). The equation to find the length $s(t)$ of an elliptical

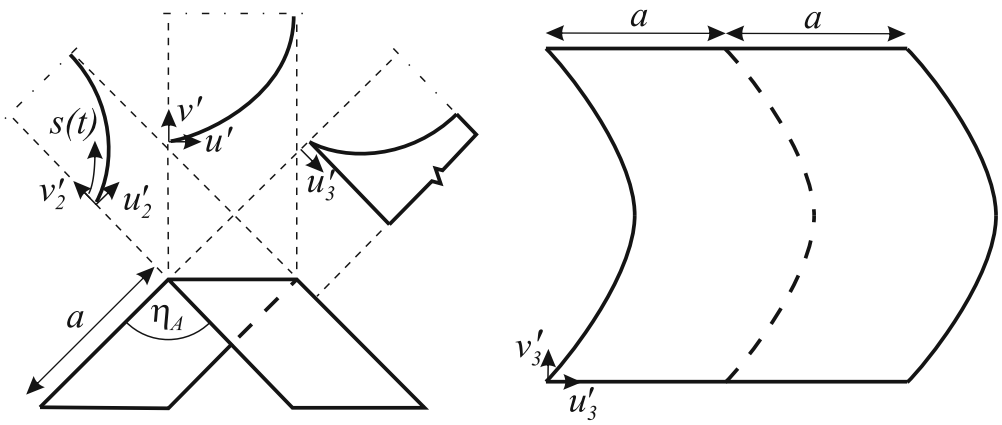


(a) Perpendicular projected ellipse (b) Unrolled pattern

Figure 4.22: Crease pattern unrolled from a folded configuration.

arc is inexact and must be integrated by parts:

$$u'_3 = u'_2 \tag{4.58}$$

$$v'_3 = s(t) \tag{4.59}$$

To summarise, the Miura pattern requires six independent parameters to define $a, b, \phi, m$, and $n$, plus any configuration variable. Using the above equations any CC-Miura configuration can therefore be found by specifying seven parameters: $a, b, \phi, m, n$, a configuration variable, and the gradient parameter $\varphi$, where $\varphi_{min} < \varphi < \varphi_{max}$.

### 4.4.2 Rigid Subdivision

The projected elliptical surface creates a developable surface, however it does not consider any bending within the structure, nor does it allow the folding motion of the surface to be easily found. As discussed in the literature review, approximating a surface as a PQ mesh is can overcome these problems. Here, a PQ mesh is created by subdividing the elliptical surface into rigid origami strips connected along common longitudinal edges. It is demonstrated next for a CC-Miura pattern.

The curved-crease pattern is split into $S$ strips for every row of panels in the prismatic base pattern, where $S$ is termed the division number. The pattern now possesses a total of $s$ longitudinal crease lines where $s = S(m-1)+1$. Specifying $S = 1$ creates a geometry corresponding to the prismatic base pattern. A higher $S$ gives a closer approximation of the curved surface, Figure 4.23. Unless otherwise stated, all CC-patterns in this chapter have $S = 4$.

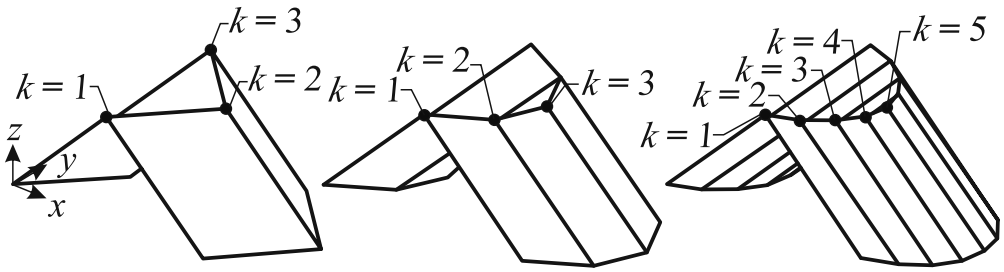


Figure 4.23: Curved crease pattern divided into $S = 1, 2$, and 4 divisions.

The spacing distribution between split crease lines can be chosen as desired. In the simplest case, the lines can be set to be equidistant in the $y$ direction. However this thesis shall adopt a slightly more complex spacing scheme in which crease lines split the elliptical curve into regular $t_{lim}/S$ angular divisions of the parameter $t$, Figure 4.24(a). This was seen to give a more regular approximation of the original elliptical surface than a laterally equidistant division scheme.

Vertices $W^{k,j}$ are calculated at the intersection of the $k^{th}$ divided longitudinal crease lines and the $j^{th}$ zigzag crease ($k = 1, 2, ..., s,\ j = 1, 2, ..., n$). Note that the $k$, $s$, and $W^{k,j}$ terms have replaced the $i$, $m$, and $V^{i,j}$ terms used to define prismatic pattern vertices. In a 3D Cartesian coordinate system with origin and orientation shown in Figure 4.23(a), the coordinate vector $(x^{k,j}, y^{k,j}, z^{k,j})$ of $W^{k,j}$ can be given as:

$$x^{k,j} = (j-1)a\sin(\eta_{A,set}/2) + u'(t^k) \tag{4.60}$$

$$y^{k,j} = (k-k'-1)\frac{b\sin(\eta_{Z,set}/2)}{S} + v'(t^k) \tag{4.61}$$

$$z^{k,j} = \begin{cases} 0 & \text{for odd } j \\ a\cos(\eta_{A,set}/2) & \text{for even } j \end{cases} \tag{4.62}$$

where $u'(t^k)$ and $v'(t^k)$ are coordinates of the subdivided elliptical curve obtained by substituting $t^k = t_{lim}(k'/S - 1)$ into Equations (4.53–54). Note that the sub-designation $k' = \text{mod}(k - 1, 2S)$ is used where it gives a more concise parametrisation and the subscript *set* denotes a pattern variable obtained from prismatic base geometry at the folded configuration used to set the CC-Miura pattern.

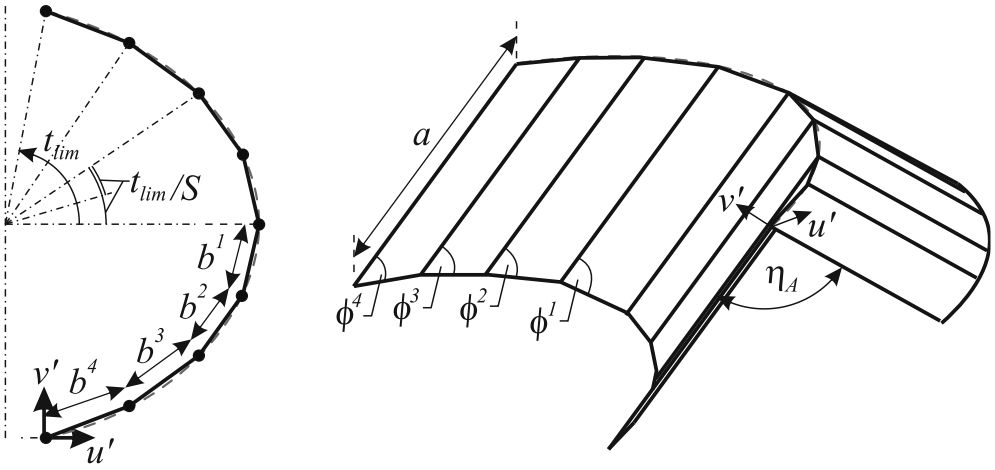


(a) Straight-line segments between subdivided points

(b) $K$ rigid strips

Figure 4.24: Projected curved surface split into rigid strips.

Closer inspection of the subdivided CC-Miura geometry shows that it forms a planar quadrangle mesh which is equivalent to a piecewise assembly of $K$ Miura pattern strips ($K = 1, 2, ..., s - 1$), where the $K^{th}$ strip is bounded by the $k$ and $k + 1$ longitudinal crease lines, and the $j = 1$ and $j = n$ zigzag crease lines. The folding motion of this piecewise assembly can be simulated once the six parameters of each Miura strip are known.

Fortunately, these parameters can be simply derived. Each Miura strip is one-plate wide, that is to say has $m^K = 2$, and possesses the same number of panels in the longitudinal direction as the prismatic base pattern, $n^K = n$. Here, the superscript $K$ denotes a parameter for the $K^{th}$ rigid strip, and non-superscripted parameters denote a parameter from the prismatic base geometry. All strips share

two additional parameters with the prismatic base pattern: longitudinal edge angle $\eta_A^K = \eta_A$ and side length $a^K = a$, Figure 4.24(b). The remaining two parameters for each segment, lateral sector angle $\phi^K$ and side length $b^K$ can be calculated from the vertex coordinates with the following equations:

$$b^K = \|W^{k+1,1} - W^{k,1}\| = \sqrt{(x^{k+1,1} - x^{k,1})^2 + (y^{k+1,1} - y^{k,1})^2} \tag{4.63}$$

$$\phi^K = \angle W^{k,1}W^{k+1,1}W^{k+1,2} = \arccos \frac{(a^K)^2 + (b^K)^2 - \|W^{k,1} - W^{k+1,2}\|^2}{2a^K b^K} \tag{4.64}$$

Expressions for the length between two vertices and the angle between three vertices will be used for other curved-crease pattern development and so it is convenient to define them in general terms:

$$\|W^{k,j} - W^{s,t}\| = \sqrt{(x^{k,j} - x^{s,t})^2 + (y^{k,j} - y^{s,t})^2 + (z^{k,j} - z^{s,t})^2} \tag{4.65}$$

$$\angle W^{k,j}W^{s,t}W^{q,r} = \arccos \frac{F^2 + G^2 - H^2}{2FG} \tag{4.66}$$

where $F = \|W^{k,j} - W^{s,t}\|$, $G = \|W^{s,t} - W^{q,r}\|$, and $H = \|W^{k,j} - W^{q,r}\|$. If convenient, terms in these expressions will be substituted for named rigid strip parameters, as was done for Equations (4.63–64).

Once $m^K$, $n^K$, $a^K$, $b^K$, and $\phi^K$ are known, the folding motion of each rigid strip can be easily found by defining pattern variable $\eta_A^K$ between upper and lower bounds $\eta_{A,max}^K$ and $\eta_{A,min}^K$. The upper bound simply occurs when the pattern is completely flat, $\eta_{A,max}^K = \pi$. The lower bound corresponds to the maximum compressible configuration of the curved-crease model, which is calculated by assuming that this state occurs when the outermost rigid strip is folded completely flat, which is to say when $\eta_Z^1 = 0$, Figure 4.25. From Equation (2.3) this occurs at:

$$\cos \eta_{A,min}^K = \sin^2 \phi^1 - \cos^2 \phi^1 \tag{4.67}$$

It is believed that this is the first analytical prediction for the maximum compressibility of curved-crease origami patterns. A comparison between the unfolded rigid strip assembly and the unrolled projected ellipse $(u_3', v_3')$ given by Equations (4.58–59) is shown in Figure 4.25(b), with good agreement seen.

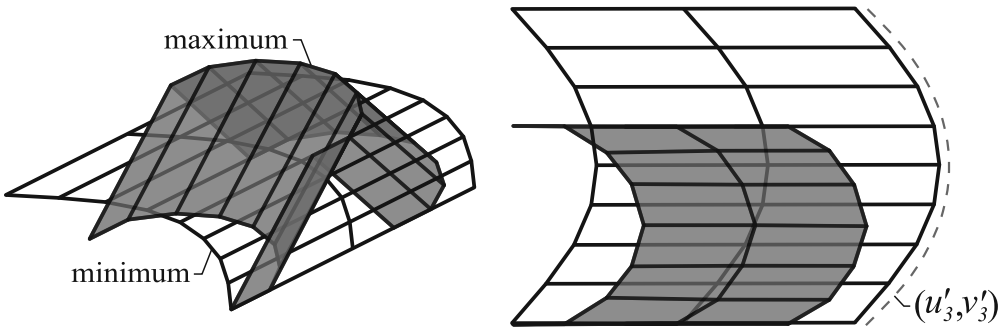


(a) Isometric view (b) Top view

Figure 4.25: Maximum and minimum limits of curved-crease foldability.

A comparison between the folding motion of the simulated geometry and the aluminium prototype, set at dimensions $a = 60$mm, $b = 60$mm, $\phi = \pi/3$, $\eta_z = \pi/2$, $m = 3$, $n = 3$, and $\varphi = \varphi_{min}$, also shows good agreement, Figure 4.26.

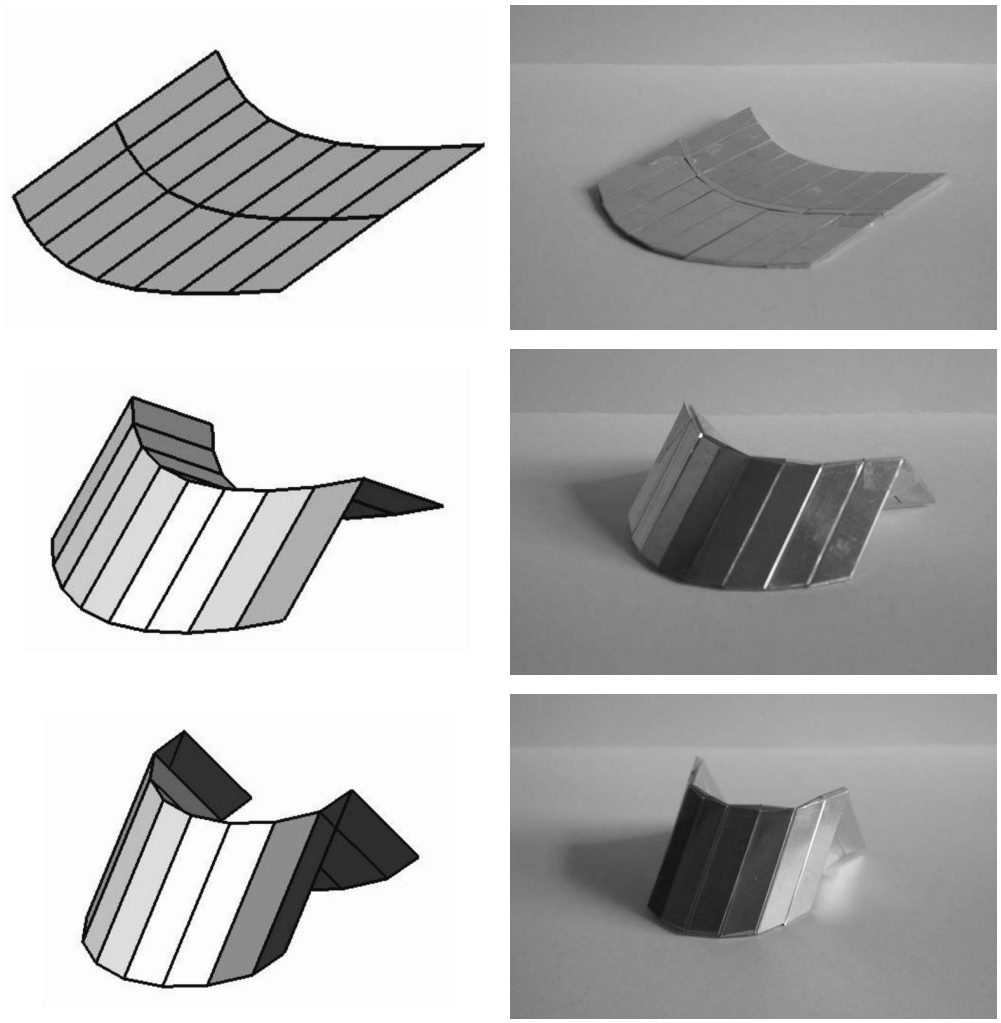

Figure 4.26: Comparison of folding motion of simulated (left) and aluminium prototype (right) CC-Miura pattern.

The PQ mesh created by the rigid subdivision is an embodiment of the piecewise geometries discussed previously and provides two major benefits: there is no need to consider local surface bending effects as the rigid strips can be assumed to remain planar during folding, and the assembly of rigid strips possesses a single degree-of-freedom kinematic mechanism that allows the folding motion of the pattern to be simply calculated.

### 4.4.3 Tessellations

As a final comment on the creation of the CC-Miura pattern, it should be noted that many different curves can be defined through three nodes on a prismatic base pattern, beyond the simple elliptical curve discussed above. More complex conic curves can be derived by fitting partial elliptical curves through half-units of the base prismatic geometry, and can still be completely defined with the single gradient parameter $\varphi$. Different curves defined with the same gradient on the same prismatic base are termed *tessellations*.

Tessellation 1 is defined as the geometry obtained by fitting the basic ellipse through sequential zigzags in the manner described above, Figure 4.27(a). Tessellation 2 is defined as the geometry obtained by fitting an ellipse and a reversed ellipse through sequential zigzags, and so corresponds to commonly seen curved-crease patterns which possess a continuous curve, Figure 4.27(b). Note that the shown Tessellation 2 pattern has a doubled number of divisor lines, $S = 8$, to better approximate the continuous curve.

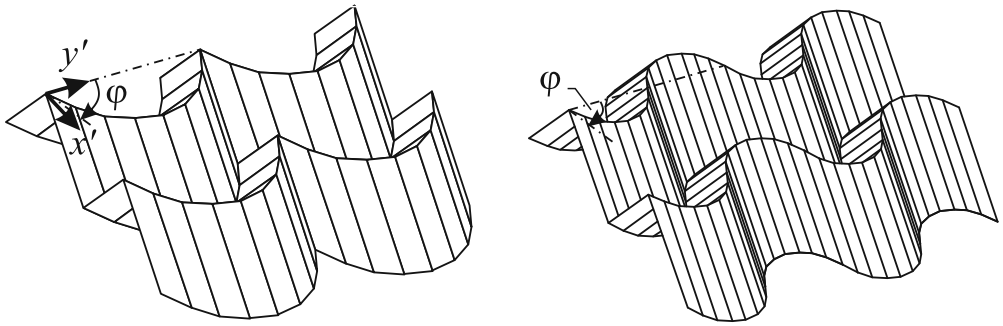


(a) Tessellation 1 (b) Tessellation 2

Figure 4.27: Two tessellations of the CC-Miura pattern unit geometry.

These alternate tessellations can be realised by pointing the $u'(t^k)$ and $v'(t^k)$ terms in Equations (4.60–61) to a different parametric curve. For example, Tessellation 2 is generated with new expressions:

$$u'(t^k) = \begin{cases} (g + c\cos(2t^k + t_{lim}))/2 & \text{for } 0 < k' \leq S+1 \\ (g + c\cos(2t^k - t_{lim}))/2 & \text{for } S+1 < k' < 2S \end{cases} \tag{4.68}$$

$$v'(t^k) = \begin{cases} (h + d\sin(2t^k + t_{lim}))/2 & \text{for } 0 < k' \leq S+1 \\ (h + d\sin(2t^k - t_{lim}))/2 & \text{for } S+1 < k' < 2S \end{cases} \tag{4.69}$$

Many other tessellations can be formed in this manner, however they are less obviously suitable for foldcore design and so are not otherwise considered in this thesis.

## 4.5 Extension to General Rigid Origami

### 4.5.1 Curved-Crease Tapered Miura Pattern

As the name suggests, the Curved-Crease Tapered Miura pattern is created by applying the ellipse creation and rigid subdivision stages to a prismatic Tapered Miura base pattern. Where the CC-Miura pattern can be conceptually thought of as the developable surface created from the inversion of a cylindrical surface, the CC-Tapered Miura pattern can be thought of as a developable surface created from the the inversion of a conical surface, Figure 4.28.

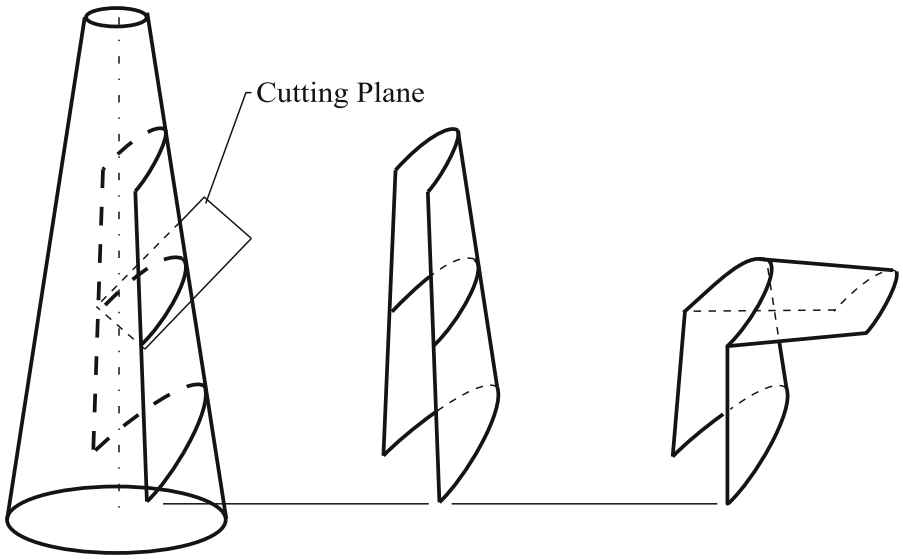


Figure 4.28: Curved-crease geometry from the inversion of a conical surface.

#### Ellipse Creation

Ellipses fitted through zigzag creases on a prismatic Tapered Miura base are shown in Figure 4.29(a). It can be seen that unlike the CC-Miura pattern, sequential ellipses expand to fit the base geometry, causing a conical surface to be projected.

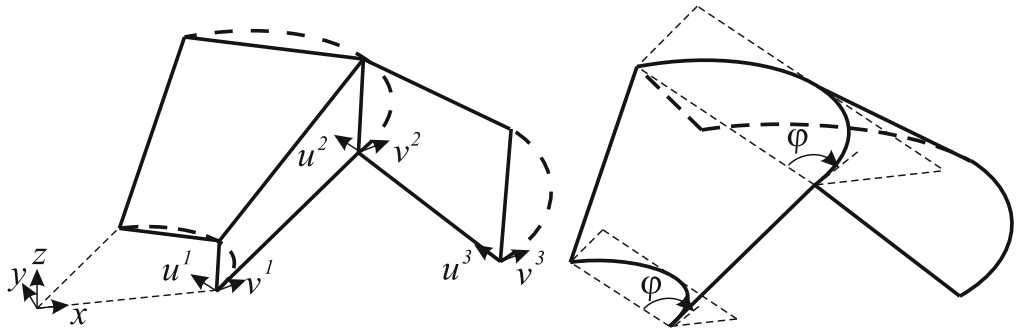


(a) Elliptical curves through zigzag creases (b) Projected surface

Figure 4.29: Curved crease geometry creation.

From Equation (4.19), it is known that the side length of sequential zigzags $b_j$ scales linearly for each $j^{th}$ zigzag crease line. Therefore in the simplest embodiment, each ellipse is assumed to have the same gradient parameter $\varphi$, Figure 4.29(b), and elliptical coefficients for the $j^{th}$ ellipse, Figure 4.29(a), are obtained by substituting the $b_j$ for $b$ in Equations (4.46–50). The coefficients are given superscripts $k^j, b^j, d^j$, and $c^j$ and substituted into Equations (4.53–54) to give the $j^{th}$ elliptical curve ($u^j$,$v^j$) as a parametric function of $t$:

$$u^j = g^j + c^j \cos t \tag{4.70}$$

$$v^j = h^j + d^j \sin t \tag{4.71}$$

where $-t_{lim} \leqslant t \leqslant t_{lim}$. As the straight crease lines in the CC-Tapered Miura pattern are not parallel, the limits for the gradient parameter $\varphi$ differ to that for the CC-Miura pattern. The lower bound $\varphi_{min}$ remains unchanged from Equation (4.51), but the upper bound is changed to $\varphi_{max} = \pi/2 + \bar{\rho}$ , recalling that $\bar{\rho}$ is the angular rotation of the folded primatic base geometry. Note that this is for the case where an ellipse is defined through the three nodes of the zigzag crease in a close-far-close vertice sequence, as shown in Figure 4.29. It is also possible to define an ellipse in a far-close-far vertice sequence. In this instance the upper limit of the gradient parameter is $\varphi_{max} = \pi/2 - \bar{\rho}$.

### Rigid Subdivision

The CC-Tapered Miura can subdivided into rigid strips in the same manner as the CC-Miura pattern, except with radial rather than parallel divisor lines. Vertices $W^{k,j}$ are calculated at the intersection of the $k^{th}$ divided radial crease lines and the $j^{th}$ zigzag crease ($k = 1, 2, ..., s,\ j = 1, 2, ..., n$). If a 3D Cartesian coordinate system with origin and orientation shown in Figure 4.29(a) is used, the coordinate vector $(x^{k,j}, y^{k,j}, z^{k,j})$ of $W^{k,j}$ can be given as:

$$x^{k,j} = R_{c,j} \cos\theta + u^{k,j}(t^k) \tag{4.72}$$

$$y^{k,j} = R_{c,j} \sin\theta + v^{k,j}(t^k) \tag{4.73}$$

$$z^{k,j} = \begin{cases} 0 & \text{for odd } j \\ a_c \cos(\eta_{cA}/2) & \text{for even } j \end{cases} \tag{4.74}$$

where $R_{c,j}$ is given by Equation (4.27), $\theta = (k - k' - 1)\bar{\rho}_{set}/S$, and rotated elliptical coordinates $(u^{k,j}, v^{k,j})$ are obtained by rotating the $(u^j, v^j)$ ellipse to match the orientation of the corresponding three-node zigzag on the base pattern:

$$\begin{bmatrix} u^{k,j}(t^k) \\ v^{k,j}(t^k) \end{bmatrix} = \begin{bmatrix} \cos(\theta + \bar{\rho}_{set}) & -\sin(\theta + \bar{\rho}_{set}) \\ \sin(\theta + \bar{\rho}_{set}) & \cos(\theta + \bar{\rho}_{set}) \end{bmatrix} \begin{bmatrix} u^j(t^k) \\ v^j(t^k) \end{bmatrix} \tag{4.75}$$

As before, $t^k = t_{lim}(k'/S - 1)$ and $k' = \text{mod}(k - 1, 2S)$. Note that a 3D Cartesian system was used, rather than the cylindrical coordinate system used previously for the Tapered Miura pattern, as it is simpler to incorporate the rotated $u^{k,j}$ and $v^{k,j}$ terms.

Inspection of subdivided CC-Tapered Miura PQ mesh shows that it is equivalent to a piecewise assembly of prismatic Tapered Miura rigid strips. As was done for the CC-Miura pattern, solving parameters for $K$ rigid strips ($K = 1, 2, ..., s - 1$) will allow the folded motion of the entire assembly to be simulated. Each rigid strip requires seven parameters to completely determine. The number of panels in

each strips are known and so parameters $m^K = 2$ and $n^K = n$ can be eliminated. Two parameters for the first strip are equivalent to the base prismatic geometry, side length $a_c^1 = a_c$, and longitudinal edge angle $\eta_{cA}^1 = \eta_{cA}$. These two parameters can be removed in the remaining strips by equating shared crease parameters, $a_c^{K+1} = a_f^K$ and $\eta_{cA}^{K+1} = \eta_{fA}^K$, Figure 4.30.

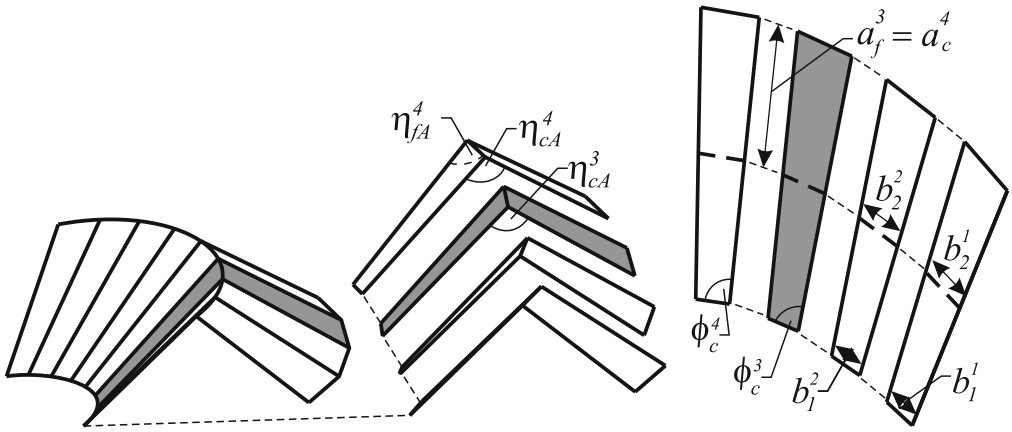


(a) Radial divisor lines and exploded rigid strips (b) Crease pattern

Figure 4.30: Rigid subdivision of CC-Tapered Miura pattern.

The three remaining constant parameters can calculated directly from pattern vertex coordinates. The simplest three independent parameters to calculate are $b_1^K$, $b_2^K$, and $\phi_c^K$. Two of these, $b_1^K$ and $\phi_c^K$, are given by Equations (4.63–64), substituting $b_1^K$ for $b^K$, $a_c^K$ for $a^K$, and $\phi_c^K$ for $\phi^K$. The final parameter is found by substituting appropriate vertices into Equation (4.65) to give the following expression:

$$b_2^K = \|W^{k+1,2} - W^{k,2}\| = \sqrt{(x^{k+1,2} - x^{k,2})^2 + (y^{k+1,2} - y^{k,2})^2} \tag{4.76}$$

To summarise, eight parameters are required to completely determine the rigid strip assembly in a CC-Tapered Miura pattern: seven for the base prismatic pattern and one additional gradient parameter. The folding motion of the rigid strip assembly can then be found by adjusting a variable parameter in the piecewise assembly, most directly with $\eta_{cA}^1$. Folding motion simulated in this manner is shown in Figure 4.31 and good correlation is seen with a comparative physical prototype.

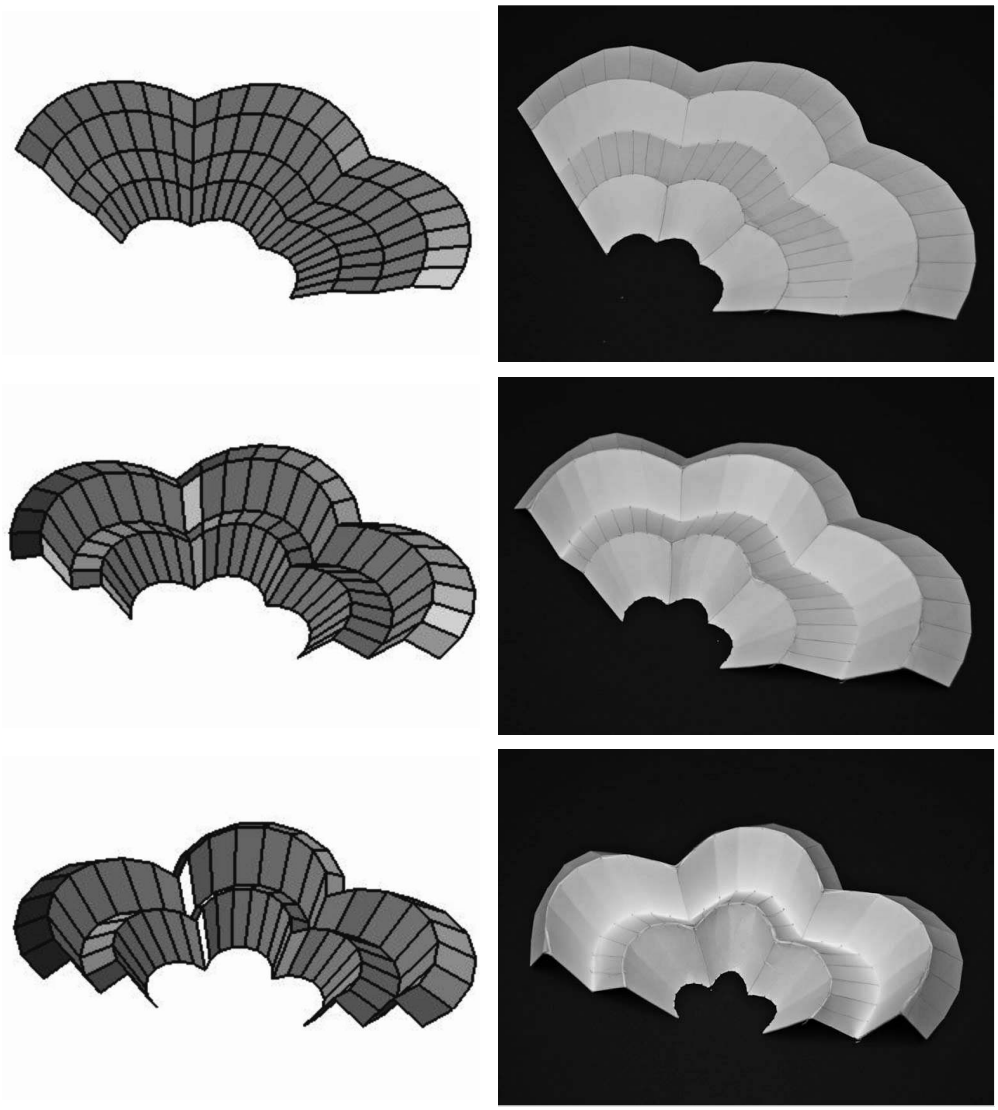

Figure 4.31: Comparison of folding motion of simulated (left) and prototype (right) CC-Tapered Miura pattern.

### 4.5.2 Curved-Crease Arc Pattern

The Curved-Crease Arc pattern is created by applying the ellipse creation and rigid subdivision steps to a prismatic Arc base pattern. Similar to the CC-Miura pattern, it can conceptually be thought of as a developable surface created by inverting the portion of cylinder intersected by cutting planes, although in the case of the CC-Arc pattern alternate cutting planes are reversed, Figure 4.32.

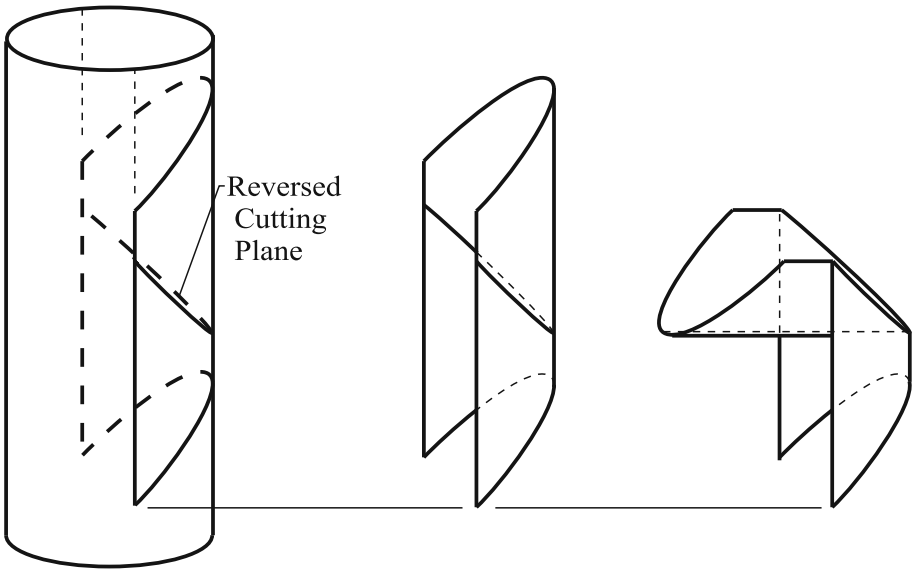


Figure 4.32: Alternate reversed cutting planes and inversion of cylindrical surface.

**Ellipse Creation**

Zigzag lines on an Arc pattern have identical side lengths, but an alternately reversed orientation. Therefore elliptical curves on a CC-Arc pattern have identical ellipse parameters for every $j^{th}$ zigzag, with alternate ellipses reversed. Defining the $j^{th}$ elliptical axis orientation $(u^j, v^j)$ as shown in Figure 4.33 allows elliptical parameters be found with Equations (4.46–49) and the elliptical curve to be plotted with Equations (4.53–54). As all ellipses are identical, the superscript $j$ is again replaced with $'$. Permissible bounds for $\varphi$ remain unchanged from that used for the CC-Miura geometry.

**Rigid Subdivision**

The projected cylindrical surface is subdivided into planar strips to generate the CC-Arc pattern. Vertices $W^{k,j}$ are calculated at the $k^{th}$ divisor lines and the $j^{th}$ zigzag crease ($k = 1, 2, ..., s,\ j = 1, 2, ..., n$). In a 3D Cartesian coordinate system with orientation as shown in Figure 4.34(a), the coordinate vector $(x^{k,j}, y^{k,j}, z^{k,j})$

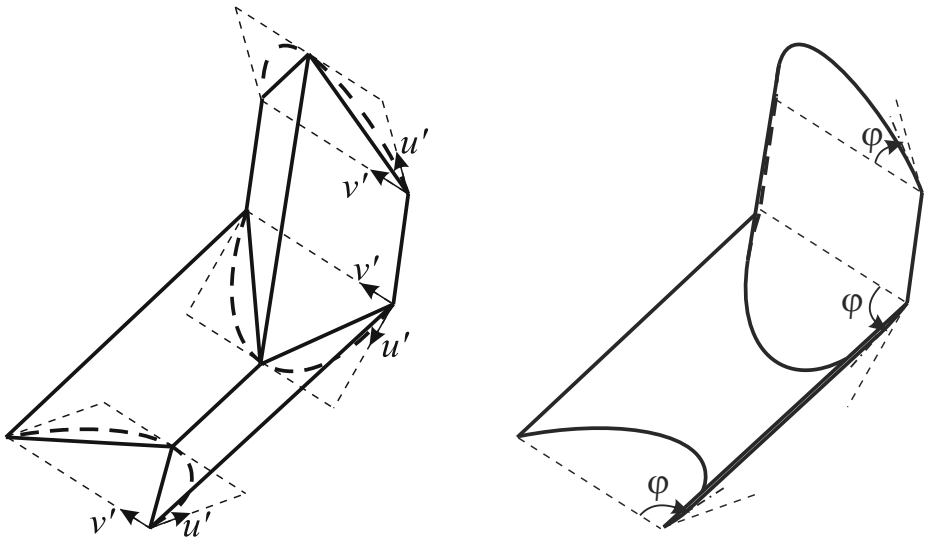


(a) Elliptical curve through three points (b) Projected curved surface

Figure 4.33: Curved-Crease Arc geometry creation.

of $W^{k,j}$ is:

$$x^{k,j} = R\cos\theta + u^{k,j}(t^k) \tag{4.77}$$

$$y^{k,j} = (k - k' - 1)\frac{b\sin(\eta_{Z,set}/2)}{S} + v^{k,j}(t^k) \tag{4.78}$$

$$z^{k,j} = R\sin\theta + w^{k,j}(t^k) \tag{4.79}$$

where $R$ is given by Equation (2.14), $\theta$ is given by odd $i$ values in Equation (2.16), and rotated elliptical coordinates $(u^{k,j}, v^{k,j}, w^{k,j})$ are obtained by rotating the $(u', v')$ ellipse to match the orientation of the corresponding three-node zigzag on the base pattern:

$$\begin{bmatrix} u^{k,j}(t^k) \\ v^{k,j}(t^k) \\ w^{k,j}(t^k) \end{bmatrix} = \begin{bmatrix} \cos(\theta + \theta^j) & 0 \\ 0 & 1 \\ \sin(\theta + \theta^j) & 0 \end{bmatrix} \begin{bmatrix} u'(t^k) \\ v'(t^k) \end{bmatrix} \tag{4.80}$$

where $\theta^j$ is the rotation of the corresponding three-node zigzag, given by:

$$\theta^j = \begin{cases} (\pi + \xi_1 + \xi_2)/2 & \text{for odd } j \\ -(\pi + \xi_1 + \xi_2)/2 & \text{for even } j \end{cases} \tag{4.81}$$

Again, a 3D Cartesian system was used, rather than a cylindrical coordinate system, as it is simpler to incorporate the rotated $u^{k,j}$,$v^{k,j}$ and $w^{k,j}$ terms.

The subdivided CC-Arc pattern gives a PQ mesh composed of prismatic Arc panels. Unlike previous CC-patterns, different rigid parameters must be formulated for each panel, rather than each strip. Therefore the PQ mesh is equivalent to a prismatic assembly of $K$ by $J$ Arc panels ($K = 1, 2, ..., s-1,\ J = 1, 2, ..., n-1$) where the ($K^{th}$,$J^{th}$) panel is bounded by the $k$ and $k+1$ longitudinal crease lines and the $j$ and $j+1$ zigzag crease lines, Figure 4.34.

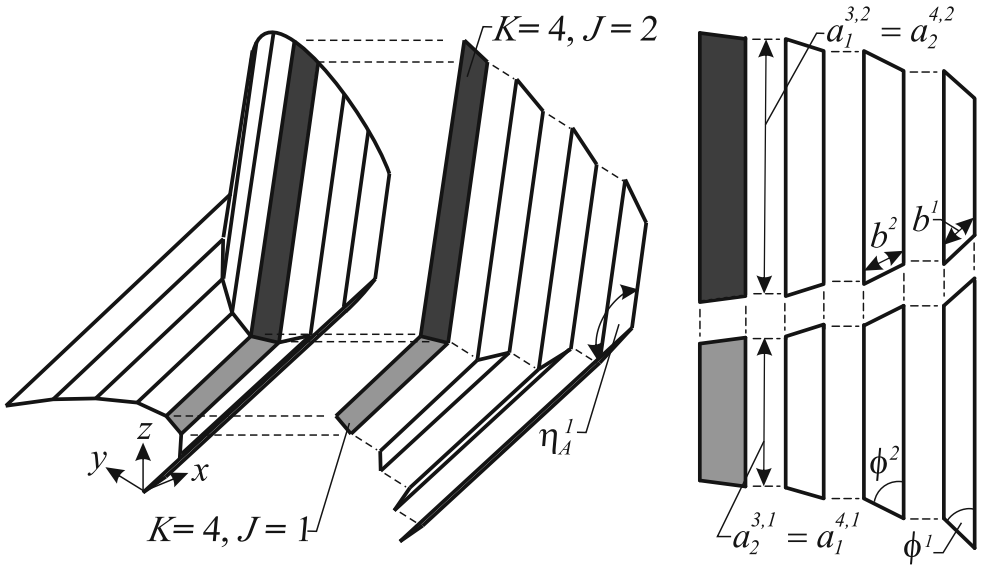


(a) Divisor lines and exploded rigid panels (b) Crease pattern

Figure 4.34: Rigid subdivision of CC-Arc pattern.

To simulate the pattern folding motion, the six parameters of every Arc panel must be defined. The two panel size parameters can be eliminated, $m^{K,J} = m^K = 2$ and $n^K = 2$, and the longitudinal edge angle is constant across all panels and equal to the base prismatic pattern, $\eta_A^K = \eta_A$. Note that the superscript $^{K,J}$ denotes a parameter for the ($K^{th}$,$J^{th}$) panel, however only the superscript $^K$ is used when all $J$ panels possess the same parameter. Parameters for the first strip correspond to the prismatic base geometry: $a_1^{K,J} = a_1$ for odd $J$ and $a_2^{K,J} = a_2$ for even $J$. Parameters in remaining panels can be related across shared edges with $a_1^{K+1,J} = a_2^{K,J}$ for odd $J$ and $a_1^{K+1,J} = a_1^{K,J}$ for even $J$. Two final, parameters, $b^K$ and $\phi^K$, are identical for all $J$ can be found by substituting $a_1^K$ for $a^K$ in Equations (4.63–64). The CC-Arc pattern can therefore be completely determined from seven parameters: six for the prismatic geometry and an additional ellipse gradient parameter.

There is seen to be good correlation between the simulated folding motion of a piecewise CC-Arc assembly and a comparative prototype, Figure 4.35.

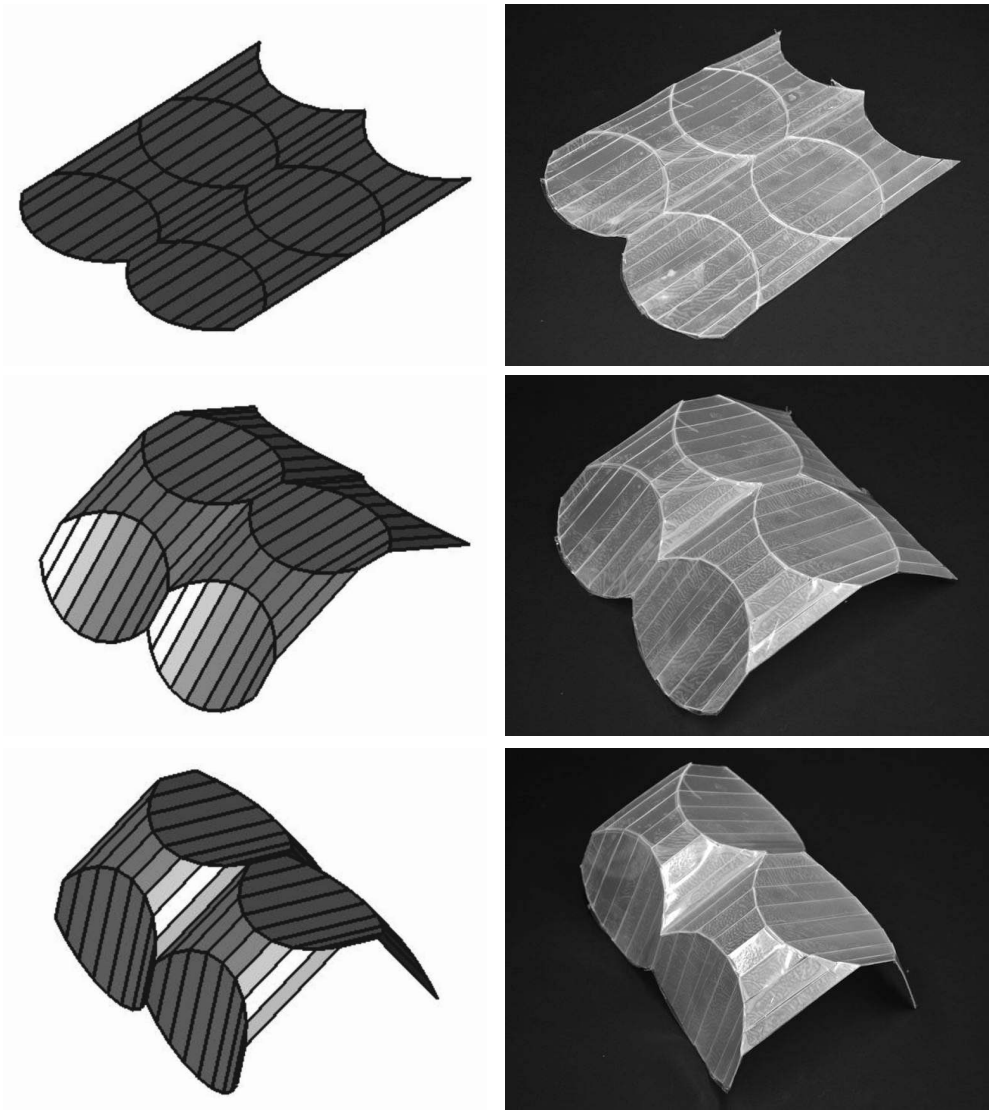

Figure 4.35: Comparison of folding motion of simulated (left) and plastic prototype (right) CC-Arc pattern.

### 4.5.3 Curved-Crease Arc-Miura Pattern

The Curved-Crease Arc-Miura pattern is created by applying the ellipse creation and rigid subdivision process to a prismatic Arc-Miura base pattern. As was seen for previous patterns, it can conceptually be thought of as a developable surface created by inverting the portion of a cylinder intersected by cutting planes, although in the case of the CC-Arc-Miura pattern, alternate cutting planes have non-parallel inclination angles.

#### Ellipse Creation

Zigzag lines on an Arc-Miura pattern have alternate lengths for odd and even $j$ creases, and so it is necessary to define two elliptical curves. The first elliptical curve is located along the Arc-Miura mountain crease and so $B^M$ and $C^M$ are found by substituting mountain crease parameters $b_1$ for $b$ and $\eta_{MZ}$ for $\eta_Z$ in Equation (4.50). Mountain ellipse parameters $c^M$, $d^M$, $g^M$, and $h^M$, can be found with an additional mountain gradient parameter $\varphi^M$ and using Equations (4.46–50). The first elliptical curve $(u^M, v^M)$, Figure 4.36(a), can then be plotted by using these parameters in Equations (4.53–54).

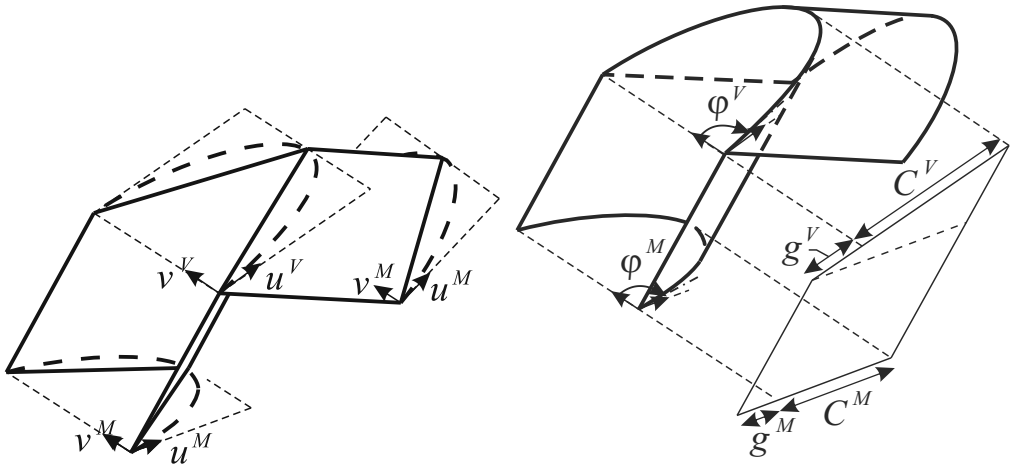


(a) Elliptical curves through three points (b) Projected curved surface

Figure 4.36: Curved-Crease Arc-Miura geometry creation.

The second ellipse is found at Arc-Miura valley creases, and it can be plotted once valley gradient parameter $\varphi^V$ is obtained. To do this, $B^V$ and $C^V$ are first defined with Equation (4.50) by substituting valley crease parameters $b_2$ for $b$ and $\eta_{VZ}$ for $\eta_Z$. Using the projected prismatic base pattern geometry shown in Figure 4.36(b), ellipse parameter $g^V$ can then be related to the first ellipse with similar triangle geometry:

$$g^V = g^M C^V / C^M \tag{4.82}$$

Substituting this value into Equation (4.47) gives:

$$\tan \varphi^V = \frac{2C^V(2 + C^V/g^V)}{B^V} \tag{4.83}$$

The remaining parameters $c^V, d^V$, and $h^V$, can be found by substituting $B^V$, $C^V$, and $g^V$ into Equations (4.46), (4.48–49). The second elliptical curve $(u^V, v^V)$ can then be plotted by using these parameters in Equations (4.53–54).

### Rigid Subdivision

The projected elliptical surface is subdivided into planar strips to generate the CC-Arc-Miura pattern. Vertices $W^{k,j}$ are calculated at the intersection of the $k^{th}$ divisor line and the $j^{th}$ zigzag crease ($k = 1, 2, ..., s,\ j = 1, 2, ..., n$). In a 3D Cartesian coordinate system with orientation as shown in Figure 4.37(a), the coordinate vector $(x^{k,j}, y^{k,j}, z^{k,j})$ of $W^{k,j}$ is:

$$x^{k,j} = R\cos\theta + u^{k,j}(t^k) \tag{4.84}$$

$$y^{k,j} = (k - k' - 1)\frac{b_2 \sin(\eta_{MZ,set}/2)}{S} + v^{k,j}(t^k) \tag{4.85}$$

$$z^{k,j} = R\sin\theta + w^{k,j}(t^k) \tag{4.86}$$

where $R$ is given by Equation (2.27) and $\theta$ is given by odd $i$ values in Equation (2.28).

Rotated elliptical coordinates $(u^{k,j}, v^{k,j}, w^{k,j})$ for odd $j$ lie along the first ellipse, and are obtained by rotating the $(u^M, v^M)$ ellipse to match the orientation of the corresponding three-node zigzag on the base pattern:

$$\begin{bmatrix} u^{k,j}(t^k) \\ v^{k,j}(t^k) \\ w^{k,j}(t^k) \end{bmatrix} = \begin{bmatrix} \cos(\theta + \pi/2 + \xi_{b1}/2) & 0 \\ 0 & 1 \\ \sin(\theta + \pi/2 + \xi_{b1}/2) & 0 \end{bmatrix} \begin{bmatrix} u^M(t^k) \\ v^M(t^k) \end{bmatrix} \quad \text{for odd } j \tag{4.87}$$

where $t^k = t_{lim}(k'/S - 1)$ and $t_{lim}$ is calculated by substituting mountain ellipse parameters into Equation (4.55). To ensure the nodes along the $k^{th}$ divisor line run parallel between mountain and valley ellipses, a different method is used to find rotated elliptical coordinates on the second elliptical curve. First, $(u^V(t^k), v^V(t^k))$ are obtained by reformulating Equations (4.53–54) such that $v^M(t^k)$ and $v^V(t^k)$ form a straight $k^{th}$ divisor line:

$$v^V(t^k) = v^M(t^k) \tag{4.88}$$

$$u^V(t^k) = g^V + c^V \sqrt{1 - \frac{(v^V(t^k) - h^V)^2}{(d^V)^2}} \tag{4.89}$$

The rotated elliptical coordinates $(u^{k,j}, v^{k,j}, w^{k,j})$ for even $j$ are then obtained with:

$$\begin{bmatrix} u^{k,j}(t^k) \\ v^{k,j}(t^k) \\ w^{k,j}(t^k) \end{bmatrix} = \begin{bmatrix} \cos(\theta + \pi/2 + \xi_{b2}/2) & 0 \\ 0 & 1 \\ \sin(\theta + \pi/2 + \xi_{b2}/2) & 0 \end{bmatrix} \begin{bmatrix} u^V(t^k) \\ v^V(t^k) \end{bmatrix} \quad \text{for even } j \tag{4.90}$$

where $\xi_{b2}$ is obtained by substituting $b_2$ for $b_1$ and $\eta_{MZ}$ for $\eta_{VZ}$ in Equation (2.31). Again, a 3D Cartesian system was used, rather than a cylindrical coordinate system, as it is simpler to incorporate the rotated $u^{k,j}$,$v^{k,j}$, and $w^{k,j}$ terms.

The subdivided CC-Arc-Miura pattern forms a PQ mesh composed of a $K$ by $J$ piecewise assembly of prismatic Arc-Miura panels, Figure 4.37(a). To simulate the folding motion of the CC-Arc-Miura assembly, the seven parameters required for each Arc-Miura panel must be defined. The two panel size parameters can be found with $m^K = n^K = 2$. All panels also possess the same folded longitudinal edge

angle as the base pattern: $\eta_{VA}^{K} = \eta_{VA}$. As was done for the CC-Arc pattern, panel superscript $^{K,J}$ is replaced with $^{K}$ when all $J$ panels possess the same parameter value.

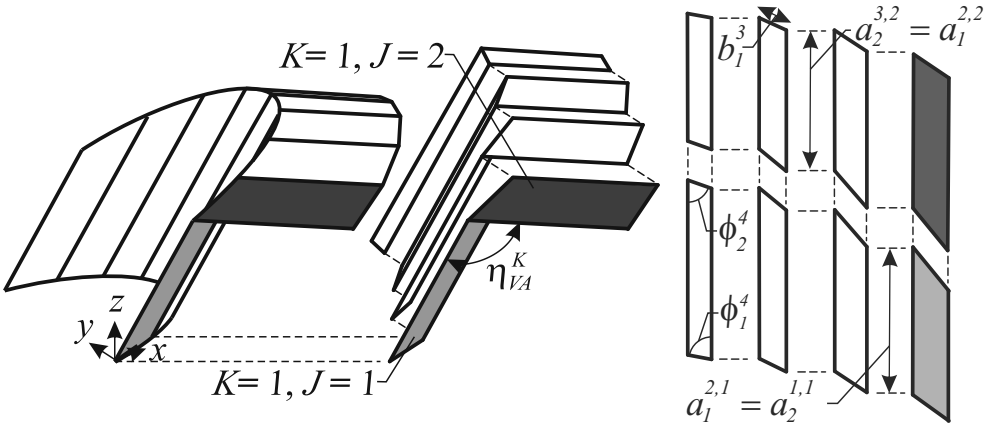


(a) Divisor lines and exploded rigid panels (b) Crease pattern

Figure 4.37: Rigid subdivision of CC-Arc-Miura pattern.

A side length parameter of the first odd $J$ panel matches the base prismatic pattern, $a_1^{1,J} = a_1$. This parameter can eliminated in remaining odd $J$ panels with common edge constraints: $a_1^{K+1,J} = a_2^{K,J}$. Similarly for the first even $J$ panel $a_2^{2,J} = a_2$, and for remaining even $J$ panels $a_2^{K+1,J} = a_1^{K,J}$. Three remaining independent constant parameters are required, $b_1^K$, $\phi_1^K$, and $\phi_2^K$, which can be calculated directly from pattern vertex locations. They are constant for all $J$. Constants $b_1^K$ and $\phi_1^K$ can be calculated by substituting $a_1^{K,J}$ for $a^K$ and $b_1^K$ for $b^K$ in Equations (4.63–64). The final constant $\phi_2^K$ is the found with:

$$\phi_2^K = \angle W^{k,1} W^{k,2} W^{k+1,2} \tag{4.91}$$

for which the general solution was given in Equation (4.66). The CC-Arc-Miura pattern can therefore be completely defined with eight parameters: seven for the base prismatic pattern plus an additional gradient parameter. The folding motion can be simulated by adjusting a variable parameter in the piecewise assembly, most directly with $\eta_{VA}^{1}$. A comparison of the simulated folding motion and prototype folding is shown in Figure 4.38 with good correlation seen.

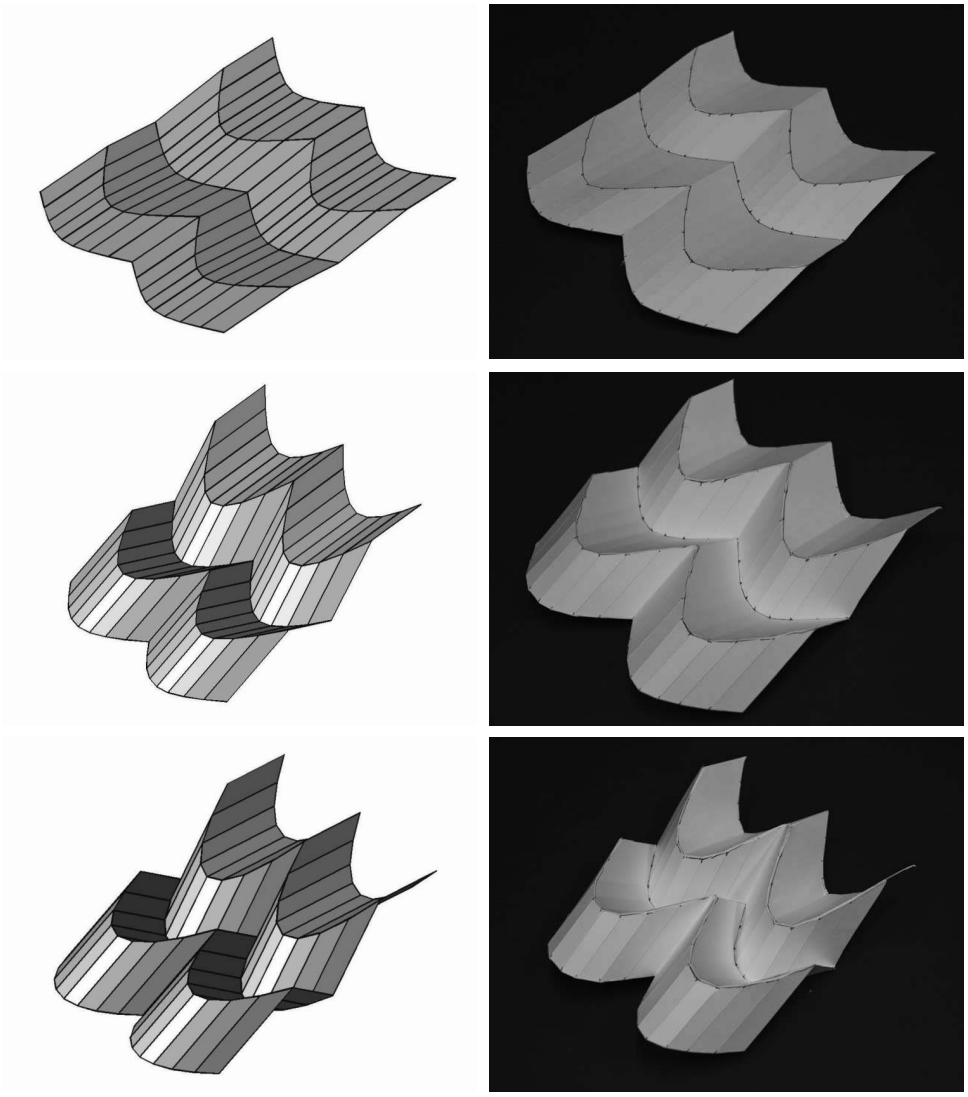

Figure 4.38: Comparison of folding motion of simulated (left) and plastic prototype (right) CC-Arc-Miura pattern.

### 4.5.4 Piecewise and Folded Sandwich Geometry

Apart from convenient parametrisation, there are numerous advantages to defining curved-crease origami patterns from a rigid prismatic base pattern, stemming from the fact that various geometric solutions for the prismatic base geometry are preserved in the curved-crease geometry. For example, the unit volume of the prismatic base is preserved in the CC-variant, which will be seen in Chapter 5 to allow direct comparison of straight-crease and curved-crease foldcore performance. It also preserves piecewise and folded sandwich assembly methods.

### Piecewise Curved-Crease Geometry

Although the curved-crease patterns developed above are piecewise geometries themselves, they can also be attached to dissimilar unit geometries to create curved-crease geometries with varying curvature. This is done most simply by defining a piecewise prismatic geometry in the manner described in Section 4.2, and then applying the ellipse creation and rigid subdivision stages.

As an example, the piecewise arch pattern shown in Figure 4.8 is taken as a base prismatic pattern. A gradient $\varphi^m$ is defined on the master Miura pattern, and an equivalent $\varphi^{s,M}$ is defined on a slave Arc-Miura pattern to preserve compatible edge geometry, Figure 4.39. This is then decomposed into rigid strips to simulate the folding motion of the entire structure.

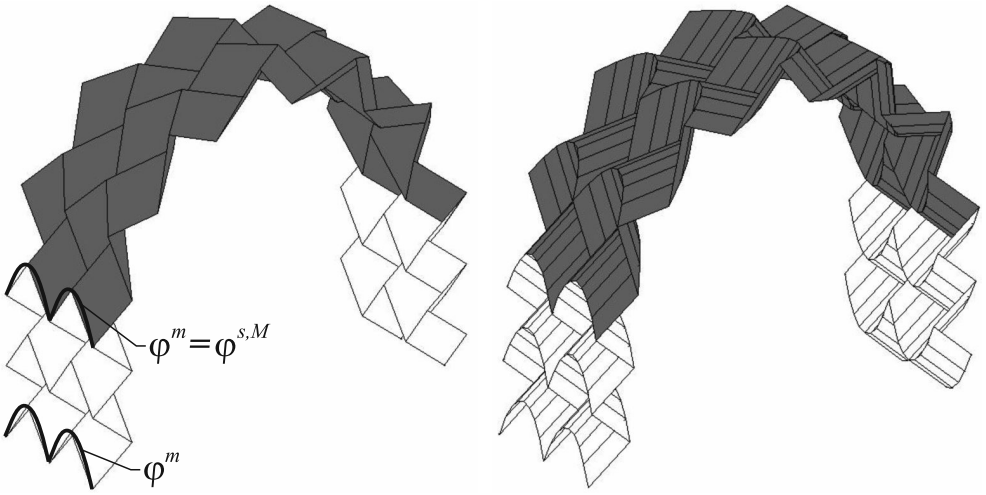


Figure 4.39: Curved-crease piecewise geometries formed from Miura/Arc-Miura assemblies.

### Folded Sandwich Structures and Pattern Closure

Equations presented in Section 4.3 for the attachment of folded sandwich faces to various prismatic base patterns are preserved in the CC-variants, allowing straightforward design of curved-crease folded shell structures. It should also be noted

that Equations for the closure conditions of the curved Tapered Miura, Arc, and Arc-Miura patterns presented in Appendix A are preserved in their CC-variants. Examples demonstrating both of these aspects are shown in shown in Figure 4.40.

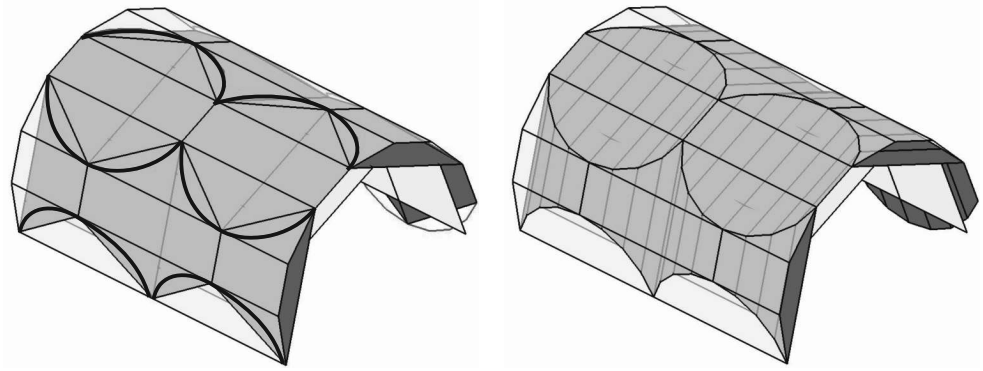

(a) Preserved folded sandwich faces for prismatic and curved-crease Arc patterns

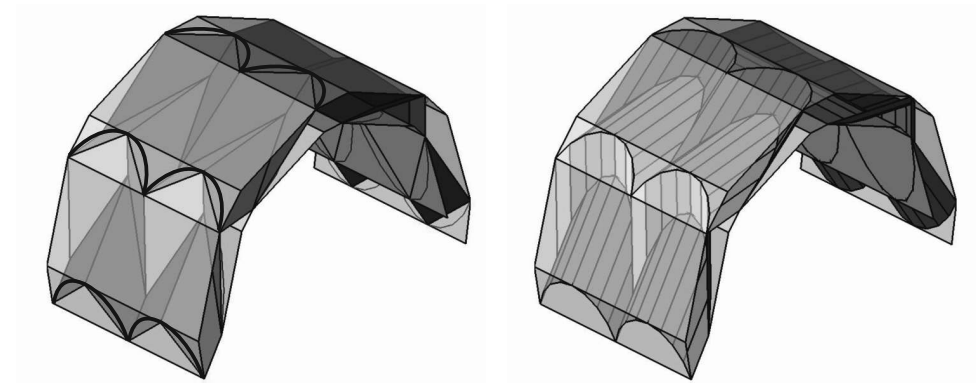

(b) Preserved folded sandwich faces for prismatic and curved-crease Arc-Miura patterns

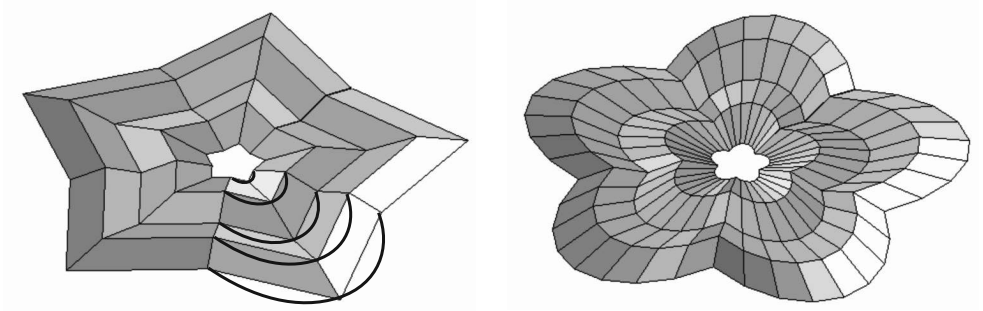

(c) Preserved closure condition in prismatic and curved-crease Tapered Miura patterns

Figure 4.40: Preserved geometric solutions for curved-crease patterns.

## 4.6 Conclusion

To conclude, this chapter has extended foldcore geometry concepts in numerous ways. Three new first-level derivative patterns were developed from a Miura-base geometry. The parametrisations allow straightforward simulated folding motion and have been validated by comparison with physical prototype folding motion. It was then shown how the consistent parametrisation across the set of first-level derivative geometries allowed for them to be combined into complex, rigid-foldable, piecewise geometries. A new method for attaching faceted faces to single-curved and piecewise cores was then shown. These folded sandwich structures were shown to possess a continuously connected edge between face and core structures. It is believed this feature will allow for the creation of much stronger sandwich panels, to be explored in the next chapter.

A new method for generating rigid-foldable, curved-crease geometry from Miura-derivative prismatic base patterns has been developed. The two stages of the method, the ellipse creation stage and rigid subdivision stage, were first demonstrated on a Miura base pattern to generate a Curved-Crease Miura pattern. It was shown that a single additional parameter was necessary to completely define the curved-crease variant. The process was then applied to the Tapered Miura, Arc, and Arc-Miura patterns to generate curved-crease variants for each. Finally, it was shown how the method provided several additional benefits in addition to the minimum parametrisation. These included the ability to alter the ellipse creation method to generate different curved-crease tessellations, and the ability to preserve geometric solutions of the prismatic base pattern, including pattern closure and faceted face geometry. All parametrisations presented in the chapter have been compiled into a MATLAB Toolbox for subsequent work.

# Chapter 5

# Extended Foldcore Analysis

The following chapter will use techniques developed in Chapter 3 to examine the impact resistance of the foldcores constructed with *curved-creases*. They will be assessed relative to the previously examined straight-crease foldcores and honeycomb cores. Additional properties for all planar core types will then be investigated, including out-of-plane stiffness and failure under low-velocity dynamic impact loads.

Assembled *foldcore sandwich panels* with attached top and bottom faces will then be examined. Differences between core and panel failure modes are assessed, and the findings used to develop a panel numerical model that incorporates core-face bonding. Finally, single-curved *foldcore sandwich shells* will be examined. Foldcore sandwich shells are constructed at two curvatures: both at and beyond the curvature limit of existing single-curved honeycomb panels.

## 5.1 Curved-Crease Foldcores

### 5.1.1 Preliminary Numerical Analysis

#### Geometry

As discussed in Section 4.4, a curved-crease geometry can be designed with a straight-crease base pattern and an additional gradient parameter $\varphi$. It is unknown what effect $\varphi$ might have on foldcore performance, so a preliminary numerical study was conducted on curved-crease foldcores with different $\varphi$ values, and a base geometry designed to be comparable with the small-scale foldcores studied in Section 3.5. As such, curved-crease geometries were designed using the Mi02 experimental configuration as a base pattern, with $a = 15$mm, $b = 7.5$mm, $\phi = 64.8°$, $\eta_A = 95°$, $\eta_Z = 109.4°$, and $\alpha = 3.0\%$. Gradient minimum and maximum bounds were calculated from Equations (4.50–52) as $\varphi_{min} = 0.955$ and $\varphi_{max} = 1.571.$ , so initial numerical models were set up for three different gradients: $\varphi_{min}$, $\varphi_{max}$, and a gradient chosen to be halfway between the two, taken as $\varphi_{avg} = 1.263$.

Different tessellations can also be defined for the same base geometry and $\varphi$, so each gradient was applied to the two tessellations discussed in Section 4.4.3, for a total of six models. Model designations $G1^{T1}$, $G2^{T1}$, and $G3^{T1}$ denote the three gradients of the first tessellation, and $G1^{T2}$, $G2^{T2}$, and $G3^{T2}$ denote the three different gradients of the second tessellation. The total plate area $A_p$ is equal to the sum of the areas of the rigid strips composing the curved-crease geometry, and was slightly different for each gradient. Therefore the plate thickness was scaled to give a matching density. Relevant parameters for all six models are listed in Table 5.1 and selected models shown in Figure 5.1.

Table 5.1: Preliminary curved-crease foldcore geometric parameters and results.

| *Model* | *Tess.* | $\varphi$ | $A_p$ (mm$^2$) | $t_p$ (mm) | $\sigma^*_{max}$ | $\sigma^*_{avg}$ | $U^*$ |
|---|---|---|---|---|---|---|---|
| G1$^{T1}$ | 1 | 0.955 | 417.1 | 0.195 | 24.5 | 13.5 | 1.81 |
| G2$^{T1}$ | 1 | 1.263 | 425.9 | 0.191 | 24.2 | 13.5 | 1.79 |
| G3$^{T1}$ | 1 | 1.571 | 436.6 | 0.187 | 23.8 | 13.2 | 1.81 |
| G1$^{T2}$ | 2 | 0.955 | 417.1 | 0.195 | 27.4 | 14.3 | 1.92 |
| G2$^{T2}$ | 2 | 1.263 | 425.9 | 0.191 | 29.9 | 16.0 | 1.87 |
| G3$^{T2}$ | 2 | 1.571 | 436.6 | 0.187 | 32.4 | 17.7 | 1.83 |

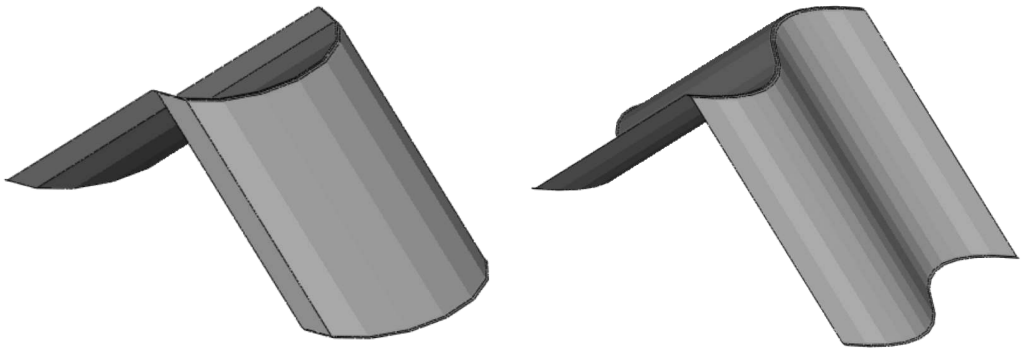

(a) G3$^{T1}$ (b) G1$^{T2}$

Figure 5.1: Unit geometries of selected curved-crease foldcore models.

### 5.1.2 Simulation Results and Discussion

The unit foldcore geometries were analysed numerically with the method described in Chapter 3 and the material properties listed in Table 3.16. These initial numerical models did not include geometric imperfections but did include a small material radius at pattern ridge locations. The dimensionless stress-strain responses of the cores are shown in Figure 5.2(a)-(b) and relevant values summarised in Table 5.1.

Comparing different gradients, it can be seen that the choice of gradient parameter did not significantly affect the performance of the first tessellation models. However it did affect the second tessellation models, with the maximum gradient model G3$^{T2}$ having a 23.8% higher $\sigma^*_{avg}$ than the minimum gradient model G1$^{T2}$. Comparing the two tessellations, it can be seen that the second tessellation significantly outperforms the first tessellation, with G3$^{T2}$ having a 34.1% higher $\sigma^*_{avg}$ than G3$^{T1}$ . All cores have comparable, low uniformity ratios.

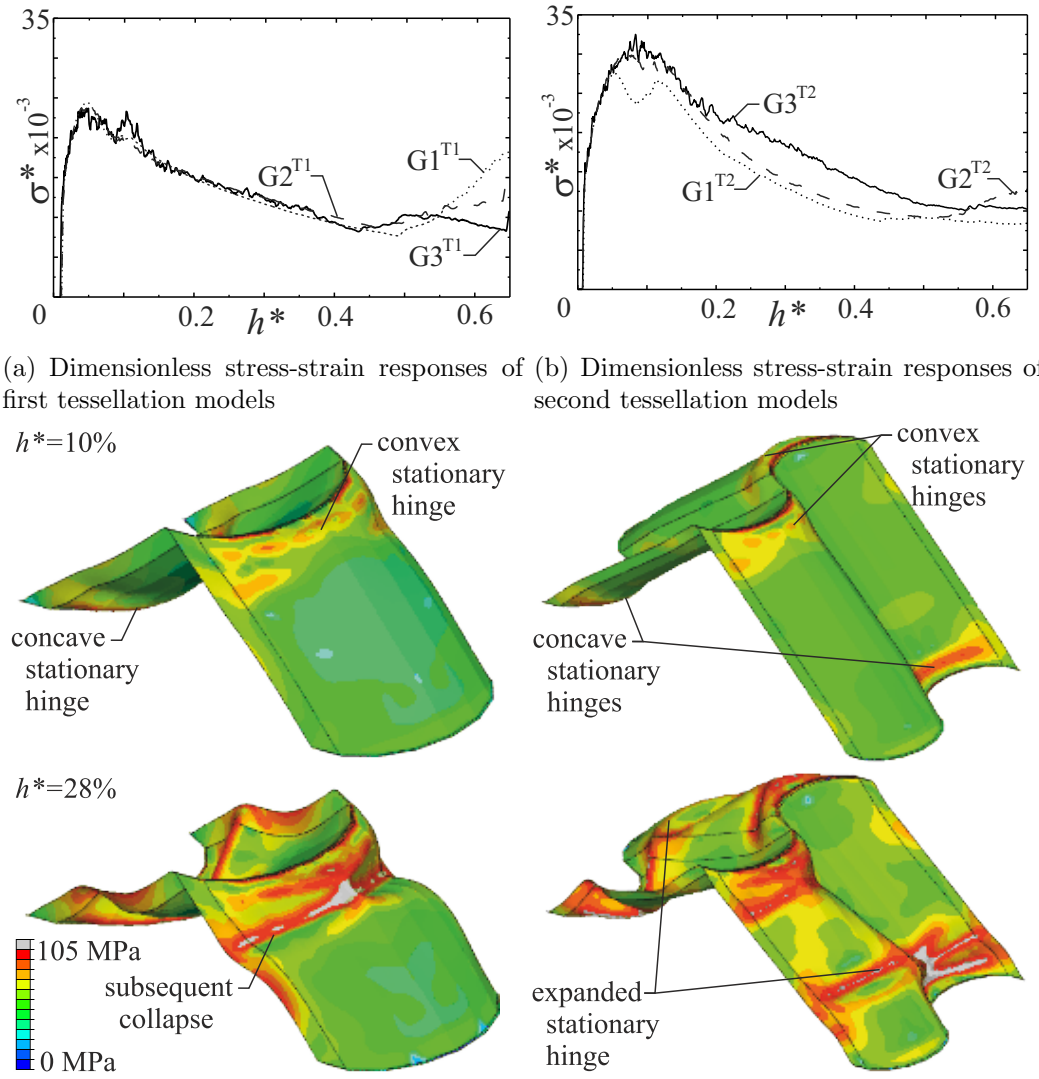


(a) Dimensionless stress-strain responses of first tessellation models

(b) Dimensionless stress-strain responses of second tessellation models

(c) Von-Mises stress in model $G3^{T1}$

(d) Von-Mises stress in model $G3^{T2}$

Figure 5.2: Results of preliminary curved-crease numerical models.

Inspection of the Von-Mises stresses, Figure 5.2(c)-(d), shows that curved-crease foldcores possess a complex cylindrical plate buckling mode. For both tessellations, initial stationary hinge lines form across the top of the convex and bottom of the concave surface. In T1 models, the core subsequently collapses about these lines. In contrast, for T2 models, the subsequent failure of the top hinges shows that top hinge lines spread diagonally across the sinusoidal profile to connect with the adjacent convex hinges lines. The bottom hinge lines spread laterally to the convex plates to create an additional convex hinge line. This might explain the stronger T2 response, or it could be attributable to the different T1 and T2 cylindrical aspects, to be discussed further in Section 5.1.4.

### 5.1.3 Experimental Analysis

#### Manufacturing Method

The method described in Section 4.4 allows for the simulation of curved-crease pattern folding motion, and so the sequential stamping manufacturing method developed in Section 3.5 can be again used to construct small-scale curved-crease prototypes. Prototypes were built for both of the tessellations discussed in the previous section, with a gradient parameter of $\varphi = \varphi_{max}$, Figure 5.3.

(a) First tessellation Ca02

(b) Second tessellation Cb02

Figure 5.3: Small-scale curved-crease aluminium prototypes.

For sequential stamping, 3D printed male and female moulds for both tessellations were designed at gradually steepening folded pattern configurations, set at $\eta_A = 150°$, $\eta_A = 120°$, and $\eta_A = 95°$, Figures 5.4(a) and 5.5(a). The process to form a sheet was identical to that described previously, where an aluminium sheet was stamped row-by-row through three steepening moulds, Figures 5.4(b) and 5.5(b). Note that due to material availability, the sheet material used for these prototypes had thickness $t_p = 0.2$mm, which was slightly thicker than the 0.187mm thickness used for the $\varphi_{max}$ models of the previous section. The resultant foldcores had a density of $\alpha = 3.2\%$ and were given the designation Ca02 for tessellation one, and Cb02 for tessellation two.

Table 5.2 shows the formed and designed dimensions of both core types at each stage of manufacture. Compared to the straight-crease formed dimensions of Table 3.15, there is a larger variation between designed and formed dimensions, particularly in the formed width $W$. In the Ca02 and Cb02 prototypes, this width was found to be on average 14.0% and 8.8% larger than the design width, respectively. This is compared to a 2.3% width variation in the straight-crease cores, and less than 4% variation in length and height dimensions. To seek an explanation of why curved-crease cores suffer width irregularities, a plot of unit width versus folded configuration was produced and marked with the unit width for each sequential mould, Figure 5.6. It can be seen that compared to straight-crease geometries, there is a much higher change in width between the second and third folded configurations of the curved-crease geometries. The formed curved-crease sheet might therefore not have properly contracted in the final manufacture stamping stage, instead stretching across the mould geometry. This is only a partial explanation of the width error, as it does not explain why the Ca02 variation was higher than the Cb02 variation when they both have the same unit width contraction. It is thought that Ca02 could have further problems from material not being drawn into the sharp crease between unit geometries. This might suggest that there are practical limits of the $\varphi_{max}$ relating to manufacturability.

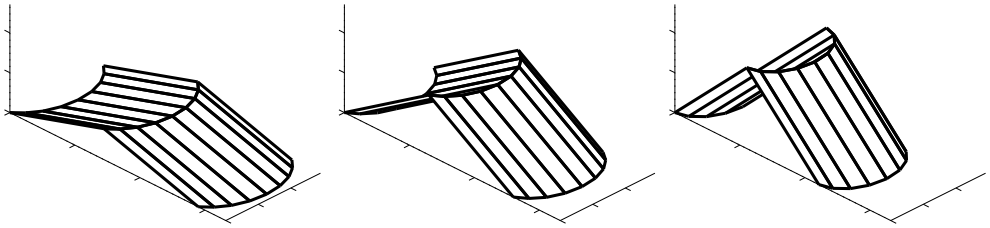

(a) Unit geometries

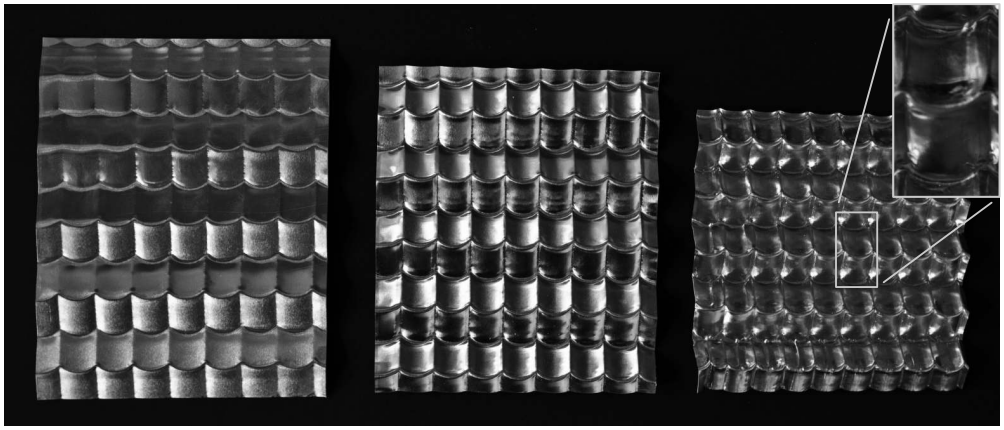

(b) Formed sheets

Figure 5.4: Sequential stamping of Ca02 at $\eta_A = 150°$, 120°, and 95°.

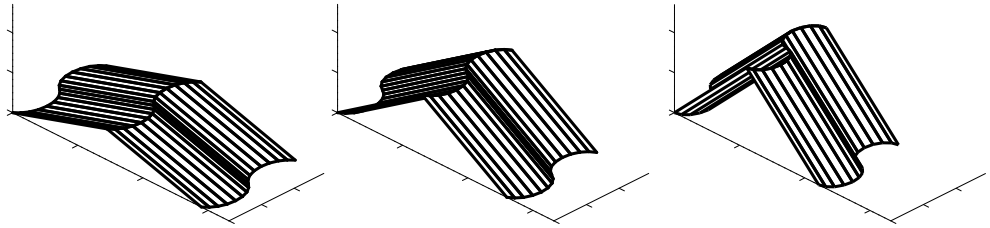

(a) Unit geometries

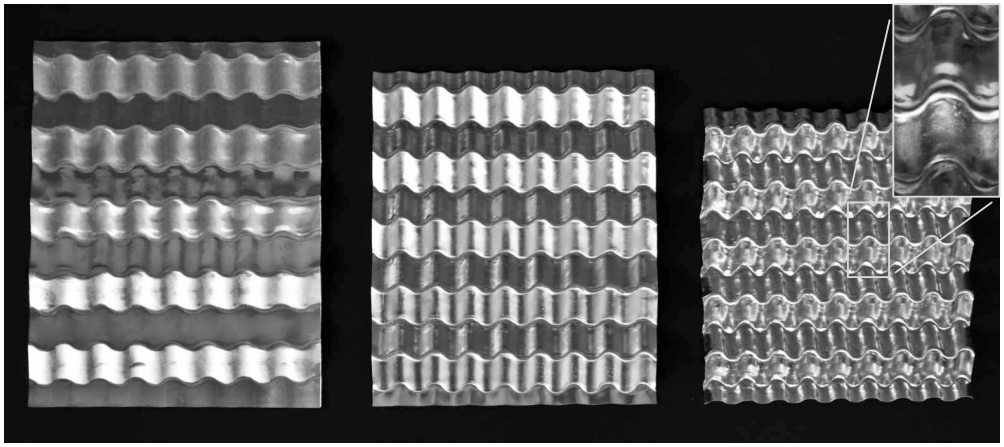

(b) Formed sheets

Figure 5.5: Sequential stamping of Cb02 at $\eta_A = 150°$, 120°, and 95°.

Table 5.2: Global dimensions of curved-crease prototypes.

| *Model* | $\eta_A$ (°) | Formed $L$ (mm) | Formed $W$ (mm) | Formed $H$ (mm) | Designed $L$ (mm) | Designed $W$ (mm) | Designed $H$ (mm) |
|---|---|---|---|---|---|---|---|
| Ca02 | 150 | 117.1 | 115.8 | 3.4 | 117.1 | 115.2 | 3.9 |
| Ca02 | 120 | 105.4 | 114.0 | 7.6 | 103.9 | 110.4 | 7.6 |
| Ca02 | 95 | 90.8 | 111.7 | 9.7 | 88.5 | 98.0 | 10.1 |
| Cb02 | 150 | 116.6 | 115.2 | 3.0 | 117.1 | 115.2 | 3.9 |
| Cb02 | 120 | 105.7 | 112.8 | 7.3 | 103.9 | 110.4 | 7.6 |
| Cb02 | 95 | 89.6 | 106.6 | 9.6 | 88.5 | 98.0 | 10.1 |

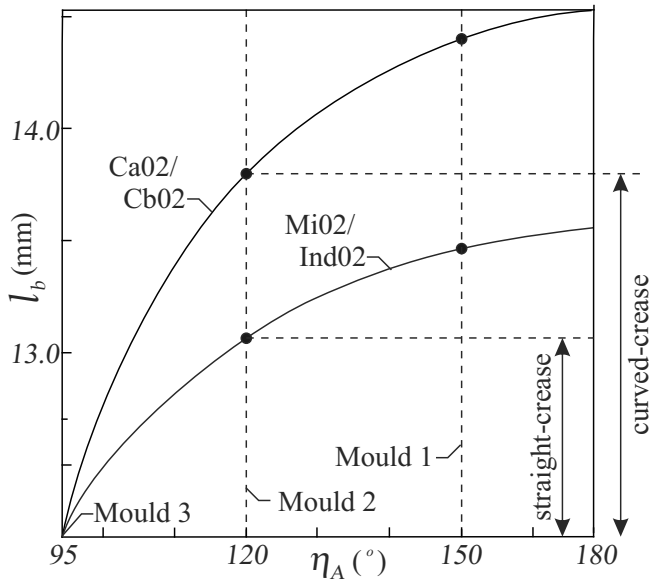


Figure 5.6: Width contraction of straight-crease and curved-crease foldcores.

These width errors could potentially be overcome with improvements to the manufacturing process. For example, additional sequential moulds could be introduced to reduce the width contraction in the final forming step, or print quality around the sharp crease in the first tessellation could be refined. However such improvements to the manufacturing process were deemed to be inconsequential at this early stage of curved-crease assessment, as errors attributable to material stretching were hypothesised to be minor compared to the geometric defects already introduced by the relatively crude hand-stamping process. This will be further examined in the following section, where a method to incorporate both material and geometric imperfections into numerical models is developed.

### Experimental Method and Results

The formed core sheets were annealed to remove residual stresses, epoxy-bonded to aluminium face sheets, and trimmed to a 70mm x 70mm area. Three samples for both tessellations were crushed in an INSTRON Universal Testing Machine in the manner described in Section 3.5. Dimensionless stress-strain values are summarised in Table 5.3 and responses shown in Figure 5.7. The non-subscripted model designations Ca02 and Cb02 are used to denote the average response of the first and second tessellations, respectively. Subscripts $1-3$ are used to denote individual prototype responses.

Table 5.3: Curved-crease prototype results.

| *Model* | $\sigma^*_{max}$ $\times 10^{-3}$ | $\sigma^*_{avg}$ $\times 10^{-3}$ | $U^*$ | *Model* | $\sigma^*_{max}$ $\times 10^{-3}$ | $\sigma^*_{avg}$ $\times 10^{-3}$ | $U^*$ |
|---|---|---|---|---|---|---|---|
| $Ca02_1$ | 17.1 | 9.0 | 1.90 | $Cb02_1$ | 19.5 | 12.2 | 1.60 |
| $Ca02_2$ | 16.1 | 8.3 | 1.95 | $Cb02_2$ | 15.4 | 9.4 | 1.64 |
| $Ca02_3$ | 15.6 | 8.9 | 1.75 | $Cb02_3$ | 16.5 | 10.2 | 1.62 |
| Ca02 | 15.7 | 8.7 | 1.80 | Cb02 | 17.1 | 10.6 | 1.62 |

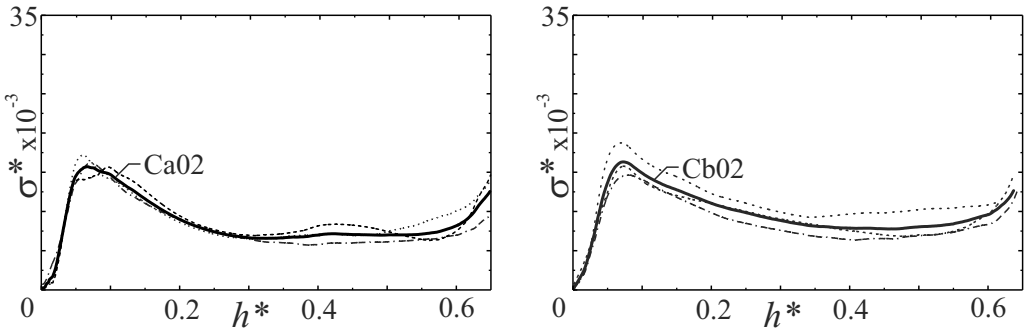


(a) Ca02 (b) Cb02

Figure 5.7: Dimensionless stress-strain response of curved-crease prototypes.

The experimental results shows reasonable repeatability. For the first tessellation, individual values for $\sigma^*_{max}$ are within 8.9% of the average, and values for $\sigma^*_{avg}$ are within 4.7% of the average. Slightly larger variation is seen in the second tessellation, where values for $\sigma^*_{max}$ are within 14.2% of the average, and values for $\sigma^*_{avg}$ are within 15.1% of the average. Crucially, prototypes for each tessellation exhibit the similar failure modes.

**Straight-Crease and Curved-Crease Experimental Comparison**

The straight-crease prototypes of Section 3.5 were built from the same material and at approximately the same density as the curved-crease prototypes, so all foldcore prototypes can be direct compared. Figure 5.8 shows the experimental responses of Mi02, Ind02, Ca02, and Cb02. It can be seen that curved-crease cores have higher reaction stresses, with Cb02 seen to have the highest energy absorption capability, slightly better than that of Ca02, with an 8.9% higher $\sigma^*_{max}$ and a 21.8% higher $\sigma^*_{avg}$. In relation to the straight-crease foldcores, Cb02 has a 40.2% higher $\sigma^*_{max}$ compared to Mi02 and a 25.0% higher $\sigma^*_{avg}$ compared to Ind02. In terms of uniformity of response, it can be seen that the indented core, still has the lowest $U^*$, and a comparatively high $\sigma^*_{avg}$ that is only slightly below that of the Ca02.

It should be noted when making these comparisons that only the indented cores were tested at an optimal geometry. The standard foldcores were tested at an equivalent, non-optimal geometry to reduce manufacturing costs, although as discussed in Section 3.5.6, are incapable of matching the low uniformity ratio of the indented cores even at an optimal geometry. The curved-crease cores were constructed using the standard geometry as a base geometry, following a minimum parameter study on the effect of the gradient parameter. As such, improvements in performance arising from curved-crease parameter optimisation are probable. This will be investigated in later sections.

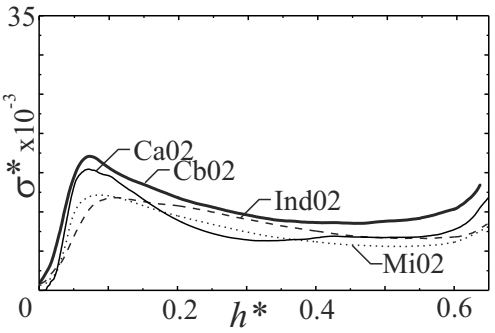


Figure 5.8: Comparison of curved-crease and straight-crease prototype responses.

### Numerical and Experimental Comparison

Comparative numerical models with perfect and imperfect geometries were set up for each tessellation in the manner described in Section 3.5.4, that is to say with geometric imperfections generated through the superposition of the first ten core buckling modes. Modes were linearly superimposed on unbuckled geometry such that the maximum displacement in each case was again equivalent to 125% $t_p$, with the worst-case mode selected as the imperfect geometry and designated FE′. Perfect models were again designated FE. Numerical and experimental results are plotted in Figure 3.44 and relevant values summarised in Table 5.4.

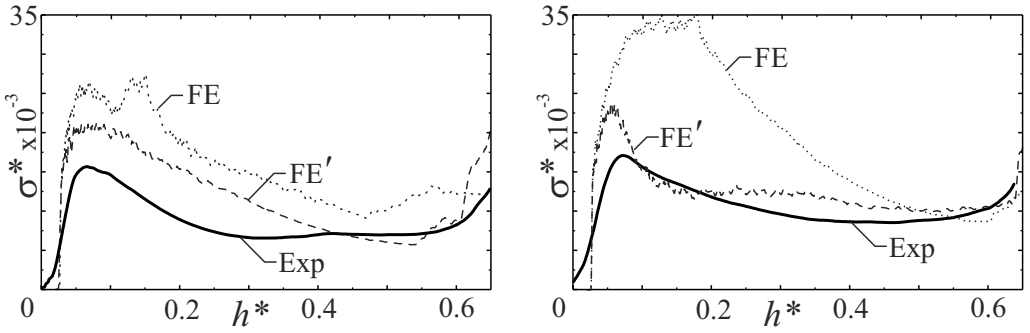


(a) Ca02 (b) Cb02

Figure 5.9: Comparison of numerical and experimental curved-crease responses.

The perfect and imperfect numerical models have different failure modes, with the imperfect models having a failure mode seen to match that of the experimental models, discussed further below. The second tessellation in particular is drastically affected by the presence of geometric imperfections, with a 37.8% reduction in $\sigma^*_{avg}$. This is compared to a 23.1% reduction for the first tessellation. Despite predicting the failure mode, it can be seen that the FE′ models give a poor prediction of experimental stresses. For tessellations one and two, predictions for $\sigma^*_{max}$ are 35.8% and 37.4% over experimental values, respectively, and predictions for $\sigma^*_{avg}$ are 35.1% and 19.1% over experimental values, respectively. This is much higher than error seen for the straight-crease cores and is more than can be accounted for by the moderate variation seen between individual experimental prototype results.

It was hypothesised that a second, material imperfection could be introduced into the curved-crease models to better approximate experimental errors and account for the forming errors discussed in preceding section. As such, a second set of numerical models were created that incorporated both geometric and material imperfections, designated FE″. The material imperfection was implemented by reducing the core sheet thickness in proportion to the degree that formed width was stretched beyond the designed width. This gave a relation of $t''_p = t_p W_{\text{designed}}/W_{\text{formed}}$, where $t''_p$ equals the imperfect material thickness and values for $W$ are those given in Table 5.2. Such a method for approximating the material stretch contains several simplifying assumptions, including that the material stretch is constant across the core and that the contribution of spring-back to the difference in formed width dimensions is negligible. However it is a very rapid method for accounting for material imperfections and will be seen below to be adequate for present purposes. The reduced sheet thicknesses were calculated as $t''_p = 0.175$mm for the first tessellation and $t''_p = 0.185$mm for the second tessellation.

Results for FE″ models are summarised in Table 5.4 and plotted in Figure 5.10. It can be seen that additional material imperfection inclusion gives significantly better predictions of experimental stresses than FE′. For tessellations one and two, FE″ predictions for $\sigma^*_{max}$ are 10.8% and 25.1% over experimental values, respectively, and predictions for $\sigma^*_{avg}$ are 5.6% and 2.9% over experimental values, respectively. It also shows that despite simplifying assumptions, the method used to approximate the material imperfections were adequate.

A comparison between experimental and FE″ unit failure modes is shown in Figure 5.11. Although not shown, there was little discernible difference between the FE′ and FE″ failure modes. The change in energy absorption from FE′ to FE″ is also much less than that from FE to FE′. This justifies the assumption of the previous section that foldcore behaviour under impact loading is more sensitive to geometric

Table 5.4: Numerical and experimental curved-crease results.

| *Result* | Ca02 | | | Cb02 | | |
|---|---|---|---|---|---|---|
| | $\sigma^*_{max}$ $\times 10^{-3}$ | $\sigma^*_{avg}$ $\times 10^{-3}$ | $U^*$ | $\sigma^*_{max}$ $\times 10^{-3}$ | $\sigma^*_{avg}$ $\times 10^{-3}$ | $U^*$ |
| Experimental | 15.7 | 8.6 | 1.82 | 17.1 | 10.5 | 1.62 |
| FE | 27.5 | 15.1 | 1.82 | 35.6 | 20.1 | 1.77 |
| FE′ | 21.3 | 11.6 | 1.83 | 23.5 | 12.5 | 1.87 |
| FE″ | 17.4 | 9.1 | 1.92 | 21.4 | 10.8 | 1.98 |

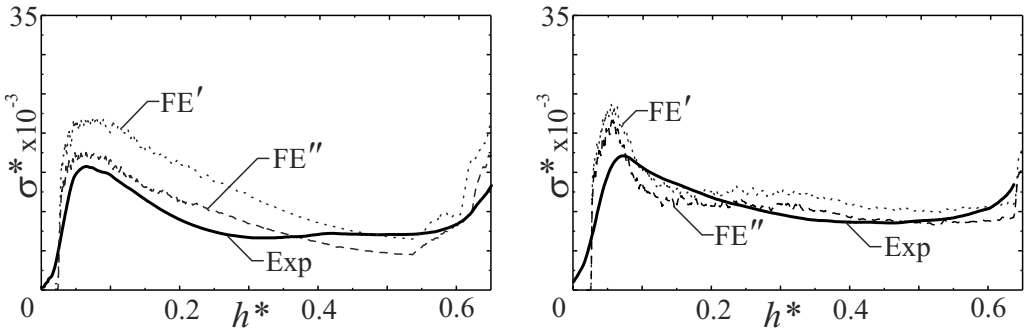


(a) Ca02 (b) Cb02

Figure 5.10: Comparison of FE″ numerical and experimental curved-crease responses.

imperfections than material imperfections. The tessellation one numerical model successfully predicts cylindrical plate buckling at the top of the convex surface and the base of the concave surface, Figure 5.11(a). The tessellation two numerical model successfully predicts plate buckling across the top of the two convex surfaces and across the bottom edge of the two concave surfaces, Figure 5.11(b).

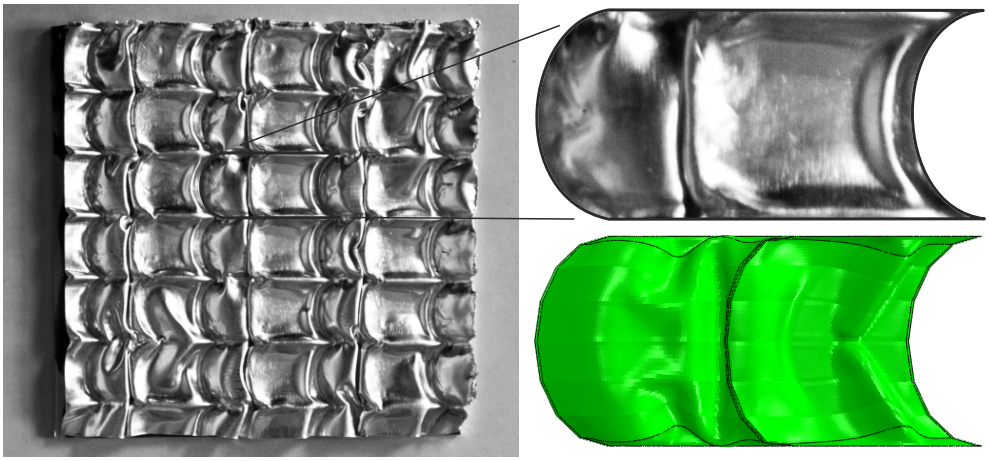

(a) Ca02

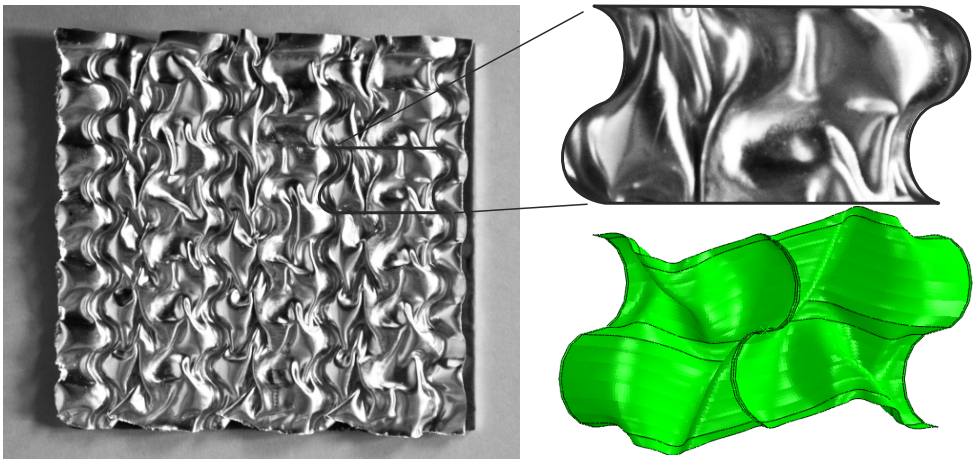

(b) Cb02

Figure 5.11: Final crushed curved-crease core samples, on left; comparison of experimental (grey) and numerical (green) unit failure modes, on right.

### 5.1.4 Parametric Study

The comparison of straight-crease and curved-crease foldcores in the previous section showed that a curved-crease configuration, at either tessellation, had superior energy-absorption to the indented and standard foldcores of Chapter 3. It was thought likely that a further improved foldcore could be found with a parametric study on curved-crease foldcore parameters.

### Geometry

The geometric parameters used to explore the standard foldcore configuration space were reused for the curved-crease parametric study. Thirteen configuration parameter values, shown in Table 3.4, were used corresponding to models B1-B5, C1-C5, and D1-D5, excluding C4 and D3 which are identical to B4. Each configuration parameter model was run at three aspect ratios, $b^* = 0.5$, 1.0, and 2.0, and two tessellations, for a total of seventy-eight models. From the results of Section 5.1.1, $\varphi_{max}$ was assumed to be optimum for all configurations and so the gradient parameter was set as $\varphi = \varphi_{max} = \pi/2$ for all models. Model designations used for the original pattern configuration models were retained, but superscripted with the aspect ratio and tessellation. For example, a second tessellation C2 model run at an aspect ratio of $b^* = 0.5$ was deemed $C2^{0.5,T2}$. Selected models are shown in Figure 5.12. Note that models $C3^{0.5,T1}$ and $C3^{0.5,T2}$ are equivalent to models $G3^{T1}$ and $G3^{T2}$ from Section 5.1.1, respectively.

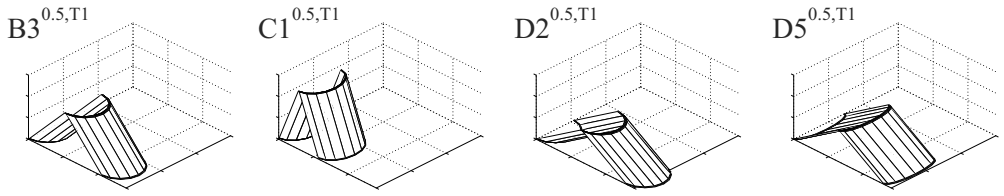


(a) $b^* = 0.5$, first tessellation

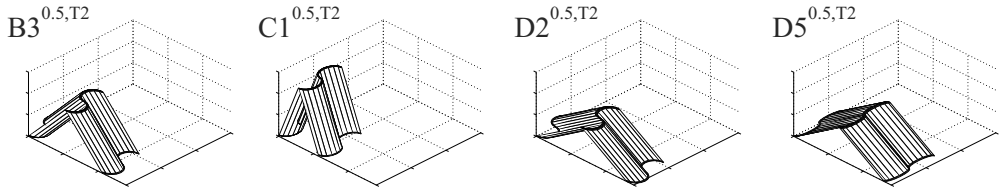


(b) $b^* = 0.5$, second tessellation

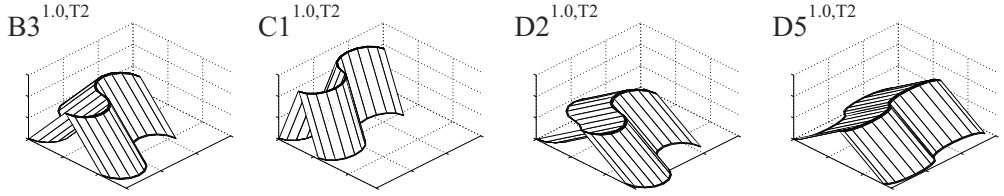


(c) $b^* = 1.0$, second tessellation

Figure 5.12: Selected curved-crease parametric study models geometry.

### Numerical Analysis

Numerical models were analysed in the manner described previously, with results summarised in Table 5.5. Results of the thirty-nine first tessellation models were collated and plotted in Figure 5.13(a). It can be seen that $C1^{0.5,T1}$ is the optimum first tessellation model. Compared to the initial geometry $C3^{0.5,T1}$, it has an 80.2% increase in $\sigma^*_{max}$ and a 52.3% increase in $\sigma^*_{avg}$, for an increase in $U^*$ of 18.2%. The results of the second tessellation models were collated and plotted in Figure 5.13(b). It can be seen that model $B2^{0.5,T2}$ is the optimum second tessellation model in terms of energy-absorption. Compared to the initial geometry $C3^{0.5,T1}$, it has a 22.5% increase in $\sigma^*_{max}$ and a 34.4% increase in $\sigma^*_{avg}$, for a reduction in $U^*$ of 8.7%. Model $C1^{0.5,T2}$ is also highlighted as it has an extremely high peak stress, 78.7% higher than $C3^{0.5,T1}$, and a similar $\sigma^*_{avg}$ to $B2^{0.5,T2}$.

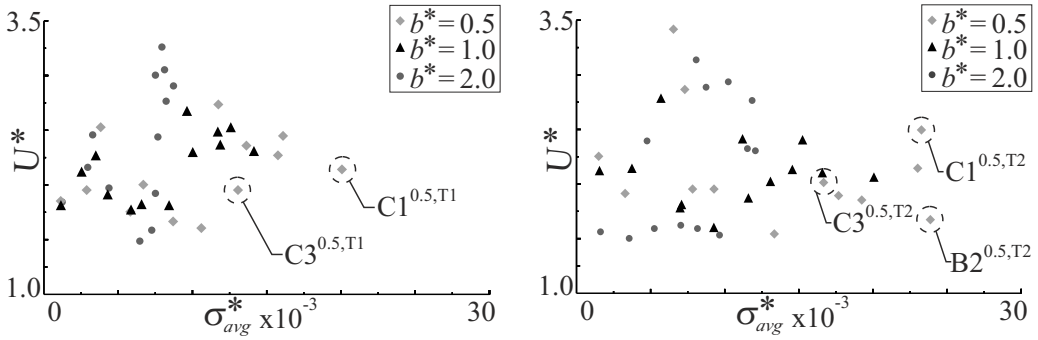


(a) First tessellation (b) Second tessellation

Figure 5.13: Energy-absorption suitability of curved-crease parametric models.

### Comparison of First and Second Tessellations

Comparing the first and second tessellation results, it is evident that the second tessellation generally has a much better energy absorption capability than the first, agreeing with the findings of Section 5.1.1. However an interesting trend is seen when comparing second tessellation $b^* = 1.0$ models with the first tessellation $b^* = 0.5$ models, Figure 5.14(a). It can be seen that they all have values of $\sigma^*_{max}$ and $\sigma^*_{avg}$ within 10% of their corresponding partner.

Table 5.5: Curved-crease parametric study results.

(a) First tessellation

| *Model* | $\sigma^*_{max}$ $\times 10^{-3}$ | $\sigma^*_{avg}$ $\times 10^{-3}$ | $U^*$ |
|---|---|---|---|
| $B1^{2.0,T1}$ | 22.7 | 7.6 | 3.01 |
| $B2^{2.0,T1}$ | 25.0 | 8.2 | 3.06 |
| $B3^{2.0,T1}$ | 22.9 | 8.3 | 2.77 |
| $B4^{2.0,T1}$ | 9.6 | 6.5 | 1.48 |
| $B5^{2.0,T1}$ | 2.4 | 1.3 | 1.84 |
| $C1^{2.0,T1}$ | 26.1 | 8.0 | 3.27 |
| $C2^{2.0,T1}$ | 25.5 | 8.8 | 2.91 |
| $C3^{2.0,T1}$ | 18.8 | 7.7 | 2.44 |
| $C5^{2.0,T1}$ | 6.5 | 3.0 | 2.16 |
| $D1^{2.0,T1}$ | 14.5 | 7.6 | 1.92 |
| $D2^{2.0,T1}$ | 11.6 | 7.3 | 1.58 |
| $D4^{2.0,T1}$ | 8.8 | 4.4 | 1.97 |
| $D5^{2.0,T1}$ | 8.2 | 3.3 | 2.46 |
| $B1^{1.0,T1}$ | 25.9 | 9.7 | 2.68 |
| $B2^{1.0,T1}$ | 31.9 | 12.6 | 2.53 |
| $B3^{1.0,T1}$ | 28.2 | 11.9 | 2.37 |
| $B4^{1.0,T1}$ | 10.5 | 5.9 | 1.77 |
| $B5^{1.0,T1}$ | 2.2 | 1.2 | 1.81 |
| $C1^{1.0,T1}$ | 32.7 | 14.2 | 2.31 |
| $C2^{1.0,T1}$ | 29.3 | 11.7 | 2.49 |
| $C3^{1.0,T1}$ | 23.1 | 10.1 | 2.30 |
| $C5^{1.0,T1}$ | 5.5 | 2.6 | 2.12 |
| $D1^{1.0,T1}$ | 15.3 | 8.5 | 1.81 |
| $D2^{1.0,T1}$ | 12.0 | 6.6 | 1.82 |
| $D4^{1.0,T1}$ | 8.3 | 4.4 | 1.91 |
| $D5^{1.0,T1}$ | 8.1 | 3.6 | 2.27 |
| $B1^{0.5,T1}$ | 32.2 | 11.8 | 2.74 |
| $B2^{0.5,T1}$ | 35.9 | 15.8 | 2.27 |
| $B3^{0.5,T1}$ | 32.2 | 13.7 | 2.36 |
| $B4^{0.5,T1}$ | 13.5 | 6.7 | 2.00 |
| $B5^{0.5,T1}$ | 2.2 | 1.2 | 1.85 |
| $C1^{0.5,T1}$ | 42.9 | 20.1 | 2.14 |
| $C2^{0.5,T1}$ | 39.4 | 16.1 | 2.45 |
| $C3^{0.5,T1}$ | 23.8 | 13.2 | 1.81 |
| $C5^{0.5,T1}$ | 5.8 | 3.0 | 1.95 |
| $D1^{0.5,T1}$ | 17.0 | 10.6 | 1.60 |
| $D2^{0.5,T1}$ | 14.5 | 8.7 | 1.66 |
| $D4^{0.5,T1}$ | 10.3 | 5.9 | 1.75 |
| $D5^{0.5,T1}$ | 9.8 | 3.9 | 2.53 |

(b) Second tessellation

| *Model* | $\sigma^*_{max}$ $\times 10^{-3}$ | $\sigma^*_{avg}$ $\times 10^{-3}$ | $U^*$ |
|---|---|---|---|
| $B1^{2.0,T2}$ | 25.1 | 8.7 | 2.88 |
| $B2^{2.0,T2}$ | 27.7 | 12.1 | 2.30 |
| $B3^{2.0,T2}$ | 26.7 | 11.5 | 2.32 |
| $B4^{2.0,T2}$ | 11.4 | 7.0 | 1.62 |
| $B5^{2.0,T2}$ | 2.5 | 1.6 | 1.56 |
| $C1^{2.0,T2}$ | 32.6 | 11.8 | 2.76 |
| $C2^{2.0,T2}$ | 30.0 | 10.2 | 2.93 |
| $C3^{2.0,T2}$ | 25.2 | 8.1 | 3.13 |
| $C5^{2.0,T2}$ | 5.3 | 3.6 | 1.50 |
| $D1^{2.0,T2}$ | 14.8 | 9.6 | 1.53 |
| $D2^{2.0,T2}$ | 13.0 | 8.2 | 1.59 |
| $D4^{2.0,T2}$ | 8.3 | 5.3 | 1.59 |
| $D5^{2.0,T2}$ | 11.4 | 4.8 | 2.39 |
| $B1^{1.0,T2}$ | 27.0 | 11.2 | 2.41 |
| $B2^{1.0,T2}$ | 34.8 | 16.6 | 2.10 |
| $B3^{1.0,T2}$ | 30.9 | 14.5 | 2.13 |
| $B4^{1.0,T2}$ | 12.4 | 7.0 | 1.78 |
| $B5^{1.0,T2}$ | 3.3 | 1.6 | 2.12 |
| $C1^{1.0,T2}$ | 41.3 | 20 | 2.06 |
| $C2^{1.0,T2}$ | 36.6 | 15.2 | 2.40 |
| $C3^{1.0,T2}$ | 26.4 | 13.1 | 2.02 |
| $C5^{1.0,T2}$ | 8.0 | 3.7 | 2.14 |
| $D1^{1.0,T2}$ | 21.6 | 11.6 | 1.87 |
| $D2^{1.0,T2}$ | 14.8 | 9.3 | 1.60 |
| $D4^{1.0,T2}$ | 12.8 | 7.1 | 1.81 |
| $D5^{1.0,T2}$ | 15.8 | 5.7 | 2.78 |
| $B1^{0.5,T2}$ | 33.4 | 16.7 | 2.01 |
| $B2^{0.5,T2}$ | 39.7 | 23.8 | 1.67 |
| $B3^{0.5,T2}$ | 35.5 | 19.2 | 1.85 |
| $B4^{0.5,T2}$ | 15.2 | 7.8 | 1.95 |
| $B5^{0.5,T2}$ | 3.4 | 1.5 | 2.25 |
| $C1^{0.5,T2}$ | 57.9 | 23.2 | 2.49 |
| $C2^{0.5,T2}$ | 49.2 | 23.0 | 2.14 |
| $C3^{0.5,T2}$ | 32.4 | 17.7 | 1.83 |
| $C5^{0.5,T2}$ | 6.3 | 3.3 | 1.91 |
| $D1^{0.5,T2}$ | 20.5 | 13.3 | 1.54 |
| $D2^{0.5,T2}$ | 18.1 | 9.3 | 1.95 |
| $D4^{0.5,T2}$ | 20.9 | 7.3 | 2.86 |
| $D5^{0.5,T2}$ | 22.3 | 6.5 | 3.41 |

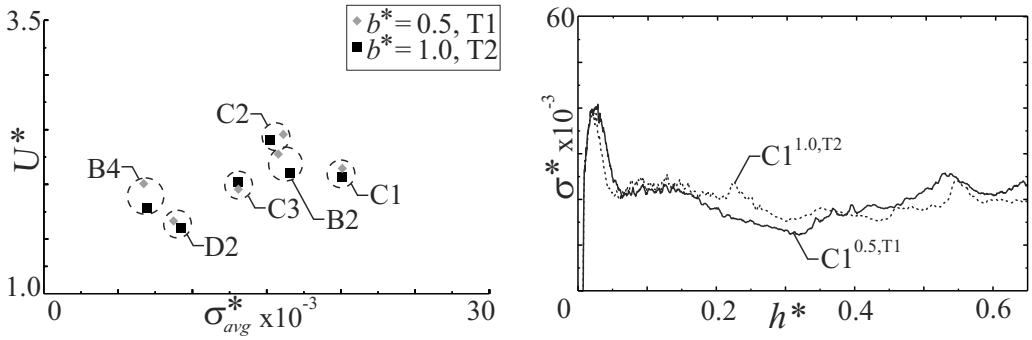


(a) Energy-absorption suitability (b) Dimensionless stress-strain responses

Figure 5.14: Comparison of selected T1 and T2 responses.

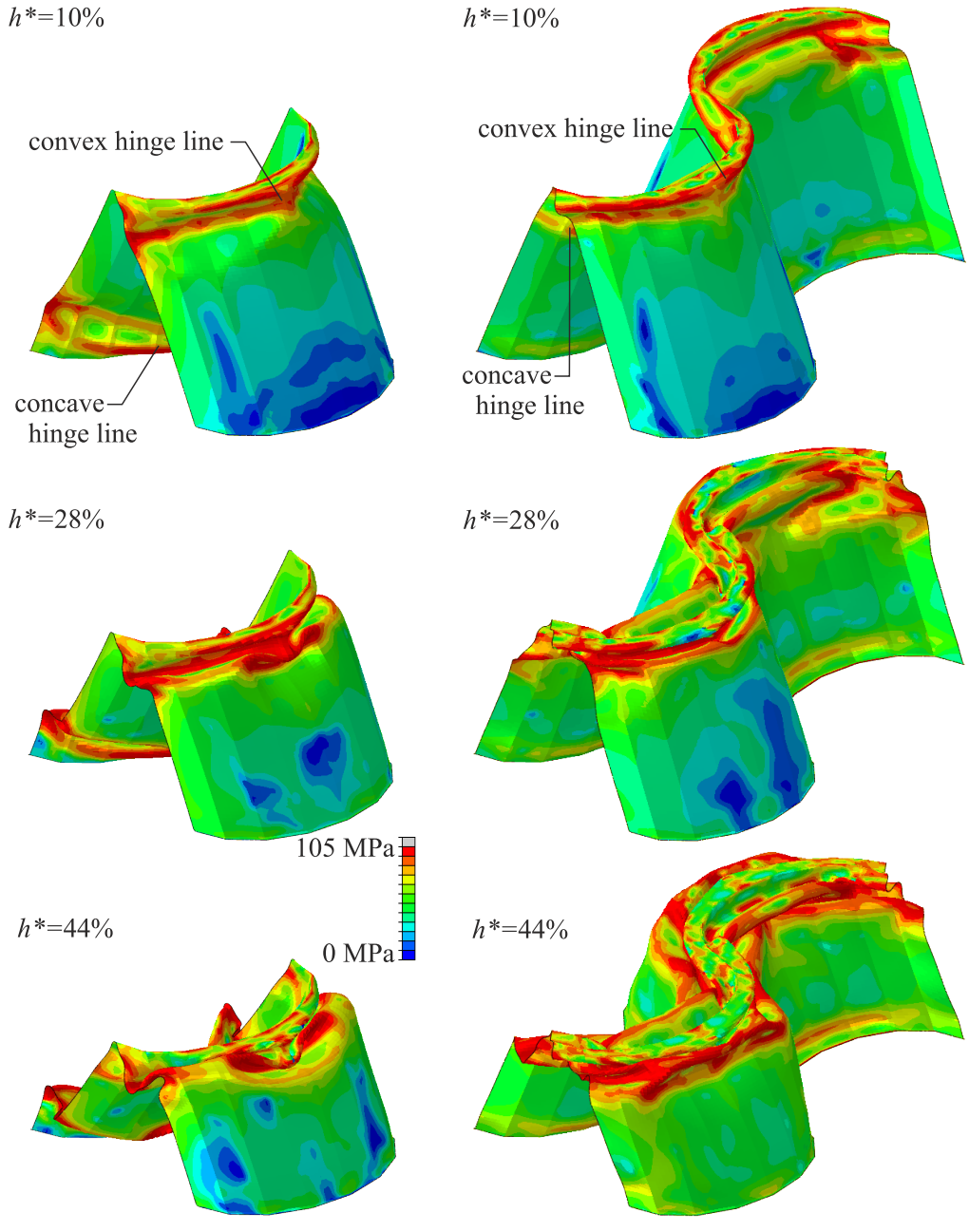


(a) $C1^{0.5,T1}$ (b) $C1^{1.0,T2}$

Figure 5.15: Von-Mises stress and failure modes of paired T1 and T2 models.

Inspection of the dimensionless stress-strain curves of one of these pairs, for example $C1^{0.5,T1}$ and $C1^{1.0,T2}$ shown in Figure 5.14(b), shows that the two have remarkably similar profiles. This is confirmed with inspection of the plate stress of both models, Figure 5.15, where it can be seen that the failure modes are almost identical. The only difference is the location of the concave hinge line, which is at the bottom of the $C1^{0.5,T1}$ but the top of $C1^{1.0,T2}$. To explain this effect, recall from Section 4.4.3 that a second tessellation curve defined on a given straight-crease base has half the period of a first tessellation, see Equations (4.68–69). Therefore a second tessellation curve at a double-width aspect ratio can be expected to give identically proportioned cylindrical segments to a first tessellation, with the only difference being that alternate segments are reversed on the second tessellation to form a continuous sinusoidal profile.

The trend is seen to a slightly lesser extent at other foldcore configurations. For example, comparing $b^* = 2.0$, T2 models with the $b^* = 1.0$, T1 models, the reaction stresses of paired tessellations are typically within 20% each other, while still exhibiting similar failure modes. This also occurs for B1, B5, C5, and D1 $b^* = 1.0$, T2 and $b^* = 0.5$, T1 models, which were omitted from Figure 5.14(a). Models for which this pattern isn't displayed include the very shallow B5, D4, and D5 models. Comparison of these failure modes, Figure 5.16 shows that T2 models, compared to T1 models, exhibit a more well-defined convex hinge line that continues from the concave hinge line on the reversed core section.

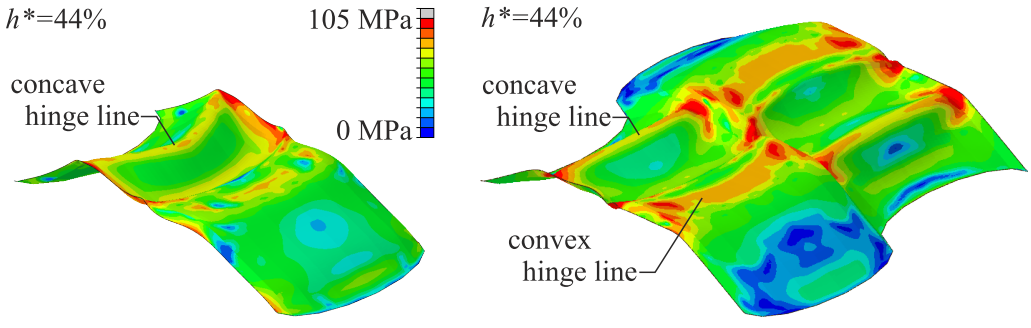


(a) $D4^{0.5,T1}$ (b) $D4^{1.0,T2}$

Figure 5.16: Comparison of paired T1 and T2 models with dissimilar failure modes.

To conclude, altering the tessellation of a curved-crease foldcore is unlikely to

provide significant energy-absorption capability beyond that achievable with direct changes to the aspect ratio. Second tessellation models typically have comparable, or slightly improved failure modes and energy-absorption to a half-aspect first tessellation model set at the same configuration. Therefore the remainder of this thesis will restrict consideration to second tessellation foldcores.

### Comparison of Optimum and Experimental T2 Configurations

Compared to the initial model $C3^{0.5,T2}$, model $B2^{0.5,T2}$ was seen to have a significantly higher $\sigma^*_{avg}$ and model $C1^{0.5,T2}$ was seen to have a significantly higher $\sigma^*_{max}$. To explain why this might have occurred, their dimensionless stress-strain responses and failure modes were compared in Figures 5.17 and 5.18, respectively. The high peak force of model $C1^{0.5,T2}$ appears to correspond with a large number of initial static hinge lines forming in the core. These hinges are highlighted with arrows in Figure 5.18(b) at $h^* = 10\%$, where it can be seen that model $C1^{0.5,T2}$ has a total of six initial hinge lines, whereas models $B2^{0.5,T2}$ and $C3^{0.5,T2}$, Figure 5.18(a) and 5.18(c), respectively, each have just four initial hinges. It is interesting to note that this proportion of initial hinge lines corresponds approximately with the relative $\sigma^*_{max}$ of models $C1^{0.5,T2}$ and $B2^{0.5,T2}$, which was $57.9 \times 10^{-3}$ and $39.7 \times 10^{-3}$, respectively.

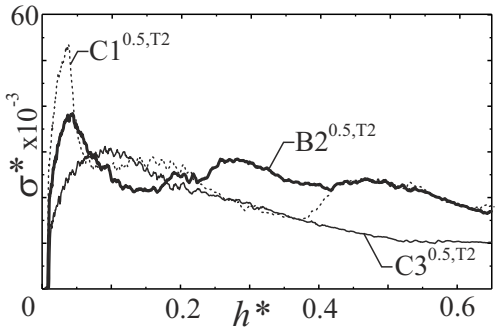


Figure 5.17: Dimensionless stress-strain responses of selected curved-crease numerical models.

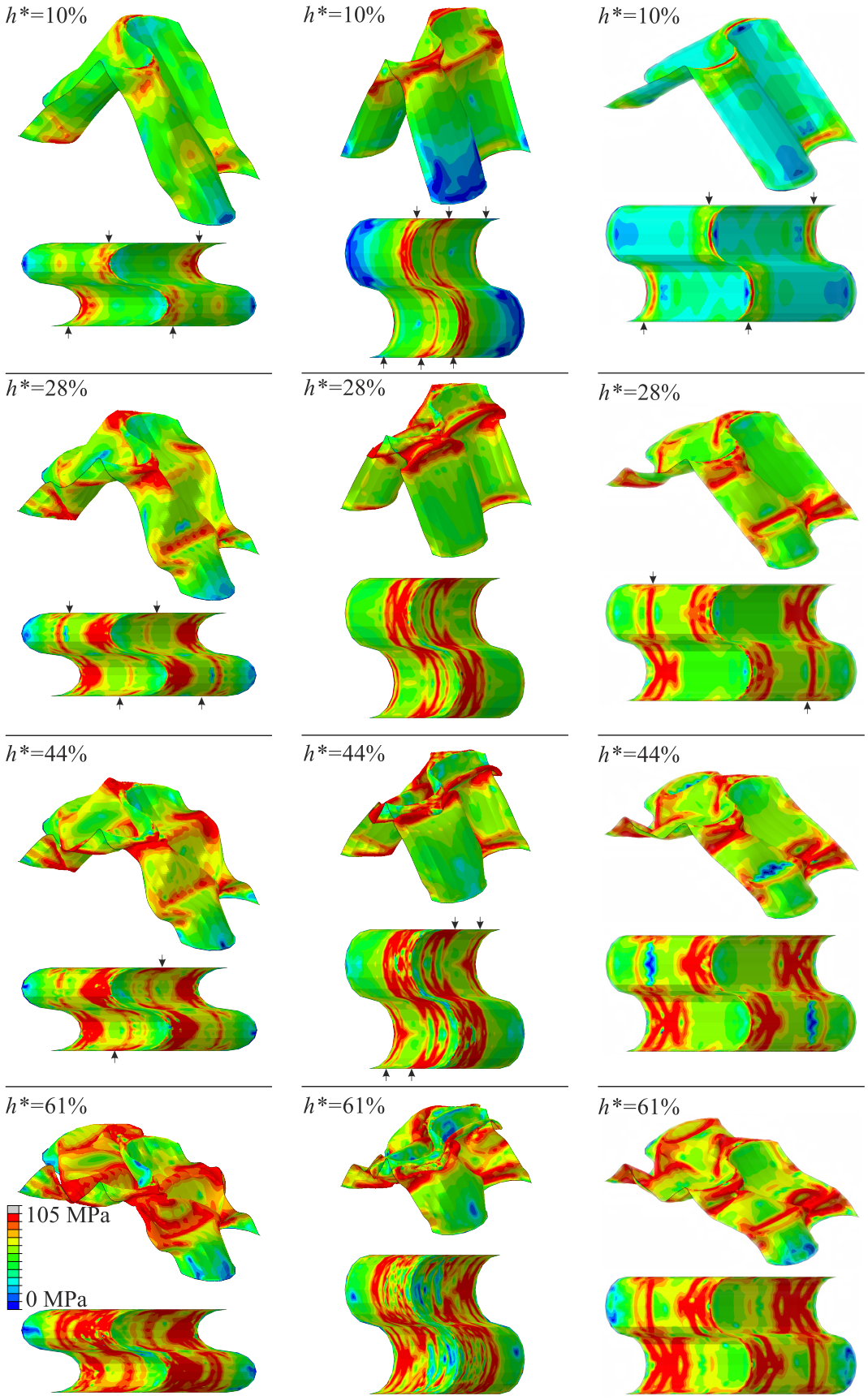


(a) $B2^{0.5,T2}$ (b) $C1^{0.5,T2}$ (c) $C3^{0.5,T2}$

Figure 5.18: Selected curved crease foldcore Von-Mises stress plots on deformed core (top) and top view of undeformed core (bottom). Arrows denote new hinge line formation.

The high average reaction stress of model $B2^{0.5,T2}$, Figure 5.18(a), appears to correspond with a high number or static hinge lines appearing with some regularity as the crush progresses. Four additional hinges appear at approximately $h^* = 28\%$ and a further two hinges at $h^* = 44\%$. Additional hinges are also seen later in model $C1^{0.5,T2}$, with four hinges at approximately $h^* = 44\%$. For both core types, these additional hinges correspond with an increase in reaction stress, Figure 5.17. Two hinges also appear in $C3^{0.5,T2}$ at approximately $h^* = 20\%$, which may be responsible for the gradual reduction in peak stress, rather than the steep reduction seen in model $C1^{0.5,T2}$. Therefore a total of ten hinges lines appears in both $B2^{0.5,T2}$ and $C1^{0.5,T2}$ models, compared to six hinge lines in model $C3^{0.5,T2}$. This is very approximately proportional to $\sigma^*_{avg}$ of the models, which was $23.8 \times 10^{-3}$, $23.2 \times 10^{-3}$, and $17.7 \times 10^{-3}$ in models $B2^{0.5,T2}$, $C1^{0.5,T2}$, and $C3^{0.5,T2}$, respectively.

These results suggest that there might be a predictable, progressive cylindrical plate buckling failure mode similar to that seen in honeycomb cores. An analytical solution for this would enable prediction of curved-crease foldcore crushing stresses, but is outside the scope of the present work. It will be considered in future work.

### Comparison of Foldcore and Honeycomb Responses

A final numerical comparison was conducted between the two improved curved-crease foldcore comparisons and the previously investigated honeycomb core. Models $C1^{0.5,T2}$ and $B2^{0.5,T2}$ were rerun with the 195MPa yield stress aluminium material given in Table 3.16(b), and designated C1-$195^{0.5,T2}$ and B2-$195^{0.5,T2}$, respectively. Both perfect FE and imperfect FE′ numerical models were constructed, with imperfect geometry again generated with a superposition of low-order buckling modes. The imperfect material models FE″ were not used here, as it was thought that minimal material imperfections were likely to be introduced were a proper manufacturing process used. Results are summarised in Table 5.6 and plotted in Figure 5.19.

Table 5.6: Results of curved-crease models with 3003-H19 material properties.

| *Result* | B2-195$^{0.5,T2}$ | | | C1-195$^{0.5,T2}$ | | |
|---|---|---|---|---|---|---|
| | $\sigma^*_{max}$ $\times 10^{-3}$ | $\sigma^*_{avg}$ $\times 10^{-3}$ | $U^*$ | $\sigma^*_{max}$ $\times 10^{-3}$ | $\sigma^*_{avg}$ $\times 10^{-3}$ | $U^*$ |
| FE | 18.6 | 6.6 | 2.82 | 24.1 | 9.0 | 2.69 |
| FE′ | 17.1 | 6.3 | 2.71 | 22.6 | 8.2 | 2.76 |

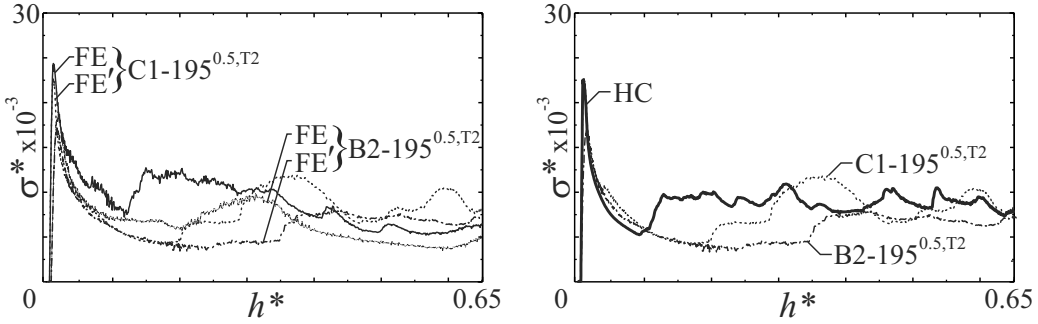


(a) Ca02-195 and Cb02-195 responses (b) FE′ comparison

Figure 5.19: Dimensionless responses of curved-crease 3003-H19 alloy models.

In terms of sensitivity of the high-strength curved-crease models, it can be seen that both are reasonably insensitive. Between FE and FE′ models, there is only a reduction in $\sigma^*_{avg}$ of 4.5% in B2-195$^{0.5,T2}$ and 8.9% in C1-195$^{0.5,T2}$. In comparison to straight-crease cores of the same material studied in Section 3.5.6, the curved-crease FE′ core is seen to be vastly superior both in terms of $\sigma^*_{max}$ and $\sigma^*_{avg}$, although Ind02-195, which retained the travelling hinge failure mode, still retains the best uniformity ratio. In comparison to the commercial honeycomb, Figure 5.19(b), it can be seen that C1-195$^{0.5,T2}$ offers comparable performance in all metrics. From values listed in Table 3.18, the honeycomb core is seen to have the same $\sigma^*_{max}$ and a 7.3% higher $\sigma^*_{avg}$, compared to C1-195$^{0.5,T2}$.

To conclude, an improved configuration of the curved-crease foldcore, obtained from a parametric study, appears to offer comparable energy-absorption capabilities to commercially available honeycomb cores. Future work will develop improved manufacturing methods and attempt to experimentally validate the numerical findings of the last two sections. Further study of the curved-crease failure modes may also lead to additional improvements, for example by introducing sub-folds that improve the observed progressive cylindrical plate buckling mode.

## 5.2 Static and Dynamic Loads

The foldcore studies presented up to this point have focused exclusively on the energy-absorption of core structures under quasi-static impact loads. For successful application, further core attributes must be assessed. This section shall conduct a brief numerical investigation into two important core behaviours: out-of-plane compressive stiffness and energy-absorption under low-velocity impact loads.

### 5.2.1 Out-of-Plane Stiffness

Sandwich panel stiffness and strength is often a critical design parameter, particularly for sandwich applications requiring combined structural and impact-resistant performance. Previous foldcore experimental studies have indirectly assessed out-of-plane strength through $\sigma^*_{max}$, but were too crude to enable direct measurement of out-of-plane stiffness. This section shall therefore use numerical models to gain a preliminary understanding of foldcore stiffness.

Six cores were selected for analysis. Four cores correspond to experimental configurations: HC, Mi02-195, Ind02-195, and Cb02-195. Two cores correspond to the optimum standard foldcore and curved-crease foldcore configurations: C2-$195^{s}$ and C1-$195^{0.5,\mathrm{T2}}$, respectively. All models were run with the 195MPa yield stress aluminium material given in Table 3.16(b). Static analyses on geometrically perfect FE and imperfect FE′ cores were conducted, with an out-of-plane loading applied as a unit line load along the top edges of the each unit cell geometry. The total applied load was averaged over the core unit area to give and out-of-plane applied pressure of $\sigma$. The resulting displacements of the top nodes were averaged to give an out-of-plane displacement $\delta_h$ and strain $\varepsilon_o = \delta_h/h$. Out-of-plane stiffness $E_o$ was then calculated as $E_o = \sigma/\varepsilon_o$. Calculated values are shown in Table 5.7.

Table 5.7: Out-of-plane stiffness of selected core types.

| | $E_o$ | |
|---|---|---|
| *Model* | FE (MPa) | FE′ (MPa) |
| HC | 1842.7 | 1584.7 |
| Mi02-195 | 447.5 | 263.9 |
| C2-195$^{s}$ | 912.0 | 702.2 |
| Ind02-195 | 293.6 | 233.6 |
| Cb02-195 | 474.7 | 450.6 |
| C1-195$^{0.5,\mathrm{T2}}$ | 1477.7 | 1445.3 |

There are several interesting behaviours seen from the core stiffness results. First, in terms of magnitude of stiffness, it can be seen that honeycomb is the stiffest overall core type, and that C1-195$^{0.5,\mathrm{T2}}$ is the stiffest foldcore. It has a comparable $E_o$ to that of honeycomb, with an FE′ value for $E_o$ that is only 8.8% below that of honeycomb. Of the remaining foldcores, it can be seen that the standard C2-195$^{s}$ has the next highest $E_o$, and that the indented Ind02-195 has the lowest $E_o$.

Comparing FE and FE′ stiffness values gives an indication of core sensitivity to geometric imperfections. It can be the curved-crease foldcores are almost completely insensitive, with C1-195$^{0.5,\mathrm{T2}}$ and Cb02-195 having a reduction in $E_o$ of only 2.2% and 5.1%, respectively, from FE to FE′. Honeycomb is also reasonably insensitive, with a reduction of 14.0%. The straight-crease foldcores are all very sensitive, with Ind02-195, C2-195$^{s}$, and Mi02-195 having a reduction in $E_o$ of 20.4%, 23.0%, and 41.0%, respectively.

To conclude, curved-crease foldcores are have a higher out-of-plane stiffness that is less sensitive to geometric imperfections, compared to straight-crease foldcores. In comparison to honeycomb cores, foldcore type C1-195$^{0.5,\mathrm{T2}}$ is the only foldcore with a comparable out-of-plane stiffness. It was also the only foldcore seen to have comparable strength and energy-absorption capabilities to honeycomb cores. As such, it might be a suitable alternative or replacement for honeycomb cores in applications requiring combined structural and impact-resistant performance.

### 5.2.2 Low-Velocity Impact Loads

An important consideration in assessing sandwich panels as energy absorption devices is the change in behaviour from quasi-static to dynamic impact loads. Many cellular cores exhibit strengthening under dynamic loading, a phenomenon which is extensively studied in literature. Zhao *et al.* (2005) identified four major mechanisms for this rate sensitivity: pressure of the air trapped in core cells, shock enhancement effects, strain rate sensitivity of the constituent materials, and micro-inertia effects. For open-cell foams and honeycombs, it was seen that air compression effects are not applicable. Similarly for low-velocity impacts, below approximately 45m/s, shock effects were seen to be negligible.

Many studies have considered the low-velocity impact of aluminium cores (Adams and Maheri, 1993; Hazizan and Cantwell, 2003; Mines *et al.*, 1998; Deshpande and Fleck, 2000). These have typically found the material to be strain rate insensitive, with Zhao *et al.* (2005) confirming that there is less than 10% increase in flow stress from constituent material strain rate sensitivity. However these and other studies have found that at dynamic loads, peak and average stresses can increase by 20-50% for velocities up to 35m/s (Goldsmith and Sackman, 1992; Zhao and Gary, 1998). It is typically observed that there are no significant changes in honeycomb progressive collapse failure mode, and so enhancements have been attributed to lateral inertia in individual folding element formations (Mines *et al.*, 1998; Harrigan *et al.*, 1999).

This section will conduct a brief numerical investigation into whether similar inertial effects are observed in foldcores. This is simply done by rerunning the six foldcore geometries considered in the previous section with a low-velocity impact speed of 20m/s. Dynamic numerical results are shown bracketed in Table 5.8, with a superscript $d$ used to denote dynamic models. Selected dimensionless stress-strain responses are plotted in Figure 5.20.

Comparing honeycomb FE′ and FE′$^d$ responses, it can be seen that $\sigma^*_{max}$ and $\sigma^*_{avg}$ increased by 36.5% and 25.9%, respectively. Inspection of the dimensionless stress-strain responses, Figure 5.20(a), show the dynamic reaction stress increases at locations corresponding to progressive folding element formation, which agrees with that previously reported in literature.

Comparing straight-crease foldcore FE′ and FE′$^d$ responses, it can be seen that Mi02-195, Ind02-195, and C2-195$^s$ have an increase in $\sigma^*_{avg}$ of 2.3%, 7.1%, and 6.7%, respectively. They also have an increase in $\sigma^*_{max}$ of 21.4%, 20.2%, and 43.0%, respectively. The large increase in $\sigma^*_{max}$ is likely attributable to inertia of the initial hinge line causing a peak stress close to that of a perfect geometry. A similar effect has been reported for pre-crushed honeycomb, where an introduced geometric imperfection lowered the peak stress under quasi-static loads, but not under dynamic loads. The low increase in $\sigma^*_{avg}$ suggests that subsequent failure is not rate sensitive. Inspection of the Mi02-195 and Ind02-195 responses, Figure 5.20(b)-(c), confirms this. The plate buckling failure mode is preserved for the standard foldcore and the travelling hinge line failure mode preserved for the indented foldcore.

Finally, comparing the curved-crease foldcore FE′ and FE′$^d$ responses, it can be seen that Cb02-195 and C1-195$^{0.5,\mathrm{T2}}$ have an increase in $\sigma^*_{avg}$ of 15.3% and 15.9%, respectively and an increase in $\sigma^*_{max}$ of 6.9% and 5.7%, respectively. The small increase in peak stress likely occurs because the quasi-static FE′ and FE models were seen to have comparable peak stresses, and so dynamically there is only a small relative increase. From the C1-195$^{0.5,\mathrm{T2}}$ response, Figure 5.20(d), it can be seen that the increase in $\sigma^*_{avg}$ is attributable to larger peak stresses at progressive hinge formations. This is similar to the effect reported for honeycomb, where micro-inertia strengthening was seen at every new hinge formation in the progressive collapse. As C1-195$^{0.5,\mathrm{T2}}$ does not strengthen to the same extent as honeycomb, the latter is judged to be have superior impact resistance under dynamic load conditions.

Table 5.8: Results of numerical dynamic models.

(a) HC

| *Model* | $\sigma^*_{max}$ $\times 10^{-3}$ | $\sigma^*_{avg}$ $\times 10^{-3}$ | $U^*$ |
|---|---|---|---|
| FE | 29.4 | 8.8 | 3.34 |
| (FE$^d$) | (35.2) | (10.1) | (3.49) |
| FE$'$ | 22.5 | 8.8 | 2.56 |
| (FE$'^d$) | (30.7) | (11.1) | (2.77) |

(b) Mi02-195

| | | | |
|---|---|---|---|
| FE | 12.9 | 4.0 | 3.23 |
| (FE$^d$) | (13.4) | (5.1) | (2.62) |
| FE$'$ | 8.3 | 3.2 | 2.59 |
| (FE$'^d$) | (10.1) | (3.3) | (3.08) |

(c) Cb02-195

| | | | |
|---|---|---|---|
| FE | 14.7 | 6.5 | 2.26 |
| (FE$^d$) | (15.0) | (7.4) | (2.02) |
| FE$'$ | 13.4 | 4.6 | 2.91 |
| (FE$'^d$) | (14.3) | (5.3) | (2.69) |

(d) Ind02-195

| *Model* | $\sigma^*_{max}$ $\times 10^{-3}$ | $\sigma^*_{avg}$ $\times 10^{-3}$ | $U^*$ |
|---|---|---|---|
| FE | 7.6 | 5.6 | 1.36 |
| (FE$^d$) | (9.4) | (7.2) | (1.3) |
| FE$'$ | 7.3 | 5.3 | 1.38 |
| (FE$'^d$) | (8.8) | (5.7) | (1.55) |

(e) C2-195$^s$

| | | | |
|---|---|---|---|
| FE | 17.4 | 5.2 | 3.36 |
| (FE$^d$) | (19.1) | (6.2) | (3.10) |
| FE$'$ | 12.0 | 3.9 | 3.07 |
| (FE$'^d$) | (17.1) | (4.2) | (4.12) |

(f) C1-195$^{0.5,T2}$

| | | | |
|---|---|---|---|
| FE | 24.1 | 9.0 | 2.68 |
| (FE$^d$) | (24.5) | (11.1) | (2.2) |
| FE$'$ | 22.6 | 8.2 | 2.76 |
| (FE$'^d$) | (23.9) | (9.5) | (2.52) |

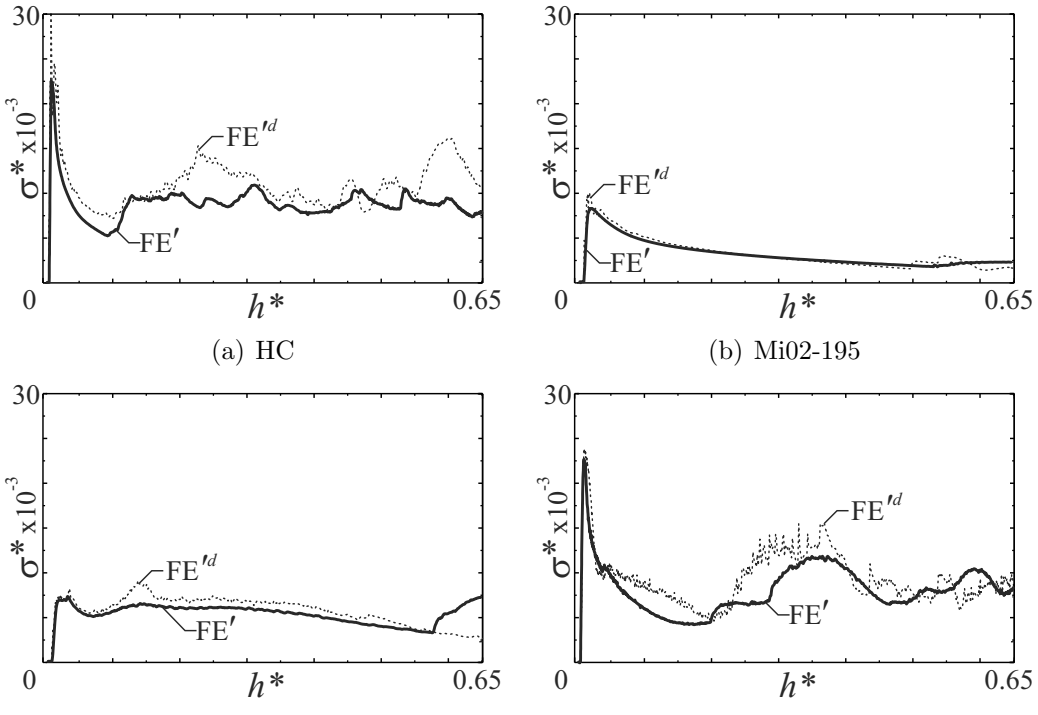


(a) HC (b) Mi02-195

(c) Ind02 (d) C1-195$^{0.5,T2}$

Figure 5.20: Dimensionless stress-strain responses of selected cores under low-velocity impact loading.

## 5.3 Foldcore Sandwich Panels

Foldcore analysis preceding this point has focused exclusively on foldcores bonded to a single face. While this enabled close observation and optimisation of core failure modes, the vast majority of energy-absorbing sandwich panel applications require both faces to be bonded to the core in order to maximise weight-specific properties. This section will conduct a brief numerical and experimental study to assess how foldcore behaviour changes when part of a full sandwich panel.

### 5.3.1 Geometry and Manufacture

Three planar foldcores are selected for further investigation: the small-scale standard foldcore Mi02 and honeycomb core HC of Section 3.5, and the second curved-crease tessellation Cb02 of Section 5.1. The indented foldcore was not included, as the attachment of a second face is certain to suppress the top-down travelling hinge failure mode, without which the indented core was seen to provide no significant benefit over the standard foldcore.

Core geometry and construction for three selected cores was identical to that described in their respective sections. Two face sheets were attached with ET538 Permabond epoxy slow-cured at room temperature for 24 hours. The face sheets were a pure aluminium sheet with thickness $t_f = 1.5$mm and material properties similar to that given in Table 3.2. The designations Mi02-S, Cb02-S, and HC-S are used to denote sandwich panel prototypes. Section views of HC-S and Cb02-S are shown in Figure 5.21. Mi02-S is not shown as it is identical in section to Cb02-S.

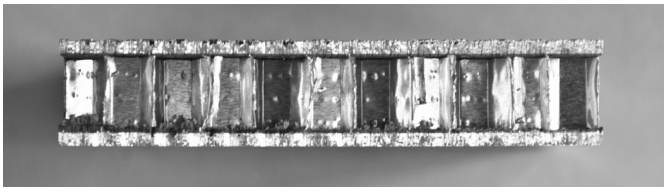

(a) HC-S

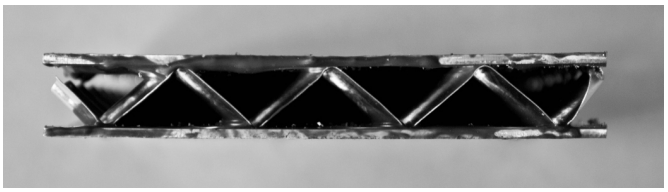

(b) Cb02-S

Figure 5.21: Section view of selected sandwich panel prototypes.

### 5.3.2 Experimental Analysis

Three samples for each sandwich type were trimmed to a 70mm x 70mm area and crushed in an INSTRON Universal Testing Machine in the manner described in Section 3.5. Relevant dimensionless stress-strain values are summarised in Table 5.9 and responses shown in Figure 5.22. Good repeatability is seen for all three sandwich types.

### 5.3.3 Numerical Analysis

Foldcore sandwich panel numerical models were set up in a manner similar to that for core-only simulations, except with two major changes: face constraints and adhesive contact surface offsets. Face constraints were included by attaching top and bottom sandwich faces to the core structure with rigid tie constraints. Rigid tie constraints were used, rather than an adhesive element, as no de-bonding was seen in experimental testing. The rigid ties were placed along node lines at the left and right bottom ridge edges, and the central top ridge edge, Figure 5.23. Periodic boundary restraints were placed on core and face sheets along all sides of the unit sandwich geometry, with a fixed restraint applied to a single node on the bottom face to prevent free body motion. Note that a honeycomb sandwich

Table 5.9: Sandwich panel prototype results.

| *Model* | $\sigma^*_{max}$ $\times 10^{-3}$ | $\sigma^*_{avg}$ $\times 10^{-3}$ | $U^*$ |
|---|---|---|---|
| Mi02-$S_1$ | 13.8 | 6.7 | 2.05 |
| Mi02-$S_2$ | 13.3 | 8.1 | 1.63 |
| Mi02-$S_3$ | 14.3 | 7.3 | 1.96 |
| Mi02-S | 13.8 | 7.3 | 1.88 |
| Cb02-$S_1$ | 21.6 | 11.6 | 1.87 |
| Cb02-$S_2$ | 21.0 | 11.1 | 1.89 |
| Cb02-$S_3$ | 20.1 | 10.9 | 1.84 |
| Cb02-S | 20.8 | 11.2 | 1.86 |

| *Model* | $\sigma^*_{max}$ $\times 10^{-3}$ | $\sigma^*_{avg}$ $\times 10^{-3}$ | $U^*$ |
|---|---|---|---|
| HC-$S_1$ | 18.3 | 9.1 | 2.01 |
| HC-$S_2$ | 17.1 | 8.9 | 1.93 |
| HC-$S_3$ | 15.8 | 8.5 | 1.86 |
| HC-S | 16.7 | 8.8 | 1.89 |

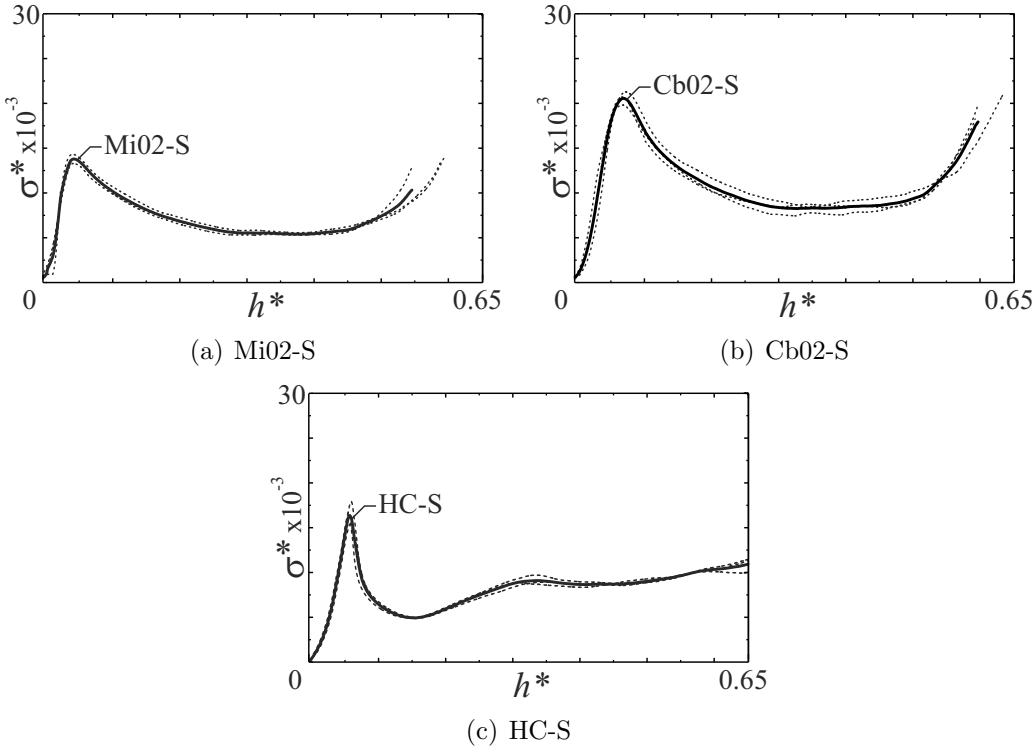


(a) Mi02-S

(b) Cb02-S

(c) HC-S

Figure 5.22: Dimensionless stress-stain responses of sandwich panel prototypes.

numerical model was not constructed as the alteration of honeycomb core failure modes with and without bonded faces has been extensively studied in literature.

From prototype measurements, the adhesive layer used to bond face and core sheets was seen to be between 0.2 and 0.7mm thick, per side. This was hypothesised to cause a reduction in foldcore stroke length, and so was incorporated in numerical models with a contact offset condition. An average contact offset of 0.4mm specified, towards the inside surface of both face sheets. The numerical sandwich models were rerun for both Mi02-S and Cb02-S geometries, with results

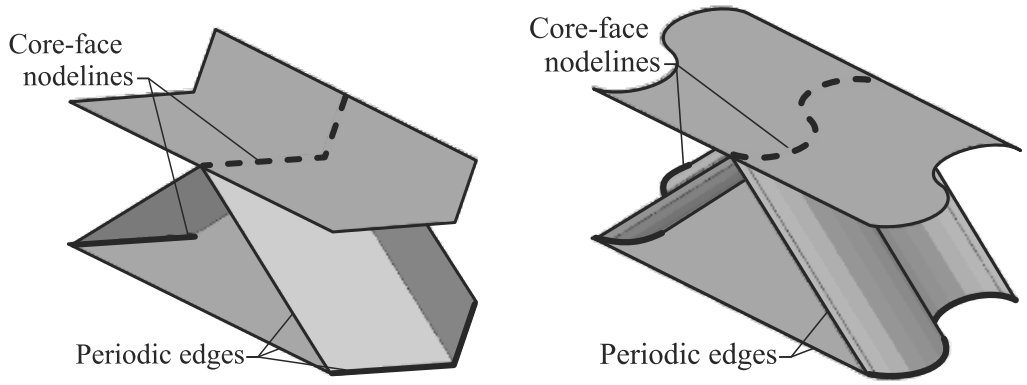


(a) Mi02-S numerical unit geometry (b) Cb02-S numerical unit geometry

Figure 5.23: Sandwich panel unit geometry and core-face node line interfaces.

summarised in Table 5.10 and selected dimensionless stress-strain results shown in Figure 5.24. Perfect FE, imperfect geometry FE′, and imperfect material and geometry FE″ models were run when appropriate, with geometric and material imperfections identical to those used for core-only numerical models.

Table 5.10: Numerical model sandwich panel results.

| *Result* | Mi02-S $\sigma^*_{max}$ $\times 10^{-3}$ | Mi02-S $\sigma^*_{avg}$ $\times 10^{-3}$ | Mi02-S $U^*$ | Cb02-S $\sigma^*_{max}$ $\times 10^{-3}$ | Cb02-S $\sigma^*_{avg}$ $\times 10^{-3}$ | Cb02-S $U^*$ |
|---|---|---|---|---|---|---|
| FE | 25.2 | 11.3 | 2.23 | 39.0 | 16.7 | 2.34 |
| FE′ | 14.1 | 8.3 | 1.71 | 29.1 | 14.0 | 2.09 |
| FE″ | | N/A | | 25.3 | 11.9 | 2.13 |

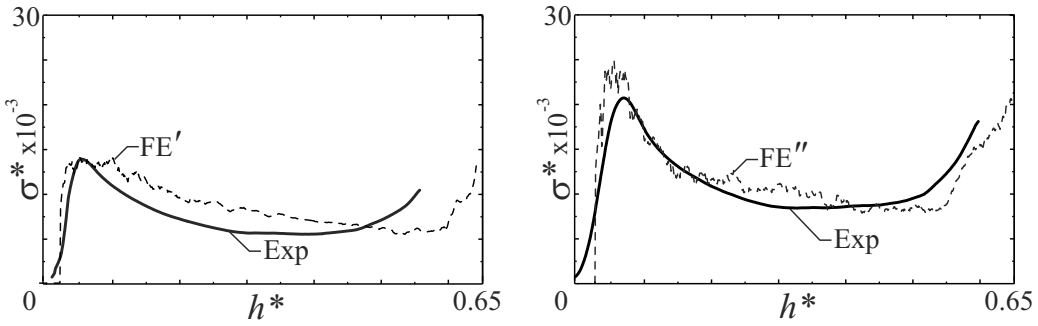


(a) Mi-S (b) Cb-S

Figure 5.24: Comparison of sandwich panel numerical and experimental dimensionless stress-strain responses.

### 5.3.4 Discussion

A comparison of the dimensionless stress-strain responses for the sandwich panels and their corresponding core-only prototypes is shown in Figure 5.25. Both

foldcores exhibit a similar change in behaviour when placed in a sandwich panel assembly, with an increase in $\sigma^*_{max}$, and a decrease in stroke length.

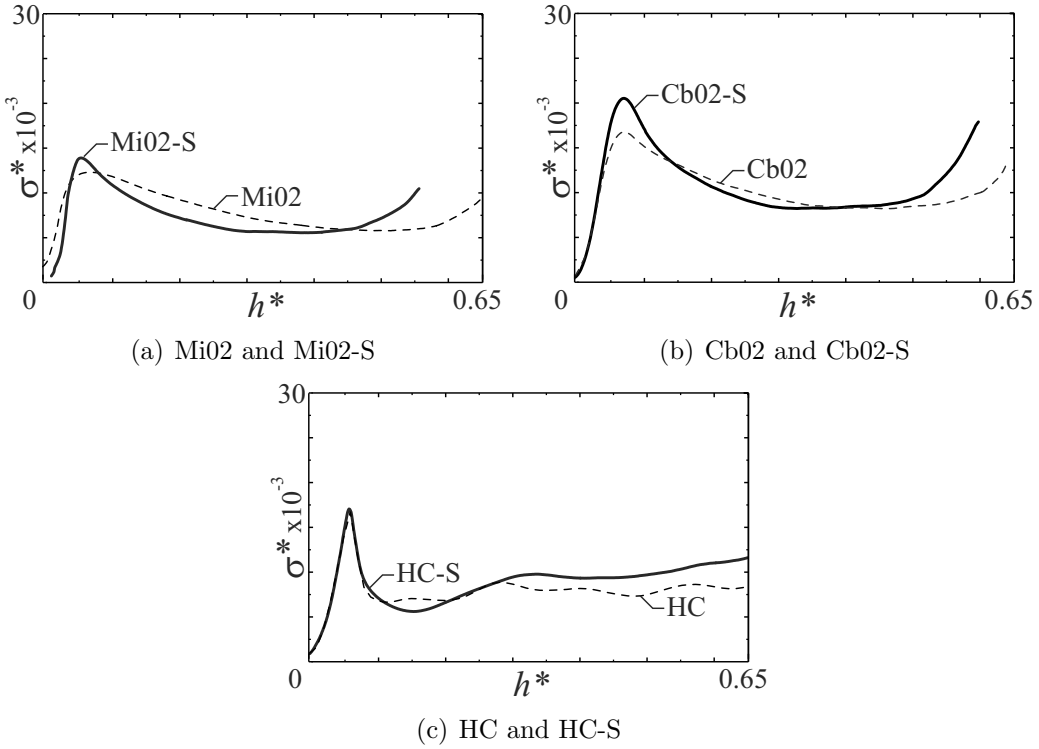


(a) Mi02 and Mi02-S

(b) Cb02 and Cb02-S

(c) HC and HC-S

Figure 5.25: Comparison of sandwich panel and core-only dimensionless stress-stain responses.

The increased peak force was hypothesised to be simply attributable to an increased core stiffness from top ridge restraint, and the decreased stroke length was hypothesised to be simply attributable to a reduction in effective crush height caused by the thickness of the face adhesive layers. As such, these two factors were incorporated into sandwich numerical models. For Mi02-S, it can be seen that the sandwich numerical models successfully predict both the increased peak stress and reduced stroke length. FE′ values for $\sigma^*_{max}$ and $\sigma^*_{avg}$ are seen to be within 2.6% and 12.7% of experimental values, respectively. Similarly, the Cb02-S model successfully predicted the experimental sandwich behaviour, with FE″ values for $\sigma^*_{max}$ and $\sigma^*_{avg}$ within 21.6% and 6.4% of experimental values, respectively.

In terms of average reaction stresses $\sigma^*_{avg}$, the foldcore sandwich panel responses are essentially unchanged from core-only models, with $\sigma^*_{avg}$ for both foldcore sandwich panels within 6% of core-only prototypes. This suggests that the failure more of the

foldcores also remained essentially unchanged. Mi02-S FE′ and Cb02-S FE″ core failures are shown in Figure 5.26, with sandwich faces removed for clarity. It can be seen that the failure modes are unchanged from the core-only numerical failure modes shown in Figures 3.45(a) and 5.11(b), respectively. Note the prototype sandwich panel core failures could not be shown, as the face sheets could not be removed without distorting the crushed core plates.

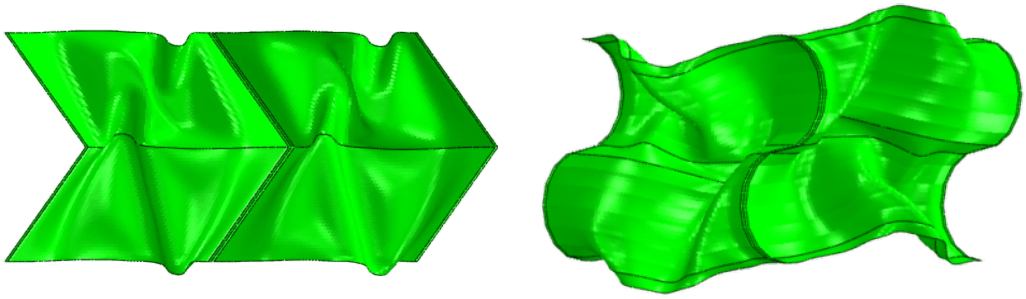

(a) Mi02-S FE′S (b) Cb02-S FE″

Figure 5.26: Crushed sandwich panel cores.

Finally, the honeycomb sandwich panel had a $\sigma^*_{max}$ and the stroke length that remained almost unchanged from the core-only response. It also showed a slight increase of 16% for $\sigma^*_{avg}$, which was simply attributed to the stabilising effect of the sandwich faces.

To conclude, the attachment of sandwich panel faces does not significantly alter the impact resistance of either the straight-crease foldcore, the curved-crease foldcore, or the honeycomb core. Therefore the conclusions made in previous honeycomb comparison Sections 3.5.6 and 5.1.3 are unchanged. This study has also successfully validated a numerical sandwich model for use in the following analysis of foldcore sandwich shells.

## 5.4 Foldcore Sandwich Shells

As discussed in Section 2.1, existing single-curved honeycomb sandwich shells are limited in terms of possible local unit geometries and global panel curvatures. The following section aims to conduct a preliminary investigation into whether straight-crease, single-curved foldcore sandwich shells offer a performance benefit over existing curved honeycomb variants, in terms of out-of-plane impact resistance.

### 5.4.1 Preliminary Numerical Analysis

#### R120 Sandwich Panel Geometry

Three foldcore shells, with Arc-Miura, Non-Developable Miura, and Non-Flat Foldable Miura core types, were designed with an inner radius of 120mm and an outer radius of 130mm. This bend radius was selected as it is equivalent to the curvature limit beyond which the shear strength coefficients of single-curved honeycomb variants deteriorate (Hexcel Corporation, 2006a). The Arc pattern was excluded as a core type, as the panel depth varies widely at different orientations, which would cause a correspondingly wide variation in impact resistance. It is therefore unsuitable for impact resistance and is excluded from the present study.

In addition to the two radii, the foldcores were designed such that they spanned a total rotation of approximately $\pi/4$, and had a configuration and density similar to the planar foldcore prototypes when constructed from a $t_p = 0.2$mm aluminium sheet. The geometric parameters for each foldcore shell are listed in Table 5.11, and the shells shown in Figure 5.27(a), (c), and (e). The model designations AM02-R, ND02-R, and NF02-R are used to denote 120mm radius foldcores with Arc-Miura, Non-Developable Miura, and Non-Flat Foldable Miura core types, respectively.

Table 5.11: Single-curved foldcore shell geometric parameters.

| *Model* | $a$ (mm) | $b$ (mm) | $\phi$ (°) | $m$ | $n$ | $\phi_2$ (°) | $b_{i/o}$ (mm) | $\theta_A$ (mm) | $d_w$ (mm) | $\alpha$ |
|---|---|---|---|---|---|---|---|---|---|---|
| AM02-R | 15 | 7.5 | 64.8 | 3 | 9 | 60.4 | - | 127.8 | 12.2 | 0.029 |
| ND02-R | 15 | 7.5 | 64.8 | 17 | 3 | - | 6.9 | 131.4 | 22.6 | 0.029 |
| NF02-R | 15 | 7.5 | 64.8 | 9 | 3 | - | 26.5 | 128.5 | 22.6 | 0.028 |
| AM02-r | 12.4 | 7.5 | 64.8 | 3 | 9 | 58.6 | - | 100.0 | 10.4 | 0.041 |
| ND02-r | 12.8 | 7.5 | 62.5 | 17 | 3 | - | 6.4 | 100.0 | 16.1 | 0.041 |
| NF02-r | 12.4 | 7.5 | 63.5 | 13 | 3 | - | 15.8 | 100.0 | 15.2 | 0.040 |

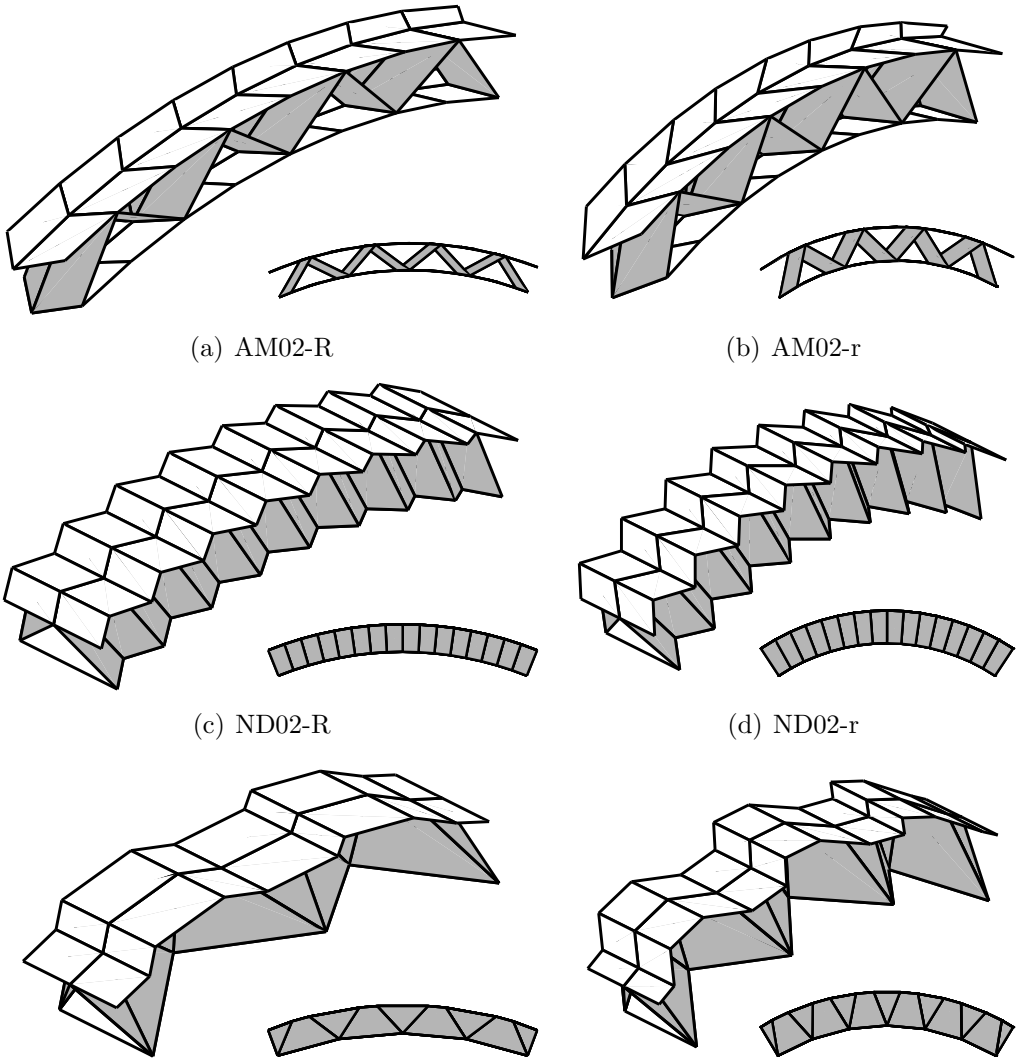

(a) AM02-R (b) AM02-r

(c) ND02-R (d) ND02-r

(e) NF02-R (f) NF02-r

Figure 5.27: Isometric and sectional views of foldcore sandwich shell geometry.

### R60 Sandwich Panel Geometry

A second set of three foldcore shells were designed at a tight curvature, with an inner radius of 60mm and an outer radius of 70mm. The same three core types were used as above, and their required geometric parameters selected with the same rationale, except with the panels spanning a total rotation of approximately $\pi/3$. The model designations AM02-r, ND02-r, and NF02-r are used to denote 60mm radius foldcores with an Arc-Miura, Non-Developable Miura, and Non-Flat Foldable Miura core types, respectively. Parameters are listed in Table 5.11 and the foldcores shown Figure 5.27(b), (d), and (f).

### Numerical Analysis and Discussion

Numerical models for each shell type were set up in a similar manner to that described in Section 5.3, with two minor differences. First, the shell numerical models consisted of a unit core geometry tessellated in the direction of curvature, and so the end periodic boundary constraints were removed. Side periodic constraints were retained. Second, the faceted face geometries developed in Section 4.3 were used for the ND and NF models, however not for the AM models, due to difficulties in meshing a common node line for core and face tie constraints. Instead, continuously curved inner and outer faces were used. These sandwich assemblies were crushed between a single-curved rigid base plate and a planar rigid top plate, in a direction perpendicular to the foldcore curvature. Remaining numerical model features, including material properties, contact conditions, loading speed, and core-face ties, were all as described previously.

The force-displacement responses of the preliminary numerical models are shown in Table 5.12 and Figure 5.28(a)-(b). Note that the dimensionless parameter $\sigma^*$ is not used in this case, as the crush area varies with crush height $h$. Instead, to

Table 5.12: Preliminary foldcore shell numerical model results.

(a) R120 foldcores

| *Model* | $P^*_{max}$ (mm) | $P^*_{avg}$ (mm) | $U^*$ |
|---|---|---|---|
| AM02-R | 1.34 | 1.00 | 1.34 |
| ND02-R | 1.14 | 0.97 | 1.17 |
| NF02-R | 0.84 | 0.60 | 1.40 |

(b) R60 foldcores

| *Model* | $P^*_{max}$ (mm) | $P^*_{avg}$ (mm) | $U^*$ |
|---|---|---|---|
| AM02-r | 2.23 | 1.61 | 1.39 |
| ND02-r | 2.12 | 1.77 | 1.20 |
| NF02-r | 1.67 | 1.10 | 1.52 |

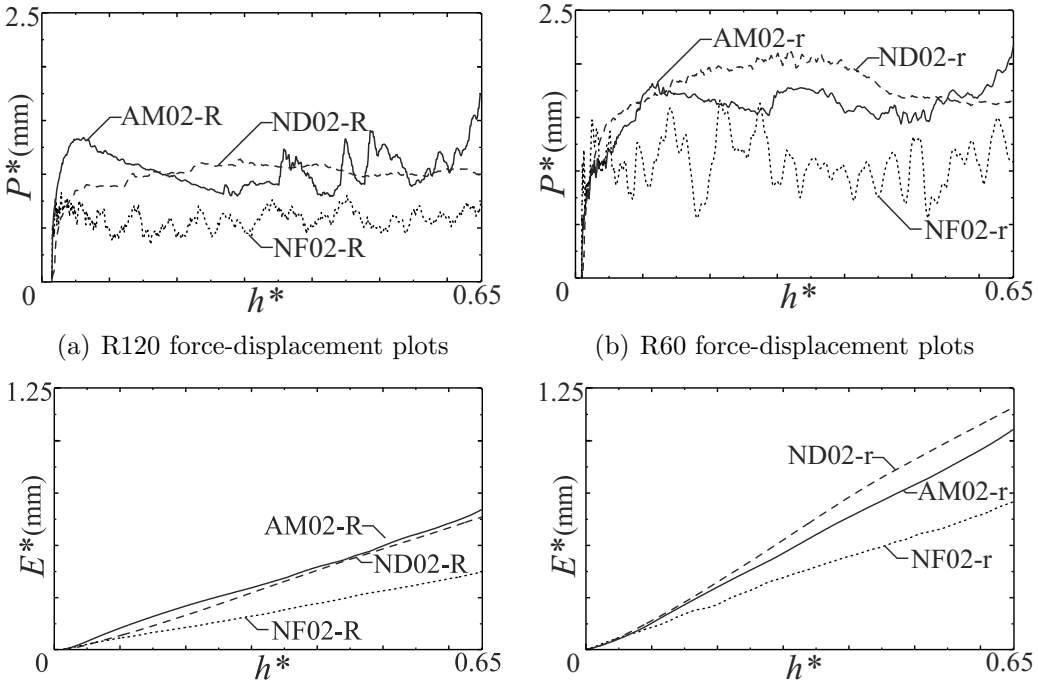


(a) R120 force-displacement plots

(b) R60 force-displacement plots

(c) R120 energy absorption plots

(d) R60 energy absorption plots

Figure 5.28: Normalised responses of preliminary numerical shell models.

enable comparison between different foldcores, the force parameter is normalised by unit width with $P^* = P/(d_w \sigma_Y)$ where unit widths $d_w$ are given in Table 5.11. The dimensionless height parameter $h^*$ is as used previously. Figure 5.28(c)-(d) shows the normalised energy absorption calculated as the integral of the $P^* - h^*$ curve.

Comparing the three R120 model responses shown in Figure 5.28(a) and (c), it can be seen that ND02-R and AM02-R have similar force-displacement responses, with $P^*_{avg}$ within 3.1% and $P^*_{max}$ within 17.5% of each other, respectively. The third foldcore NF02-R has a different force-displacement response, which is seen to be much weaker than the ND02-R and AM02-R responses. All three R120 foldcores have very uniform failures, with a minimum uniformity of $U^* = 1.17$

in ND02-R approaching the ideal ratio of unity. A similar trend is seen in the R60 foldcore responses, Figure 5.28(b) and (d), where it can be seen that AM02-r and ND02-r possess similar behaviours, and NF02-r possesses a different, weaker response. The R60 foldcores are all seen to have a stronger response than their R120 comparators, however this is most likely largely attributable to the increased density of the R60 foldcores. There is still good uniformity for all R60 core failure responses.

To explain the similarity between ND and AM responses, and the uniformity of the foldcore responses, the failure modes and Von-Mises stresses of all six foldcores are plotted in section and projected onto an unfolded pattern geometry, Figure 5.29. Note that as the non-developable ND02-R and ND02-r cores cannot be unfolded, their stress is projected onto an equivalent area Miura pattern. From the stress distributions in the unit cell geometries, it can be seen that the ND and AM cores have similar plate buckling failures in unit cells, particularly in cells which are impacted in a near-perpendicular direction. The slightly higher $P^*_{max}$ of the AM-type cores can be attributed to two such cells being initially impacted simultaneously. The failure mode of the units is seen to be similar to the Mi02 cores of Chapter 3, suggesting that a planar Miura-base foldcore unit can be altered for single-curvature and be expected to retain a similar failure mode. The failure of the NF cores shows that the different NF unit geometry causes a weaker, wide-plate type buckling mode. The larger spacing between impacted NF units also causes it to be have a less uniform response than the ND or AM types, at both curvatures. The ND cores have a smooth collapse progression across adjacent unit cells, and so have the most uniform response.

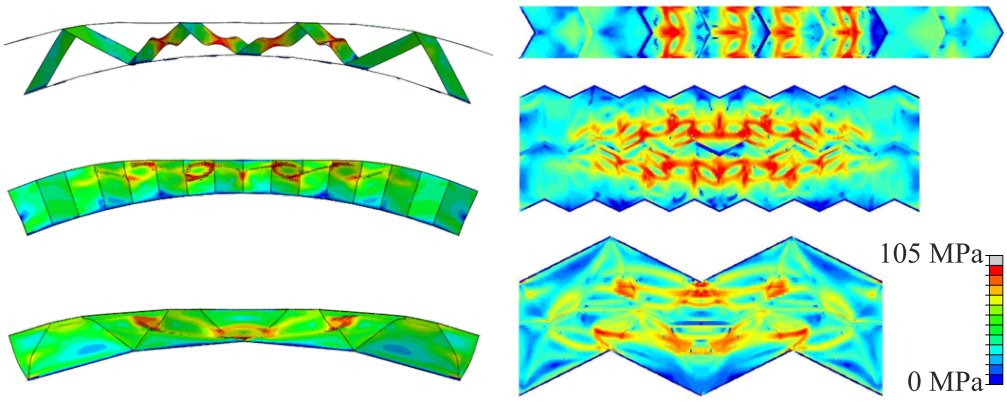


(a) From top to bottom, AM120, ND120, and NF120, at $h^* = 32\%$

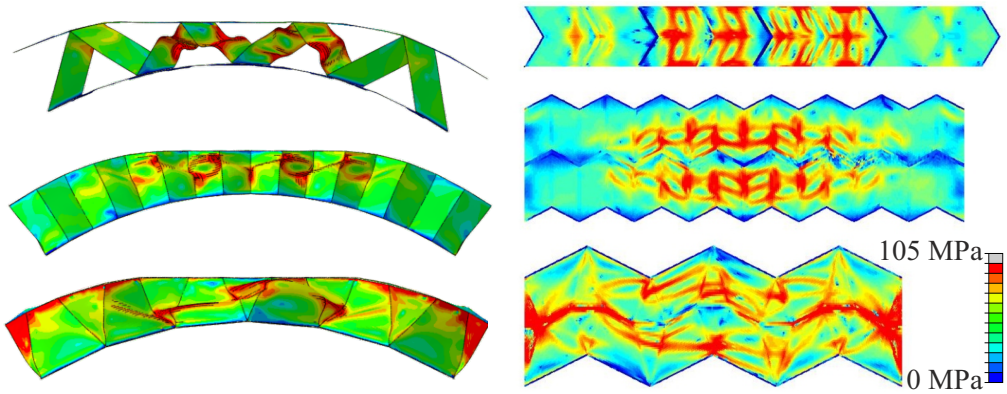


(b) From top to bottom, AM60, ND60, and NF60, at $h^* = 32\%$

Figure 5.29: Von-Mises stress plots in sectional view, on left; and unfolded projection, on right.

### 5.4.2 Experimental Analysis

Results from the preliminary numerical study suggest that the ND and AM type foldcores are capable of preserving significant impact resistance at longitudinal and lateral curvatures, respectively. Therefore the next stage of the single-curved foldcore investigation will construct prototypes of these two foldcores for comparison with a single-curved honeycomb variant. An Ox-core honeycomb variant was chosen for comparison, as it can be manufactured by over expanding the honeycomb used for the planar HC prototypes in Section 3.5.

### R120 Core Manufacture

The foldcore shells were manufactured using a two-stage sequential stamping process similar to that used for the small-scale indented foldcores. First, planar foldcores with similar unit cell geometry were manufactured as described in Section 3.5. Second, the planar cores were stamped in a further mould pair corresponding to the final curved R120 geometry, with the additional moulds for AM02-R and ND02-R shown in Figure 5.30. As the curved unit cell geometry was only slightly different to the planar unit cell geometry, is was thought that such a process would introduce few additional imperfections, and indeed inspection of the formed foldcores, 5.31(a)-(b), shows that the foldcore shells have acceptably few visible defects.

To form the comparative honeycomb core, the Corex 1/4" 3000 Alloy Series honeycomb used previously was over-expanded as shown in Figure 5.31(c), and subsequently bent to the desired radius. The over-expanded core has a slightly reduced density compared to the original honeycomb, with a core density of approximately $\alpha = 2.8\%$.

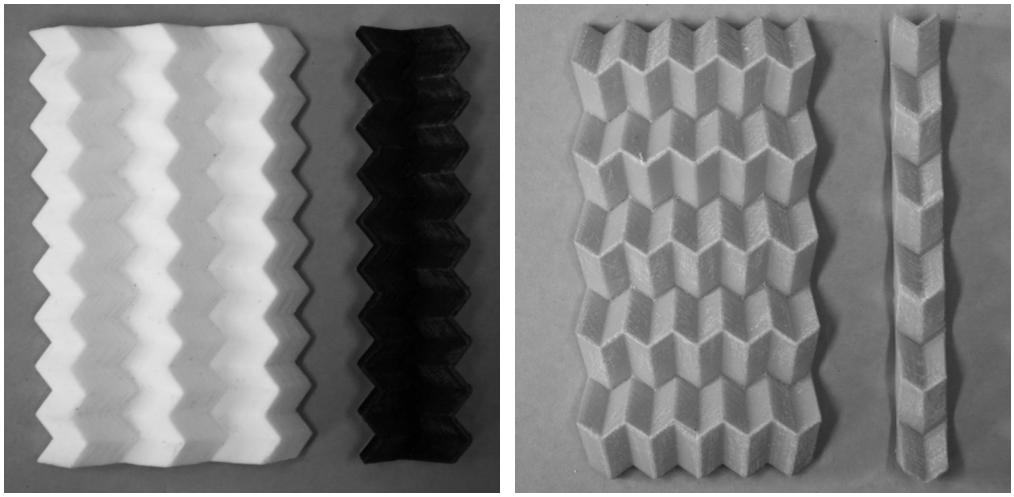

Figure 5.30: AM02-R mould geometry, on left; ND02-R mould geometry, on right.

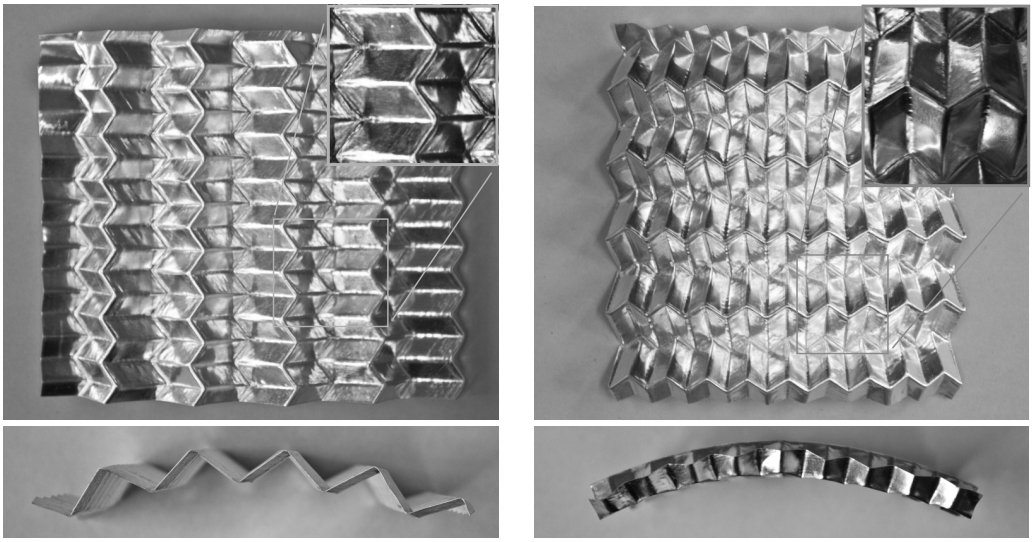

(a) AM02-R core

(b) ND02-R core

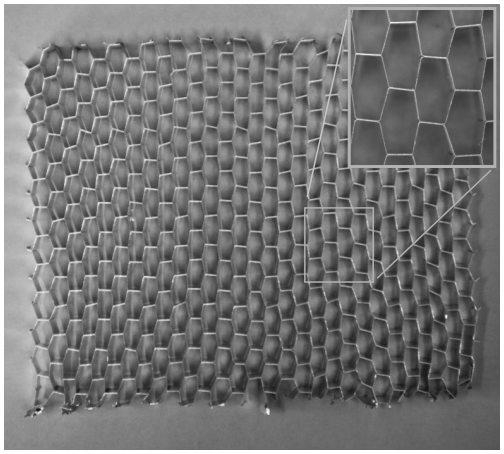

(c) Unbent OX-R core

Figure 5.31: R120 prototype formed cores.

### R60 Core Manufacture

The construction of R60 foldcores, AM02-r and ND02-r, was attempted using the process described for the R120 core manufacture, expect with a different first-stage planar geometry. The planar geometry was designed with parameters $a = 12.4$mm, $b = 7.5$mm, $\phi = 63.5°$, $m = 9$, $n = 5$, and sequential folded configurations set at $\eta_A = 142°$, $105°$, and $75.5°$. The two subsequent curved mould pairs were set corresponding to the final shape of the AM02-r and ND02-r cores. The final formed cores are shown in Figure 5.32 and it can be seen that there is extensive damage in the core structures, with widespread cracking at crease locations in both foldcores.

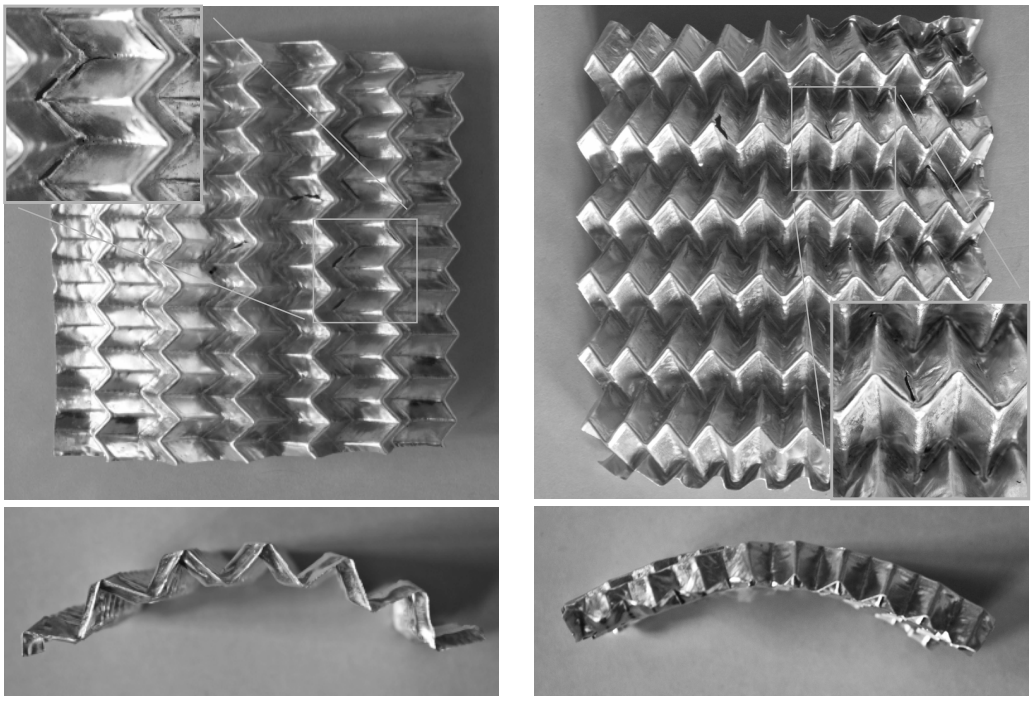

(a) AM02-r core (b) ND02-r core

Figure 5.32: R60 prototype formed cores.

This cracking occurred in the final stage of the planar core stamping, and is thought primarily attributable to the very large width contraction required for the unit geometry. This unit width contraction, from unfolded to final configuration, is 3.1mm, compared to 2.1 mm required for the curved-crease prototypes, and 1.3mm required for the straight-crease and R120 prototypes. It is possible that additional moulds could successfully form R60 foldcore prototypes, but due to time and budget constraints these are excluded from the present study. An R60 Ox-core prototype, deemed OX-r, is still constructed for later numerical comparison purposes, using the over-expanded core shown in Figure 5.31(c).

### Experimental Method and Results

Continuously curved top and bottom faces were manufactured for the three R120 cores and the OX60 core by rolling 1.5mm aluminium plates through a sheet metal bender to the desired face radius. These were bonded to the curved foldcores in the manner described previosly, and were trimmed to approximately an 80mm width

and 90mm arc length, in the case of the R120 prototypes, and 60mm arc length, in the case of the OX-r prototype, Figure 5.33. Three samples for both tessellations were crushed in an INSTRON Universal Testing Machine in the manner described in Section 3.5, except with a curved hardwood baseplate designed to fit the inside core radius, Figure 5.34.

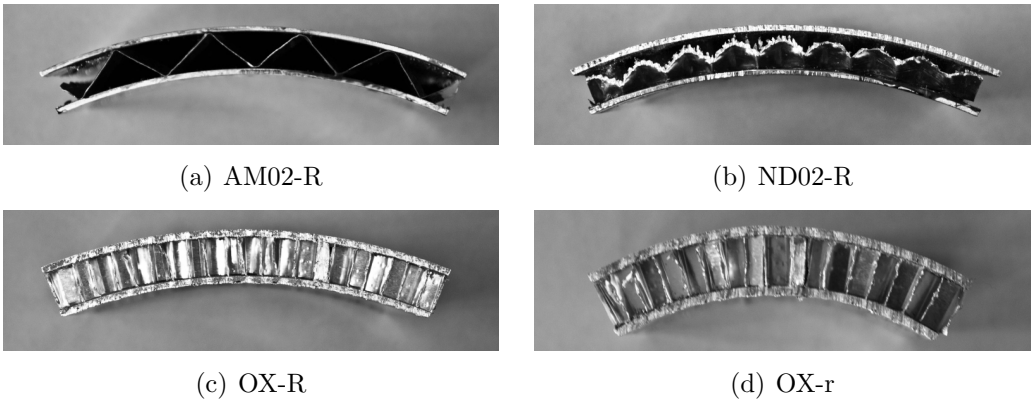

(a) AM02-R (b) ND02-R

(c) OX-R (d) OX-r

Figure 5.33: Single-curved sandwich shell prototypes.

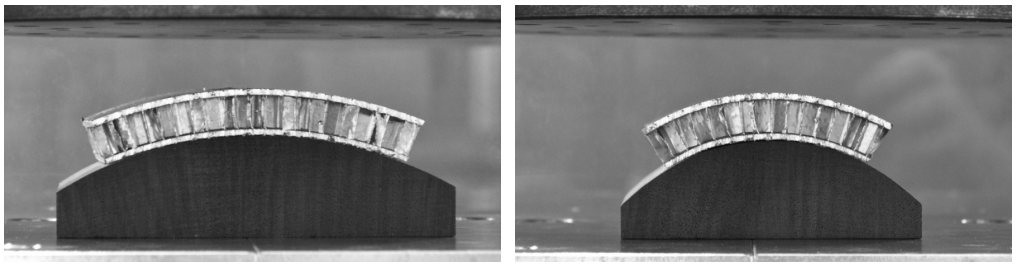

Figure 5.34: R120 and R60 rigid base plates.

Relevant values for the single-curved prototypes are summarised in Table 5.13 and the normalised force-displacement responses plotted in Figure 5.35. The non-subscripted model designations AM02-R, ND02-R, OX-R, and OX-r are used to denote the average response of the corresponding three individual prototype responses, designated with subscripts $1-3$. It can be seen that there is good repeatability for all prototypes.

### Numerical Analysis

Comparative numerical models with perfect and imperfect geometries were set up for the AM02-R and ND02-R experimental prototypes, with FE models identical

Table 5.13: Single-curved prototype results.

| *Model* | $P^*_{max}$ (mm) | $P^*_{avg}$ (mm) | $U^*$ | *Model* | $P^*_{max}$ (mm) | $P^*_{avg}$ (mm) | $U^*$ |
|---|---|---|---|---|---|---|---|
| AM02-$R_1$ | 0.74 | 0.61 | 1.21 | OX-$R_1$ | 0.57 | 0.41 | 1.38 |
| AM02-$R_2$ | 0.72 | 0.54 | 1.33 | OX-$R_2$ | 0.59 | 0.45 | 1.30 |
| AM02-$R_3$ | 0.80 | 0.61 | 1.31 | OX-$R_3$ | 0.58 | 0.44 | 1.30 |
| AM02-R | 0.75 | 0.59 | 1.27 | OX-R | 0.58 | 0.44 | 1.33 |
| ND02-$R_1$ | 0.83 | 0.66 | 1.26 | OX-$r_1$ | 0.53 | 0.37 | 1.45 |
| ND02-$R_2$ | 0.82 | 0.66 | 1.25 | OX-$r_2$ | 0.51 | 0.38 | 1.34 |
| ND02-$R_3$ | 0.84 | 0.67 | 1.26 | OX-$r_3$ | 0.49 | 0.34 | 1.46 |
| ND02-R | 0.83 | 0.66 | 1.25 | OX-r | 0.51 | 0.36 | 1.41 |

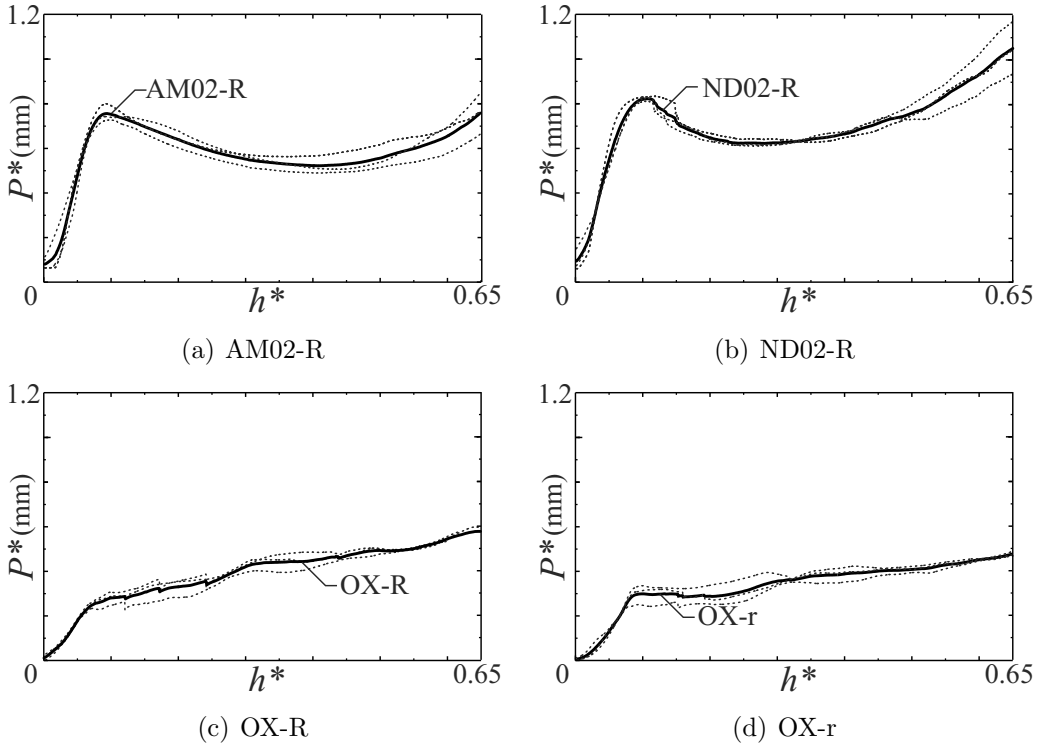


(a) AM02-R (b) ND02-R

(c) OX-R (d) OX-r

Figure 5.35: Normalised force-displacement responses of single-curved prototypes.

to those used in the preliminary numerical study. Imperfect geometry was generated by superimposing buckling modes generated from an inwards radial unit load applied along the outer core ridges. Note that a second method for generating buckled imperfections, calculated from a buckled single cell unit geometry tessellated along the radius of curvature, was trialled and was seen to provide a near-identical force-displacement response as the first imperfection generation method.

Relevant values from numerical models are summarised in Table 5.14, and results plotted in Figure 5.36(a)-(b). The perfect and imperfect sandwich models are given the designation FE-S and FE-S′, respectively. Comparing FE-S and FE-S′ models, it can be seen that the single-curved shells are much less sensitive to the geometric imperfections, compared to planar panels. This is thought to be attributable to the oblique angle with which single-curved core units are impacted. This causes an eccentric load to be applied to the core units, which is likely to cause a low-energy failure mode formation prior to the introduction of imperfect numerical geometry.

Comparing numerical and experimental results, it can be seen that there is reasonable correlation between FE-S′ models and experimental results, although the error is higher than for previous planar model comparisons. For AM02-R, the maximum variation in $P^*_{max}$ and $P^*_{avg}$ is 24.6% and 32.7%, respectively. For ND02-R, the maximum variation in $P^*_{max}$ and $P^*_{avg}$ is 17.9% and 20.2%, respectively. These additional sources of error are likely due to a complex variety of factors, including material deformation occurring as a result of the fourth stamping stage, imperfect bonding and trimming during sandwich panel assembly, and differences between the alignment of numerical and experimental cores relative to the top crushing plate.

However one additional factor, de-bonding between core and face panels, is thought to be the main cause for the numerical-experimental discrepancies. Some de-bonding was seen in both AM02-R and ND02-R prototypes, typically at the outermost core units towards the middle and final stages of the crush. As numerical models use rigid ties constraints between core and face surfaces, this de-bonding behaviour was not accounted for in the numerical simulation. As an approximate method for assessing the effect of de-bonding, core-only numerical models were analysed. This was done as core-only geometry was considered analogous to an extreme lower-bound corresponding to complete de-bonding. These models were given the designations FE-C and FE-C′ and results are shown in Table 5.14 and

Table 5.14: Comparison of numerical and experimental foldcore shell results.

| *Result* | AM02-R | | | ND02-R | | |
|---|---|---|---|---|---|---|
| | $P^*_{max}$ (mm) | $P^*_{avg}$ (mm) | $U^*$ | $P^*_{max}$ (mm) | $P^*_{avg}$ (mm) | $U^*$ |
| Experimental | 0.75 | 0.59 | 1.27 | 0.83 | 0.66 | 1.25 |
| FE-S | 1.34 | 1.00 | 1.34 | 1.14 | 0.97 | 1.17 |
| FE-S′ | 0.94 | 0.78 | 1.19 | 0.98 | 0.79 | 1.23 |
| FE-C | 0.91 | 0.67 | 1.37 | 0.81 | 0.65 | 1.25 |
| FE-C′ | 0.61 | 0.54 | 1.15 | 0.75 | 0.57 | 1.31 |

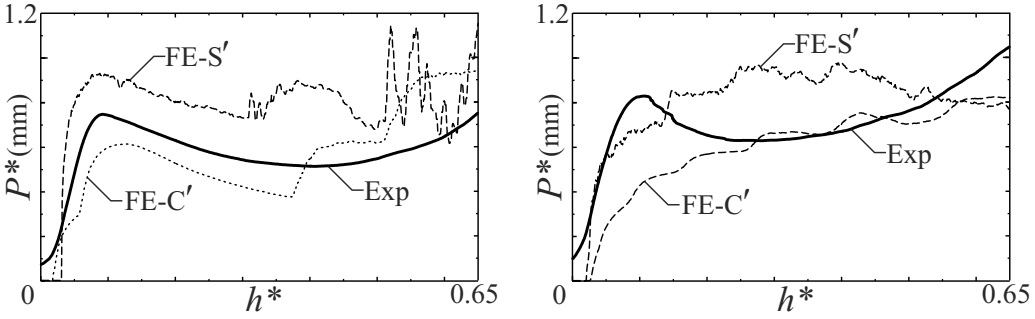


(a) AM02-R (b) ND02-R

Figure 5.36: Comparison of experimental and numerical FE-S′ and FE-C′ responses.

Figure 5.36(c)-(d). It can be seen that there is better correlation with experiments in the middle and final stages of the crush, suggesting that experimental face debonding, and the lack of such behaviour in comparative FE-S models, is the main cause of numerical and experimental discrepancies.

It is possible to include core-face de-bonding in numerical models, but only after an extensive adhesive testing process. This is only tangentially relevant to the primary purpose of the present study, which is to investigate single-curved core failure modes and energy absorption mechanisms. The FE-S′ numerical models are judged to be adequate the this purpose and so will not be further refined.

### 5.4.3 Discussion

#### Foldcore Sandwich Shell Comparison

A direct comparison between R120 foldcore prototypes is shown in Figure 5.37. It can be seen that the ND120 type shell is slightly stronger than the AM02-R type, with a 10.7% higher $P^*_{max}$ and an 11.9% higher $P^*_{avg}$. This is a fairly negligible difference that is within the tolerance of manufacturing and experimental errors. As such, the conclusions made in Section 5.4.1, specifically that ND and AM type shells have similar plate buckling unit failures and correspondingly similar energy-absorption capabilities, are unchanged.

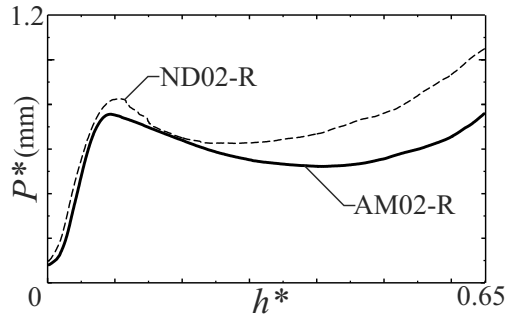


Figure 5.37: Comparison of ND02-R and AM02-R experimental prototypes.

#### R120 Honeycomb Comparison

For direct comparison with the honeycomb sandwich shells, the AM02-R and ND02-R FE-S′ models were rerun with the honeycomb material properties given in Table 3.16(b). Note that only core properties were changed to the high-strength alloy, with face sheet material remaining unchanged from previous models, which matched the constructed OX prototypes. The new foldcore models were given the designation AM02-R-195 and ND02-R-195. Relevant values are summarised in Table 5.15(a), the normalised force-displacement responses of the two foldcore FE-S′ numerical models are plotted alongside the response of the OX-R experimental results in Figure 5.38(a), and the normalised energy absorption of the three

Table 5.15: Results of shell models with 3003-H19 material properties.

(a) R120 results

| *Model* | $P^*_{max}$ (mm) | $P^*_{avg}$ (mm) | $U^*$ |
|---|---|---|---|
| OX-R | 0.58 | 0.44 | 1.33 |
| AM02-R-195 | 0.43 | 0.31 | 1.40 |
| ND02-R-195 | 0.37 | 0.30 | 1.23 |

(b) R60 results

| *Model* | $P^*_{max}$ (mm) | $P^*_{avg}$ (mm) | $U^*$ |
|---|---|---|---|
| OX-r | 0.51 | 0.36 | 1.41 |
| AM-r-195 | 0.35 | 0.24 | 1.42 |
| ND-r-195 | 0.27 | 0.21 | 1.28 |

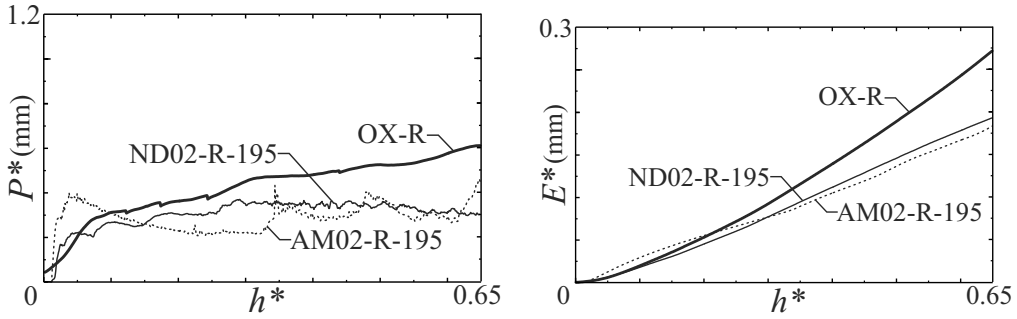


(a) Force-displacement comparison (b) Energy absorption comparison

Figure 5.38: Normalised responses of R120 3003-H19 shells.

responses are shown in Figure 5.38(b).

In comparing the shell responses, there are several interesting features to note. First, it can be seen that the honeycomb shell is stronger than either of the foldcores, with a 35-57% higher $P^*_{max}$ and 42-47% higher $P^*_{avg}$. However, it can be seen that despite having an overall lower peak stress, the AM02-R-195 core has a higher initial stress, which suggests that is might be capable of higher static strength than an Ox-Core. Also of note is the ND02-R-195 response, which is seen to have an extremely good uniformity ratio of $U^* = 1.23$. As with the indented foldcore, this low uniformity might therefore make the ND-type foldcore suitable for applications where uniformity of response is critical, for example bicycle helmets. Both of these favourable foldcore features are likely to be controllable or improvable with changes to foldcore geometric parameters, an ability that is not possible with commercial honeycomb. This will be examined in the next section.

### R60 Honeycomb Comparison

Although the R60 foldcore prototype construction was not successful, exploratory AM02-r and ND02-r FE-S′ numerical models can be constructed in the same manner as was done for R120 numerical comparison models. R60 core geometry is obtained from Section 5.4.1, with material thickness reduced to $t_p = 0.15$mm so that the foldcores and OX-r core had comparable densities of approximately 3%. The foldcore FE-S′ models were run directly with high-strength alloy material properties and given the designations AM02-r-195 and ND02-r-195. The numerical, normalised foldcore responses are plotted alongside the OX-r experimental response in Figure 5.39. Relevant values are summarised in Table 5.15(b).

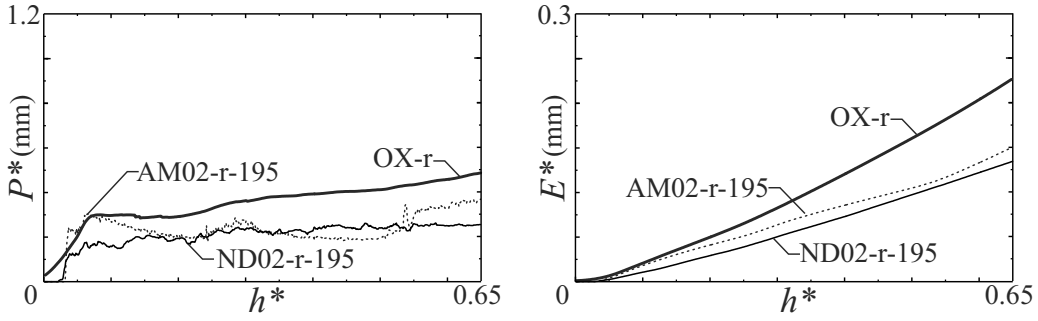


(a) Force-displacement comparison (b) Energy absorption comparison

Figure 5.39: Normalised responses of R60 3003-H19 shells.

The honeycomb again has the strongest overall force, the AM-type core has the highest initial force, and the ND-type core has the most uniform response. It should again be reiterated that these findings are preliminary, as non-validated numerical foldcore models are being compared to experimental honeycomb results. The overestimation of foldcore performance by rigid-tie numerical bonding constraints is likely to be more extensive for R60 cores than it was for R120 cores. However, the R60 foldcore performance has been penalised with extensive geometric imperfections, with the buckled geometry displacement magnitude of 0.25mm giving geometric imperfections of $167\%t_p$ relative to the reduced R60 core thickness.

### 5.4.4 Parametric Study

As has been seen previously, a parametric study on foldcore geometry can significantly improve energy absorption capability. A brief parametric study is conducted here on an ND-type R120 shell to similarly assess potential improvements to failure modes and energy absorption capabilities.

#### Geometry

A set of ND-type foldcores was designed according to the R120 geometric constraints, that is an inner radius of 120mm, an outer radius of 130mm, a total rotation of $\pi/4$, and a density of approximately 3%. A Non-Developable Miura-type geometry requires seven parameters to completely define, not including the $t_p$ parameter which is altered directly to give the required density. Applying the above design constraints results in a four free variables. As the core has side periodic boundary constraints and is normalised by panel depth, $n$ is set to 3. The remaining three variables therefore make up the configuration space, and are set as $m$, $\phi$, and a dimensionless parameter $\Delta b^* = \Delta b/a = (b_o - b_i)/(2a)$. These three parameters, along with the design dimensions, are substituted into Equations (A.4), (4.6–7) to solve for dimensional constants and the configuration variable.

Four values of $\phi$ were selected corresponding to those used for the planar D2-D5 models, that is $\phi = 52.50°$, $64.8°$, $70.6°$, and $77.1°$. These were each run at $m = 17$ and $m = 11$ and $\Delta b^* = 1/50$ and $\Delta b^* = 1/37.5$. Designations P1-P4 were used to denote models with a given $\phi$, and superscripted to denote a given $\Delta b^*$ and $m$. For example, $\text{P2}^{50,17}$ has $\phi = 64.8°$, $\Delta b^* = 1/50$, and $m = 17$, which closely corresponds to the ND02-R experimental configuration. Model parameters are listed in Table 5.16 and shell geometries are shown in Figure 5.40.

Table 5.16: ND-type sandwich shell parameter study parameters.

| *Model* | $a$ (mm) | $b_i$ (mm) | $b_o$ (mm) | $\phi$ (°) | $m$ | $n$ | $t_p$ (mm) | $\theta_A$ (°) | $d_w$ (mm) |
|---|---|---|---|---|---|---|---|---|---|
| $P1^{50,17}$ | 18.2 | 8.8 | 9.5 | 52.5 | 17 | 3 | 0.21 | 119.7 | 30.5 |
| $P2^{50,17}$ | 15.2 | 7.3 | 7.9 | 64.8 | 17 | 3 | 0.20 | 131.4 | 22.8 |
| $P3^{50,17}$ | 14.2 | 6.8 | 7.4 | 70.6 | 17 | 3 | 0.19 | 138.9 | 20.1 |
| $P4^{50,17}$ | 13.3 | 6.4 | 6.9 | 77.1 | 17 | 3 | 0.19 | 149.7 | 17.5 |
| $P1^{37.5,17}$ | 15.5 | 9.9 | 10.8 | 52.5 | 17 | 3 | 0.17 | 99.4 | 23.7 |
| $P2^{37.5,17}$ | 12.8 | 8.2 | 8.9 | 64.8 | 17 | 3 | 0.15 | 108.1 | 16.0 |
| $P3^{37.5,17}$ | 11.9 | 7.6 | 8.2 | 70.6 | 17 | 3 | 0.13 | 113.7 | 12.9 |
| $P4^{37.5,17}$ | 11.0 | 7.1 | 7.7 | 77.1 | 17 | 3 | 0.11 | 121.5 | 9.4 |
| $P1^{50,11}$ | 26.6 | 12.7 | 13.8 | 52.5 | 11 | 3 | 0.26 | 143.7 | 49.2 |
| $P2^{50,11}$ | 22.7 | 10.9 | 11.8 | 64.8 | 11 | 3 | 0.26 | 153.4 | 40.9 |
| $P3^{50,11}$ | 21.6 | 10.4 | 11.2 | 70.6 | 11 | 3 | 0.25 | 158.8 | 38.3 |
| $P4^{50,11}$ | 20.7 | 9.9 | 10.8 | 77.1 | 11 | 3 | 0.25 | 165.5 | 36.3 |
| $P1^{37.5,11}$ | 20.8 | 13.3 | 14.5 | 52.5 | 11 | 3 | 0.23 | 130.5 | 36.6 |
| $P2^{37.5,11}$ | 17.6 | 11.2 | 12.2 | 64.8 | 11 | 3 | 0.23 | 142.0 | 28.9 |
| $P3^{37.5,11}$ | 16.5 | 10.6 | 11.5 | 70.6 | 11 | 3 | 0.22 | 149.0 | 26.3 |
| $P4^{37.5,11}$ | 15.7 | 10.0 | 10.9 | 77.1 | 11 | 3 | 0.22 | 158.2 | 24.2 |

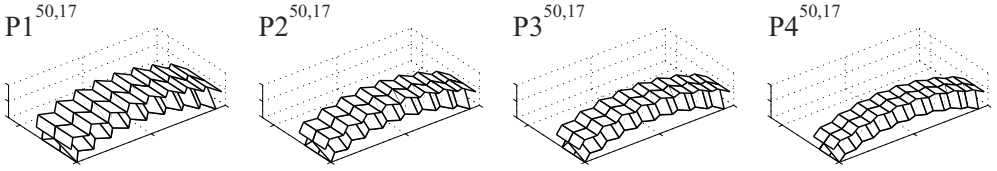


(a) $\Delta b^* = 1/50$, $m = 17$

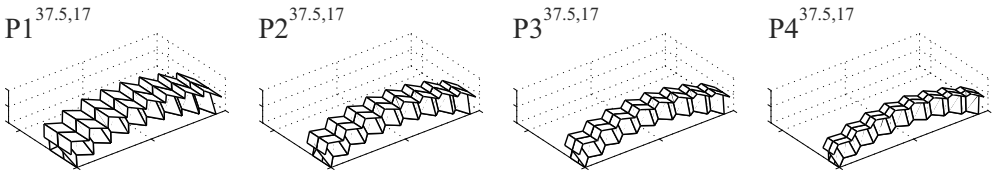


(b) $\Delta b^* = 1/37.5$, $m = 17$

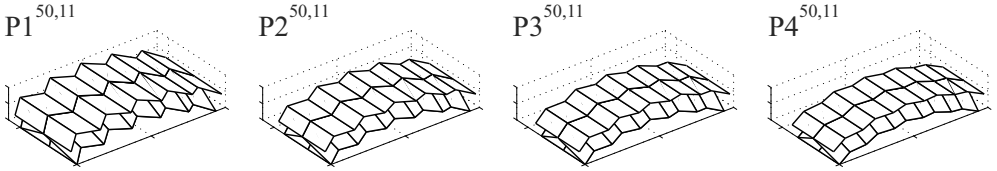


(c) $\Delta b^* = 1/50$, $m = 11$

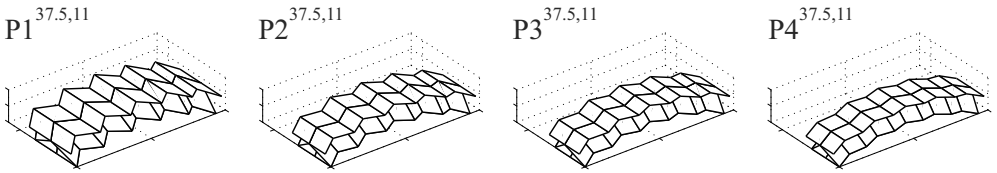


(d) $\Delta b^* = 1/37.5$, $m = 11$

Figure 5.40: ND-type sandwich shell parametric study models.

### Numerical Analysis and Discussion

Numerical models were analysed in the manner described previously, with results summarised in Table 5.17 and a scatter plot of the relative model energy-absorption suitability shown in Figure 5.41(a).

Table 5.17: Results of ND-Type sandwich shell parametric study models.

| *Model* | $P^*_{max}$ (mm) | $P^*_{avg}$ (mm) | $U^*$ | *Model* | $P^*_{max}$ (mm) | $P^*_{avg}$ (mm) | $U^*$ |
|---|---|---|---|---|---|---|---|
| $P1^{50,17}$ | 0.89 | 0.79 | 1.13 | $P1^{50,11}$ | 0.43 | 0.34 | 1.26 |
| $P2^{50,17}$ | 1.14 | 0.97 | 1.17 | $P2^{50,11}$ | 0.54 | 0.40 | 1.35 |
| $P3^{50,17}$ | 1.34 | 1.01 | 1.33 | $P3^{50,11}$ | 0.50 | 0.38 | 1.32 |
| $P4^{50,17}$ | 1.40 | 1.01 | 1.39 | $P4^{50,11}$ | 0.51 | 0.35 | 1.46 |
| $P1^{35,17}$ | 1.12 | 0.92 | 1.22 | $P1^{35,11}$ | 0.69 | 0.53 | 1.30 |
| $P2^{35,17}$ | 1.32 | 1.10 | 1.20 | $P2^{35,11}$ | 0.78 | 0.61 | 1.28 |
| $P3^{35,17}$ | 1.35 | 1.15 | 1.17 | $P3^{35,11}$ | 0.74 | 0.63 | 1.17 |
| $P4^{35,17}$ | 1.46 | 1.12 | 1.30 | $P4^{35,11}$ | 0.87 | 0.69 | 1.26 |

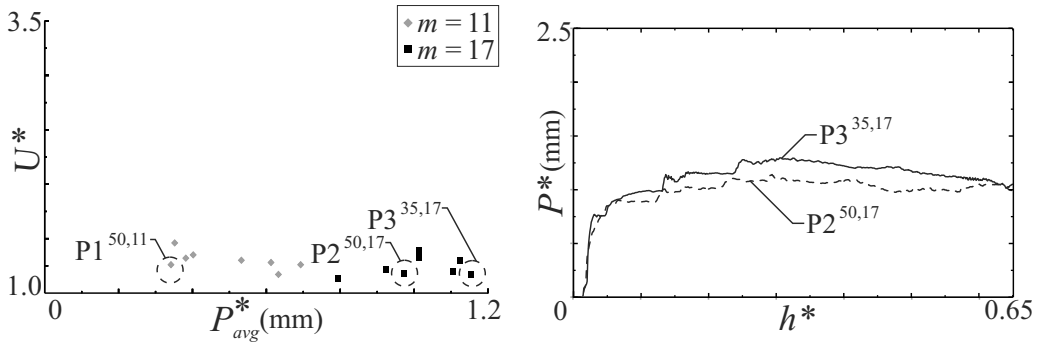


(a) Energy absorption suitability (b) Normalised force-displacement responses

Figure 5.41: Numerical responses of ND-Type shell parameter study models.

It can be seen that the parametric study yields a configuration with modest improvement in energy-absorption capacity, $P3^{35,17}$. Compared to the experimental configuration $P2^{50,17}$, it has an increase in $P^*_{max}$ of 18.4% and an increase in $P^*_{avg}$ of 18.5%, for a comparable uniformity. Comparison of the two $P2^{50,17}$ and $P3^{35,17}$ normalised force-displacement responses, Figure 5.41(b), shows they have a very similar shape, suggesting similar failure modes. Inspection of the Von-Mises stress of both cores, Figure 5.42(a)-(b), confirms this. It can be seen that they both possess the plate buckling failure mode discussed in Section 5.4.1, with core failure smoothly progressing across adjacent unit cell collapses to give a very uniform

reaction stress.

Referring again to Figure 5.41(a), the lowest performing single-curved foldcore is $P1^{50,11}$. Compared to the optimum $P3^{35,17}$, it has a 61.7% lower $P^*_{max}$ and a 70.4% lower $P^*_{avg}$, although inspection of the Von-Mises stresses, 5.42(c) shows that it has a similar unit cell failure. The low performance of $P1^{50,11}$ might simply be explained by the fact that it has the highest foldcore unit cell volume relative to the crush height, and so has a low reaction force when normalised over the impacted panel width $d_w$. $P3^{35,17}$ has the second- lowest of foldcore unit volume, just behind $P4^{35,17}$. This suggests that in general, for a given design radius, a foldcore shell configuration with a lower unit cell volume will have a higher energy-absorption capability, although exceptions exist at geometric extremes, i.e. $P4^{35,17}$, so this is only an approximate relationship.

To conclude, this study has shown that even over a limited, three-variable configuration space, a parametric study on an ND-type foldcore shell can generate significant changes in energy-absorption capability, without necessarily causing a change in failure mode. Foldcore shells with different core types and design radii were excluded from the present study, due to the aforementioned shortcomings of the existing numerical and experimental methods. Future studies will develop more robust experimental construction methods, and improved core-face bonding properties for numerical simulations, to allow a more comprehensive parametric investigation of foldcore shell performance.

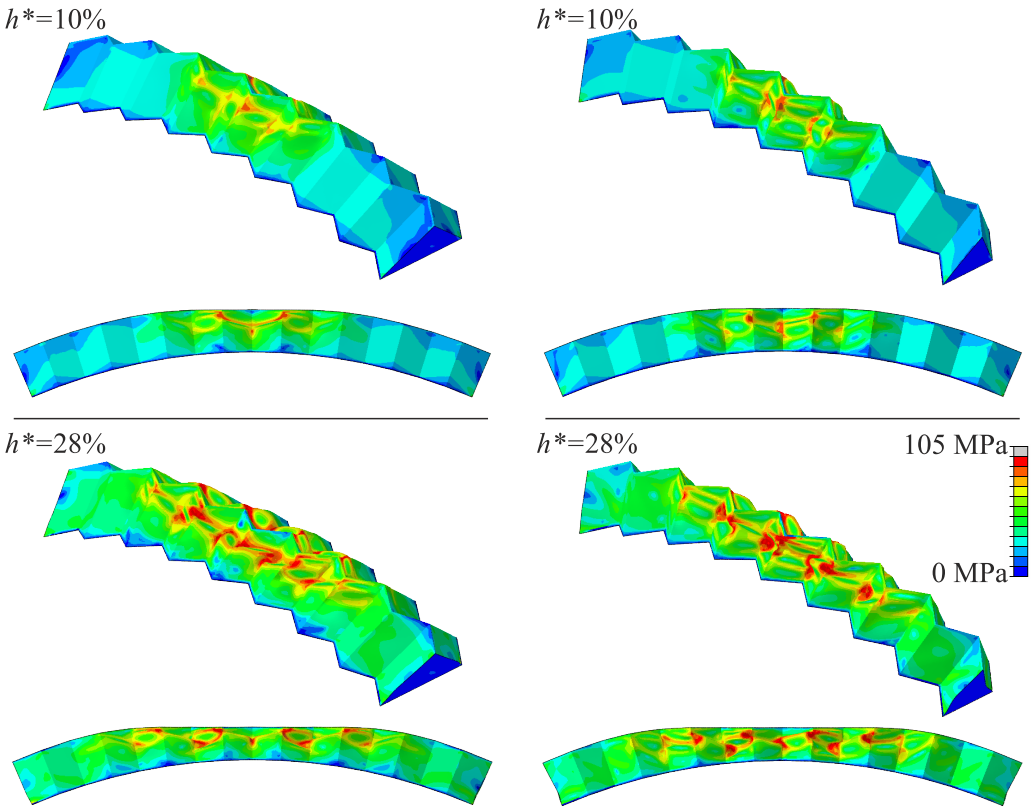


(a) $P2^{50,17}$ (b) $P3^{35,17}$

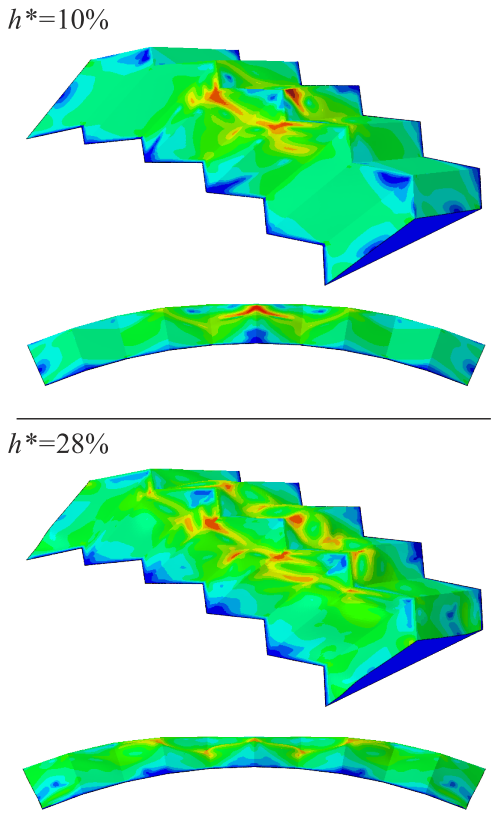


(c) $P1^{50,11}$

Figure 5.42: Selected foldcore shell Von-Mises stress and core failure modes in isometric view (top) and section view (bottom). Top shell face is omitted for clarity.

## 5.5 Conclusion

This chapter has presented several findings relating to the performance of extended foldcore geometries under impact loading. First, numerical analyses and experimental testing on planar curved-crease geometries showed that a maximum value for the gradient parameter gave the best energy-absorption for a given configuration. An experimental study was then conducted on curved-crease geometries with an optimum gradient parameter, with small-scale curved-crease prototypes constructed that were comparable to the small-scale foldcores of Chapter 3. There was generally good correlation between experimental and simulated responses and failure modes, although several shortcomings of the present manufacturing method were highlighted, relating to improper material contraction across the curved-crease foldcore width. A parametric study on curved-crease parameters established an optimum configuration that had comparable energy-absorption to a honeycomb core, and superior energy-absorption to the standard and indented straight-crease foldcores.

Three brief studies were then conducted on other important markers of foldcore performance. The first study assessed the out-of-plane stiffness of various foldcore types. In general, curved-crease foldcores were stiffer than straight-crease foldcores, with the optimum curved-crease configuration having a comaprable stiffness to honeycomb. The second study assessed inertial effects in foldcores under low-velocity impacts. It was seen that there was minimal strengthening in the standard and indented foldcores, and moderate strengthening in the curved-crease foldcores, although not to the extent seen for honeycomb. Finally, the failure of complete sandwich panels was assessed. It was seen that the attachment of sandwich faces did not significantly alter the impact resistance of any of the core types.

A numerical and experimental investigation was then conducted into single-curved foldcore sandwich shells. An initial study showed Non-Developable Miura and Arc-Miura type foldcores to have similar impact resistance to each other, and superior impact resistance to Non-Flat Foldable type foldcores. Prototypes of ND and AM-type sandwich panels were then successfully constructed at a 120mm inside radius of curvature, but could not be constructed at a tighter 60mm inside radius of curvature. Experimental prototypes were tested under quasi-static impact loads and the results used to validate numerical models. These were rerun with high-strength aluminium material properties and compared to the experimental performance of an over-expanded type honeycomb sandwich panel. It was seen that the the Ox-Core has superior impact resistance than either foldcore type, however the AM-type shells possessed superior initial strength, and the ND-type shells possessed superior response uniformity, properties which might be exploitable with further single-curved foldcore shell research. A brief parametric study on ND-type shells was seen to produce modest improvements in energy-absorption capability but no change in failure mode.

There are several short-comings in the present single-curved sandwich shell investigation. It was seen that the rigid-tie core-face constraints did not accurately predict face de-bonding behaviour. Similarly, it was seen that existing manufacturing methods were unable to produce R60 foldcores and so it is unknown if the numerical models used to predict foldcore behaviour at this radius are accurate. However, numerical models were judged to be adequate to give preliminary insight into shell energy-absorption mechanisms, which was the primary goal of this study. It is expected that numerical and experimental shortcomings will be rectified in future foldcore shell investigations. Future investigations should also consider curved-crease foldcore shell geometries and non-local impact loading scenarios, for example global failure of arch-like structures under impact loading.

# Chapter 6

# Conclusion

This thesis has been primarily concerned with the development and improvement of foldcore sandwich panels suitable for high-performance energy absorption applications. The major findings of this thesis can be briefly summarised with the following four conclusions:

- The introduction of sub-folds to existing foldcore geometry can alter foldcore failure modes and generate significant improvements in foldcore energy absorption capabilities.
- Rigid origami design principles can be used to vastly extend the range of available foldcore geometries.
- Curved-crease foldcore geometries were seen to have significantly improved energy absorption capabilities compared to straight-crease foldcores, and can potentially match the strength, energy absorption under quasi-static impact loads, and out-of-plane stiffness of a honeycomb core.
- Single-curved foldcore sandwich shells could not match the energy absorption capability of an over-expanded honeycomb shell, but certain core types did exhibit other attributes that might be exploitable with future research, including superior initial strength and superior uniformity of response.

## 6.1 Summary of Findings

### 6.1.1 Indented Foldcores

Chapter 3 presented a new, indented foldcore developed by introducing sub-folds in the form of a small indent along the top ridge of a standard foldcore. It was shown that the indent can successfully trigger a high-order failure mode known as a travelling hinge line failure mode. This failure mode was seen to have a much higher and more uniform energy absorption than the plate buckling failure mode seen in standard foldcores. A numerical analysis established an optimum standard and indented geometry with maximum energy absorption. Based on numerical observations, a theoretical prediction for the energy absorption of an idealised indented foldcore failure mode was developed, which was able to provide a good approximation of the maximum crushing stress of the optimum indented geometry, but not for other geometries that also exhibit travelling hinge modes.

Two experimental studies were conducted to validate and expand the numerical and theoretical findings. Large-scale prototypes, with no visible geometric imperfections, exhibited travelling hinge line failure modes as predicted. A new method for prototyping foldcores utilising 3D printed moulds was then developed, which enabled construction of standard and indented aluminium foldcores that were directly comparable to existing commercial honeycombs. This manufacturing method introduced geometric imperfections into foldcore prototypes, which were seen to suppress indented foldcore travelling hinge line failure modes. These imperfections were incorporated into numerical models to give good prediction of experimental results, both for stress-strain responses and observed failure modes. Imperfect numerical models were rerun with honeycomb aluminium material properties, and it was shown that compared to honeycomb cores, the indented foldcore have an improved uniformity of energy absorption, but a weaker overall response.

### 6.1.2 Extended Foldcore Geometry

Chapter 4 utilised rigid origami design principles to develop extended foldcore geometry in several ways. Three new patterns were parametrised to complete a set of Miura-base first-level derivative geometries. The parametrisations allowed simple simulation of pattern folding motion and were validated by comparison with physical prototypes. It was then shown how the consistent parametrisation across the set of first-level derivative geometries allowed for them to be combined into complex, rigid-foldable, piecewise geometries. A new method for attaching faceted sandwich faces to single-curved and piecewise cores was then shown, with faceted faces shown to possess a continuously connected edge between face and core structures.

A new method for generating rigid-foldable, curved-crease geometry from Miura-derivative prismatic base patterns was then developed. The two stages of the method, the ellipse creation stage and rigid subdivision stage, were first demonstrated on a Miura base pattern to generate a Curved-Crease Miura pattern. It was shown that a single additional parameter was sufficient to completely define the curved-crease variant. The process was then applied to the Tapered Miura, Arc, and Arc-Miura patterns to generate curved-crease variants for each. Finally, it was shown how the method provided several benefits in addition to the minimum parametrisation. These included the ability to alter the ellipse creation method to generate different curved-crease tessellations, and the ability to preserve geometric solutions of the prismatic base pattern such as closure and faceted face geometry. All parametrisations presented in this thesis have been compiled into a MATLAB Toolbox that is freely available to use for research purposes. It can be downloaded from `www.joegattas.com/resources`.

### 6.1.3 Extended Foldcore Analysis

Chapter 5 conducted numerical and experimental analyses on several of the extended foldcore geometries developed in Chapter 4. An experimental study on curved-crease geometries with $\varphi = \varphi_{max}$ showed that curved-crease foldcores were significantly stronger than straight-crease foldcores, but more susceptible to material stretching during manufacture. A parametric study on curved-crease foldcore was then conducted, with two main findings. First, second tessellation models were seen to have comparable failure modes and energy-absorption to half-aspect first tessellation models. From this it was concluded that altering the tessellation of a curved-crease foldcore was unlikely to provide significant energy-absorption capability beyond that achievable with direct changes to the plate aspect ratio. Second, an improved configuration of the curved-crease foldcore was found, which appeared to offer a comparable strength and energy-absorption capabilities to a honeycomb core.

Three brief studies were then conducted on related aspects of straight-crease and curved-crease planar foldcore performance. The first study considered core out-of-plane stiffnesses. Curved-crease foldcores were seen to have a higher out-of-plane stiffness that was less sensitive to geometric imperfections, compared to straight-crease foldcores. The optimum curved-crease foldcore configuration was the only foldcore with a comparable out-of-plane stiffness to a honeycomb core. The second study considered change in core failure with dynamic, rather than quasi-static loading. Curved-crease foldcores were the only foldcore that saw a substantial increase in energy absorption under dynamic loading. This was attributed to micro-inertial strengthening of progressive hinge lines during collapse, similar to that seen in honeycomb. Despite this, it did not strengthen to the same extent as honeycomb, and so the latter was judged to be have superior impact resistance under dynamic load conditions. The third study considered how the attachment

of sandwich panel faces would alter the impact resistance and failure modes of various core types, excluding consideration of the indented foldcore. Failure was not significantly altered for any sandwich type, although the small changes in sandwich performance were successfully incorporated into sandwich numerical models.

The final study of Chapter 5 considered the performance of straight-crease, single-curved sandwich shells. It was shown that Non-Developable Miura and Arc-Miura type shells have similar impact resistance to each other, and superior impact resistance to Non-Flat Foldable type shells. Prototypes of ND and AM-type sandwich shells were successfully constructed at a 120mm inside radius of curvature, but could not be constructed at at tighter 60mm inside radius of curvature. Foldcore numerical models were run with high-strength aluminium material properties and compared to the experimental performance of an over-expanded honeycomb sandwich shell. It was seen that the over-expanded honeycomb had a better energy absorption capacity than either of the foldcores. However the AM-type foldcore possessed superior initial strength, and the ND-type possessed superior response uniformity. A brief parametric study on ND-type shells suggested that in general, for a given design radius, a foldcore shell configuration with a lower unit cell volume will have a higher energy-absorption capability.

## 6.2 Future Work

This thesis has established preliminary results for a large number of new types of foldcore sandwich structures, and as such has opened up many more avenues for research. In brief, the majority of these open research questions pertain to applying the foldcore improvement methods developed in Chapter 3 to extended geometries of Chapter 5. Specifically, altering the core failure mode through the introduction of sub-folds was seen to substantially increase the standard Miura-type foldcore response. Such an alteration might therefore also be capable of improving curved-crease foldcores and single-curved foldcore shells. Similarly, curved-crease geometry was seen to provide significant improvement to straight-crease geometries for planar foldcores, and so it likely that curved-crease single-curved shells would improve upon the performance of the studied single-curved straight-crease shells. The development of improved manufacturing methods would assist with these investigations, and also allow experimental validation of the optimum curved-crease configuration performance, and a better investigation of tight-radius foldcores and foldcore shell de-bonding.

In terms of geometry development, the rigid-foldable curved-crease approximation developed in this thesis provides a convenient method to fold curved-crease geometries, but does not answer many fundamental questions pertaining to such shapes. For instance, it is unknown how a rigid-strip curved-crease approximation is different to an exact, curved-crease surface, and whether these differences affect curved-crease foldcore modelling, manufacture, and performance. In pursuit of improved foldcore shells, it might also be useful to develop Non-Developable Miura and Non-Flat Foldable Miura curved-crease variants.

# Bibliography

Adams, R. and Maheri, M. (1993). The dynamic shear properties of structural honeycomb materials. *Composites science and technology*, **47**(1), 15–23.

Albermani, F., Khalilpasha, H., and Karampour, H. (2011). Propagation buckling in deep sub-sea pipelines. *Engineering Structures*, **33**(9), 2547–2553.

Alekseev, K. A. (2011). Geometrical simulation of regular and irregular folded structures. *Russian Aeronautics (Iz VUZ)*, **54**(1), 84–88.

Asadi, M., Vollaire, A., Ashmead, M., and Shirvani, H. (2007). Experimental test and finite element modelling of pedestrian headform impact on honeycomb sandwich panel. In *18th Engineering Mechanics Division Conference (EMD2007)*.

Ashby, M. F. (2000). *Metal foams: a design guide*. Butterworth-Heinemann.

Basily, B. B. and Elsayed, E. A. (2004). Dynamic axial crushing of multi-layer core structures of folded chevron patterns. *International Journal of Materials and Product Technology*, **21**(1/2/3), 169–185.

Boyer, H. (2002). *Atlas of Stress-Strain Curves*. ASM International, Materials Park, Ohio, 2nd edition.

Buri, H., Stotz, I., and Weinand, Y. (2011). Curved folded plate timber structures.

In *IABSE-IASS 2011 London Symposium, vol. CD-ROM IABSE-IASS, 2011*, London, England.

Corex Honeycomb (2013). Aluminium honeycomb core. [online] Available at: `http://www.corex-honeycomb.com/`. Accessed March 2013.

Crupi, V. and Montanini, R. (2007). Aluminium foam sandwiches collapse modes under static and dynamic three-point bending. *International Journal of Impact Engineering*, **34**(3), 509–521.

Crupi, V., Epasto, G., and Guglielmino, E. (2013). Comparison of aluminium sandwiches for lightweight ship structures: Honeycomb vs. foam. *Marine Structures*, **30**, 74–96.

De Temmerman, N., Mollaert, M., Van Mele, T., and De Laet, L. (2007). Design and analysis of a foldable mobile shelter system. *International Journal of Space Structures*, **22**(3), 161–168.

Demaine, E., Demaine, M., Koschitz, D., and Tachi, T. (2011a). Curved crease folding: a review on art, design and mathematics. In *Proceedings of the IABSE-IASS Symposium: Taller, Longer, Lighter (IABSE-IASS2011), London, England, September 20-23*, London, England.

Demaine, E., Demaine, M., and Koschitz, D. (2011b). Reconstructing David Huffman's legacy in curved-crease folding. In P. Wang-Iverson, R. J. Lang, and M. Yim, editors, *Origami 5: Fifth International Meeting of Origami Science, Mathematics, and Education*, pages 39–52. Taylor & Francis Group.

Deshpande, V. and Fleck, N. (2000). High strain rate compressive behaviour of aluminium alloy foams. *International Journal of Impact Engineering*, **24**(3), 277–298.

Deshpande, V. S. and Fleck, N. A. (2003). Energy absorption of an egg-box material. *Journal of the Mechanics and Physics of Solids*, **51**(1), 187–208.

Di Landro, L., Sala, G., and Olivieri, D. (2002). Deformation mechanisms and energy absorption of polystyrene foams for protective helmets. *Polymer Testing*, **21**(2), 217–228.

Epps, G. and Verma, S. (2013). Curved folding: Design to fabrication process of robofold. *Shape Modeling International 2013*, pages 75–83.

Fischer, S., Drechsler, K., Kilchert, S., and Johnson, A. (2009). Mechanical tests for foldcore base material properties. *Composites Part A: Applied Science and Manufacturing*, **40**(12), 1941–1952.

Gay, D. and Hoa, S. V. (2007). Sandwich Structures. In *Composite Materials: Design and Applications*, pages 53–68. Taylor & Francis Group, Boca Raton, Florida.

Giglio, M., Manes, A., and Gilioli, A. (2012). Investigations on sandwich core properties through an experimental- numerical approach. *Composites Part B: Engineering*, **43**(2), 361–374.

Gioia, F., Dureisseix, D., Motro, R., and Maurin, B. (2012). Design and analysis of a foldable/unfoldable corrugated architectural curved envelop. *Journal of Mechanical Design, Transactions of the ASME*, **134**(3).

Goldsmith, W. and Sackman, J. L. (1992). An experimental study of energy absorption in impact on sandwich plates. *International Journal of Impact Engineering*, **12**(2), 241–262.

Guida, M., Marulo, F., Meo, M., and Riccio, M. (2008). Analysis of bird impact on a composite tailplane leading edge. *Applied Composite Materials*, **15**(4-6), 241–257.

Harrigan, J., Reid, S., and Peng, C. (1999). Inertia effects in impact energy absorbing materials and structures. *International Journal of Impact Engineering*, **22**(9), 955–979.

Hazizan, M. A. and Cantwell, W. (2003). The low velocity impact response of an aluminium honeycomb sandwich structure. *Composites Part B: Engineering*, **34**(8), 679–687.

Heimbs, S. (2013). Foldcore sandwich structures and their impact behaviour: an overview. In *Dynamic Failure of Composite and Sandwich Structures SE - 11*, volume 192 of *Solid Mechanics and Its Applications*, pages 491–544. Springer Netherlands.

Heimbs, S., Middendorf, P., Kilchert, S., Johnson, A. F., and Maier, M. (2007). Experimental and numerical analysis of composite folded sandwich core structures under compression. *Applied Composite Materials*, **14**(5-6), 363–377.

Heimbs, S., Cichosz, J., Klaus, M., Kilchert, S., and Johnson, A. F. (2010). Sandwich structures with textile-reinforced composite foldcores under impact loads. *Composite Structures*, **92**(6), 1485–1497.

Hexcel Corporation (1999). HexWeb$^{TM}$honeycomb attributes and properties. [online] Available at: `http://www.hexcel.com/Resources/DataSheets/Brochure-Data-Sheets/Honeycomb_Attributes_and_Properties.pdf`. Accessed May 2013.

Hexcel Corporation (2006a). HexWeb ®aluminium Flex-Core ®formable aluminium honeycomb. [online] Available at: `http://www.hexcel.com/Resources/DataSheets/Honeycomb-Data-Sheets/Flexcore_US.pdf`. Accessed May 2013.

Hexcel Corporation (2006b). HexWeb®Honeycomb energy absorption systems design data. [online] Available at: `http://www.hexcel.com/Resources/DataSheets/Brochure-Data-Sheets/Honeycomb_Energy_Absorption_Systems.pdf`. Accessed May 2013.

Huffman, D. A. (1976). Curvature and creases: a primer on paper. *IEEE Transactions on Computers*, **C-25**(10), 1010–1019.

Hull, T. (2006). Exploring flat vertex folds. In *Project Origami: Activities for Exploring Mathematics*, pages 215–230. A K Peters, Ltd., Wellesley, Massachusetts.

Kawasaki, T. (1989). On the relation between mountain-creases and valley-creases of a flat origami. In *Proceedings of the 1st International Meeting of Origami Science and Technology*, pages 229–237.

Kee Paik, J., Thayamballi, A. K., and Sung Kim, G. (1999). Strength characteristics of aluminum honeycomb sandwich panels. *Thin-Walled Structures*, **35**(3), 205–231.

Khaliulin, V. I. (2005). A technique for synthesizing the structures of folded cores of sandwich panels. *Russian Aeronautics*, **48**(1), 8–16.

Kilian, M., Flöry, S., Chen, Z., Mitra, N. J., Sheffer, A., and Pottmann, H. (2008). Curved folding. In *ACM Transactions on Graphics (TOG)*, volume 27, page 75. ACM.

Klett, Y. and Drechsler, K. (2011). Designing technical tessellations. In P. Wang-Iverson, R. J. Lang, and M. Yim, editors, *Origami 5: Fifth International Meeting of Origami Science, Mathematics, and Education*, pages 305–322. Taylor & Francis Group.

Kling, D. H. (2006). Folding methods, structures and apparatuses. US Patent App. 11/440,263.

Künstler, A. and Trautz, M. (2011). Deployable folding patterns using stiff plate elements. *Bautechnik*, **88**(2), 86–93.

Lu, G. and Yu, T. (2003). *Energy Absorption of Structures and Materials*. Woodhead Publishing Limited, Cambridge, England.

Ma, J. and You, Z. (2011). The origami crash box. In P. Wang-Iverson, R. J. Lang, and M. Yim, editors, *Origami 5: Fifth International Meeting of Origami Science, Mathematics, and Education*, pages 277–290. Taylor & Francis Group.

McKown, S., Shen, Y., Brookes, W., Sutcliffe, C., Cantwell, W., Langdon, G., Nurick, G., and Theobald, M. (2008). The quasi-static and blast loading response of lattice structures. *International Journal of Impact Engineering*, **35**(8), 795–810.

Meng, F. X., Zhou, Q., and Yang, J. L. (2009). Improvement of crashworthiness behaviour for simplified structural models of aircraft fuselage. *International Journal of Crashworthiness*, **14**(1), 83–97.

Mines, R., Worrall, C., and Gibson, A. (1998). Low velocity perforation behaviour of polymer composite sandwich panels. *International Journal of Impact Engineering*, **21**(10), 855–879.

Miura, K. (1972). Zeta-core sandwich- its concept and realization. *Inst. of Space and Aeronautical Science, University of Tokyo*, (480), 137–164.

Miura, K. (2009). The science of Miura-ori: a review. In R. J. Lang, editor, *Origami4 : Fourth International Meeting of Origami Science, Mathematics, and Education*, pages 87–99. A K Peters, Ltd., Natick, Massachusetts.

Nguyen, M. Q., Jacombs, S. S., Thomson, R. S., Hachenberg, D., and Scott, M. L. (2005). Simulation of impact on sandwich structures. *Composite Structures*, **67**(2 SPEC. ISS.), 217–227.

Nojima, T. and Saito, K. (2006). Development of newly designed ultra-light core structures. *JSME International Journal, Series A: Solid Mechanics and Material Engineering*, **49**(1), 38–42.

Rouillard, V. and Sek, M. A. (2007). Behaviour of multi-layered corrugated paperboard cushioning systems under impact loads. *Strain*, **43**(4), 345–347.

Ryan, S., Hedman, T., and Christiansen, E. (2010). Honeycomb vs. foam: Evaluating potential upgrades to iss module shielding. *Acta Astronautica*, **67**(7), 818–825.

Santosa, S. (2000). Experimental and numerical studies of foam-filled sections. *International Journal of Impact Engineering*, **24**(5), 509–534.

Schenk, M., Allwood, J., and Guest, S. (2011). Cold gas-pressure folding of Miura-ori sheets. In *Proceedings of International Conference on Technology of Plasticity (ICTP 2011), September 25-30th*, Aachen, Germany.

Shen, J., Lu, G., Wang, Z., and Zhao, L. (2010). Experiments on curved sandwich panels under blast loading. *International Journal of Impact Engineering*, **37**(9), 960–970.

Simulia (2009). *ABAQUS 6.9 Analysis User Manual*. Simulia Corp., Providence, RI, USA.

Smith, M., Cantwell, W., Guan, Z., Tsopanos, S., Theobald, M., Nurick, G., and Langdon, G. (2011). The quasi-static and blast response of steel lattice structures. *Journal of Sandwich Structures and Materials*, **13**(4), 479–501.

Tachi, T. (2009). Generalization of rigid-foldable quadrilateral-mesh origami. *Journal of the International Association for Shell and Spatial Structures*, **50**(162), 173–179.

Tachi, T. (2010). Freeform rigid-foldable structure using bidirectionally flat-foldable planar quadrilateral mesh. In C. Ceccato, L. Hesselgren, M. Pauly, H. Pottmann, and J. Wallner, editors, *Advances in Architectural Geometry 2010 SE - 6*, pages 87–102. Springer Vienna.

Tachi, T. (2011). Rigid-foldable thick origami. In P. Wang-Iverson, R. J. Lang, and M. Yim, editors, *Origami 5: Fifth International Meeting of Origami Science, Mathematics, and Education*, pages 253–264. Taylor & Francis.

Talakov, M. A. (2010). Investigation of folded structure geometry with double curvature. *Russian Aeronautics*, **53**(3), 334–338.

Tessellated Group (2013). Tessellated Group. [online] Available at: `www.tessellated.com`. Accessed April 2013.

Wang, Z.-W. *et al.* (2011). Energy absorption properties of multi-layered corrugated paperboard in various ambient humidities. *Materials & Design*, **32**(6), 3476–3485.

Weinand, Y. (2009). Innovative timber constructions. In *Symposium of the International Association for Shell and Spatial Structures (50th. 2009. Valencia). Evolution and Trends in Design, Analysis and Construction of Shell and Spatial Structures: Proceedings*. Editorial de la Universitat Politécnica de Valencia.

Wierzbicki, T. (1983). Crushing analysis of metal honeycombs. *International Journal of Impact Engineering*, **1**(2), 157 – 174.

Wierzbicki, T. and Abramowicz, W. (1984). On the crushing mechanics of thin-walled structures. *Journal of Applied Mechanics*, **50**(83), 727–734.

Wu, W. (2010). *Rigid Origami: Modelling, Application in Pre-folded Cylinders and Manufacturing*. Ph.D. thesis, University of Oxford.

Yang, M. and Qiao, P. (2008). Quasi-static crushing behavior of aluminum honeycomb materials. *Journal of Sandwich Structures and Materials*, **10**(2), 133–160.

Zakirov, I. and Alexeev, K. (2006). New folded structures for sandwich panels. In *Proceedings of SAMPE Conference*, Long Beach, California.

Zakirov, I. M. and Alekseev, K. A. (2007). Parameters of a creasing-bending machine as applied to the scheme of transverse rotary shaping of chevron structures. *Russian Aeronautics (Iz VUZ)*, **50**(2), 186–192.

Zarei Mahmoudabadi, M. and Sadighi, M. (2011). A theoretical and experimental study on metal hexagonal honeycomb crushing under quasi-static and low velocity impact loading. *Materials Science and Engineering A*, **528**(15), 4958–4966.

Zhao, H. and Gary, G. (1998). Crushing behaviour of aluminium honeycombs under impact loading. *International Journal of Impact Engineering*, **21**(10), 827–836.

Zhao, H., Elnasri, I., and Abdennadher, S. (2005). An experimental study on the behaviour under impact loading of metallic cellular materials. *International Journal of Mechanical Sciences*, **47**(4), 757–774.

Zheng, J., Xiang, J., Luo, Z., and Ren, Y. (2011). Crashworthiness design of transport aircraft subfloor using polymer foams. *International Journal of Crashworthiness*, **16**(4), 375–383.

Zhou, J., Guan, Z., and Cantwell, W. (2012). The impact response of graded foam sandwich structures. *Composite Structures*, **43**(2), 361 – 374.

# Appendix A

# Pattern Closure and Bi-Stability

Curved shells are often employed in applications requiring a cylindrical or semi-cylindrical geometry. Although the folded shells developed in the thesis were not used in this particular way, the geometric closure conditions for closed cylindrical configurations are defined here for completion. While deriving closure conditions, it was noticed that several patterns displayed geometric behaviour that might be useful in creating new bi-stable structures. Again, this particular application was outside the scope of this thesis, but is highlighted here for completion.

### Tapered Miura Pattern

The Tapered Miura pattern is a planar pattern, so closure conditions refer to the point during pattern folding at which the polar creases form a closed ring. From geometry shown in Figure 4.6, it can be seen that this occurs at:

$$\bar{\rho}' = \frac{2\pi}{m-1} \text{ for } m = 5, 7, 9... \tag{A.1}$$

where the superscript $'$ is used to denote a closed pattern parameter. By combining Equations (4.21), (4.23–24), and (4.26), is it possible to obtain an expression for

$\bar{\rho}$ as a function of a single variable $\eta_{fZ}$, and constants $\phi_c$ and $\phi_f$:

$$\bar{\rho} = \frac{\eta_{fZ}}{2} - \arccos\left(\frac{\cos\phi_c}{\sqrt{1 - \frac{\sin^2\phi_c}{\sin^2\phi_f}(1 - \frac{\cos^2\phi_f}{\cos^2(\eta_{fZ}/2)})}}\right) \tag{A.2}$$

Figure A.1(a) shows $\bar{\rho}$ plotted against variable $\eta_{fZ}$ for different values of $\phi_c$ and $\phi_f$. If the closed parameter $\bar{\rho}'$ is plotted for a certain pattern, in this case a Tapered Miura pattern with $a_c = 20$, $b_1 = 10$, $\phi_1 = 60°$, $\phi_2 = 70°$, $m = 35$, $n = 5$, there are two possible configurations that coincide with the closure condition. Plotting these configurations, Figure A.1(b), confirms that the same Tapered Miura pattern has two closed states. It is possible that this phenomenon may be used to create bi-stable folded plate structure, for example if core plates are able to deform elastically up to a certain point, the structure might snap between the alternative unstressed configurations.

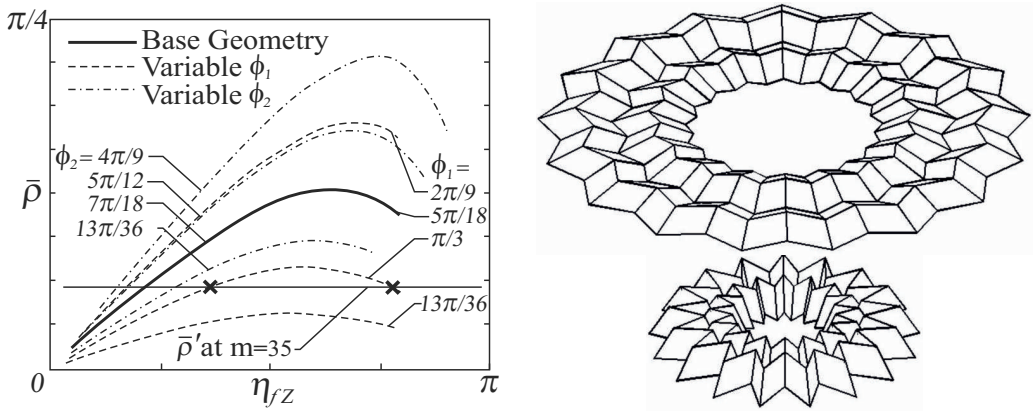


(a) Variation of $\bar{\rho}$ with $\phi_1$, $\phi_2$, and $\eta_{fZ}$ (b) Two closed configurations

Figure A.1: Closure conditions of Tapered Miura pattern.

### Non-Developable Miura Closure Conditions

From geometry shown in Figure 4.1, it can be seen that a Non-Developable Miura pattern forms a closed cylinder when:

$$\gamma' = \frac{\pi}{m-1} \text{for } m = 5, 7, 9... \tag{A.3}$$

By combining Equations (2.1) and (4.1), is it possible to obtain the following expression for $\gamma$ as function of constants $\Delta b/a$ and $\phi$ and a single variable $\eta_A$:

$$\gamma = \arctan\left(\frac{\Delta b}{a}\sqrt{\frac{2(1-\cos\eta_A - 2\cos^2\phi)}{\sin^2\eta_A}}\right)$$

By plotting $\gamma$ against $\eta_A$ it is possible to show the effect of $\Delta b/a$ and $\phi$ on the rate of closure of the cylinder, Figure A.2(a). It can be seen that there is a one-to-one mapping between the $\eta_A$ domain and $\gamma$ range, and so there can only be a single closed configuration at $\gamma'$ for a given pattern. The unique closed configuration of a Non-Developable pattern with $a = 30$, $b_i = 30$, $b_o = 40$, $\phi = \pi/3$, $m = 13$, and $n = 7$ is shown in Figure A.2(b).

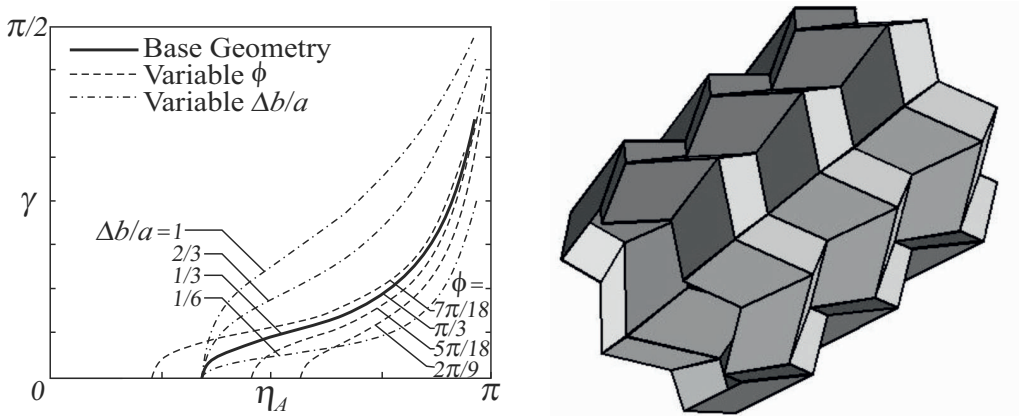


(a) Variation of $\gamma$ with $\Delta b/a$, $\phi$, and $\eta_A$ (b) Unique closed configuration

Figure A.2: Closure conditions of Non-Developable Miura pattern.

**Non-Flat Foldable Miura**

From geometry shown in Figure 4.4, it can be seen that a Non-Flat Foldable Miura pattern forms a closed cylinder at:

$$\zeta' = \frac{\pi}{m-1} \text{ for } m = 5, 9, 13... \tag{A.4}$$

By combining Equations (4.1) and (4.11–12), is it possible to obtain an expression for $\zeta$ as function of constants $\Delta b/a$ and $\phi$ and a single variable $\eta_A$:

$$\zeta = \pi/2 + \gamma + \arccos\left(\frac{\Delta b \sin\phi}{a\cos(\eta_A/2)}\cos\gamma\right) \tag{A.5}$$

where $\gamma$ is a function of $\Delta b/a$, $\phi$, and $\eta_A$ as given by Equation (A.4). By plotting $\zeta$ against $\eta_A$ it is possible to show the effect of $\Delta b/a$ and $\phi$ on the rate of closure of the cylinder, Figure A.3(a). Similar to that seen in the Non-Developable Miura pattern, there is a one-to-one mapping between the $\eta_A$ domain and $\zeta$ range. Therefore there is at most a single closed configuration for a given Non-Flat Foldable cylinder, with an example shown for a geometry with $a = 40$, $b_i = 20$, $b_o = 60$, $\phi = \pi/3$, $m = 45$, $n = 7$ in Figure A.3(b).

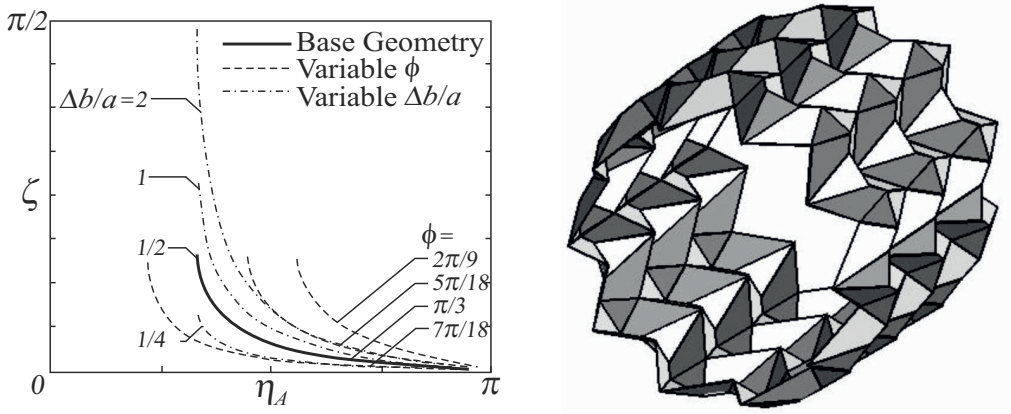


(a) Variation of $\zeta$ with $\Delta b/a$, $\phi$, and $\eta_A$ (b) Unique closed configuration

Figure A.3: Closure of a Non-Flat Foldable Miura pattern.

### Arc-Miura Closure Conditions

The following two equations are obtained from Wu (2010) to describe the closure condition of an Arc-Miura pattern and the variable $\xi$ as a function of two constants, $\phi_1$ and $\phi_2$, and a single variable $\eta_{MA}$:

$$\xi' = 4\pi/(n-1) \text{ for odd } n \tag{A.6}$$

$$\xi = \arccos\left(\frac{A + B\cos\eta_{MA}}{B + A\cos\eta_{MA}}\right) - \eta_{MA} \tag{A.7}$$

where $A = \cos 2\phi_1 - \cos 2\phi_2$ and $B = 1 - \cos 2\phi_1 \cos 2\phi_2$. The variation of this equation with relevant parameters was not explored in Wu (2010) and is shown here for completion. The effect of $\phi_1$, $\phi_2$, and $\eta_{MA}$ on the closure rate is shown in Figure A.4(a). It can be seen that for certain pattern geometries, there are two possible

configurations that coincide with the closure condition for a given geometry. The two closed configurations of an example geometry with $a_1 = 30$, $b_1 = 30$, $\phi_1 = 60°$, $\phi_2 = 45°$, $m = 4$, $n = 25$ are shown in Figure A.4(b). Similar to that seen in the Tapered Miura pattern, this feature may allow for the creation of bi-stable folded plate structures that are able to snap between stress-free configurations.

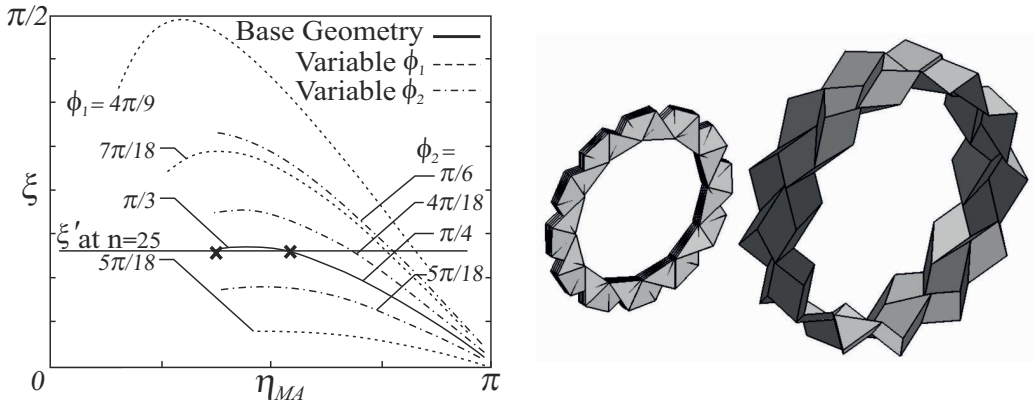


(a) Variation of $\xi$ with $\phi_1$ and $\phi_2$. (b) Two closed configurations

Figure A.4: Closure conditions of Arc-Miura pattern.

### Arc Closure Conditions

As with the Arc-Miura pattern, the closure condition for an Arc pattern is obtained from Wu (2010) as:

$$\eta'_A = \frac{(n-3)\pi}{(n-1)} \text{ for odd } n \tag{A.8}$$

From Equation (2.1), plotted in Figure 3.5, it can be seen that $\eta_A$ is a function of a single pattern constant $\phi$ and pattern variable $\eta_Z$, a relationship which is known to produce a one-to-one mapping between the two dihedral angles. Therefore the Arc pattern has at most a single closed configuration for a given pattern geometry.